

International Journal of Engineering, Construction and Computing (IJECC)

ISSN: 2209-332X(Print)



Volume 1 Issue 1
November 2019

IJECC

International Journal of Engineering,
Construction and Computing



Published by Science Technology and Management Crescent Australia Ltd, ACN 634 288 083, P O Box 170, Minto, New South Wales 2565, Sydney, Australia

in association with

Global Circle for Scientific, Technological and Management Research (GCSTMR), Sydney, Australia
(<http://www.gcstmr.com.au/Home.aspx>)

Copyright ©2019, Science, Technology and Management Crescent Australia Ltd, New South Wales, Australia. Reproduction for academic, research and non-profit purposes are permitted. Responsibility for the contents of the papers in this journal rests upon the authors and not the Editors, Science, Technology and Management Crescent Australia Ltd and Global Circle for Scientific, Technological and Management Research (GCSTMR).

Editorial Board

Chief Editor: Prof Dr Chin Leo, Western Sydney University, Australia

Editors:

Prof Dr Ataur Rahman, Australia (Water Engineering and Education)
Associate Prof Dr Fidelis Mashiri, Australia (Structural Engineering)
Dr Qinghua Zeng, Australia (Chemical and Metallurgical Engineering, Nanomaterials)
Prof Dr Henry Wong Kwai Kwan, France (Geomechanics and Geotechnical Engineering)
Prof Dr Taha B M J Ouarda, Canada (Water and Environmental Engineering)
Dr Rafiqul Islam, Australia (Computer Engineering)
Associate Prof Dr Srikanta Bandyopadhyay, Australia (Materials Science and Engineering)
Prof Dr Phill Kyu Rhee, South Korea (Artificial Intelligence)
Prof Dr Abdallah Shanableh, United Arab Emirates (Water and Environmental Engineering)
Associate Prof Dr Swapan Saha, Australia (Construction Project Management and Engineering)
Prof Dr Vivian Tam, Australia (Construction Project Management and Construction Engineering)
Associate Prof Dr Samantha Liyanapathirana, Australia (Geotechnical Engineering and Education)

Associate Editors:

Dr Vojislav Ilic, Australia
Associate Prof Dr Ramesh Teegavarapu, USA
Prof Dr Chi Zhang, China
Dr Md Rezaul Bashar, Australia
Dr Hasan Hafizur Rahman, Australia
Dr M Muhitur Rahman, Saudi Arabia
Dr Md Kamrul Hassan, Australia
Dr Md Mahmudul Haque, Australia
Dr Payam Rahnamayiezekavat, Australia
Prof Dr Baisakhi Chakraborty, India
Dr M Ashiqur Rahman, Australia
Dr Syed Mohammed Shamsul Islam, Australia
Prof Dr Dipankar Das, Bangladesh

Editorial Coordinators:

Dr Md Kamrul Hassan, Australia
Mrs Jenis Farzana Islam, Australia

Preface

This is the inaugural issue of the *International Journal of Engineering, Construction and Computing (IJECC)*, a peer-reviewed journal devoted to the broad disciplines that the title represents. As diverse as these disciplines may seem to be, they are in fact also very much interconnected and overlapping. The solutions of the complex problems in today's world increasingly require an approach that transcends different disciplines: researchers working together drawing on their disciplinary knowledge, integrating their methods and designs. This journal embodies such an approach. Its mission is to enable academia and industry an avenue to publish research not only within a particular discipline, but also across and at the intersections of the different disciplines of Engineering, Construction and Computing.

Moreover, IJECC is intended as a channel for researchers, including but not limited to those in early career, to disseminate new knowledge and developments from theory to practice. It will cover research papers reporting new theoretical developments, advancements in computational methods, recent experimental findings, innovative design and practice in the real world. As the journal grew out of Western Sydney University, it especially welcomes papers with an educational and research focus. Indeed the inaugural issue features papers that span the broad spectrum from the computational to experimental and field investigation in the real world, including one on water education.

This being the inaugural issue, I would especially like to thank the Editorial Board Members, the reviewers and many others who have made this possible. I am indebted to Jenis Farzana Islam and Dr Md Kamrul Hassan for their editorial coordination and to Sumya Rahman for English editing of the manuscripts. Above all, I am very grateful to Prof Dr Ataur Rahman who has worked tirelessly and single-mindedly to push for this journal to come into fruition.

Prof Chin Leo, PhD

Chief Editor

International Journal of Engineering, Construction and Computing (IJECC)

School of Engineering, University of Western Sydney, New South Wales, Australia,

c.leo@westernsydney.edu.au

The publisher does not take any responsibility for the contents of the papers in this journal. Before using information published in this journal, the contents/materials must be verified by the user at his/her own responsibility. The publisher does not take any liability or loss whatsoever incurred by a user who has used information from this journal.

List of Reviewers

Prof Dr Ataur Rahman
Associate Prof Ming Zhao
Associate Prof Haiping Zhu
Associate Prof Dr Md Humaun Kabir
Associate Prof Abdul Kadar Muhammad
Associate Prof Dr Zia Uddin
Dr Md Mahfuzar Rahman
Dr Helen Wu
Dr Rafiqul Islam
Dr Sameera Wijesiri Pathirana
Dr Muhithur Rahman
Dr Hui Xie
Dr Amimul Ahsan
Dr Mahmodul Haque
Dr Md Kamrul Hassan
Dr Abdullah Al-Mamoon
Dr Ashiqur Rahman
Dr Minhaz Ahmed
Dr Hekang Wang
Dr Abdul Alim
Dr Kevin Xiao
Dr Sayka Jahan
Engineer Caleb Amos
Engineer Shafi Noor
Engineer Anwar Hossain
Engineer Bulbul Ahmed
Engineer Laura Rima

Peer Review Process: Each of the published papers in International Journal of Engineering, Construction and Computing (IJECC), Vol. 1, Issue 1 has been reviewed by at least two independent reviewers. Papers are revised as per reviewers' comments before being finally accepted for publication by the handling Editor and Chief Editor.

Table of Contents

Stability analysis of continuous welded rails using new non-destructive technology <i>Ralph Zhang, Helen Wu, and Chunhui Yang</i>	1
Experimental and numerical studies on SCFs of empty SHS-SHS T-joints under in-plane bending. <i>Feleb N Matti1 and Fidelis R Mashiri</i>	17
Numerical investigation of modified splice plate beam-to-beam connections for prefabricated composite structure. <i>Md Kamrul Hassan and Susma Tajhya</i>	27
Experimental study of bending stiffness variation during a full rotation of cracked shafts. <i>Erfan Taheri, Helen Wu and Ming Zhao</i>	36
Modal analysis of cracked shafts. <i>Erfan Taheri, Helen Wu and Ming Zhao</i>	42
The influence of irrigation area and roof size on the economics of rainwater harvesting use in urban agriculture: a case study in Sydney, Australia. <i>Caleb Christian Amos and Fazlul Karim</i>	48
Energy and exergy analyses of a flat plate solar collector using different nanofluids. <i>Mohammad A. Alim, M.A. Khairul, M. Fazal, R. Saidur, Md Jaynul Abden</i>	59
Morphological assessment of a selected reach of the Jamuna River using the Delft3D Model. <i>Orpita Urmi Laz and Umme Kulsum Navera</i>	72
Impact of urbanization on CO2 and TVOC in an oasis city in Saudi Arabia <i>Muhammad Muhitir Rahman, Ziad Shatnawi, Md Kamrul Islam and Ammar Al-Shayeb</i>	82
Selection of the Best-fit Probability Distribution for Brisbane River Catchment <i>S M Anwar Hossain</i>	90
Water Education: A Case Study in New South Wales Australia <i>Jenis F Islam, Sumya Rahman and Imran Rahman</i>	104
Application of water quality index to identify deteriorated river sections—A case study for the Hawkesbury Nepean River System in Australia <i>Upeka Kuruppu and M Azizur Rahman</i>	124
IoT Based Car Accident Prevention and Detection Using Machine Learning <i>Mohammad Sanaullah Chowdhury and Mubashir Murshed</i>	132

Stability Analysis of Continuous Welded Rails Using New Non-Destructive Technology

Ralph Zhang, Helen Wu, and Chunhui Yang

School of Computing, Engineering and Mathematics, Western Sydney University, Penrith, Locked bag 1797, NSW 2751, Australia

*Corresponding author's email: wei.zhnag@transport.nsw.gov.au

Peer review history

Manuscript submitted: 23 April 2019

Review process completed: 19 August 2019

Manuscript finally accepted: 19 August 2019

Handling Editor: Professor Chin Leo

Abstract: For the safety management of CWR track, the primary is to obtain the accurate neutral temperature of the CWR track (i.e. the value and distribution of the longitudinal stress within the rail). In the recent decade, some newly developed technologies have been utilised for the non-destructive neutral temperature measurement. The Magnetic Barkhausen Noise (MBN) technology is one of them. Within this paper, a series of in-field verifications and data comparison results which are obtained on Australian heavy haul mainline tracks are presented. These results have shown that this MBN measurement system can provide high accurate and reliable neutral temperature results. By using this effective measurement tool, the

neutral temperature on several critical rail lines has been measured. Among these lines, the track structures and conditions are in high diversity. To study the details of the longitudinal stress distribution within the variable CWR tracks, the non-linear finite element analysis modelling is utilised to simulate the track conditions, ambient temperature changing and structural features. The major outcomes from this study including: Firstly, the fastening system and sleeper spacing for a specified CWR track module can significantly impact to its stability. Secondly, for the CWR tracks which are installed on the sharp curves and steep slope, the neutral temperature (longitudinal stress) is not evenly distributed within the CWR module. Thirdly, bending stress in the rails that installed on the sharp curves can influence the thermal stress distribution in the longitudinal direction and it seems it is sensitive with the radius of the curve.

Keywords: High-rise buildings, transfer plate, finite elements, two-stage analysis.

1. Introduction

Obtaining the longitudinal stress (also known as “Neutral temperature” of CWR track in railway industry (Kerr, 2003)) by the non-destructive method is the “Holy Grail” of the continuous welded rails (CWR) track maintenance (Moller, Radmann & Zhang, 2009). Using the non-destructive method to measure the longitudinal thermal stress in CWR tracks is the major important effort direction for railway track engineers and researchers for decades. In the recent years, especially in the last decade, some relative “matured” technologies have been applied for the non-destructive measurement of the longitudinal stresses in the CWR track. The Magnetic Barkhausen Noise is one of them and it has been tested and improved for more than two decades (Wegner, 2004 and Wegner, 2007). Using the finite element method to study the stability of CWR track is started since the beginning of this century (Zhang & Wu, 2006 & Wang, 2015). The utilisation of finite element software ANSYS for this study also can go back to that time (Yang & Gu, 2006).

The Sydney-Broken Hill railway line is now part of the transcontinental railway from Sydney to Perth, which plays very important roles in Australian railway network. The railway line started to connect Sydney (the biggest chief-city on the East Coast of Australia) with the inner of the Australian continental since 1855, until an isolated section of standard gauge line was opened from Menindee to Broken Hill in 1919. In 1969 the last section of the Broken Hill line's gauge was standardised, completing the Sydney - Perth standard gauge link. Originally, this rail line was designed and constructed in the early 20 century with a lower standards and price. On this line, many low strengthen track modules are existed, such as lower rail type (53kg/m rail), low strengthen timber sleepers, sharp curves, steep gradient, etc. To maintenance the stability of the CWR tracks in the very harsh environments passing central desert and facing extremely hot weather in summer time are a great challenge to the permanent of way (Kish, 2009).

To keep the stability of the CWR tracks for the growing freight revenue, the owner of this line found they are facing great challenges from high cost, shortage of man-power, hazard environment conditions and without effective and reliable

inspection equipment. To solve these problems, the RailScan™ system (the equipment based on the MBN technology) was applied as one of the non-destructive CWR neutral temperature testing systems for a feasibility study (Wegner, Hofmann, Radmann, Zhang & Dubbins, 2011). The results represented in this paper are based on two in-field measurements in 2008 and 2009, in Ivanhoe, Menindee, Kinalung, and Broken Hill areas, NSW, respectively.

2. Magnetic Barkhausen Noise Technology

The magnetic Barkhausen noise technology was equipped within a smartly designed machine - RailScan system to carry out the measurement of longitudinal stress distribution in the CWR tracks. Based on the micro-magnetic theory, every part of ferromagnetic materials contributes to the uniform magnetisation. The internal magnetisation is not uniform down to a microscopic scale. Many magnetic domains are magnetised in different directions. The magnetisation inside each domain is made up of many microstructural zones which are lined up by the action of their exchange forces. The schematic drawing of the domain structure is shown in Figure 1.

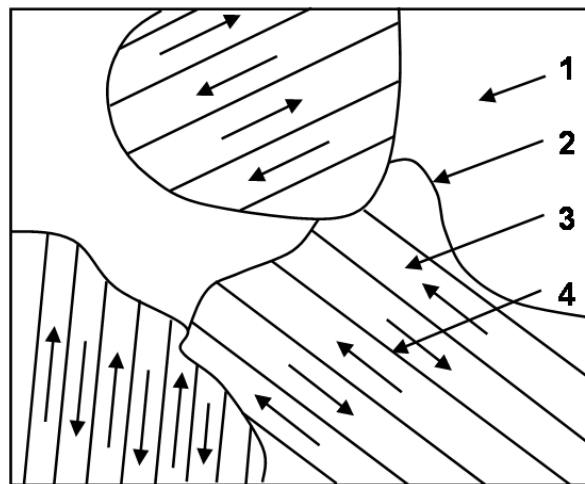


Figure 1: Domain structure of ferromagnetic substances (1-crystallite, 2-grain boundary, 3-Weiss's domain, and 4-Bloch-wall), Chikazumi (1964).

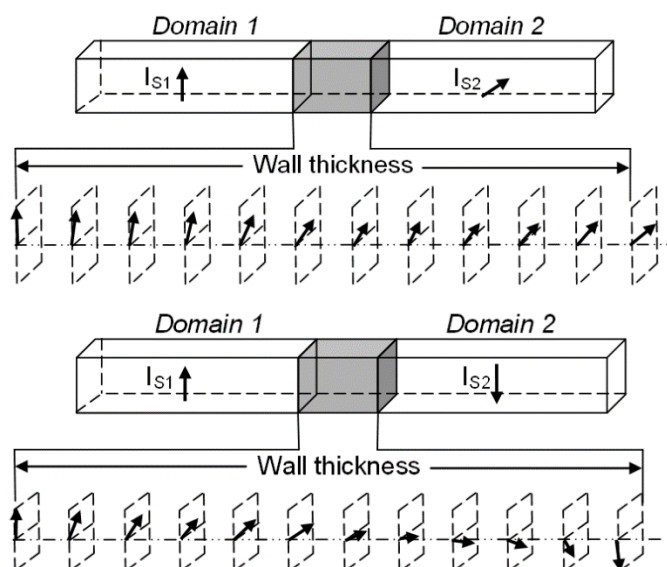


Figure 2: Change of the magnetisation vector in Bloch-walls. 90°-Bloch-wall (BW1-upper figure) and 180°-Bloch-walls (BW2-lower figure, Chikazumi (1964))

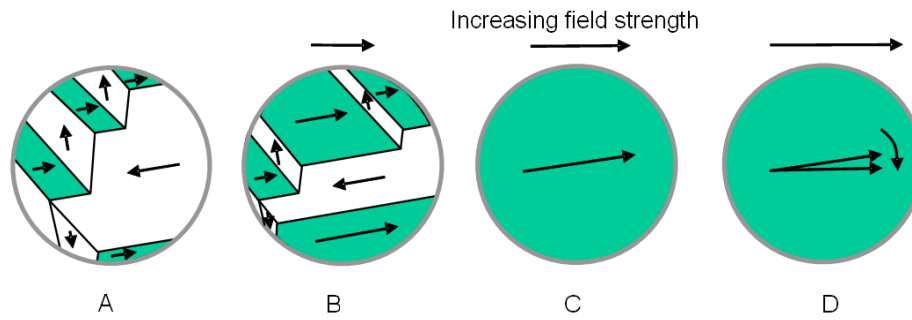


Figure 3: Magnetisation in a [110] direction of Si-Fe: A: domain structure, B-D: orientation process under the action of an increasing magnetic field, Chikazumi (1964).

The crystallites are limited by grain boundaries while the magnetic domains are limited by the Bloch-walls. The domain structure was first predicted by Weiss in 1907 and experimentally verified by Barkhausen in 1919. In 1932, Bloch described that the boundary between the domains is not sharp on an atomic scale but is spread over a certain thickness wherein the direction of spins changes gradually (Chikazumi, 1964). The effect of the existence of such Bloch-walls is shown in Figure 2. Two kinds of Bloch-walls are defined in this figure ---- the 90°- (BW1) and the 180°-Bloch-wall (BW2).

If a magnetic field is applied, the two kinds of domains whose magnetisation directions are closest to the field direction increase their volumes and finally cover the whole domain (Figures 3 B-D). If the field is increased further, the magnetisations in each domain rotate from their easy directions toward the field direction, and finally the saturation magnetisation can be reached (Figure 3d). This process is typical as one important feature of ferromagnetic substances. They exhibit a fairly complex change in magnetisation upon the application of a magnetic field.

This behaviour can be described by a magnetisation curve possessing three distinct regions (Figure 4). Starting from a demagnetised state, the magnetisation increases (broken curve) and finally reaches the saturation magnetisation. In the region "I" the process of magnetisation is almost reversible. That is, the magnetisation comes back to zero upon removal of the field. The domain walls move reversibly and will return to their original position if the field is removed. Beyond this region the processes of magnetisation are no longer reversible. In the low-field region "II" the domain wall movement occurs irreversibly as walls overcome barriers presented by pinning centres in the microstructure. In the highest field region "III" only little domain wall motion occurs and further magnetisation is predominantly due to rotation of the magnetisation vector within individual domains.

In the domain of irreversible wall movement the hysteresis loop has the shape of a stair and Barkhausen jumps occur in the form of micro- eddy currents (enlarged increments on the left side of Figure 4)

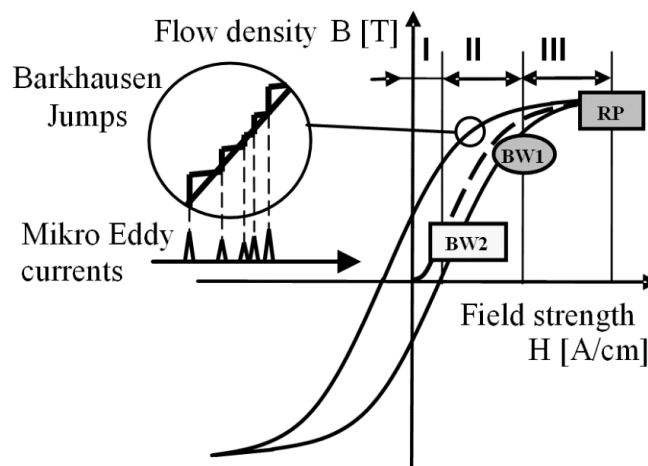


Figure 4: Hysteresis loop: Magnetisation regions I, II and III starting from a demagnetised state and field dependent magnetisation processes by Bloch-wall types BW1 and BW2.

It is essential for further understanding to know the interactions of the different Bloch-walls during the magnetisation. Bloch-walls of the first kind (BW1) are walls which separate magnetic domains in which the residual stresses do not vanish in adjoining domains. In iron all (100)-90° BWs are of this type. Bloch-walls of the second kind (BW2) produce only residual stresses within themselves. In iron all 180° Bloch-walls and the (110)-90° walls are of this type. BW2s separate areas with the same magnetostrictive behaviour and consequently no elastic energy will be changed during their movements. Therefore, BW2s do not interact with macro stresses RS1 and micro stresses RS2. Beside BW1 all rotation processes (RP) are stress sensitive.

BW1, BW2 and RP exist at different magnetic field strengths to the magnetisation process (Figure 4). Following previous work, in polycrystalline ferrous materials BW2 contribute to the magnetisation in a dominant way around the coercive field strength H_c . Outside of this field region BW1 becomes more and more dominant. If magnetisation becomes saturated, BW density decrease and finally remagnetisation processes take place contributed by RPs (Figure 3). Because of these micromagnetic interactions with the microstructures, all the parameters can be recorded with one set of micromagnetic quantities. Hereby stresses are measured by values mainly determined by BW1.

At the microstructural level, the magnetisation process consists of many small discontinuous flux changes, which correspond to the irreversible movement and flopping of Bloch-walls and domains. During this process, micro eddy currents are induced in the domain (Figure 4), enlarged increments of hysteresis loop. These so-called Barkhausen jumps can be measured by using an appropriate detector. Along the hysteresis loop, the MBN shows two maxima around the coercive field strength H_c . The effective value of MBN is generally recognised as a measure for quantitative non-destructive evaluations. It contains the generated pulses and has a noise-like spectrum.

The stress sensitivity of BW1 and RP can be used to measure the longitudinal stress in the rail. In any load stresses applied, the permeability for the applied magnetic field changes. Tension leads to an increase of the permeability. The higher the longitudinal stress, the higher the increase of permeability. The rail becomes more and more magnetisable then.

When compression stress is applied, the rail becomes magnetically hard with increasing compression. The permeability for the magnetic field decreases. This Villari-effect is measurable by analysing Magnetic Barkhausen Noise (MBN) signals. The MBN contains the eddy currents of the stress sensitive parameters BW1 and RP and depends significantly of the longitudinal stress in the rail. Tension increases the amplitude of the MBN, whilst compression leads to decreases. The higher the longitudinal stress, the higher the signal amplitude of the MBN. MBN has the sensitivity with stress conditions in metal materials, which was found by physicists since last century, and it can be equipped with different types of devices to measure the stress condition in CWR rails for decades.

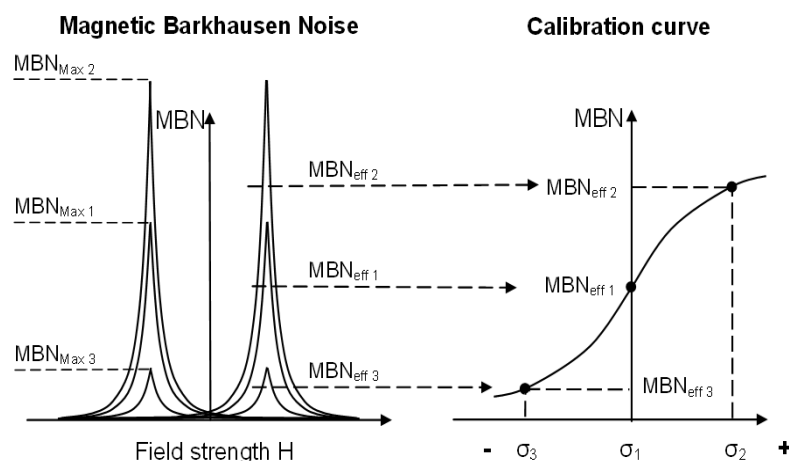


Figure 5: Stress dependence of the MBN used for reconstructing a MBN-stress relationship

3. Measurement Device and Its Operation

The RailScan® system was designed to measure the stress distribution and the Neutral Temperature of continuously welded rails (CWR). The device operates by means of non-contact gauging using the magneto-elastic principle and allows

fast measurement and documentation of the actual Neutral Temperature of rails. The longitudinal stress and the Neutral Temperature are determined by measuring characteristic magnetic values.

The rail is magnetised by applying an alternating magnetic field. Interactions of the magnetic field with the magnetic microstructure are orientation dependant and can be measured with an appropriate probe. The measured signals contain the pulses generated in the rail and have noise-like spectrums. The amplitude of this Magnetic Barkhausen Noise (MBN) depends significantly on the longitudinal stress in the rail. Tension increases the amplitude of the MBN, whilst compression leads to decreases. The higher the longitudinal stress, the higher the signal amplitude.



Figure 6: TRACKSAFE RELEASE (the updated version of RailScan® system) unit

The RailScan® system consists of a manually operated railcar, a central unit, and a pair of probe (Figure 6). The central unit contains the computer-operated measuring electronics. A separate battery provides the power supply for the equipment. The probe consists of two yokes that are pressed around the rail-head with the help of a Bowden wire and springs. The replaceable probe is geometrically adapted to the rail type. The rail temperature is measured with an integral infrared thermometer.

Before performing the measurement the rail was marked. The measurement was made after positioning the device above each mark in turn. The rail was energised by a magnetic field in the acoustic frequency range, and the level of the Magnetic Barkhausen Noise at the surface of the energised region was measured. One measurement series consisted of 50 marked points.

Evaluation was performed automatically after the measurement. The measurement result can be stored and visualised on a PC via data transfer. Data can be read and processed by using Microsoft Office

4. Calibration

Before the RailScan measurements, for each type of rail, the RailScan device must be calibrated in the laboratory using at least three calibration rails, which are the same type and under similar condition with the rails were measured on the track. The calibration rail samples were gauged by strain gauges. The calibration work was carried out by hydraulic rail tensor, and the data are analysed by Weibull factor. On this occasion, measurements of the MBN are taken for different longitudinal stresses and used for obtaining a calibration curve of the MBN as a function of longitudinal stress. The calibration curve of AIS 107LB rail (which is a type of widely used rail on Australian railway network) from these three rail samples is shown in Figure 7. The calibration curve was be used as the base line and collation form, and it worked together with the in-field testing results to determine the neutral temperature of a specified rail track section. Hence, this procedure is a very important section of the measurement. Its results can greatly influence the accuracy of the whole work.

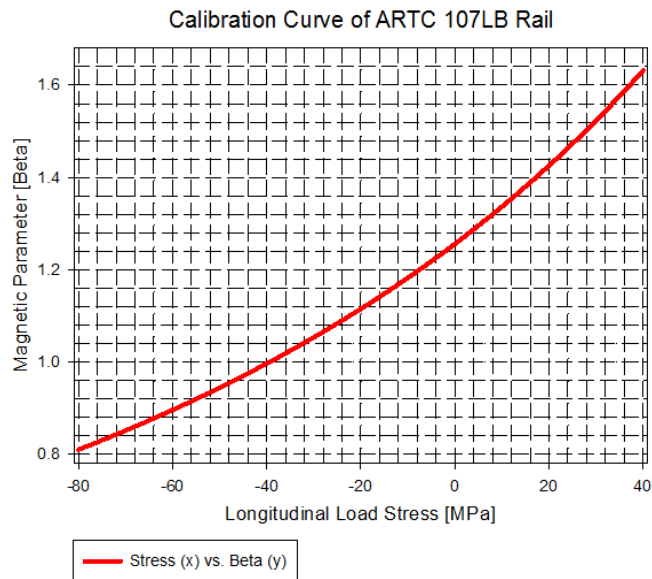


Figure 7: Calibration curve of AIS 107LB plain carbon rail

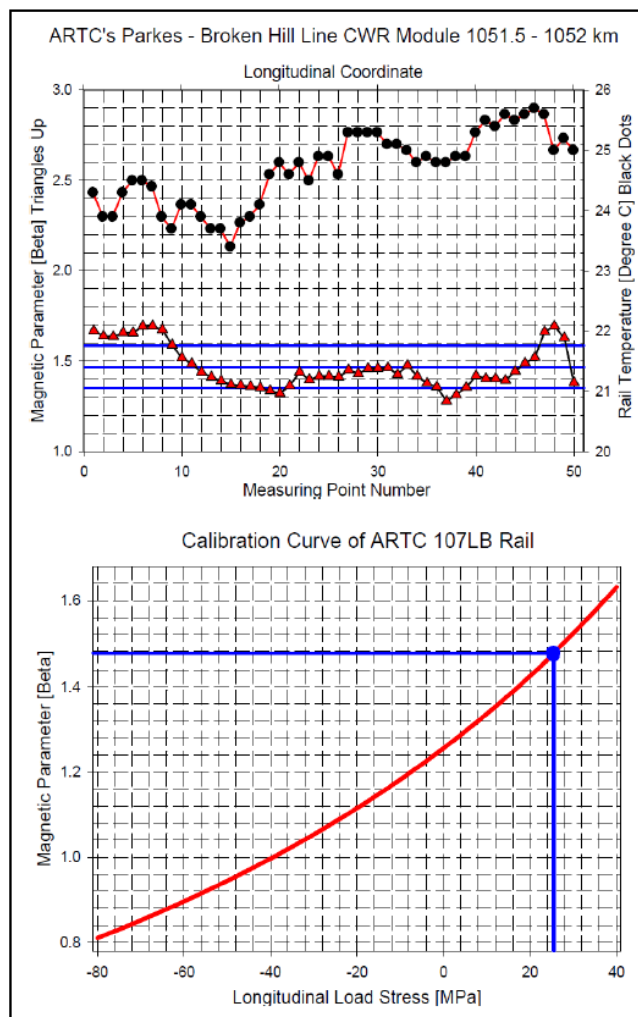


Figure 8: Above: Stress sensitive parameter and rail temperature, plotted vs. longitudinal coordinate. Bottom: Longitudinal load stress determined by means of the rail specific calibration curve.

5. Data Analysis

After completing the measurements the raw data were downloaded to a laptop for further evaluation. The final results were obtained by evaluating and plotting the measured values of the magnetic parameter and rail temperature vs. the longitudinal coordinate and measuring point number and further by depicting the load stress determined by means of the averaged magnetic parameters and calibration curve. The final results were obtained by evaluating and plotting the measured values of the magnetic parameter and rail temperature vs. the longitudinal coordinate and measuring point number and further by depicting the load stress determined by means of the averaged magnetic parameters and calibration curve. As an example, the results and relative calibration information of the CWR module at 1051.5 km - 1052 km are shown as in Figure 8.

The neutral temperature can be calculated by means of the following equation:

$$T_N = \frac{\sigma_L}{E \times \alpha} + T_{Rail}$$

Where:

T_N - The neutral temperature before de-stressing;

T_{rail} - Rail temperature when doing the RailScan measurement;

σ_L - The longitudinal stress in the CWR rail;

α - Thermal coefficient of rail, using 11.5×10^{-6} (m/°C);

E - Elastic modulus, using 2.07×10^5 MPa.

6. Comparison and Confirmation of RailScan Results

Since the year 2006, around 300-km CWR track measurements were conducted on Australian heavy haul operated railway lines. The in-field measurement results were compared with some widely acknowledged method/equipment to confirm the accuracy and reliability of the RailScan system. The results are represented in this paper are from two in-field measurements in 2008 and 2009 on Parkes – Broken Hill Line, respectively. One is in Ivanhoe, and the other is in Menindee.

A series of data comparisons were performed on the data from the in-field testing with the results from VERSE System (which is a commercial product of VORTOK International) and A-Frame (which is a simplified VERSE system).

Considering the Verse system is significantly limited by the operational rail temperature (As the method only can be applied to tracks in tension, the ambient temperature must be lower than the true T_N) and the characteristics of track modules (do not has very accurate track modules for the variable track condition of “timber sleeper assembled by low toe load dog spike” as an input for neutral temperature calculation which combined with the directly in-field measurement results), the results obtained by using the two systems were measured with similar or significant different ambient conditions, hence, the comparisons were conducted separately.

a. Different time but closer rail temperature

Because when VERSE performs its neutral temperature measurement, the track must be un-clipped. Usually, the air temperature when performing the un-clipping works is different to the neutral temperature, and the original neutral temperature can be changed by this way. Hence, the RailScan measurements were carried out before the VERSE system. The results of RailScan and VERSE measured at the closer rail/ambient temperature conditions ($\pm 5^\circ\text{C}$) are represented in Figure 9.

For the situation of the two methods carried out the measurement at different time but closer rail temperature, the results are quite close. The average difference between these two methods is 1.47°C , which is very close. In addition, for these modules the RailScan measurement can be early or later for the Verse measurement and the time gaps are also changed from one day to 3 weeks.

Theoretically, it can be explained as the “change” of the original neutral temperature that caused by the Verse measurement was “destressed” by the railway traffic and relatively lower track frame stiffness (because of the lower toe load of the fasteners).

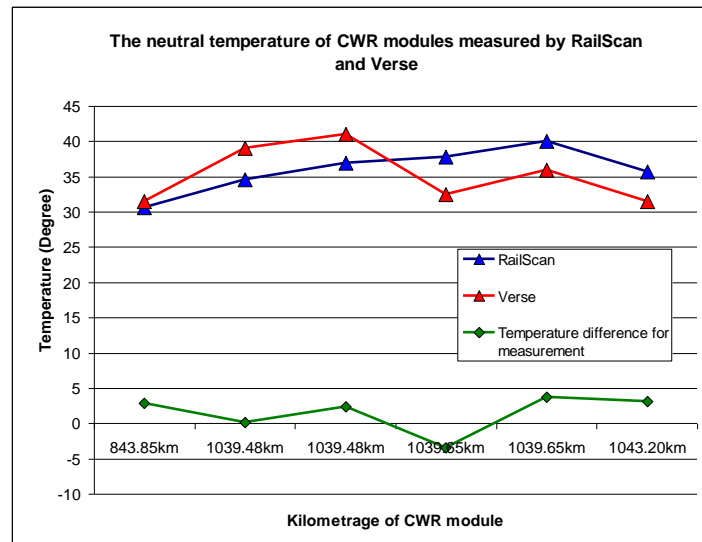


Figure 9: The neutral temperatures of CWR modules measured by RailScan and VERSE

b. Different time with significant different rail temperature

As shown in Figure 10, the results from RailScan and VERSE are significantly different. Because of the VERSE system can only operate in a narrow rail temperature range, therefore, for these modules the rail temperature measured using RailScan and VERSE has an average of 16.7 °C. In addition, the structural strength of the CWR track on the Broken-Hill line was found also relatively low. For example, the track was installed with timber sleepers, reused steel sleepers and dog-spike fasteners, with the extreme high temperature conditions, the creep of CWR track could happened. This creep can be explained as the major reason that caused the 11.5 °C of average neutral temperature result between RailScan and VERSE measurement with an averagely rail temperature difference of 16.7 °C.

Studying the CWR resistant load from the fasteners, the basic concept of fastener design is the longitudinal resistance from the fastener must higher than the ballast resistance on the sleeper, hence, to ensure the rail will not creep on the top surface of the rail seat of sleeper. Therefore, the sleeper, fasteners, and ballast can work together as a frame to provide adequate resistant force for the stability of CWR track.

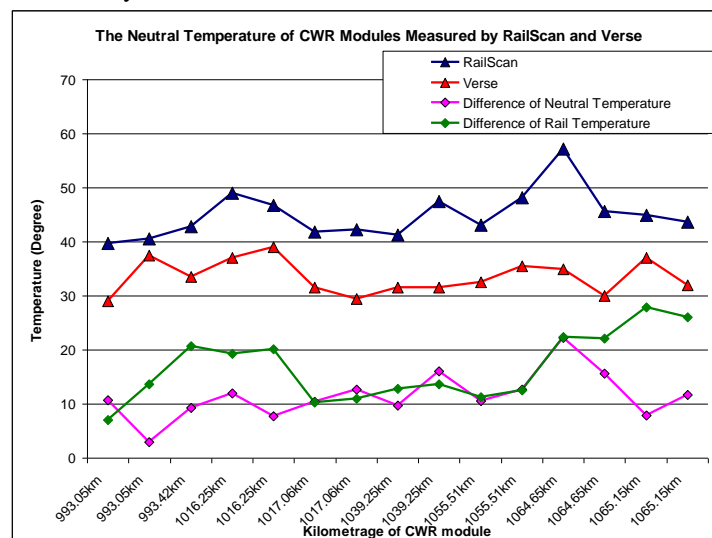


Figure 10: The neutral temperature of CWR modules measured by RailScan and Verse

For a specified CWR track module (1064.65 km):

- With dog-spike fastener, the average toe load using 6 kN (very tightly connected with rail) to very low (for the spike pull-out condition), practically, for the CWR track design, the recommended value by Chinese Railway is 1.25 kN/spike.
- With Trak-Lok fastener, the average toe load using 6 kN/fastener (the usage times surpass its fatigue limitation).

- With Pandrol PR 300 fastener, the average toe load using 6.2 kN/fastener.

For the anchors, they were installed in the style of one in forth as shown in Figure 11. Regarding to the resistance load that provided by the one anchor on one direction, assuming its capability is 15 kN in good installation condition.

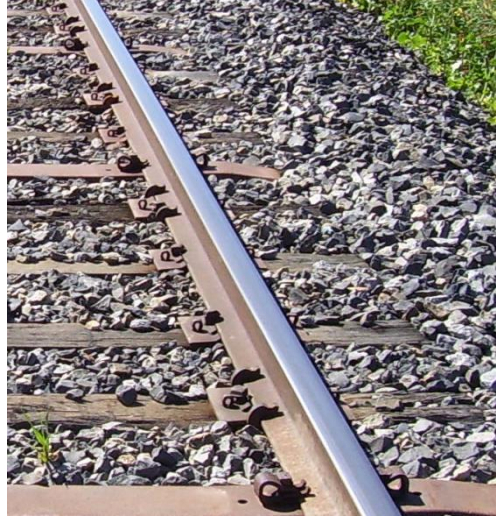


Figure 11: The anchors installed of the CWR track

Table 1: Detailed of the sleeper of the module of 1064.65 km

Frequency number	Sleeper/Fastener type	Frequency number	Sleeper/Fastener type
1	Timber/dog-spike	26	Timber/dog-spike
2	Steel/Trak-Lok	27	Steel/Trak-Lok
3	Timber/Pandrol PR 300	28	Timber/dog-spike
4	Timber/dog-spike	29	Timber/dog-spike
5	Timber/dog-spike	30	Timber/dog-spike
6	Steel/Trak-Lok	31	Timber/dog-spike
7	Timber/dog-spike	32	Timber/dog-spike
8	Timber/Pandrol PR 300	33	Timber/dog-spike
9	Timber/dog-spike	34	Steel/Trak-Lok
10	Timber/dog-spike	35	Timber/dog-spike
11	Timber/dog-spike	36	Timber/dog-spike
12	Timber/dog-spike	37	Timber/Pandrol PR 300
13	Timber/dog-spike	38	Timber/dog-spike
14	Steel/Trak-Lok	39	Timber/dog-spike
15	Timber/dog-spike	40	Timber/dog-spike
16	Timber/dog-spike	41	Timber/dog-spike
17	Timber/dog-spike	42	Timber/dog-spike
18	Timber/dog-spike	43	Timber/dog-spike
19	Timber/dog-spike	44	Timber/dog-spike
20	Timber/dog-spike	45	Steel/Trak-Lok
21	Timber/dog-spike	46	Timber/dog-spike
22	Timber/dog-spike	47	Timber/dog-spike
23	Timber/dog-spike	48	Timber/dog-spike
24	Timber/dog-spike	49	Timber/dog-spike
25	Timber/dog-spike	50	Timber/dog-spike

For the longitudinal axial resistance of timber sleeper, according to the study carried out by Dr. Arnold Kerr in USA (Kerr, 2003), the maximum value is around 9 kN for timber sleeper with 600 mm spacing. In addition, the friction coefficient factor between rail and steel fastener is: 0.2. Using the sleeper data of the module of 1064.65 km, as shown in Table 1, as input data and we obtained the average fastener resistance on each sleeper against one rail is:

$$\{[(\text{Dog-spike: } 42) \times 1.25 + (\text{Trak-lok: } 6) \times 6 + (\text{Pandrol PR: } 2) \times 6.2] \times 4 \times 0.2 + (\text{Steel Anchor one direction: } 11) \times 15 \times 2\} / 50 = [(52.5 + 36 + 12.4) \times 4 \times 0.2 + 165 \times 2] / 50 = 8.2 \text{ kN}$$

The 8.2-kN average resistance load is significantly lower than the requirement of per sleeper ballast resistance which is 9.5 kN for timber sleepers with 600 mm spacing. That means the long rail can creep longitudinally along the rail seat of sleeper, when the rail temperature is different with the neutral temperature.

The above phenomena were confirmed by many in-field results, for example, the results of the CWR module 1065 km – 1065.5 km down rail at Kinalung. The neutral temperature distribution within the CWR module of 1065 km – 1065.5 km (Down rail) was measured twice on 11th and 12th of August, 2009 at different rail temperature. Compare their results in Figure 12 by plotting the result in one figure, it can be found that, the neutral temperature results are different, and the rail temperature on 11th August is significantly higher than that on 12th August. The difference of rail temperature is almost constant and generally the trade of the difference of neutral temperature is also similar. Studying their average values, the average difference for rail temperature is about 6 °C and the average difference of neutral temperature is 5.7 °C. It is very clear that the long rail can creep longitudinally along the rail seat of the sleepers, when the rail temperature is different than the neutral temperature

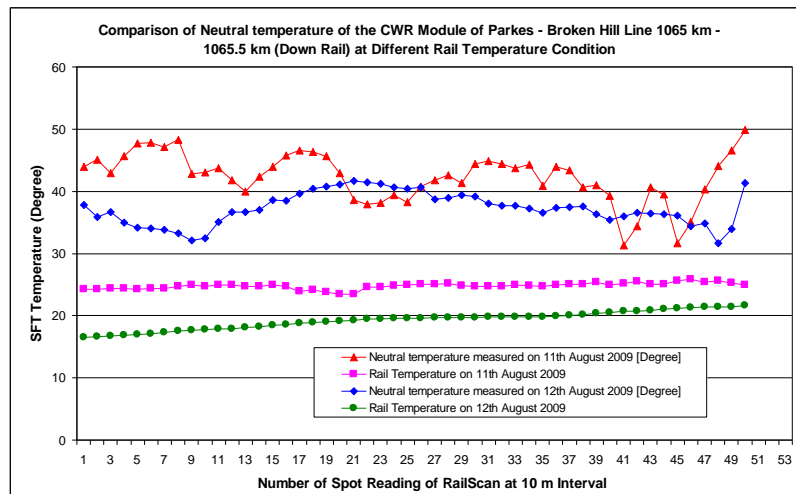


Figure 12: Comparison of neutral temperature of the CWR module of Parkes – Broken Hill Line 1065 km – 1065.5 km (Down rail) at different rail temperature conditions

a. Further study on steep slope CWR modules

The RailScan results can present the neutral temperature changes that caused by some special track structures, such as sharp curve, steep slope, etc. For example, for the CWR module of 1051.5 km – 1052 km, it has a steep slope with the falling is 1:152 (as shown in Figure 13).

The neutral temperatures, obtained from RailScan for the up rail and down rail and diagram of slope, are overlap-plotted in Figure 14. From these figures it can be found that from the start point of steep slope the neutral temperature is going to decrease and reach the minimum results at the location around the bottom of the steep slope. Hence, for the CWR module like this, the critical neutral temperature is the lowest result at the bottom at the slope.

a. Further study on sharp curves

To facilitate the analysis, details of some sharp curve CWR track modules such as the actual radius, super-elevation, start and end kilometrage of transition curve and circular curve were obtained from a database. A curve module and the β factor obtained from Rail Scan at the 50 points are plotted in Figure 15. This module was measured when it was just finish the de-stressing. The kilometrage of the CWR module is 319.630km - 319.911km (North Coast Line), which is located between two steel girder bridges (one of the bridge on the transition curve section). Some findings from the comparison of Rail Scan results and designed destressing results are presented as following:



Figure 13: CWR module of 1051.5 km – 1052 km with a steep slope of falling is 1 in 152

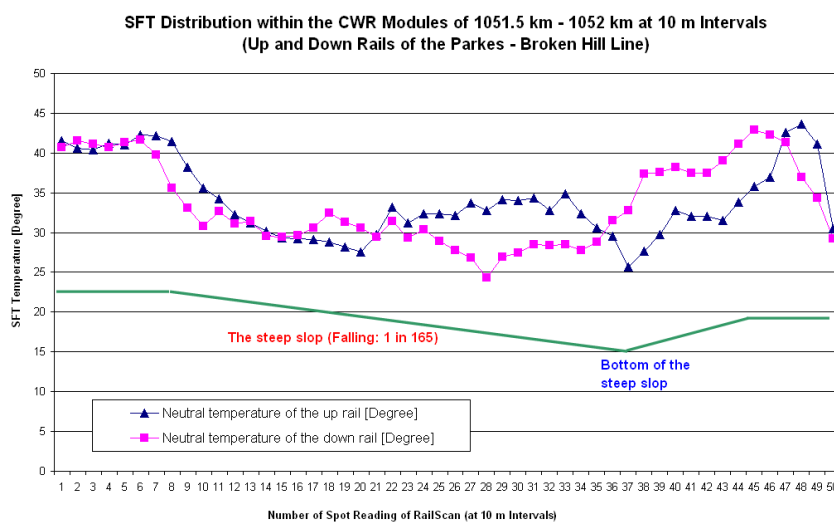


Figure 14: Neutral temperature distribution within the CWR module of 1051.5 km 1052 km (Up and down rail)

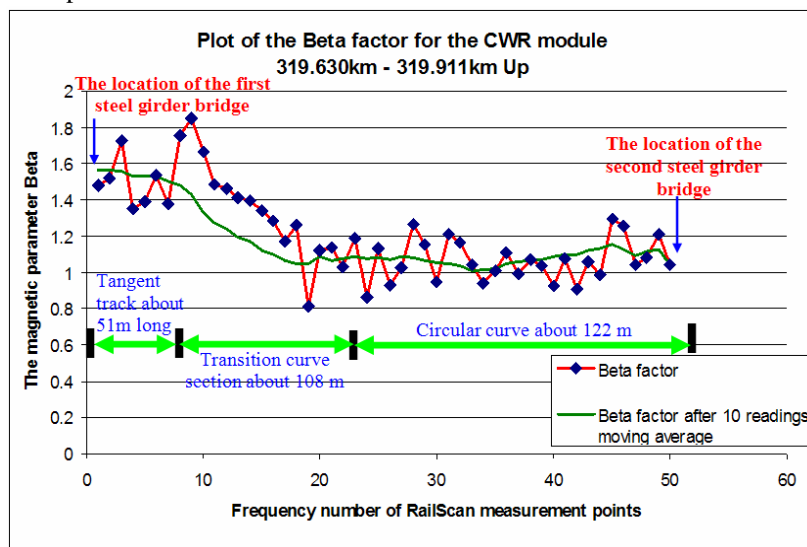


Figure 15: Plot of the factor that obtained from RailScan at the 50 points for a curve module

From Figure 15 and other sharp-curved CWR modules, a significant phenomenon is that the magnetic parameter β is not evenly distributed along the whole curve from transition curve to circular curve. For the module 319.630 km - 319.911 km, it is a combination of about 51 m tangent track, 108 m transition curve, and 122 m circular curve, for the average of their β values, it is 1.5456, 1.24606, and 1.075795, respectively. Combined with their rail temperature, the neutral temperatures are: $T_N = 46.96$ °C for tangent section, $T_N = 34.5$ °C for transition curve, and $T_N = 21.54$ °C for circular

curve. It means that in a sharp curve module, the real neutral temperature at tangent track and transition curve is dramatically higher than circular curve. Based on the knowledge of structural mechanic it can be explained as on the sharp curves the longitudinal thermal stress can be deducted by the bending stress from the sharp curvature bending moment. This phenomenon also happened with every curve modules and influenced by the radius of the curve.

7. Numerical Study of Rail Tracks

To study the details of the longitudinal stress distribution within the variable CWR tracks, the non-linear finite element analysis modelling is utilised to simulate the track conditions, ambient temperature changing and structural features.

a. Finite element modelling of bending of rail track

To understand the amount of the curvature bending moment affect to the longitudinal thermal stress, a finite element model was created to carry out the numerical study. In brief, the strategy of the numerical method was to create a finite element model of a 10 meter length rail (the length is same as the 10 m chord for versine measurement), with applying the side pressure on the rail, and the displacement in the middle of the 10 m rail equal to the versine (10 m chord) of a specified rail radius. Hence, the bending stress in the longitudinal direction that caused by the curvature of curved track can be obtained from the simulation. Then, the longitudinal stress caused by the bending can be calculated to equivalent rail temperature changing. By this way, the deduction of the neutral temperature that induced by the curvature bending track can be understood. The commonly-used finite element software – ANSYS was applied to carry out the numerical study.

For this case study, the versine value at the circular curve of a sharp curve which radius is equal to 300 m was calculated out. The worked out versine value is applied as the target deformation value in the x-direction on the finite element model. For this example the versine was calculated as 41.7 mm. For the devised finite element model, the rail was simulated as the rail profile of the AIS 107LB rail with a 2.86° to the horizontal direction, which is used to simulate the slope of rail seat of 1:20. The rail will be simulated as the low rail of a sharp curve. To achieve the deformation in the x-direction, the pressure load which is 6 kN/m^2 was applied on the rail side surface. Regarding to the boundary conditions, the rail was assumed as the side supported which is similar to a three point bending test support condition.

The x-direction deformation of the finite element analysis is 42.4 mm, very close to the designated versine value which is 41.7 mm. The deformation shape is shown in Figure 16. The most important concern is the distribution of the stress on the longitudinal direction (Z-direction) at the bottom of rail head and the neck.

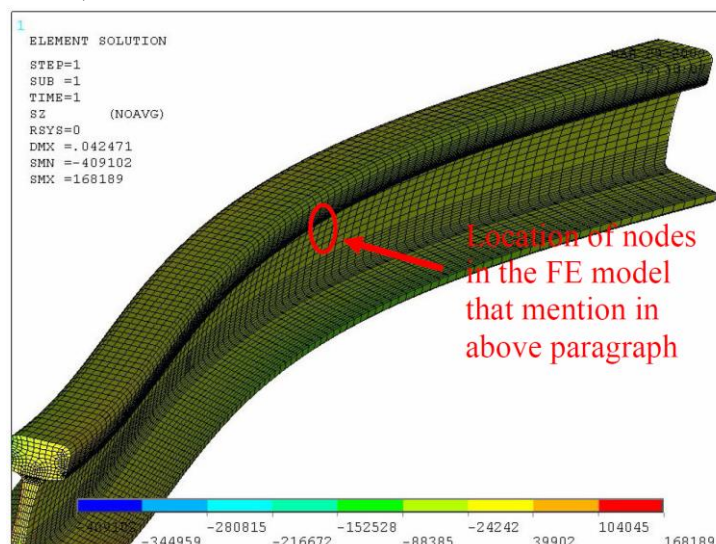


Figure 16: Z-component stress distribution and its deformation shape (scale is 10 times to the actual) of the convex rail's FE model

In addition, the detailed plot of convex side at the maximum versine value which is 42.4 mm located at the middle of the 10 meter rail model shown in Figure 16. From the finite element results, the z-direction stress at the location that has the maximum versine value was studied. At the position of the bottom of the rail head and the rail neck area (the locations to

carry out the RailScan measurement), the stress values at z-direction from the up nodes to bottom nodes are -30.258 MPa, -25.223 MPa, -20.126 MPa, -15.037 MPa, -12.103MPa, -9.9 MPa, respectively. For the CWR track 2.4 MPa stress in the longitudinal direction equal to 1 °C neutral temperature change. Hence, for the above stress values it means on the $R = 300\text{m}$ shape curves on the low rail of the circular curve, the bending from the rail curvature can induce -4.1 to -12.6 °C neutral temperature deduction. The average value is equal to -7.82 °C.

Comparing with the sharp curve CWR module with the radius of $R = 300\text{ m}$ (the CWR module 319.630km-319.911km), the difference between the RailScan result and cutting rail method is -7.21 °C. It is very close to the result from finite element analysis, which is -7.82 °C.

b. Finite element modelling of track strengthening

To understand the amount of influence of ambient temperature change on longitudinal stress distribution on the CWR track, a finite element model was also created to carry out the numerical study by using ANSYS again. To ensure the high accuracy of the FEA model and minimise the influence of its boundary condition, a full scale model of a 100-m curve track was created. Rail and concrete sleepers were simulated by using beam elements with the cross-section input data that are the same as its original shape profile.

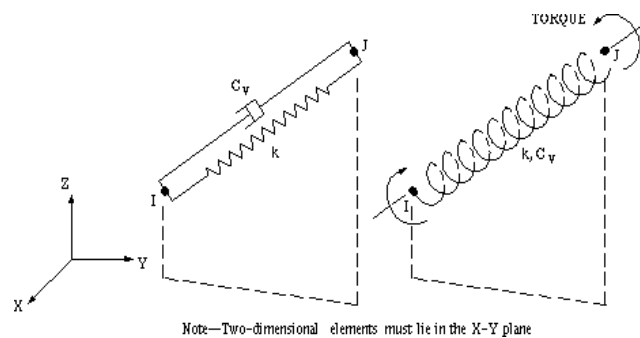


Figure 17: Combined spring-damper element (COMBIN14) used to simulate the ballast resistance on concrete sleeper, ANSYS Co., 2007.



Figure 18: The FEA model which is created to simulate a 100-meter length CWR track of the Sydney – Broken Hill line

Non-linear node-to-node contact elements were applied to simulate the contact and interaction of fasteners and steel rails. The contact problems of the FEA model involve of small relative sliding between contact surfaces and the geometric nonlinearities of the whole structure. The toe load of fasteners were input as the “normal stiffness” k_N . The “sticking stiffness” k_S represents the stiffness in the tangent direction and a input data 0.22 is chosen as the coefficient of friction between the fastener and steel rail plus coefficient between steel and rubber pad.

Lateral and longitudinal resistances of ballast on each sleeper were simulated by using the combined spring-damper with different specified equivalent input stiffness values, which was modelled by using spring-damper element (COMBIN14). The torsion capability of the spring-damper element was fixed for simplification. These elements were directly connected with the beam element of concrete sleepers in the longitudinal and lateral directions.

The boundary conditions of the CWR rails were assumed to be fixed-fixed on one end and fixed in the Y direction on the other end. The spring elements that representing the ballast lateral resistance are fixed on their field side directions, which are the same as the condition of ballast where outside of concrete sleepers. For the nonlinearities of the majority materials in the FEA model, multi-linear Kinematic hardening and von Mises equivalent stress theories were followed.

The thermal load that is equal to 10 °C was applied on the end of the AIS107LB rails. From the FEA solution it can be found that the results of the longitudinal stress changing along the two rails under the thermal load is averagely equal to 9.5 °C of neutral temperature changing. This is confirmed that the average 8.2-kN low toe load of the fastener could not provide enough resistance loading to control the originally set-upped neutral temperature. And it can be seen as evidence to show the high accuracy of the RailScan system.

8. Main Research Findings

A large number of results from MBN technology based measurements and testing works in recent years have shown that the RailScan system is a sophisticated but cost effective method of providing accurate and reliable data to monitor the condition of neutral temperature and stress distribution in a railway section. It is also a very useful tool for track maintenance and research on CWR.

The stability of a specified CWR track module is highly depends on its track strengthen (i.e. condition and type of rail, sleeper, sleeper spacing, fastening systems, ballast profile, etc.). For the railway track on the Broken Hill line, on many sections, the structural strength of the CWR track are relatively low, because of the timber sleepers, fatigued steel sleepers, dog-spike fastening systems which usually cannot provide enough resistant force to control the creep of the long rail under the very harsh environment. Hence, on some track sections, the neutral temperature of the CWR track can be changing during one day from cold night to very hot noon time.

The neutral temperature at each point along a curve was found to be dependent on the curve geometry, being lower for a circular curve and higher in transition curves. From the measurements results which are represented in section 7, it was found that the neutral temperature can be higher in curve transitions than in the curve itself. The bending stress in rail installed in sharp curves can influence the thermal stress distribution in the longitudinal direction. This was shown to be related to the radius of the curve, the smaller the radius the greater the decrease in longitudinal stress.

For the track modules that installed on steep slope, the gradient can significantly impact the distribution of the longitudinal stress. From the results of in-field measurement, the bottom point of a steep slope located track module is the lowest neutral temperature point. Hence, the weakest point of a CWR track which installed on the steep slope is located at the lowest point of the slope.

Moreover, the nonlinear finite element model is a very useful tool to carry out the analysis of the CWR track at different specified locations. Some further studies will be carried out when the FEA models are further improved.

9. Acknowledgement

The authors would like to express gratitude to Mr. Ken Sherwood, the former Managing Director of Pandrol Australia Pty Ltd and Mr. Robert Rex, the Managing Director of Rex Lok Pty Ltd. for their kind help for the rail fastening system knowledge and condition analysis. Without their assistant and support this paper could not have been finished.

10. References

- Chikazumi S (1964). *Physics of magnetism*. John Wiley & Sons.
- Kerr A (2003). *Fundamentals of railway track engineering*. Simmons-Boardman Books.
- Kish A (2009). *Guidelines to best practices for heavy haul railway operations - Infrastructure construction and maintenance issues*. International Heavy Haul Associations.
- ANSYS Co. (2007). *Theory reference for ANSYS and ANSYS workbench, Release 11.0*. ANSYS Inc. and ANSYS Europe Ltd.
- Wang P and Liu X (2007). *The theory of calculation and design method of CWR track within turnout*. The Xinan Jiaotong University Publisher.

Maertens M (2018). Modelling of track stability in crossings with a finite element model. Master thesis of science in civil engineering. Department of Civil Engineering, Faculty of Engineering and Architecture, Ghent University. 2018, Ghent, Belgium.

Landuyt B (2017). Modelling of track stability in turnouts with a finite element model. Department of Civil Engineering, Faculty of Engineering and Architecture, Ghent University. 2017, Ghent, Belgium.

Zhang R and Wu H (2011). Using magnetic Barkhausen noise technology and finite element method to study the condition of continuous welded rails on the Darwin-Alice Springs line. *Journal of Civil Engineering and Architecture*, ISSN 1934-7359, USA, July 2011, Volume 5, No. 7 (Serial No. 44), 596-605.

Yang Y and Gu A (2006). Using ANSYS software to study the stability of CWR track. *Railway Engineering*. September. 2006. (in Chinese).

Zhang R, Wu H, Karsten A, Yang R & Pleasance L (2015). Better Understanding of Stability of Turnouts in CWR Track by In-Field Measurement and Numerical Study. Proceeding of 12th International Heavy Haul Conference. P337-344. 21-24 June, 2015. Perth, Australia.

Moller R, Radmann P, and Zhang R (2009). Using magnetic Barkhausen noise technology and numerical method to study the condition of continuous welded rails on Australian heavy axle track. *9th International Heavy Haul Conference*. June, 2009. Shanghai, China.

Wegner A (2004). Non-destructive determination of the stress free temperature in CWR tracks. *International Rail Forum*. Madrid. November, 2004.

Wegner A (2007). Prevention of track buckling and rail fracture by non-destructive testing of the neutral temperature in cw-rails. *8th International Heavy Haul Conference on "High Tech in Heavy Haul"*. June, 2007. Kiruna, Sweden.

Wegner A, Hofmann M, Radmann P, Zhang R, and Dubbins F (2011). Management of longitudinal rail forces by non-destructive SFT monitoring in CW Tracks. 10th International Heavy Haul Conference. June, 2011. Calgary, Canada.

Experimental and numerical studies on SCFs of empty SHS-SHS T-joints under in-plane bending

Feleb N Matti, * and Fidelis R Mashiri

School of Computing, Engineering and Mathematics, Western Sydney University, Penrith, Locked bag 1797, NSW 2751, Australia

*Corresponding author's email: f.matti@westernsydney.edu.au

Peer review history

Manuscript submitted: 23 April 2019

Review process completed: 3 August 2019

Manuscript finally accepted: 5 August 2019

Handling Editor: Professor Ataur Rahman

Abstract: This paper presents an experimental and numerical study on square hollow section (SHS) T-joints ($t \leq 4$ mm) subjected to in-plane bending (IPB) on the brace. In the experimental investigation, strain gauges were used to measure the strains and determine the stress concentration factor (SCFs) at the potential hot spot locations (Lines A-E) for each SHS-SHS T-joint specimen. The numerical study was performed by developing three-dimensional finite element models through the use of ABAQUS

software to capture the distribution of the SCF at the weld toes. In this investigation, the empty T-joints are made up of an empty SHS brace and empty SHS chord member. Six empty SHS-SHS T-joints were tested and modelled under static in-plane bending load. The maximum experimental and numerical SCFs will be compared with the SCFs obtained from CIDECT Design Guide 8. There is a good agreement between the numerical results and the experimental results for each identical T-joint connection. This paper provided additional results for smaller β values and larger β values. Results show a similar trend of the variation of SCF with β from experiments and numerical analysis.

Keywords: Stress concentration factor; Empty SHS T-joints; Experimental investigation, Finite element analysis; In-plane bending.

1. Introduction

Thin walled ($t \leq 4$ mm) tubular SHS-SHS T-joints are widely used in truss bridges, high rise buildings, cranes and towers. The T-joint connections in an engineering structure may be subjected to cyclic in-plane bending loads which may cause a structure to collapse. Limited numerical and experimental investigations on unfilled and composite SHS tubular T-joints are available. Feng and Young (2010) conducted a numerical study and design on SHS and rectangular hollow section (RHS) stainless steel tubular T- and X-joints with concrete-filled chords under static compression loading. Tong et al., (2012) tested eight empty circular hollow sections (CHS) to SHS T-connections and developed 3D FE models to determine the SCFs. The CHS-SHS T-connections were tested under axial loading and in-plane bending. In addition, Mashiri et al., (2004) carried out fatigue tests on T-connections made up of CHS brace to SHS chord. Mashiri et al., (2004) measured stress distributions at hot spot locations, where cracks initiated and propagated resulting fatigue failure. Feng et al., (2017) carried out a numerical and experimental static behaviour investigation on both collar plate and doubler plate reinforced SHS T-joints. Eleven SHS T-joints were tested under axial compression. In their investigation, they concluded that large value of β ratio benefits the initial stiffness and the joint strength but deteriorates the ductility.

Mashiri and Zhao (2010) tested empty and concrete-filled SHS-SHS steel tubular T-joints under in-plane bending. Matti and Mashiri (2018) used ABAQUS software to model identical T-joints used in Mashiri and Zhao (2010) experimental investigation to obtain SCFs and compare the SCF determined from the numerical study with the experimental study. The non-dimensional parameter (β) range of the specimens used in Mashiri and Zhao (2010) investigation is $0.35 \leq \beta \leq 0.67$. Therefore, in this paper, more SCF investigations of SHS T-joints was carried out in order to provide more information on the behavior of SHS T-joint specimens. This is achieved by testing SHS T-joints with larger β values ($\beta > 0.67$) and smaller β values ($\beta < 0.35$). There is a good agreement between the numerical SCFs and the experimental SCFs. The experimental and numerical results show a similar trend of the variation of SCF with β .

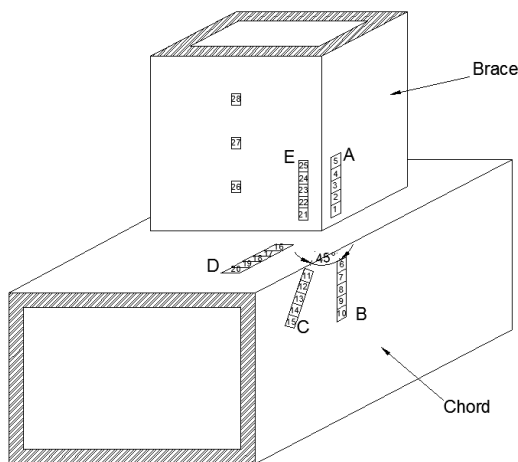
2. Methodology

2.1 Test series and materials

Six empty SHS-SHS T-joints were tested experimentally and numerically. Table 1 lists the six empty T-joint connections with their dimensions and non-dimensional parameters. The SHS T-joints have non-dimensional parameters, β ranging from 0.25 to 1, 2γ ranging from 25 to 33.33 and τ ranging from 0.75 to 1.0. As shown in Table 1, the steel SHSs used in this investigation are cold-formed and have a steel grade of C350LO which comply with AS1163-2009 (Standards Australia Online 2009). The external corner radii of the empty tubes were calculated according to OneSteel Market Mills (2004). The corner radii were determined based on the size and thickness of the sections. The design tensile strength of the steel is 430 MPa, in accordance to AS 4100-1998 (Standards Australia Online 1998). The SHS chord of each T-joint connection is welded to an SHS brace at right angles. The size of the weld defined by the leg length and throat thickness was determined in accordance to AS 4100-1998 (Standards Australia Online 1998) which equal to 6 mm and 4.24 mm, respectively. According to AS 4100-1998 (Standards Australia Online 1998), the nominal tensile strength of the weld metal is 480 MPa.

Table 1. Connection series used in this numerical investigation to determine the SCFs.

Series	Chord	Brace size	Non-dimensional parameters			Steel grade	Length	
	$d_o \times b_o \times t_o$ mm \times mm \times mm	$d_1 \times b_1 \times t_1$ mm \times mm \times mm	$\beta = \frac{b_1}{b_o}$	$2\gamma = \frac{b_o}{t_o}$	$\tau = \frac{t_1}{t_o}$		Brace (mm)	Chord (mm)
S6S1	100 \times 100 \times 4 SHS	25 \times 25 \times 3 SHS	0.25	25	0.75	C350LO	500	600
S5S1	100 \times 100 \times 3 SHS	25 \times 25 \times 3 SHS	0.25	33.33	1.00		500	600
S6S2	100 \times 100 \times 4 SHS	40 \times 40 \times 3 SHS	0.40	25	0.75		500	600
S6S3	100 \times 100 \times 4 SHS	50 \times 50 \times 3 SHS	0.50	25	0.75		500	600
S6S4	100 \times 100 \times 4 SHS	75 \times 75 \times 3 SHS	0.75	25	0.75		500	600
S5S5	100 \times 100 \times 3 SHS	100 \times 100 \times 3 SHS	1.00	33.33	1.00		500	600



(a)

(b)

Figure 1. Locations of strain gauges: (a) Schematic diagram; and (b) Test rig: in-plane bending.

2.2 Instrumentation and test setup

Single and strip strain gauges were attached onto six empty SHS T-joint specimens to measure the strains. The locations of the single and strip strain gauges are shown in Figure 1(a). Each specimen consisted of 3 single strain gauges and 5 strip strain gauges. The strip strain gauges comprise of 5-element single strain gauges. The gauges in a strip strain gauge are at 2 mm apart. The strain gauges were installed using Cyanoacrylate Strain Gauge Glue. As shown in Figure 1(a), strip strain gauges were installed along the chord and brace intersections at lines A, B, C, D and E. As recommended by Zhao et al., (2001), the distance of the strain gauge from the weld toe is the lesser of $0.4t$ or 4 mm but a minimum of 4 mm. For this investigation, the first strain gauge of the strip strain gauge closest to the weld toe was installed at 4 mm from the weld toe as all tubes had a thickness less than 10 mm.

The T-joint specimens were connected to the test rig through M12 bolts of grade 8.8 snug tight. The testing of the specimens was setup under in-plane bending loads on the brace. The test setup displayed in Figure 1(b) was used to measure the strain distribution. In-plane bending moment loads were applied to each specimen. In-plane bending means that the load is being applied to the brace in the direction of the longitudinal axis of the chord. In order to carry out high-cycle fatigue tests or determine SCFs, the loads that are applied to each T-joint specimen are within the elastic response range of the load-deformation curve of the SHS-SHS T-joint. Each specimen consisted of two end plates which were bolted to the end brackets to support the T-joint connection.

2.3 Finite element modelling (FEM)

The finite element method (FEM) is a great method in determining the SCFs of a connection. Linear elastic FEA modelling was carried out to determine the SCFs at the location of interest at which the SCFs were experimentally determined, line A to E. Six empty SHS-SHS T-joints were modelled and tested under static in-plane bending load on the brace using ABAQUS software. The non-dimensional parameters of the empty T-joints specimens are the same as the T-joint models. Since there is no buckling in the T-joint and the load is within the elastic response region, geometric imperfections were not included in the finite element modelling. The pinned supports can resist vertical and horizontal forces but not a moment which will allow the T-joint specimens to rotate about the x-direction. The weld was tied to the end plates and the chord ends as well as the top plate and the top end of the brace. Furthermore, the weld was tied with the brace and chord intersection.

The finite element type that has been used for the models is 8 noded ABAQUS C3D8R 3D linear hexahedral solid elements. A static horizontal in-plane bending load was applied in the middle of the T-joints' top plate as shown in Figure 2 using the Static, General procedure available in the ABAQUS library. The SHS-SHS T-joint models were subjected to in-plane bending load on the brace. The load that is applied to each concrete-filled SHS-SHS T-joint specimens is within the elastic response range of the load-deformation curve of the SHS-SHS T-joint. Since tension is more critical for fatigue, crack opening and crack growth, the stress values at lines A, B, C, D and E will be obtained on the side under tension. The hot spot locations to measure the stresses are shown in Figure 2. As shown in Figure 2, each line comprises of 5 nodes representing the number of strain gauges in a strip strain gauge since each strip gauge consist of five strain gauges. The mesh for the welded T-joints was generated on parts that were created within ABAQUS. Whole models were meshed and included in the simulation. Figure 2 shows a typical meshed model with different mesh densities to meet the needs of this analysis. Feleb and Mashiri (2018) conducted a mesh sensitivity analysis to find the optimum mesh for these connections. Finer element edge, 1 mm in length was used at lines A-E.

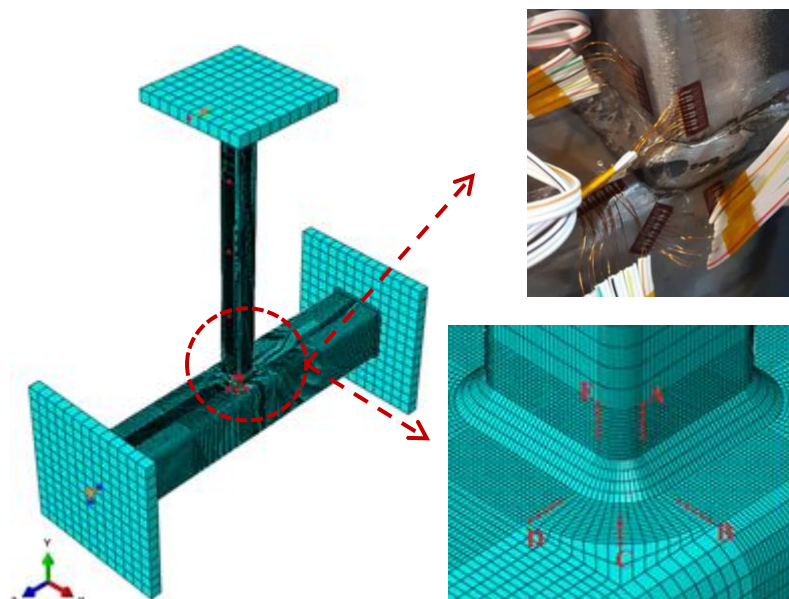


Figure 2. FE mesh model with hot spot locations.

3. Stress concentration factors (SCFs)

3.1 Experimental SCF

The SCF_{SHS} at a hot spot location in the square hollow section T-joints was calculated using equation 1 as recommended by Zhao et al., (2001). The $SNCF_{SHS}$ for each load case was calculated using equation 2.

$$SCF_{SHS, Experimental, A-E} = 1.1 \times SNCF_{SHS} \quad (1)$$

$$SNCF_{SHS} = \frac{\text{Hot Spot Strain (HSSN)}}{\text{Nominal Strain}} \quad (2)$$

The hot spot strain for each load case was calculated through the use of quadratic extrapolation. Figure 3 compares the two extrapolation methods; linear and quadratic extrapolation in determining the hot spot strains for a typical T-joint specimen along line A. Figure 3 shows that the quadratic hot spot strains are higher than the linear hot spot strains. In rectangular hollow sections (or SHS), Zhao et al., (2001) recommended the use of the quadratic extrapolation method as the distribution of the stresses is non-linear. Mashiri and Zhao (2010) used quadratic extrapolation for the determination of the hot spot stresses. Quadratic extrapolation was therefore adopted in this investigation for lines A to E.

The values of the nominal strain values for in-plane bending were calculated by the linear extrapolation method using the extrapolation points on the tension side of the brace, see Figure 2. Since strains were measured at four (4) load levels, four (4) $SNCFs$ values were calculated for each strip strain gauge and for each location from line A to E. The average value of the $SNCFs$ is the strain concentration factor for the connection ($SNCF_{SHS}$) for each strip strain gauge.

3.2 Numerical SCF

Mashiri (2001) defined the stress concentration factor to be the ratio of the hot spot stress (σ_{hss}) and the nominal stress (σ_{nom}) for a member in a chord-brace connection subjected to in-plane bending load on a brace member. Equation 3 expresses the numerical SCF for each hot spot location (line A-E).

$$SCF_{SHS, Numerical, A-E} = \frac{\text{hot spot stress } (\sigma_{hss})}{\text{nominal stress } (\sigma_{nom})} \quad (3)$$

The hot spot stress for each hot spot location (line A-E) was calculated through the use of quadratic extrapolation. Figure 4 compares linear and quadratic extrapolation in determining the hot spot stress at the weld toe for a typical T-joint specimen. The hot spot stresses occur at the weld toe. Furthermore, Figure 4 shows that the quadratic hot spot stresses are higher than the linear hot spot stresses. Numerical nominal stresses were calculated using the linear extrapolation method, as shown in Figure 5(a). For comparison, beam theory nominal stresses were also calculated using the ratio of the bending moment (M) in the brace and the elastic section modulus of the brace (Z). This method is known as the simple beam theory which expresses nominal stress as follows: $\sigma_{nom} = M/Z$. As illustrated in Table 2 and Figure 5(b), the value of the numerical nominal stress (FEA) for each SHS T-joint is similar to the beam theory nominal stress.

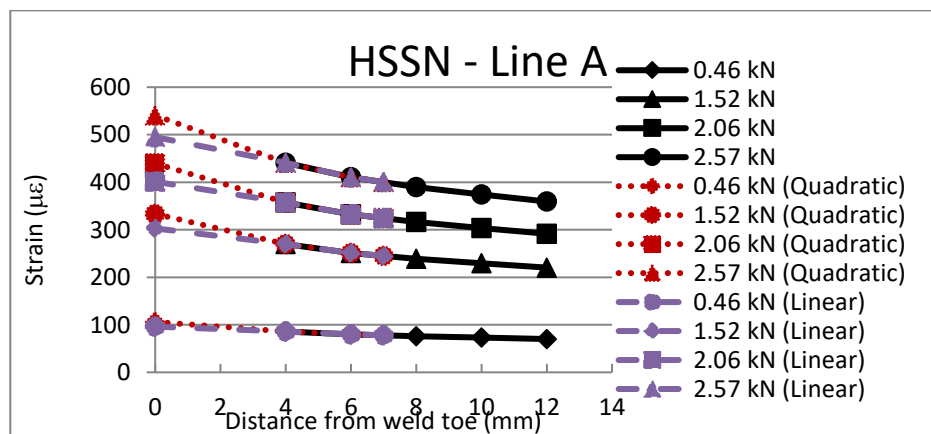


Figure 3. Determination of hot spot strain (HSSN)

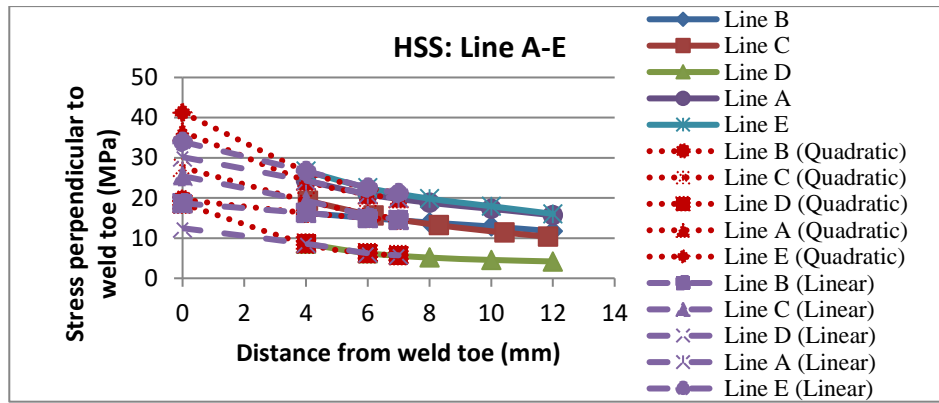


Figure 4. Determination of hot spot stress (σ_{hss}).

In finite element modelling, the typical stress distribution of an SHS-SHS T-joint specimen is shown in Figure 6(a) and (b). This figure shows that the SHS T-joint specimens with lower non-dimensional parameter, β have greater stresses than the SHS T-joint specimen with higher β if subjected to same loading.

Table 2. Nominal stresses.

Model	$D_{B.MID}$ (mm)	$\sigma_{B.MID}$ (MPa)	$D_{B.QTR}$ (mm)	$\sigma_{B.QTR}$ (MPa)	$D_{B.END}$ (mm)	$\sigma_{nom.num}$ Numerical (MPa)	$\sigma_{nom.exp}$ Beam Theory (MPa)	Ratio $\frac{\sigma_{nom.exp}}{\sigma_{nom.num}}$
S6S1	250	99.39	375	51.27	0	195.62	208.16	1.06
S5S1	250	99.39	375	51.27	0	195.62	208.16	1.06
S6S2	250	32.10	375	16.56	0	63.19	65.67	1.04
S6S3	250	19.36	375	9.99	0	38.11	39.28	1.03
S6S4	250	7.97	375	4.11	0	15.70	16.02	1.02
S5S5	250	4.32	375	2.23	0	8.51	8.64	1.01
Average								1.04

Note: $D_{B.MID}$ = distance.brace.middle; $\sigma_{B.MID}$ = stress.brace.middle; $D_{B.QTR}$ = distance.brace.quarter; $\sigma_{B.QTR}$ = stress.brace.quarter; $D_{B.END}$ = distance.brace.end; $\sigma_{nom.exp}$ = experimental nominal stress; $\sigma_{nom.num}$ = numerical nominal stress.

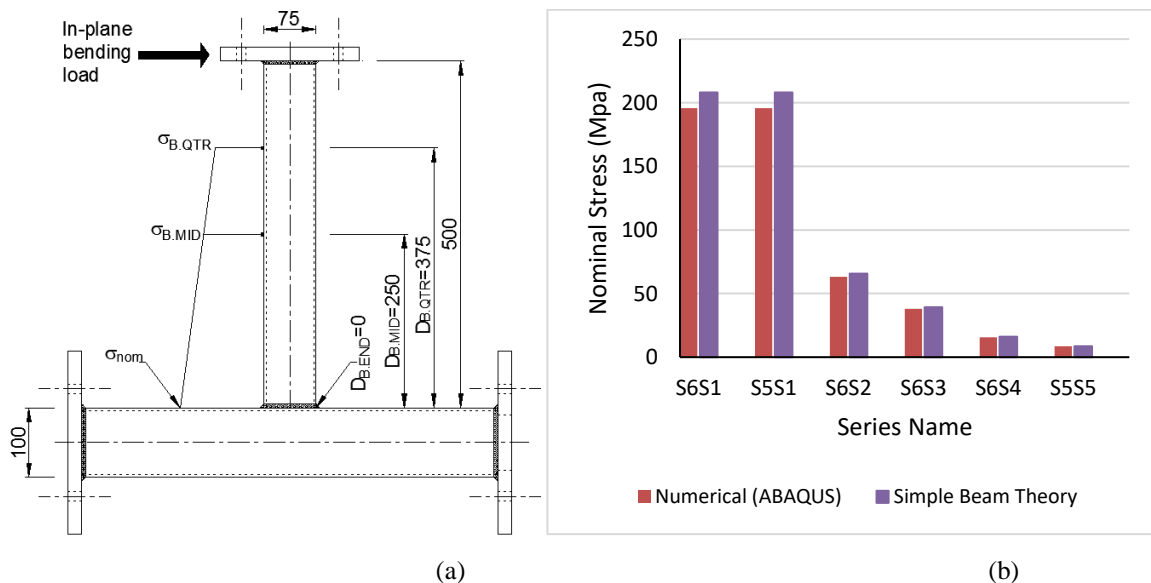


Figure 5. Nominal stresses: (a) extrapolation points; and (b) numerical and beam theory results.

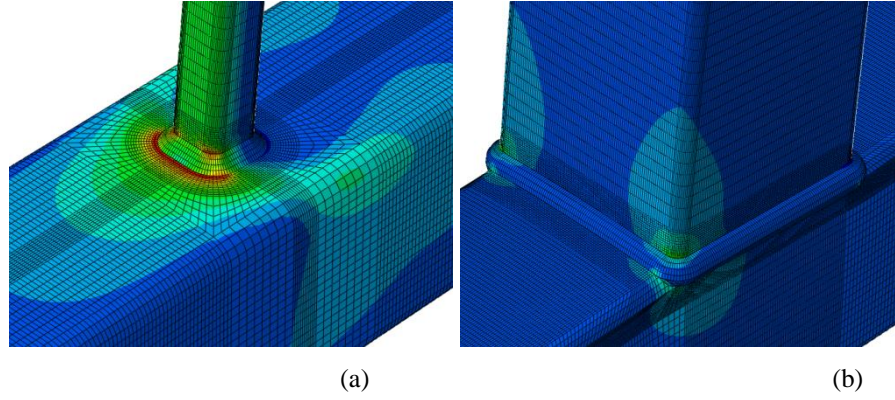


Figure 6. Stress distribution of empty T-joints subjected to IPB: (a) Empty S6S1; and (b) Empty S5S5.

3.3 SCF using CIDECT Design Guide

The SCFs for hollow SHS-SHS T-joint under in-plane bending on the brace were calculated through the use of CIDECT Design Guide 8 (Zhao et al., 2001). The SCFs obtained from the Design Guide (empty SHS-SHS T-joints) will be compared with the SCFs determined from the experimental and numerical studies. Comparing the SCFs results between the Design Guide with experiment and the finite element models, will enable the validation of the results. Equations 4-7 were used to determine the SCFs of empty SHS-SHS T-joints under in-plane bending along lines A to E:

$$SCF_{B,ipb} = (-0.011 + 0.085 \times \beta - 0.073 \times \beta^2) \times (2\gamma)^{(1.722+1.151 \times \beta - 0.697 \times \beta^2)} \times \tau^{0.75} \quad (4)$$

$$SCF_{C,ipb} = (0.952 - 3.062 \times \beta + 2.382 \times \beta^2 + 0.0228 \times 2\gamma) \times (2\gamma)^{(-0.690+5.817 \times \beta - 4.685 \times \beta^2)} \times \tau^{0.75} \quad (5)$$

$$SCF_{D,ipb} = (-0.054 + 0.332 \times \beta - 0.258 \times \beta^2) \times (2\gamma)^{(2.084-1.062 \times \beta + 0.527 \times \beta^2)} \times \tau^{0.75} \quad (6)$$

$$SCF_{A,ipb} = SCF_{E,ipb} = 1.4 \times (0.390 - 1.054 \times \beta + 1.115 \times \beta^2) \times (2\gamma)^{(-0.154+4.555 \times \beta - 3.809 \times \beta^2)} \quad (7)$$

4. Results and discussion

4.1. SCFs

Table 3 and Figure 7 show the distribution of the SCF and the maximum SCFs in the six empty SHS-SHS T-joints. The ratios of the maximum SCF in FEA model to that in experiment; $(SCF_{ABAQUS}/SCF_{Experiment})$ are given in Table 3. These ratios are close to 1 and the average ratio is 1.04. Therefore, it can be stated that a good agreement is achieved between the numerical SCF results and the experimental SCF results for each identical T-joint connection.

On the other hand, the average ratio of the maximum empty SCF in FEA model to that in CIDECT Design guide; $(SCF_{ABAQUS}/SCF_{CIDECT})$ is 0.58, given in Table 3. The SCFs of the CIDECT Design Guide are higher than both the experimental and the numerical SCFs. This is beneficial for fatigue design assessments as a conservative estimate of life is given by higher SCF. Figure 7 shows that for the majority of the SCF results, similar trends can be seen between CIDECT, Experimental and numerical SCFs. The maximum SCFs on the FE models in S6S1, S5S1, S6S2, S6S3, S6S4 and S5S5 occurred along line C, D, C, C, B and E, respectively. The maximum experimental SCFs in S6S1, S5S1, S6S2, S6S3, S6S4 and S5S5 occurred along line D, C, D, D, A and A, respectively. Similarly, the maximum SCFs based on the CIDECT Design Guide in S6S1, S5S1, S6S2, S6S3, S6S4 and S5S5 occurred along line D, D, C, C, C and A (and E), respectively.

In summary, the majority of the maximum SCFs occurred at line C and D excluding S5S5 where the maximum experimental, numerical and CIDECT SCFs occurred on the brace at line A and/ or E. The non-dimensional parameter (β) of S5S5 T-joint connection is 1.

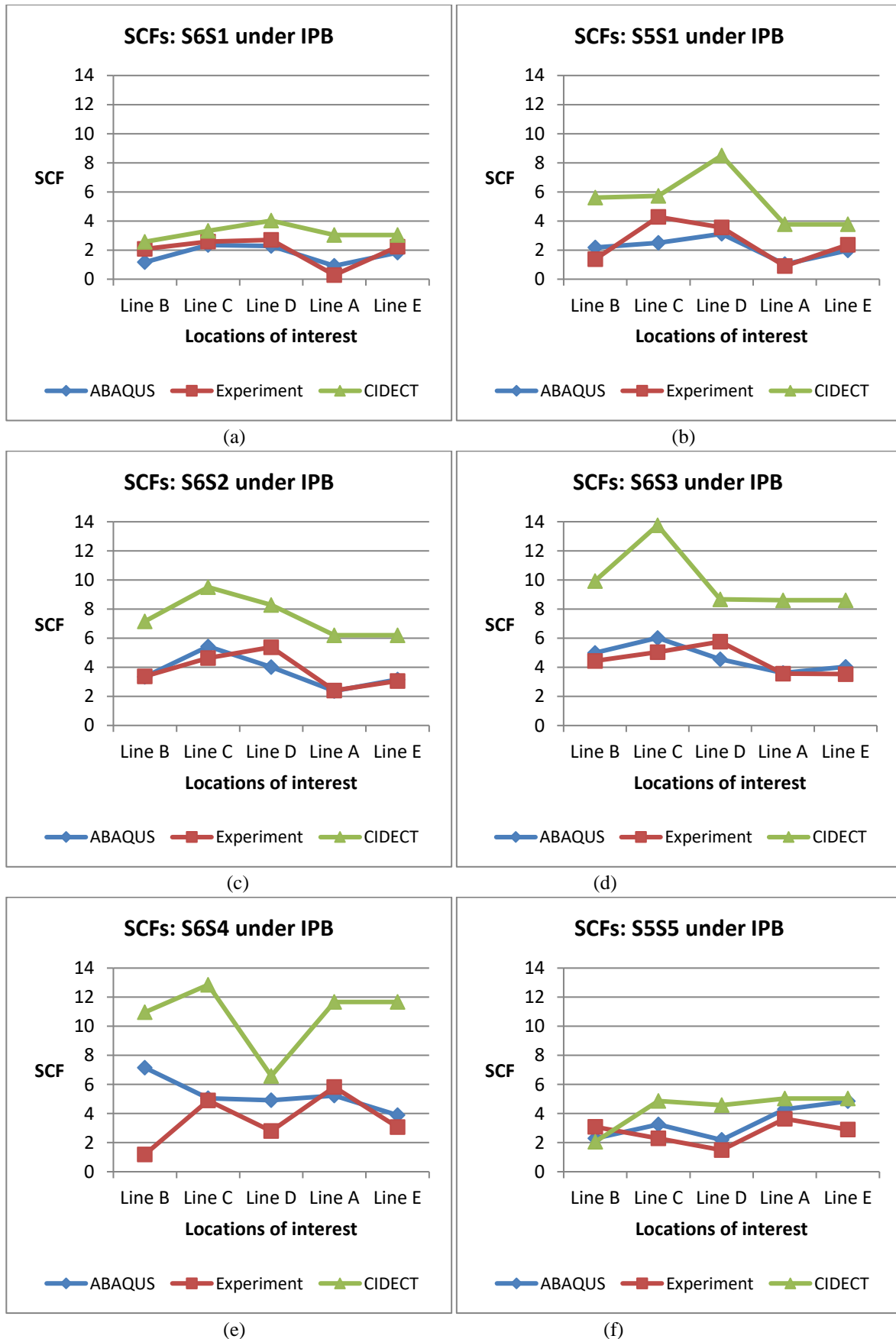


Figure 7. Comparison of SCFs in empty SHS-SHS T-joints under in-plane bending: (a) Empty S6S1; (b) Empty S5S1; (c) Empty S6S2; (d) Empty S6S3; (e) Empty S6S4; and (f) Empty S5S5.

Table 3. SCFs in unfilled T-joints under in-plane bending.

Series name	ABAQUS/ Experiment/ CIDECT	SCF (quadratic) Empty SHS T-joints					Ratio of maximum SCFs	
		B	C	D	A	E	$\frac{SCF_{ABAQUS}}{SCF_{Experiment}}$	$\frac{SCF_{ABAQUS}}{SCF_{CIDECT}}$
S6S1	ABAQUS	1.16	2.35	2.28	0.92	1.82	0.87	0.58
	Experiment	2.07	2.58	2.70	0.28	2.22		
	CIDECT	2.57	3.33	4.02	3.04	3.04		
S5S1	ABAQUS	2.18	2.50	3.11	1.03	1.98	0.73	0.37
	Experiment	1.37	4.27	3.55	0.90	2.37		
	CIDECT	5.61	5.72	8.50	3.77	3.77		
S6S2	ABAQUS	3.34	5.43	4.02	2.37	3.17	1.00	0.57
	Experiment	3.38	4.65	5.38	2.41	3.06		
	CIDECT	7.16	9.51	8.28	6.20	6.20		
S6S3	ABAQUS	5.00	6.02	4.55	3.61	4.03	1.05	0.44
	Experiment	4.45	5.04	5.76	3.57	3.54		
	CIDECT	9.92	13.76	8.67	8.61	8.61		
S6S4	ABAQUS	7.15	5.06	4.92	5.24	3.89	1.23	0.56
	Experiment	1.19	4.90	2.80	5.82	3.07		
	CIDECT	10.96	12.85	6.58	11.66	11.66		
S5S5	ABAQUS	2.30	3.24	2.19	4.29	4.85	1.33	0.96
	Experiment	3.08	2.29	1.49	3.64	2.90		
	CIDECT	2.06	4.86	4.57	5.03	5.03		
Average							1.04	0.58

4.2. The influence of β

The geometric parameters' influence on fatigue strength and SCFs under in-plane bending was investigated. The chord width (b_0) of each specimen is the same. Therefore, it can be stated that the change in brace width (b_1) of each SHS-SHS T-joint connection influences the non-dimension parameter (β), see Table 1. Since the non-dimensional parameter (β) of the specimens is not the same, different SCFs were obtained under in-plane bending. Figure 8 shows the maximum SCF against the non-dimensional parameter, β for empty SHS-SHS T-joints under in-plane bending. As shown in Figure 8 (a), the values of the maximum experimental and numerical SCFs of SHS T-joints with $2\gamma=25$ and $\tau=0.75$ increase with the increased value of β . The maximum SCF using CIDECT Design Guide also increases with the increased value of β but slightly decreased when $\beta=0.75$. Furthermore, as shown in Figure 8 (b), the values of the numerical and CIDECT SCFs of SHS T-joints with $2\gamma=33.33$ and $\tau=1$ increase with the increased value of β and decreased when β equals to 1. It should be noted that the two experimental SCFs at $\beta = 0.35$ and 0.5 shown in Figure 8 (b) were obtained from Mashiri and Zhao (2010) since these two T-joint specimens were not tested in this experimental study. Figure 8 (b) shows that the maximum experimental SCF reduced when $\beta = 0.5$ and continued reducing when $\beta=1$. In summary, similar trends can be observed between CIDECT, Experiment and numerical peak SCFs.

4.3. Failure mode

As shown in Figure 9, for empty T-joint under in-plane bending, the chord face deformation is in both tensile and compressive region. Similar failure mode between CIDECT Design Guide 3 (Packer et al., 2009) and the FE model was achieved.

5. Conclusion

An experimental and a numerical study on unfilled square hollow section (SHS) T-joints under static in-plane bending were carried out. For the experimental investigation, strain gauges were installed onto six empty SHS T-joints to determine the stress concentration factor (SCF) at the hot spot locations (Lines A-E). The numerical study was carried out by developing 3D T-joint models identical to the experimental T-joint specimens using ABAQUS software to capture the distribution of the SCF. SCFs under in-plane bending using CIDECT Design Guide 8 (Zhao et al., 2001) were also obtained and compared with the experimental and numerical SCFs.

A good agreement is achieved between the numerical results and the experimental results for each identical non-dimensional parameter T-joint. The ratios of the maximum empty SCF in FEA model to that in experiment; ($SCF_{ABAQUS}/SCF_{Experiment}$) are close to 1 and the average ratio is 1.04. The average ratio of the maximum empty SCF in

FEA model to that in CIDECT Design guide; ($SCF_{ABAQUS}/SCF_{CIDECT}$) is 0.58. The SCFs of the CIDECT Design Guide are higher than both the experimental and the numerical SCFs. This is beneficial for fatigue design assessments as a conservative estimate of life is given by higher SCF.

The majority of the maximum SCFs occurred at line C and D excluding S5S5 where the maximum experimental, numerical and CIDECT SCFs occurred on the brace at line A and/ or E. Furthermore, the failure mode of the welded empty tubular T-joints under in-plane bending between CIDECT Design Guide 3 (Packer et al., 2009) and the FE model are the same. For empty T-joints, the chord face deformations are in both tensile and compressive regions.

The non-dimension parameter (β) influences on fatigue strength and SCFs under in-plane bending. Since the non-dimensional parameter (β) of the specimens is not the same, different SCFs were obtained under in-plane bending. The values of the maximum experimental and numerical SCFs increase with the increased value of β . The maximum SCF using CIDECT Design Guide also increases with the increased value of β but slightly decreased when $\beta=0.75$. The numerical and CIDECT SCFs increase with the increased value of β and decreased when β equals to 1. The maximum experimental SCF reduced when $\beta = 0.5$ and continued reducing when $\beta = 1$.

In the future, experimental, numerical and parametric studies on empty SHS T-joints under axial loads and out-of-plane bending on the brace will be explored. Furthermore, experimental, numerical and parametric studies on SHS T-joints with concrete-filled chord will be investigated under axial loadings, in-plane bending and out-of-plane bending.

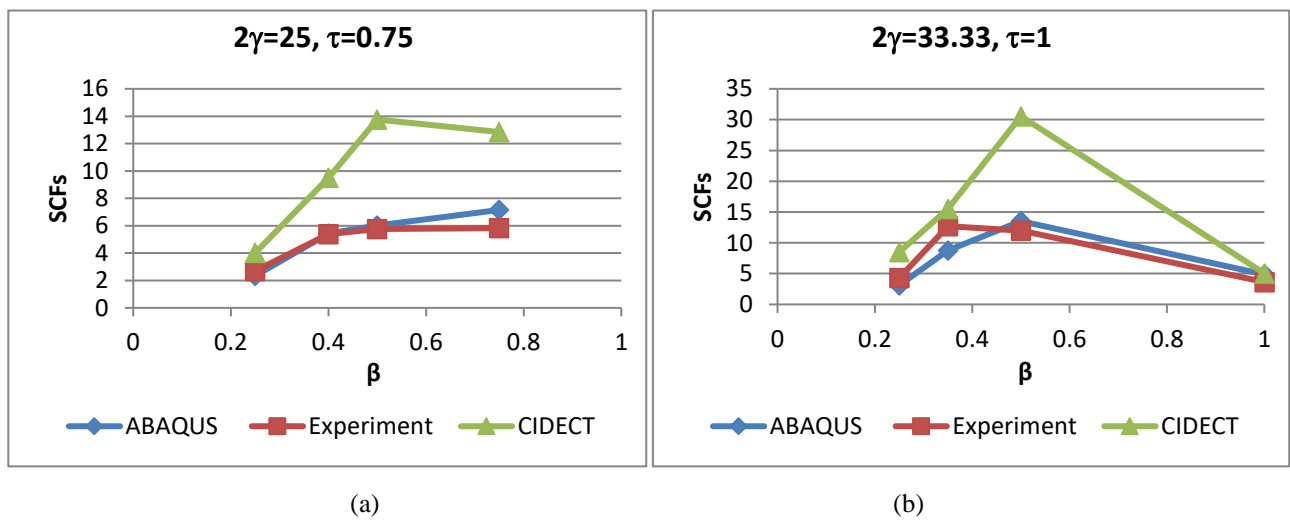


Figure 8. Variations of maximum SCFs with β under IPB: (a) $2\gamma=25, \tau=0.75$; and (b) $2\gamma=33.33, \tau=1$.

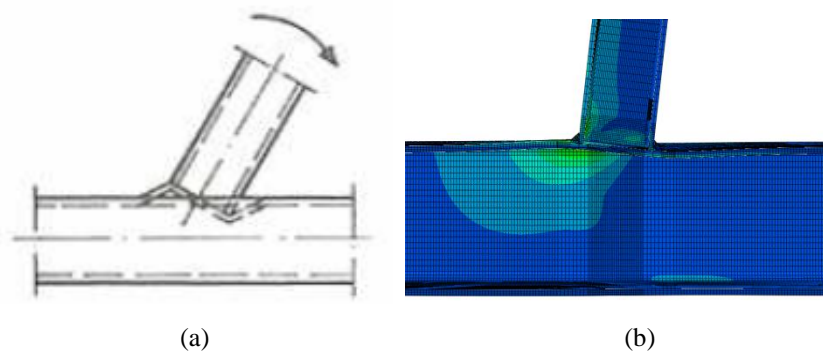


Figure 9. Failure mode under IPB: (a) Empty (Packer et al., 2009); and (b) Typical empty (FE model).

6. Acknowledgements

The authors are thankful to Western Sydney University (WSU) for funding sources and supporting this project. The authors wish to thank the WSU laboratory staff; Mr. Murray Bolden and Mr. Robert Marshall for their assistance in performing the experimental test in the lab.

7. References

- Zhao, X. L., Herion, S., Packer, J. A., Puthli, R. S., Sedlacek, G., Wardenier, J., Weynand, K., van Wingerde, A. M., & Yeomans, N. F. (2001). Design guide for circular and rectangular hollow section welded joints under fatigue loading. TÜV-Verlag.
- Feng, R., & Young, B. (2010). Design of concrete-filled stainless steel tubular connections, *Advances in Structural Engineering*, 13(3), 471-92.
- Tong, L.W., Zheng, H.Z., Mashiri, F. R., & Zhao, X. L. (2012). Stress-concentration factors in circular hollow section and square hollow section T-connections: experiments, finite-element analysis, and formulas. *Journal of Structural Engineering*, 139(11), 1866-81.
- Mashiri, F. R., Zhao, X. L., & Grundy, P. (2004). Stress concentration factors and fatigue behaviour of welded thin-walled CHS-SHS T-joints under in-plane bending. *Engineering Structures*, 26(13), 1861-75.
- Feng, R., Chen, Y., & Chen, D. (2017). Experimental and numerical investigations on collar plate and doubler plate reinforced SHS T-joints under axial compression. *Thin-Walled Structures*, 110, 75-87.
- Mashiri, F. R., & Zhao, X. L. (2010). Square hollow section (SHS) T-joints with concrete-filled chords subjected to in-plane fatigue loading in the brace. *Thin-Walled Structures*, 48(2), 150-8.
- Matti, F.N., & Mashiri, F. R. (2018). Numerical study on SCFs of empty and concrete-filled SHS-SHS T-joints under in-plane bending. In *Proceedings of the 9th International Conference on Advances in Steel Structures* (P. 875-886). China.
- Standards Australia Online. (2009). Cold-formed structural steel hollow sections. AS 1163-2009, viewed 24 July 2017, SAI Global database.
- OneSteel Market Mills. (2004). Cold formed structural hollow sections & profiles. 4th edn.
- Standards Australia Online. (1998). Steel structures. AS 4100-1998 viewed 27 November 2017, SAI Global database.
- Mashiri, F. (2001). Thin-walled tubular connections under fatigue loading. Doctor of Philosophy thesis, Monash University.
- Packer, J. A., Wardenier, J., Zhao, X. L., van der vegte, G. J., & Kurobane, Y. (2009). Design guide for rectangular hollow section (RHS) joints under predominantly static loading. 2nd edn, Verlag TÜV Rheinland.

Numerical investigation of modified splice plate beam-to-beam connections for prefabricated composite structure

Md Kamrul Hassan^{1,*} and Susma Tajhya²

¹ Centre for Infrastructure Engineering, Western Sydney University, Kingswood Campus, NSW, Australia

² School of Computing, Engineering and Mathematics, Western Sydney University, Kingswood Campus, NSW, Australia

*Corresponding author's email: k.hassan@westernsydney.edu.au

Peer review history

Manuscript submitted: 19 June 2019

Review process completed: 28 October 2019

Manuscript finally accepted: 28 October 2019

Handling Editor: Professor Chin Leo

Abstract: Prefabricated construction has been rising dramatically in the construction industry in recent times. On the other hand, it is equally complicated and laborious to design and install the prefabricated structures on site. The reason behind this can be credited to the limited design guidelines available and the massive structural parts. This research has been carried out to overcome shortcomings of the prefabricated composite construction. In this paper, the idea of discontinuous beams and a beam-to-beam connection system has been proposed for the prefabricated construction. Modified splice plate bolted connection has been suggested for the

discontinuous beams. The proposed connection is similar to splice plate bolted connection, but welding between splice plate and beam web is introduced. This paper mainly investigated the behaviour of modified splice plate bolted connections using finite element (FE) analysis and compared its results with continuous beam. Based on FE modelling results, it has been found that the proposed connection system having welding provides higher strength to the discontinuous beam compared to the same discontinuous beams connected by conventional splice plate bolted connection systems. Splice plates welded to the web of the steel beam need to be fabricated in a factory and normal bolts are installed on the site of the building construction. Thus, it can be concluded from this research that the massive continuous beams can be replaced by discontinuous beams through a presented connection system for prefabricated construction.

Keywords: Prefabricated constructions; Discontinuous beam; Beam-to-beam connection; Splice plate bolted connection system; Finite element modelling.

1. Introduction

Steel construction has the emerging market in the construction industries. In conjunction with this, prefabricated concrete structures have been rapidly replacing the in-situ construction in these growing construction industries (Shechter et al., 1984). The numerous benefits such as improved construction quality, reduced construction cost, less construction time, lower site disruption, better site safety, easy repair and maintenance, higher sustainability, recyclable waste etc. can be credited for the rapid growth of this construction technology (Hassan et al, 2018). This construction procedure has its extensive use all over the world: accounting for more than 80 % in Sweden, around 20 % in New Zealand and Japan and the figure is around only 10 % in Australia (Heaton et al., 2017; Hassan et al., 2018). It has been foreseen that this practice would have been double in the coming 5 years in Australia (Heaton, 2017).

Steel beams have been universally used in the construction of composite structures due to its high constructional and structural amelioration (Wu et al., 2007; Katwal et al., 2018). Reporting its benefits, different literature has suggested for the combined application of steel beams connected to floor slabs using the shear connectors/ bolts rather than steel beams and reinforced concrete slabs without composite actions (Hick & Lawson, 2003). Nonetheless, the practice of using composite beam with RC slab is very limited in prefabrication construction.

Despite its rising popularity, limited guidance on a detailed design is available for their application in steel framed structures. Consequently, prefabrication has been specialised in the structural system as a single material steel, timber or reinforced concrete rather than composite prefabricated structure (Lam et al., 2000). This has provided a good platform for a number of researchers. A number of researches have been carried out for the prefabricated composite structures. However, all the research and outcomes are implied for the design of the continuous beam (Uy et al., 2017; Lam et al.,

2002; Lam et al., 2017). This project has been undertaken with a purpose to investigate the response of the discontinuous beam interconnected with each other under normal loading conditions.

Traditional continuous beams can be designed to a targeted strength. Despite this, it is laborious to carry long and heavy beams up to the site and install for prefabrication construction. This drawback can be conquered by the concept of discontinuous beams as it increases the portability and flexibility in connection. However, it is very challenging to design the connection of discontinuous beams and to obtain the same strength as a continuous beam. The current research will address this challenge with a proper connection design. For the conventional construction of steel structures, splice plate connections have been used to connect the steel beam to steel beam. In this type of connection, two or more splice plates and a number of bolts are used to the beams each other. In this paper, modified splice plate (MSP) connections are proposed for the prefabricated construction of steel beam-to-steel beam connections. In this paper, the feasibility study of proposed connections for discontinuous beams without slab will be studied using finite element (FE) analysis to understand the structural behaviour of the proposed connections.

2. Methodology

2.1 Proposed Beam-to-Beam Connections

In this research, the hypothesis made is that the ultimate strength of the discontinuous beam being used in prefabricated construction will be as close to the ultimate strength of the continuous beam under the same loading condition and beam-to-beam connections will be designed based on this strength assumption. It is targeted to get the discrepancy of $\pm 10\%$. For beam-to-beam connection, the point of contra-flexure is to be selected as at this point of the bending moment becomes zero and hence to some extent becomes easier to overcome the flexural failure of beam. Another hypothesis is that the connection system can overcome the shear failure easily of bolts. For prefabricated construction of steel-concrete composite structures, modified

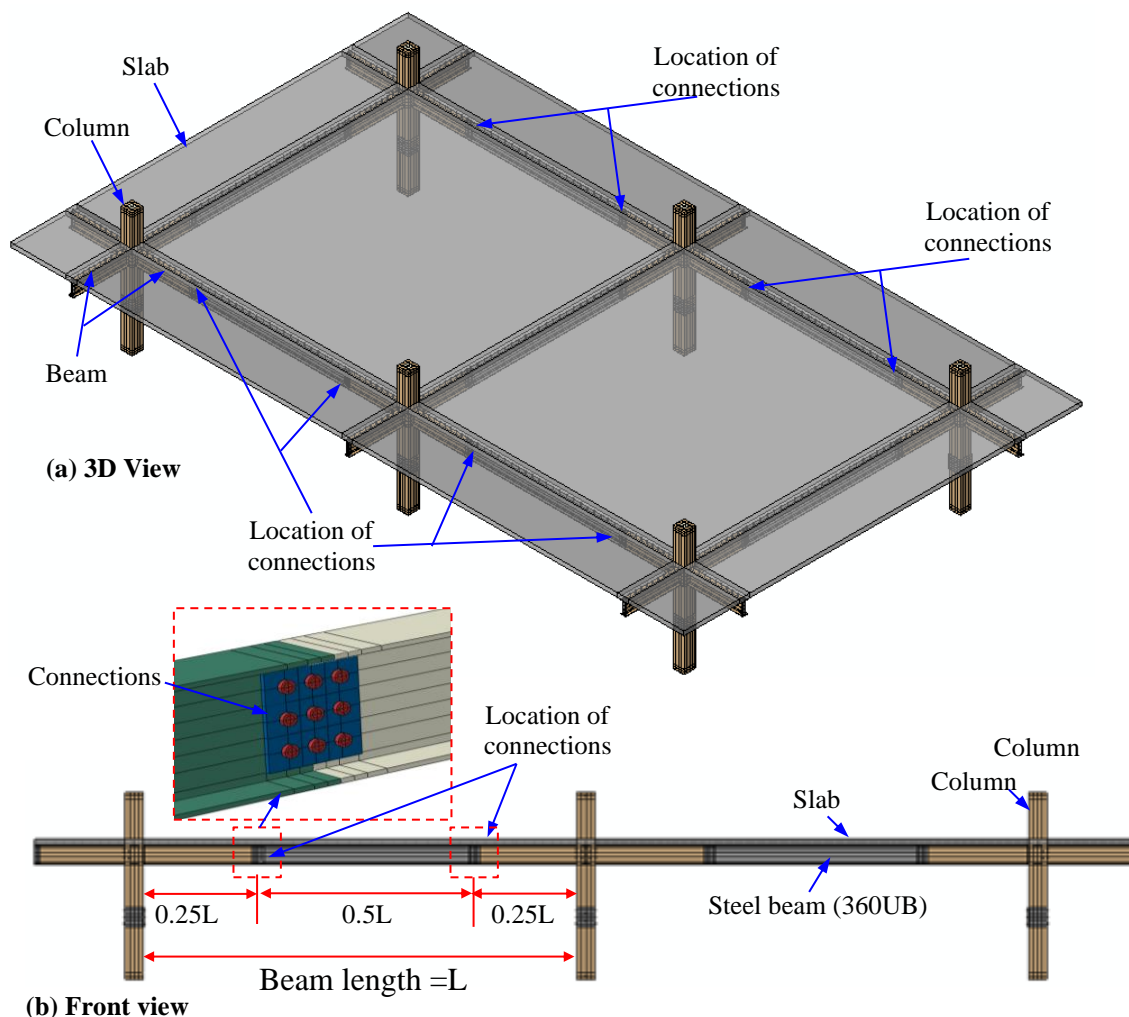


Figure 1. Location of beam-to-beam connections for prefabricated composite structures

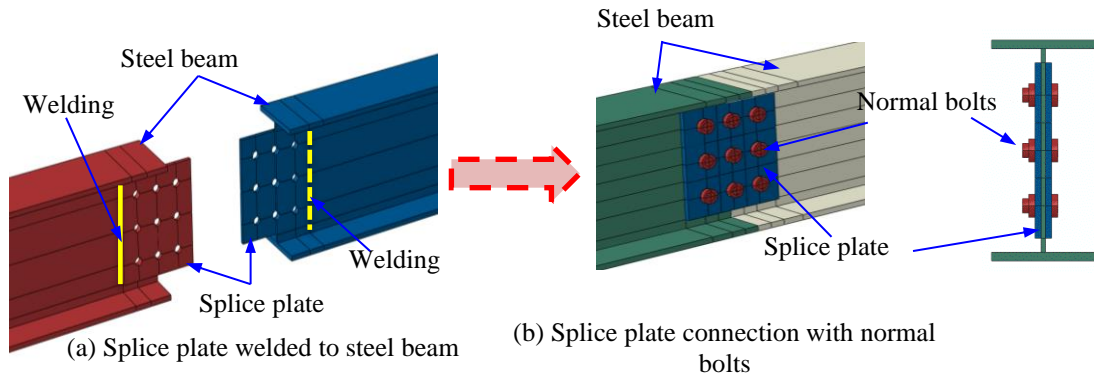


Figure 2. Details of proposed beam-to-beam connections with splice plates and normal bolts

splice plate connections are proposed where splice plates welded to the steel beam will be fabricated in the factory and then bolts will be used to connect the two discontinuous steel beams on the construction site only. In this method, the strength capacity of the proposed connections can be enhanced as well as the installation cost to handling the splice plates at the construction site can be minimised, due to the welding between the steel beam and splice plate. Figure 1 shows the location of the proposed connections that can be used for the prefabricated constructions. Figure 2 (a) shows the two connection component plates are attached to each part of the beam through welded connection. These two separate parts are assembled and connected by the bolt to make a beam-to-beam connection as shown in Figure 2(b).

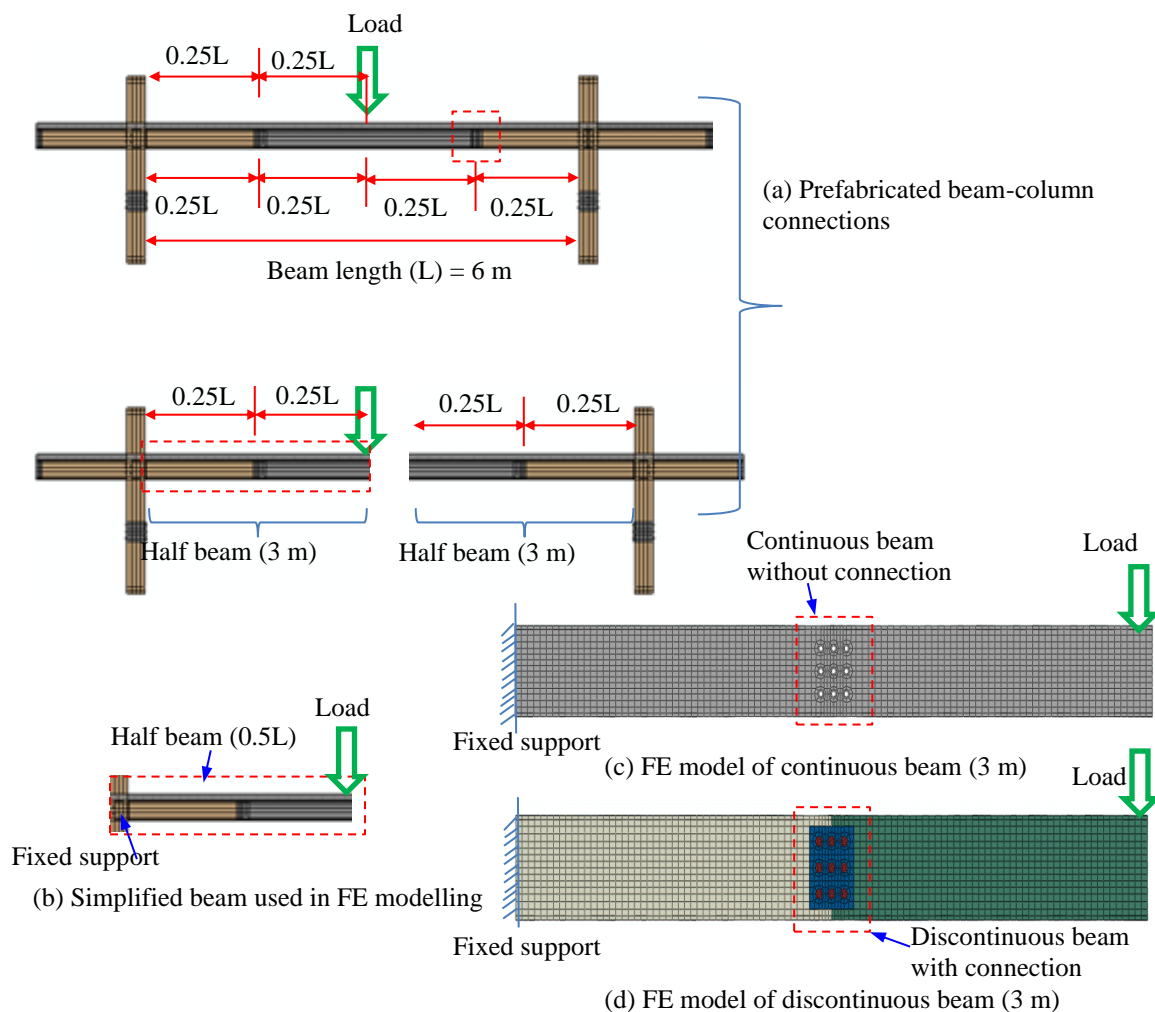


Figure 3. Details of half beam used in FE modelling

2.2 FE modelling of proposed connections

Finite element (FE) model has been established using general FE analysis software ABAQUS. The steel beams (310 UB 46.2), splice plates (210×244× 8 mm) and bolts (8.8 grade M20) are simulated using C3D8I elements [Hassan et al., 2014]. The minimum and maximum sizes used in the meshing of all components are 10 mm to 30 mm. Tie constraints are used for welding between the splice plate and steel beam web; remaining contacts are defined using hard surface-to-surface contacts. The friction coefficient used for hard contact is 0.25 for steel to steel contact [Hassan et al., 2014; Hassan et al., 2016]. For the simplicity of analysis, half of the beam is considered in FE modelling as shown in Figure.3 (b).

2.3 Material Models

The full-range stress-strain material models are used to simulate the strain hardening and softening behaviour of steel beam as shown in Figure. 4(a) and structural bolts as shown in Figure. 4(b). These two models were developed by Hassan [2016] based on Tao model (2013). The details of these two models are given in Hassan [2016]. The yield strength, ultimate strength and elastic modulus used in the FE modelling of the steel beam, splice plate and bolt are given in Table 1.

Table 1 Material properties of structural steels and structural bolts

Materials Properties	Beam flange	Beam flange	Splice plate	Bolt
Yield stress (MPa)	352	370	388	640
Ultimate stress (MPa)	535	534	506	800
Elastic modulus(GPa)	198	203	206	200

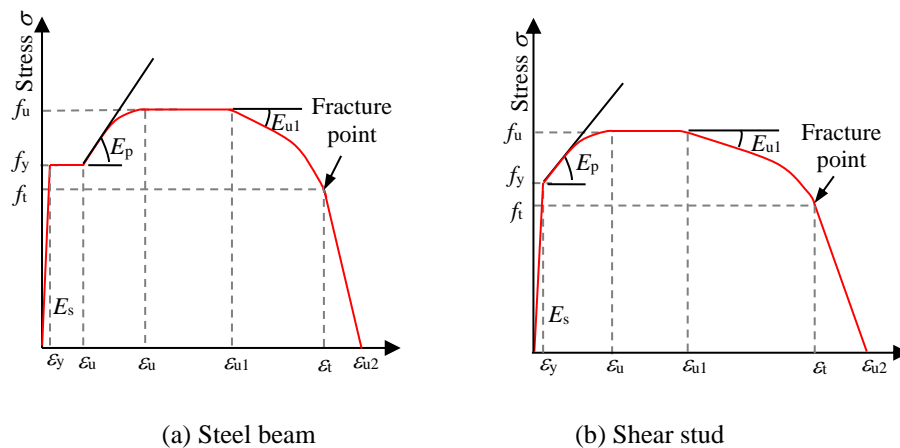


Figure 4. Full-range stress-strain curves for steel beams and shear studs (Hassan, 2016)

2.4 Load and Boundary Conditions

The load is applied at the end of the steel beam. As the steel beams are connected to columns using either welding or bolting, one end of the steel beam is considered as rigid connections. Based on this assumption, one end of the steel beam is restrained against UX, UY, UZ, RX and RZ as shown in Figure 3(c) for continuous beam and in Figure 3(d) for discontinuous beam. Nonlinear FE analysis has been conducted by considering the material nonlinearity i.e. nonlinear stress-strain curves, geometric non-linearity and boundary nonlinearity. Geometric and boundary nonlinearities are assigned using NLGEOM and CONTACT PAIR comments respectively in ABAQUS. The load is applied under displacement control method using a dynamic implicit method.

2.5 Verification

To verify the FE model, the test specimen is modelled using ABAQUS. Wang et al. (2009) conducted tests on blind-bolted endplate connections to CFST column (CJM1). The comparative results of the FE model and test of the specimen CJM1 subjected to bending are shown in Figure 6. The predicted load–displacement curves obtained from the FE models of these specimens agree very closely with the test results.

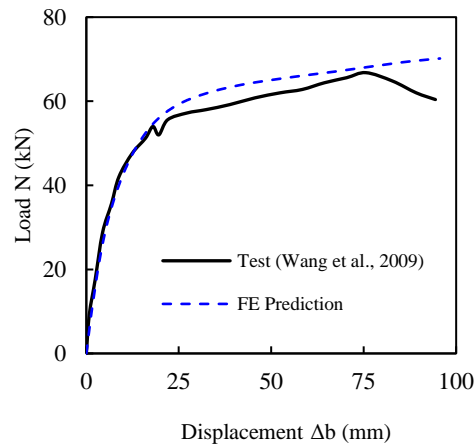


Figure 6. Comparison of FE model result with test result of cantilever beam i.e. blind-bolted endplate connections in bending load

3. Results and discussion

3.1 Comparison between continuous and discontinuous beams

The continuous beam and splice plate bolted (SPB) discontinuous beam has been modelled using finite element software ABAQUS to understand the behaviour differences in term of ultimate capacity and stiffness. In both cases, the same universal steel beam (360 UB 46.2) has been used. As mentioned in the previous section, the SPB discontinuous beam introduced in this paper is mainly fabricated from two segments of beams by connecting the splice plates (210×244× 10 mm) and normal structural bolts (M20). The results obtained from the analysis of the continuous beam and discontinuous beam with different connection systems has been discussed in below.

Figure 7 shows how the load-deformation curves of continuous and SPB1 discontinuous beams. It can clearly be seen that the ultimate capacity of the discontinuous beam is significantly reduced compared to the continuous beam, which is well expected because of the discontinuity. It is also noticed that the deflection of discontinuous beams at the connection point is higher than the continuous beam. In Figure 7, SPB1 is a discontinuous beam without pretension force. From the FE modelling results, it is observed that the continuous beam can resist a very high load of up to 88.81 KN. However, for the discontinuous beam at the same deformation, the ultimate failure occurs even at a very small load of 45.32 KN. When pretension force is applied to the bolt, the ultimate capacity (56.53 KN) of SPB2 discontinuous beam, as shown in Figure 8, is increased compared to the SPB1 discontinuous beam without pretension force. It was also noticed that the initial stiffness of both the discontinuous beams (SPB1 & SPB2) is significantly lower compared to the continuous beam.

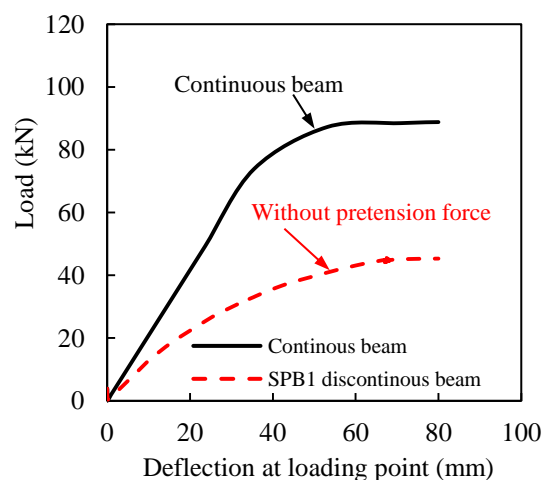


Figure 7. Load vs displacement curves of continuous and SPB1 discontinuous beam

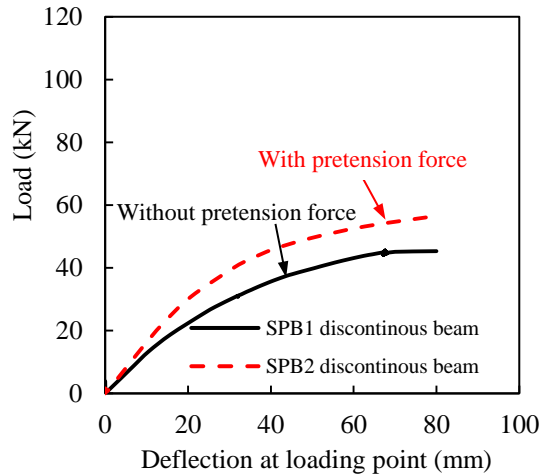


Figure 8. Effect of bolt pretension force on the discontinuous beam

3.2 Effect of welding between splice plate and beam web

The conventional splice plate bolted (SPB) discontinuous beam has been modified by introducing welding between splice and beam web, which is referred to here as a modified splice plate bolted (MSPB) discontinuous beam. The dimension used in MSPB discontinuous beams (MSPB1 & MSPB2) is similar to the conventional SPB discontinuous beam (SPB2). The main difference between the MSPB1 & MSPB2 is the welding area. For MSPB1 discontinuous beam, welding is made between one side of the splice plate and web of a beam whereas for the MSPB2 discontinuous beam, welding is made between three sides of the splice plate and web of a beam. The welding locations of these two MSPB discontinuous beams are shown in Figure 9. It can be seen that in the MSPB1 discontinuous beam, the plates and the beam web are connected by the vertical welding connection and for the MSPB2 discontinuous beam, the welded connection was upgraded to bidirectional welding between the plate and web of beam.

Figure 10 shows the FE modelling results of the modified SPB discontinuous beams (MSPB1 & MSPB2). The FE modelling results of the MSPB1 and MSPB2 discontinuous beams are also compared with the continuous beam and the conventional SPB discontinuous beam. The FE results show that the strength of MSPB1 discontinuous beam (84.38 kN) is increased significantly compared to the convention SPB2 discontinuous beam (56.53 kN). This 49.65% strength increase is due to the welding between one side of the splice plate and beam web. When three sides of welding are used in the MSPB2 discontinuous beam, the maximum ultimate load at same deformation is 86.29 kN, which is 2.2% higher compared to the one side welding used in the MSPB1 discontinuous beam. When FE modelling results of the modified SPB discontinuous beams are compared with continuous beams, their strength is found to be very close to the continuous beam (88.81 kN). The strength difference between the modified SPB discontinuous beams and the continuous beam is found to be 2.9-5.25 %, which is below 10%.

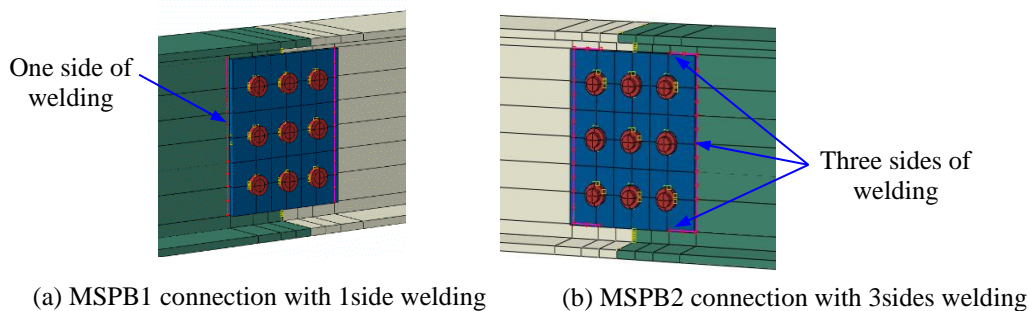


Figure 9. Welding locations of MSPB1 and MSPB2 discontinuous beams

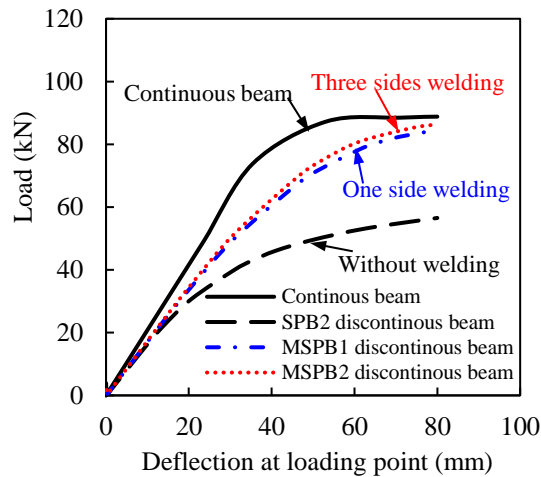


Figure 10. Load vs displacement curves of conventional and modified SPB discontinuous beams

3.3 Stress generated on beams due to conventional and modified SPB connections

Stress analysis has been performed using FE analysis to determine the stress distribution on the discontinuous steel beams due to different conditions of SPB connections. The FE results of stress analysis as shown in Figure 11 are presented in term of Von Mises stress to identify the failure condition. The Von Mises stress failure criterion has been used to identify the material failure condition. In the Von Mises stress failure criterion, when the Von Mises stress at a particular location exceeds the yield material strength, then the material yields at that location. If the Von Mises stress at a particular location exceeds the ultimate material strength, the material ruptures at that location. From the Von Mises failure criterion and the stress contour plot as shown in Figure 11(a), it is observed that the steel beam failure is more remarked near all bolt holes of the SPB2 discontinuous beams connected by conventional SPB connection. However, when a modified SPB connection is used to connect two beams, the stress concentration on the MSPB1 and MSPB2 discontinuous beams is less significant as shown in Figure 11(b) and Figure 11(c), respectively, compared to the SPB2 discontinuous beam.

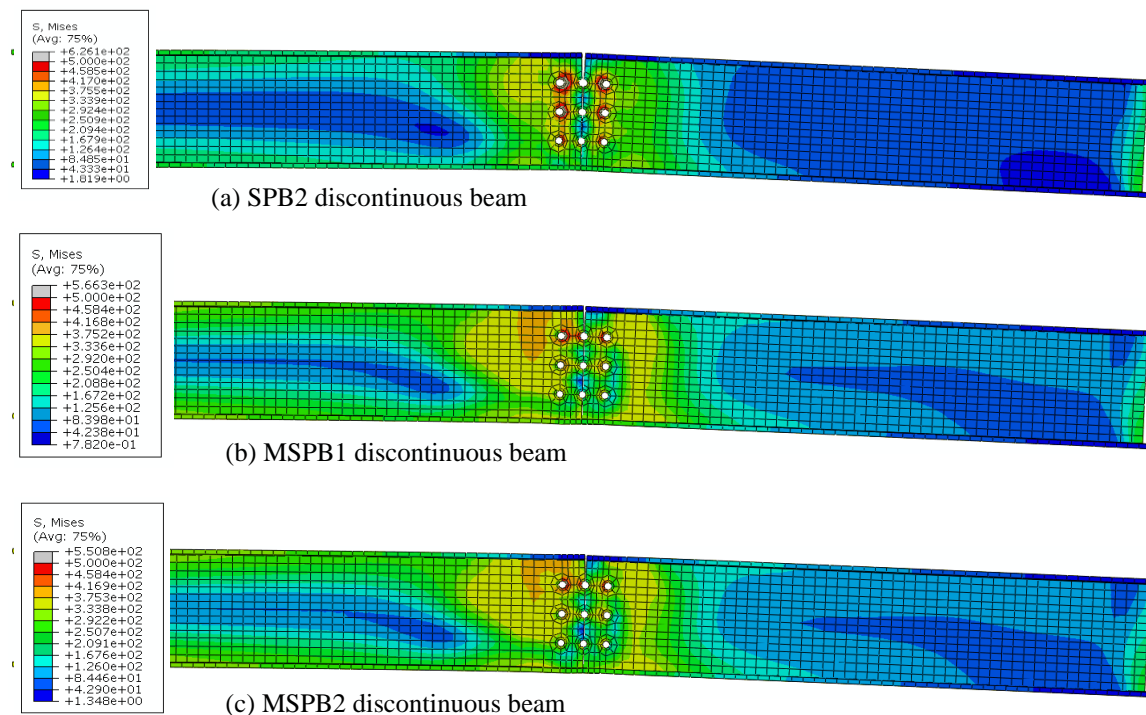


Figure 11. Stress generated on beam due to the conventional and modified SPB connections

3.4 Stress generated on bolts due to conventional and modified SPB connections

Figure 12 shows the stress distribution on the bolts due to the different types of SPB connections. When conventional bolts are used to connect the two beams of SPB2 discontinuous beams, the stress concentration on the bolts exceeded the

ultimate strength of bolts ($f_u = 800\text{MPa}$). This indicates that the SPB2 discontinuous beam failed due to the rupture of the bolts. However, when proposed modified SPB connections are used in the MSPB1 and MSPB2 discontinuous beams, the stress concentration is lower than the ultimate strength of bolts. This indicates that the MSPB1 and MSPB2 discontinuous beams failed due to the yield of the bolt material not rupturing.

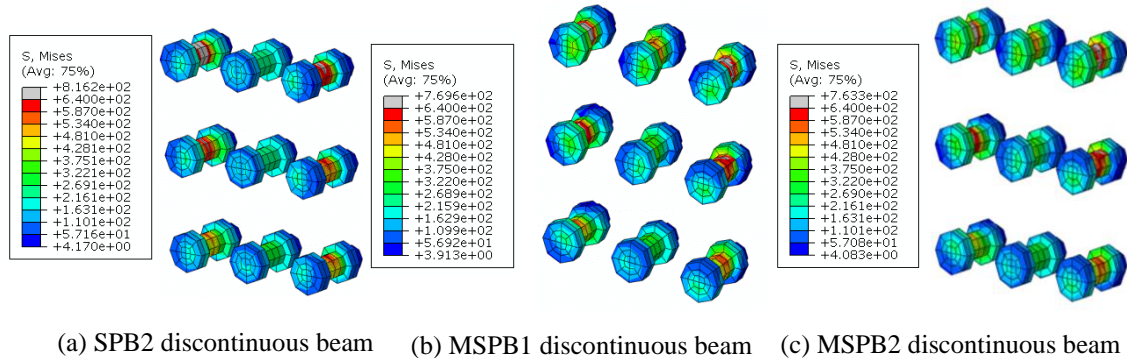


Figure 12. Stress generated on bolts due to the conventional and modified SPB connections

3.5 Stress generated on splice plate due to conventional and modified SPB connections

The stress distribution on the splice plate due to the different types of SPB connections is shown in Figure 13. The stress generated on the splice plate due to the conventional SPB connection as shown in Figure 13(a) is lower than the yield strength of the splice plate ($f_y = 388\text{ MPa}$). However, for the modified SPB connection, the stress observed on splice plate as shown in Figure 13(b) for MSPB1 discontinuous beams and Figure 13(c) for MSPB2 discontinuous beams is higher than its yield strength ($f_y = 506\text{ MPa}$), but lower than the ultimate strength. This also indicates that MSPB1 and MSPB2 discontinuous beams failed due to combined yielding of the splice plate and bolts. But for the SPB2 discontinuous beams, the failure is due to the failure of bolts. When structure fails due to the bolts, it would be a catastrophic failure, which is not expected. It can be concluded from the stress analysis of the beam, bolts and plate that when one side welding is considered in the conventional SPB connections to connect two beams of the discontinuous beams, the failure can be control by the combined failure of beam, bolt and splice plate. Such a design can be economical for the prefabricated construction as the same configuration of connections can resist more loads which will be closed to the continuous beam.

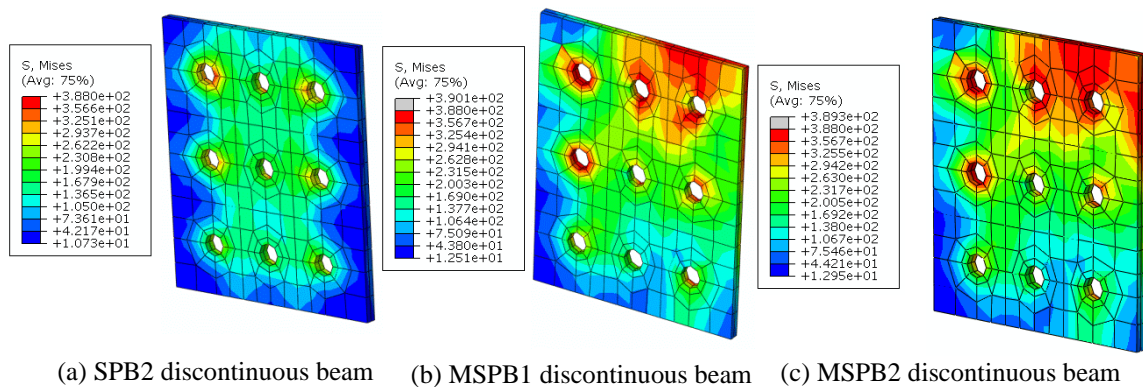


Figure 13. Stress generated on splice plate due to the conventional and modified SPB connections

4 CONCLUSION

A modified splice plate bolted connection has been proposed to connect steel beams to steel beams for the prefabricated construction. This paper mainly investigated the behaviour of modified splice plate bolted connections using finite element (FE) analysis. The following conclusion can be drawn based on the FE modelling results reported in this paper:

- (1) When two beams are connected using conventional splice plate bolted connections, the ultimate capacity of discontinuous beams is reduced significantly compared to the continuous beam.
- (2) When welding between the splice plate and beam web is considered in the conventional splice plate bolted connections to connect two beams, the ultimate capacity of the discontinuous beams is enhanced significantly

compared to the discontinuous beams having conventional splice plate bolted connections, but lower than the continuous beam.

- (3) When one side or three sides welding is considered in modified splice plate bolted connections, the strength difference between continuous and discontinuous beams is below 10%.
- (4) When modified splice plate bolted connections are used, the failure of discontinuous beams can be controlled by the combined failure of beam, bolt and splice plate. Hence it can be said that a discontinuous beam can be used instead of a continuous beam by proper design of modified splice plate bolted connections.

Further experimental research needs to be conducted to verify the proposed modified splice plate bolted connections. The number and locations of bolts and splice plate thickness can also be optimised in future study.

5. ACKNOWLEDGEMENTS

The authors acknowledge the computational support for numerical study, provided by the School of Computing, Engineering and Mathematics, Western Sydney University. The author would also like to extend immense thanks to Western Sydney University for providing a research platform.

6. REFERENCES

- Hassan M.K., Tao Z., Mirza O., Song T.Y. & Han L.H. (2014). Finite element analysis of steel beam-CFST column joints with blind bolts. *Proceedings of the Australian Structural Engineering Conference (ASEC 2014)*, 56, Auckland, New Zealand.
- Hassan M.K. (2016). Behaviour of Hybrid Stainless-carbon Steel Composite Beam-column Joints. *PhD thesis*, Western Sydney University, Sydney, Australia
- Hassan M.K., Tao Z., Song T.Y. & Han L.H. (2016). Effects of floor slabs on the structural performance of blind-bolted composite joints. *Proceedings of the 24th Australasian Conference on the Mechanics of Structures and Materials (ACMSM24)*, Perth, Australia.
- Hassan, M.K., Tao, Z. & Liao, L. (2018). Numerical study of column-column connections for prefabricated concrete-filled steel columns. *Proceedings of the 25th Australasian Conference on Mechanics of Structures and Materials (ACMSM24)*, Brisbane, Australia.
- Heaton A. (2017). *Australia must break through prefabrication barriers*. Available from: <https://sourceable.net/australia-must-break-through-prefabrication-barriers>.
- Hicks, S.J. & Lawson, R.M. (2003). Design of composite beams using precast concrete slabs. Publication 287, *Steel Construction Institute Ascot*.
- Katwal, U., Tao, Z. & Hassan, M.K., 2018. Finite element modeling of steel-concrete composite beams with profiled steel sheeting. *Journal of Constructional Steel Research*, 146: 1-15.
- Lam D., Dai X., Ashour A. & Rehman N. (2017). Recent research on composite beams with demountable shear connectors. *Steel Construction*, 10(2): 125-134.
- Lam, D., 2002. Composite steel beams with precast hollow core slabs: behavior and design. *Progress in Structural Engineering and Materials*, 4(2):179-185.
- Lam, D., Elliott, K.S. & Nethercot, D.A. (2000). Parametric study on composite steel beams with precast concrete hollow core floor slabs. *Journal of Constructional Steel Research*, 54(2), 283-304.
- Shechter, M. (1984). Method of prefabricated construction, and building structure constructed in accordance with such method. In: *Google Patents*.
- Tao Z., Wang Z.B. & Yu Q. (2013). Finite element modelling of concrete-filled steel stub columns under axial compression. *Journal of Constructional Steel Research*, 89: 121-131.
- Uy B., Patel V., Li D., & Aslani F. (2017). Behaviour and design of connections for demountable steel and composite structures. *Structures*, 9: 1-12.
- Wang, J.F, Han, L.H. & Uy, B. (2009). Behaviour of flush end plate joints to concrete-filled steel tubular columns. *Journal of Constructional Steel Research*, 65: 925-939.
- Wu, L.Y., Chung, L.L, Tsai, S.F., Lu, C.F. & Huang, G.L. (2007). Seismic behavior of bidirectional bolted connections for CFT columns and H-beams. *Engineering Structures*, 29(3), 395-407.

Experimental study of bending stiffness variation during a full rotation of cracked shafts

Erfan Taheri, Helen Wu and Ming Zhao

School of Computing, Engineering and Mathematics, Western Sydney University, Australia.

*Corresponding author's email: 17783747@student.westernsydney.edu.au

Peer review history

Manuscript submitted: 7 June 2019

Review process completed: 18 July 2019

Manuscript finally accepted: 25 July 2019

Handling Editor: Professor Aatur Rahman

Abstract: *The mechanical shaft is a key element in the majority of mechanical systems. It is responsible for delivering power from one end of the drive train to another. The rotating shaft undergoes rapid fluctuations of bending moment stresses and when combined with their long operational hours, it can eventually form a crack and thus lead to shaft failure. Therefore, it is imperative that a method is developed in order to detect cracks whilst the shaft is in motion. In this paper, an experimental analysis is conducted to obtain the bending stiffness values, and to*

contribute to the literature of rotor-dynamics so that eventually a method for early crack detection during dynamic operation can be developed. The experimental research involves the creation of cracked shaft models (0.1 mm wire cutting into the shaft, 0.3 mm wire cutting into the shaft, having two 0.3 mm wire cutting into the shaft and developing a 0.3 mm crack by welding joinery). This method of creating the cracked shaft models is relatively quick, easy and cost effective. A three-point-bending test is then conducted on the cracked shaft models to evaluate the shaft's stiffness variation through varying angular positions. The results show that all the cracked shaft models exhibit the breathing mechanism corresponding to the cracks location during rotation.

Keywords: *Cracked; Shaft; Rotor; Dynamics; Breathing.*

1. Introduction

Mechanical shafts are present in almost every mechanical system, including motor vehicles, aircrafts, boats, mining equipment etc. Due to the shaft's dynamic nature, it is prone to experiencing internal forces, rapid changes in bending moments, stresses and tension forces. These constant forces acting on the shaft may contribute to the formation of cracks. When a shaft develops a crack, it may go unnoticed and eventually lead to shaft failure. Shaft failure occurs when the shaft breaks into two or more pieces. As most industrial processes rely upon a form of mechanical machinery, it is important to be able to detect a crack in a shaft, prior to the onset of failure. Shaft failure could lead to injuries and potential fatalities, i.e. failure occurring in an aircraft engine.

Many large-scale industries such as mining, agriculture and manufacturing factories heavily rely on their machinery for business operation and generating revenue. If shaft failure occurs, then the outcome would be costly causing delays and loss of revenue. There are no current methods for detecting a crack in a shaft whilst the shaft is in operation. Therefore, this topic serves as one of the most important issues in rotor dynamics and a solution will inevitably save on costs, reduce fatal accidents and avoid injuries.

An interesting phenomenon, known as crack breathing, occurs when analysing the dynamic motion of a cracked shaft. The moving rotation of a shaft also means that the respective location of the crack is also moving. The cracked portion rotates through two distinct regions, a region of compression and a region of tension. When the crack is in a compression zone, then the crack is closed and conversely, when the crack is in a tension zone, it is considered fully open. As the crack goes from being in a compressive zone (closed) to a tension zone (fully open), the gap (of the crack) gradually starts closing until it is in a full compressed zone. Subsequently, when the crack goes from the compression zone to the tension zone, it starts to gradually open until it is completely open. This process keeps repeating for every 360-degree rotation. Thus as the shaft is rotating, the crack is constantly changing how much it is open and closed, and this phenomenon is referred to as the "crack breathing" mechanism (Georgantzinos et al., 2008). This constant changing phenomenon adds a layer of difficulty to being able to predict a crack prior to it reaching failure.

Al-Shufeifat and Butcher (2011) researched the effects of cracked shafts using analytical, experimental and mathematical methods. They also discuss a mechanical system that can be modelled by three components, i.e. mass, stiffness value and damping factor. It was noted that when a crack is formed in a shaft, the actual mass of the shaft is not affected (negligible) and the damping factor is not affected either. The primary variable which changes is the stiffness value and thus when physically experimenting on shaft models, then the factor of interest would be its stiffness value (Jun, et al., 2008). As the shafts gap is constantly changing during a full revolution (crack breathing phenomenon), then testing the stiffness value at different angles, relative to the crack's starting position, will provide data on the crack breathing phenomenon and the effect on a cracked shaft's stiffness.

It will be possible to test the breathing phenomenon for certain models and to derive new data by experimentally testing for the fluctuating levels of stiffness as the shaft undergoes rotations. The testing would involve creating several models of cracked shafts through methods of wire cutting and welding. Once the cracked shaft models have been formed, then a three-point bending stress machine is used to calculate the deflection of the crack under a certain load. The shaft would have the load applied to it every 30 degrees for a full 360-degree revolution.

2. Methodology

2.1 Creating cracked shaft models

There had to be various models of cracked shafts made in order to conduct a stiffness study. The shaft models experimented on are 85 cm long circular shafts made of AISI 1040 Steel. The shafts have a 19 mm diameter. A wire-cut was performed to make the first model; this was done by using a very thin wire (0.3 mm wide). Figure 1 below shows the Funac wire-cutting apparatus. A single strand of wire (composed of 65% copper and 35% zinc) is used to cut the shaft in the centre of it (42.5 cm from either edge inwards). The cut was performed at 40% of the shaft's diameter (cutting 7.6 mm into the shaft). The next shaft was prepared exactly the same way as the previous shaft but with an additional cut, as seen in Figure 2 below. An additional shaft was used for a 0.1 mm wide wire-cut (also cut once in the centre of the shaft and the cut being 40% of the shafts diameter). Figure 3 below shows an enlarged image of the wire-cutting process, there is deionized water being poured on the cut area whilst the single strand is making the cut to ensure there is no overheating.



Figure 1. Fanuc wire-cutting Machine

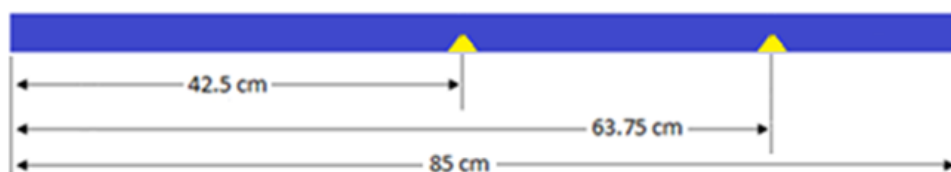


Figure 2. Diagram of shaft with cutting dimensions



Figure 3. Enlarged view of 0.1 mm wire-cutting process

A fifth shaft was used to make the last cracked model. This method aimed to make the smallest gap possible and it was acquired by using a welding technique. Figure 4 below, shows the main stages in developing the welding crack. The steps in creating a welding crack were firstly, the shaft was cut in half. The amount of crack wanted was 40% of the shafts diameter (19 mm) which equates to 7.6 mm. Therefore, a milling process was used to cut out 11.4 mm from both ends of the shaft. Use a donor shaft to cut out the material to the shape that was cut out of both halves of the shaft but this time having it as one piece. Place the two halves together and weld around the donor piece and the two halves to join them together. The two halves will be pushed together and then a very minute crack is formed. The development of the welding crack is shown in Figure 4 below with (a) showing the shaft halved and milled, (b) showing the donor piece and (c) representing the area that is being welded in red and the yellow line showing the minute welding crack. The welding crack represents the smallest crack model (measured at around 0.03 mm). All the cracked shaft models are shown in Figure 5 below.



Figure 4. Procedure of welding crack (a) two halves milled (b) donor piece (c) welded together (red lines) and yellow representing 0.03 mm welding crack



Figure 5. (a) 0.3 mm wire-cut crack (b) 0.1 mm wire-cut crack (c) 0.03 mm welding crack (d) two 0.3 mm wire-cut cracks

2.2 Experimental set up and testing

To experiment on the shafts, it was necessary to use a machine that is capable of producing a force and then measuring the deflection caused by the force. The Instron 3365 machine was selected to perform this task. The type of test needed was a

three-point bending test, where the shaft sits on two points and a force point is applied in-between the two points the shaft is held in. Figure 6 shows the shaft in the three-point-bending apparatus, with the force being applied to the centre of the shaft (crack location). The supports are located 5 cm on either side of the centre of the shaft. Each shaft, including an intact one as the control, was placed on the machine. The goal of the experiment is to observe the changes in stiffness as the shaft undergoes rotation. When the shaft was placed into the machine, the orientation of the shaft relative to the crack was important, and the initial position was the crack facing upwards. The crack facing upwards was selected as 0 degrees, and every 30 degree was marked on the shaft from the starting 0-degree position. A force of 3000 Newton was then applied, and the deflection was measured. This was done from 0 to 330 degrees at 30-degree intervals. Once the deflection is measured for each shaft (Intact, 0.1 mm wire cut, 0.3 mm wire cut, 2x 0.3 mm wire-cuts and welding crack) at twelve different angles for each one, then it would be possible to graph the stiffness effects, due to the different angles in the various cracked shaft models.

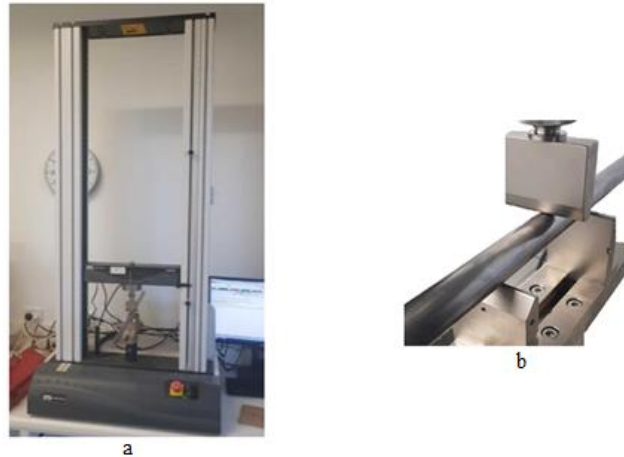


Figure 6. (a) Three-point bending test using Instron 3365 (b) Enlargement of testing section

Table 1. Stiffness values (0.1 mm wire-cut crack)

Rotation angle θ (Degree)	Force (N)	Deflection $\times 10^3$ (m)	Stiffness (N/m)
0	3000	0.279	12.940
30	3000	0.274	13.047
60	3000	0.264	13.090
90	3000	0.240	13.056
120	3000	0.236	13.143
150	3000	0.257	13.038
180	3000	0.262	13.116
210	3000	0.254	13.266
240	3000	0.236	13.372
270	3000	0.241	13.209
300	3000	0.262	13.182
330	3000	0.274	12.956
360	3000	0.279	12.940

3. Results and discussion

The three-point bending stress was performed on every shaft. At every 30-degree interval there was a force applied in the middle of the shaft, until it reached a maximum load of 3000 Newtons, and at that point, the deflection of the shaft was measured. Table 1 shows the deflection which occurred due to the 3000 Newton force at every angle interval for the 0.1 mm wire-cut crack. The stiffness was then calculated by dividing the maximum force of 3000 newtons by the deflection in metres. Table 2 shows the stiffness for the rest of the shafts that were experimented on.

The stiffness values at varying angular positions were graphed for each shaft, as depicted in Figure 7. For the Intact shaft, as there is no crack, it is expected that the stiffness should not change no matter which angle it is placed at. The stiffness differs with a standard deviation of 0.130 (N/m) from the minimum stiffness being 12.940 (N/m) and the maximum being

13.372 (N/mm). The experimental result gathered is considered accurate and only in theoretical testing could a straight line be achieved.

It is known that the breathing mechanism takes place as the cracked portion of the shaft rotates throughout zones of compression and tension. For the 0.1 mm wire-cut crack, Figure 7 shows a pattern that is symmetrical at nearly 180 degrees which validates that the experimental data obtained is correct and a breathing effect is seen. As the rotation angle continues, the stiffness is seen increasing (peaking at 120 degrees) and then decreasing until it reaches halfway (180 degrees) and the pattern is repeated from 180 degrees to 360 degrees.

Table 2. Stiffness values for shafts

Rotation angle θ (Degree)	Intact shaft (N/m)	Stiffness (N/m) 0.1 mm wire- cut crack	Stiffness (N/m) 0.3 mm wire- cut crack	Stiffness (N/m) Welding crack	Stiffness (N/m) two 0.3 mm wire-cut cracks
0	12.940	10.753	10.909	11.499	10.969
30	13.047	10.949	10.791	11.714	10.897
60	13.090	11.385	10.753	12.000	11.853
90	13.056	12.495	12.898	12.448	12.937
120	13.143	12.701	12.320	12.151	12.341
150	13.038	11.664	11.802	10.870	11.763
180	13.116	11.450	11.173	10.156	11.364
210	13.266	11.830	11.806	10.642	11.990
240	13.372	12.706	12.146	11.806	12.886
270	13.209	12.428	12.842	12.443	13.106
300	13.182	11.450	10.616	12.157	11.025
330	12.956	10.949	10.826	12.082	10.625
360	12.940	10.753	10.909	11.499	10.969

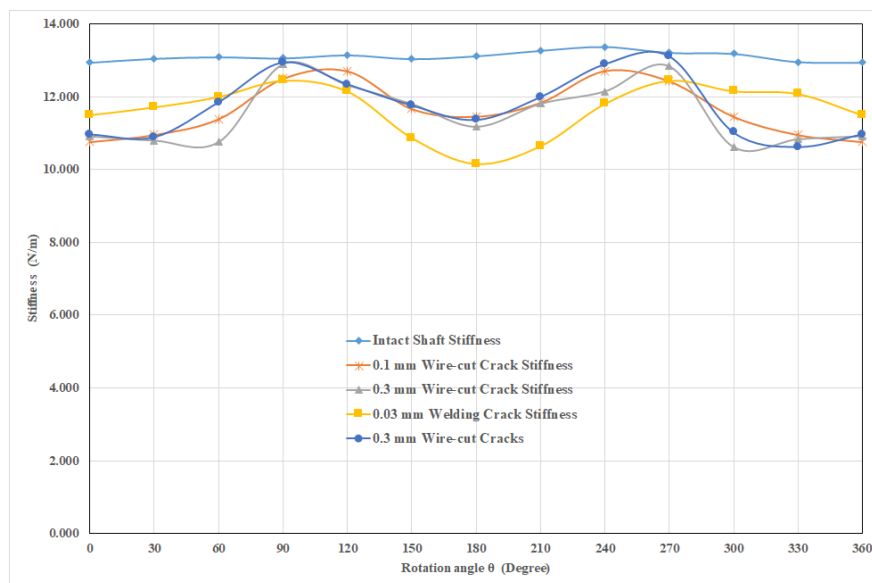


Figure 7. Shaft stiffness values at varying angular positions

For the 0.3 mm wire-cut crack, the graph in Figure 7 shows a pattern that is symmetrical at nearly 180 degrees which validates that the experimental data obtained is correct and a breathing effect was seen. As the rotation angle continues, the stiffness slightly dips and is then seen increasing until it is peaking at 90 degrees. It then begins decreasing until it reaches halfway (180 degrees) and then peaking again at 270 degrees.

For the welding crack, the graph in Figure 7 shows a pattern that is symmetrical at nearly 180 degrees which suggests that the experimental data obtained is correct as a breathing effect is seen. As the rotation angle starts, the stiffness is seen to slightly increase until a peak is reached at 120 degrees. It slowly dips until the minimum stiffness at 180 degrees and then the pattern is mirrored with it rising again and peaking at 270 degrees.

For the two 0.3 mm wire-cut cracks, the graph in Figure 7 shows a pattern that is symmetrical at nearly 90 degrees which suggests that the experimental data obtained is correct as a breathing effect is seen. As the rotation angle starts the stiffness is seen to slightly increase until a peak is reached at 90 degrees. It slowly dips until the minimum stiffness reaches 180 degrees and then the pattern is mirrored with it rising again and peaking at 270 degrees.

The intact shaft behaved as expected within experimental testing and showed minimum stiffness changes despite its angular position. The cracked shaft models all depicted the trend of the stiffness increasing and decreasing until 180 degrees, where the pattern is then repeated in a mirror image. All the shafts displayed symmetrical curvature, confirming the 'crack breathing' phenomenon. As the shafts with a crack rotate through a tension zone, it is expected that the stiffness at that point should match closely to the stiffness of the intact shaft (the crack is considered closed, and thus the stiffness should be similar to the intact shaft which has no crack).

4. Conclusion

The research objectives were to find out the correlation a cracked shaft has on stiffness study with varying crack parameters. Firstly, models of cracked shafts had to be developed and they were done so from wire cutting (0.1 mm wire cut, 0.3 mm wire cut and two 0.3 mm wire cuts) and a welding process to form a minute crack (approximately gap of 0.03 mm). Once these models were produced then a force of 3000 newton was applied at the crack location. The shaft was marked at an angle and was rotated every 30 degrees from zero to 360 degrees, thus going through a full revolution. At every 30 degree rotation, the 3000 newton force was applied and the apparatus measured the amount of deflection at that point. The stiffness was then calculated by dividing the force with the deflection and then graphed. The results obtained showed that the graphs were symmetrical at 180 degrees and thus confirming that the experiment was conducted correctly. The physical findings confirmed the theoretical research that a phenomenon known as 'crack breathing' occurs when there is a crack present in a shaft. The results obtained are valuable and very important, as the findings are new. The results obtained will lower the research gaps in rotor dynamics and will assist in a method eventually being developed for early crack detection during dynamic shaft operation.

5. Acknowledgements

The authors gratefully acknowledge the financial support from the School of Computing, Engineering, and Mathematics, Western Sydney University, Australia.

6. References

- Al-Shudeifat, M. A., & Butcher, E. A. (2011). New breathing functions for the transverse breathing crack of the cracked rotor system: Approach for critical and subcritical harmonic analysis. *Journal of Sound and Vibration*, 330(3), 526-544.
- Georgantinos, S., & Anifantis, N. (2008). An insight into the breathing mechanism of a crack in a rotating shaft. *Journal of Sound and Vibration*, 318(1-2), 279-295.
- Jun, O. S., & Gadala, M. S. (2008). Dynamic behavior analysis of cracked rotor. *Journal of Sound and Vibration*, 309(1-2), 210-245.

Modal analysis of cracked shafts

Erfan Taheri, Helen Wu and Ming Zhao

School of Computing, Engineering and Mathematics, Western Sydney University, Australia.

*Corresponding author's email: 17783747@student.westernsydney.edu.au

Peer review history

Manuscript submitted: 5 September 2019

Review process completed: 23 September 2019

Manuscript finally accepted: 9 October 2019

Handling Editor: Professor Ataur Rahman

Abstract: *The mechanical shaft is a key component in most mechanical systems. It is in charge of transferring power from one part of the machine to another part. As the shaft spins over long operational hours it may become prone to forming a fatigue crack. Often cracks show no symptoms until the shaft reaches failure. It is with utmost importance to develop a method to detect a cracked shaft before it reaches failure. Modal analysis is the first step to reach the goal and understand the*

vibration behaviour of a machine. In this work, Finite Element analysis is performed to acquire the mode shapes from cracked shaft models developed through Abaqus. The models include various shafts, such as an intact shaft, a shaft with varying crack depth ratios [0.5, 1, and 1.5], crack locations and the number of cracks [1 and 2 cracks]. Each shaft model developed will have 5 modes tested and the natural frequency will be derived for each mode. Comparison of the frequencies shows that shaft stiffnesses are significantly reduced for a shaft with a larger crack, and also a shaft with more cracks. The results gathered are new and provide a contribution to rotor-dynamics for eventual development of a method for early crack detection.

Keywords: *Crack; Shaft; Rotor; Frequency.*

1. Introduction

Almost all mechanical machines in the fields of transportation and manufacturing require a shaft. As the shaft is rotating at high speeds, it faces internal pressures and quick changes in bending moment stresses. These pressures and stresses may lead to a shaft developing a fatigue crack. When a shaft initially develops a crack, it may exhibit no symptoms until it is too late, and reaches failure (when the shaft splits into two or more pieces). Shaft failure could lead to financial loss and be potentially lethal to humans by causing injuries or fatalities (e.g. shaft failure in an operating aircraft). There are currently no known methods for early crack detection while a machine is in operation (dynamic movement). Therefore, this field is of high importance to rotor dynamic studies as finding a solution will prevent loss of business downtime, injuries and fatalities.

The modal and vibrational signature of a shaft without a crack could be measured and graphed, hence the characteristics of a "normal" shaft could be gathered. Then the vibration on a shaft with a crack could be measured to compare against the non-cracked shaft. Multiple parameters are incorporated, such as the crack's depth (ratio of the cracks length relative to the shafts diameter), crack's location (the location of the crack with respect to the shaft) and adding multiple cracks. The aim will be to first develop a simulation of a shaft with a crack and then to test all the parameters. This will yield radically new results that will significantly contribute to the literature of early crack detection. A shaft with fixed ends and two discs will be used. The exact dimensions of the shaft with its properties is presented in the research methodology section of this paper.

Mechanical systems are prone to resonance which is frequency that can eventually cause damage to the structure. By being able to measure the frequencies, which cause a structure to resonate, it would be possible to understand the effects of different frequencies on the structure. Modal testing involves finding the modes of vibration of whatever is being measured.

Sekhar (2004) conducted research based on a modal analysis to identify cracks in a rotor. The approach that was carried out in this study was the modal-based method which was applied to identify the crack in the rotor at a steady speed. A model-based technique by (Jain et al., 2003) was used for the crack identification, in which the full system state is reconstructed from a number of measured quantities by an observer during the iterative process. For the different crack locations and depths at different rotor speeds, it was found that the model based identification technique with modal expansion was successful. While the cause of the cracks was ascertained using the Fast Fourier method, the effectiveness

of the identification process depends to a good extent on the number of measured locations (DOF). Modal analysis of a rotating shaft with a crack can give detailed knowledge on the nature of the structure. Through finding the modal shapes of a non-cracked shaft and then comparing it to a shaft with cracks, (with varying parameters) it can find distinguished characteristics and aid in early diagnostics of crack detection.

A material's mass, stiffness factor and damping value affect the material's modes. Every mode has a correlating frequency and a shape. Therefore, if the properties of a material are altered (i.e. a crack or varying crack parameters), then the modes will also change. A modal shape represents the oscillation of a component based on its frequency.

Multiple mode shapes can be present for the same component and thus each specific mode shape is related to its individual characteristic of its natural frequency.

The research will be done analytically by producing a shaft and testing several of the parameters mentioned above. The data collected will be tabled and graphed by the mode shapes and frequency. The results will be of significant value as it is narrowing the gaps to eventually developing a method of early crack detection during dynamic operation.

2. Methodology

2.1 Modelling cracked shaft

In order to test the modal and vibrational effects on a shaft with a crack, it is important to first model the system in a software and then to run simulations from it. A Finite Element Analysis software (FEA), Abaqus by Dassalt systems, was used to perform this task. Once the models are designed then a simulation is performed to obtain the modal signatures and corresponding frequencies for the cracked shaft models. Table 1 below shows the specifications for the shaft which was developed on Abaqus.

Table 1. Shaft specifications for development on Abaqus

Component	Measurements
Length of shaft	724 mm
Radius of shaft	6.35 mm
Inner radius of disk	6.35 mm
Outer radius of disk	54.5 mm
Crack locations	Variable
Distance to disk 1	181 mm on the positive x-axis
Distance to disk 2	543 mm on the positive x-axis
Weight of shaft (Gravity)	$9.81 \times 10^{-3} \text{ mm/s}^2$
Mass of disk 1	0.5 kg
Mass of disk 2 (Additional mass added to create unbalancing force effect on the shaft)	0.5 kg + Variable (unbalancing force mass)
Stress	$210 \times 10^3 \text{ (N/mm}^2\text{)}$
Density of shaft	$7.8 \times 10^{-9} \text{ (kg}^3\text{)/mm}^3\text{)}$

To create a shaft, which can simulate a crack, it has to have conditions that replicate real life conditions (with friction being taken into account, effect of gravity etc.). Abaqus was used to develop a shaft and the methodology lists the main steps that were undertaken in order to create such a shaft. Essentially there were three separate parts that were made, the shaft, the discs and the cracked part. After the parts were made, they were assembled together and the ends became fixed supports. The material, density of the shaft and poisson's ratio were all implemented into the material design (as per the parameters above in Table 1). Mesh was added to the component so the effects could be visualised and finer mesh was applied to the area of the crack. Figure 1 below shows the mesh used for the shaft prior to extrusion. The mesh size chosen was employed using elements which use eight node linear bricks, and thus the meshes density increases near the crack location for accurate results (Mobarak et al., 2017). The mesh value around the crack is $\Delta x_{crack} = 0.04$ for the measurements of the shaft's radius (listed in Table 1) and length of 5mm extruding to both directions from the crack. For

every other component in the model, the mesh size $\Delta x_{other} = 0.2$, extending along the transversal and longitudinal direction of the shaft with measurements also in Table 1. Once the shaft is assembled it is possible to do modal analysis. 5 modes were selected to compare the results. Modal analysis to obtain the frequencies was done to a shaft without a crack, a shaft with a crack (with three different crack depths) and a shaft with varying crack locations (three locations; the centre of the shaft at 362 mm from either end and a crack near the left support before disc 1 and a crack to the right of disc 2 near the fixed end, both 90 mm inwards respective from the fixed ends). The final set up is shown below in Figure 2.

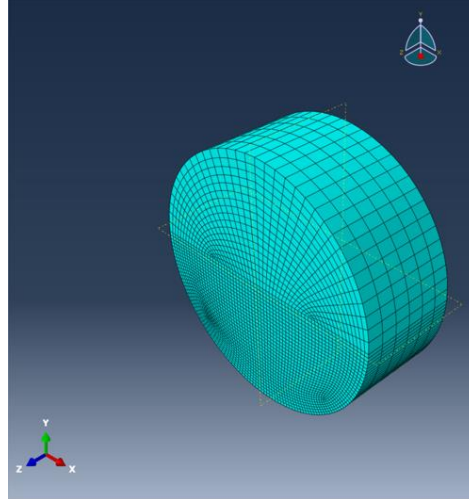


Figure 1. Abaqus modelled shaft showing mesh

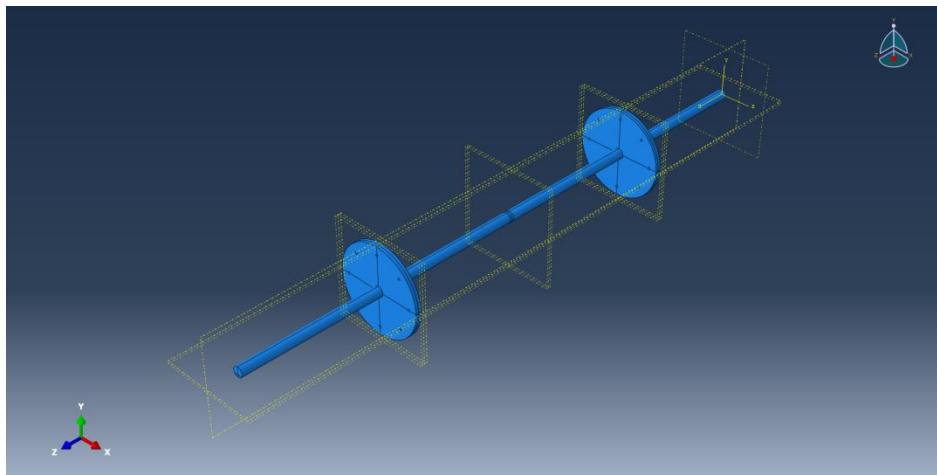


Figure 2. Abaqus model of shaft set up

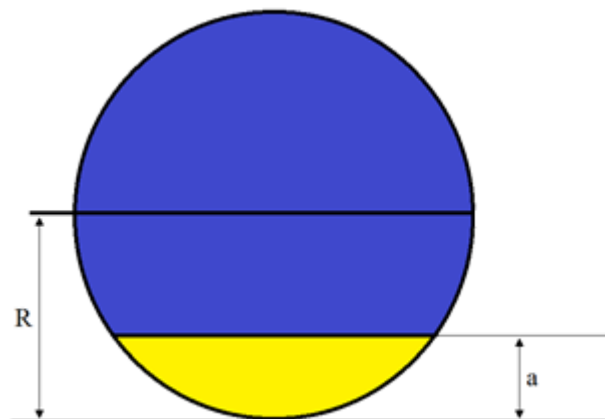


Figure 3. Diagram representing crack depth ratio

2.2 Shaft parameters

The crack depth ratio is the ratio between the crack's depth with respect to the radius of the shaft ($\mu = \frac{a}{R}$), as seen in Figure 3. There will be experimentation of a shaft with no crack followed with three crack ratios as shown below. The three crack depth ratios used for the preliminary results are $\mu = 0.5, 1$ and 1.5 . Figure 4 represents the crack's location with respect to the shaft. There are three different crack locations used for gathering the preliminary results. A crack located in the centre of the shaft, Lc2. The crack near the left fixed support at 90mm (from positive x axis), Lc1, and a crack on the right support at 634mm (from the positive x axis), Lc3. The cracks near the fixed ends are also on either side of the discs, with a crack depth ratio of 1. The effect that multiple cracks have on the modal frequency will be investigated. The control is a shaft with no crack. Then a shaft with one crack can be compared to a shaft two cracks (with crack depth ratio equal to 1), in two locations at the same time (Lc1 & Lc2).

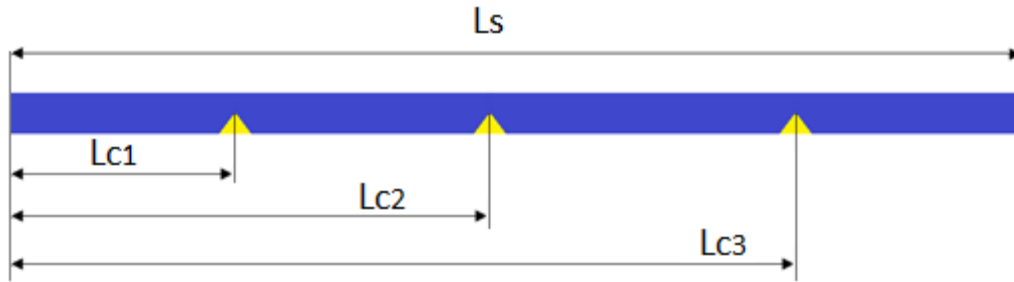


Figure 4. Crack locations

3. Results and discussion

Modal analysis using five nodes was conducted on a shaft with no crack (as the control), three different crack depth ratios ($\mu = 0.5, 1$ and 1.5), three different crack locations (Lc1, Lc2 and Lc3) and with multiple cracks (Lc1 and Lc2). Table 2 shows the first mode signatures for a shaft with no crack, and the three crack depth ratios. The full results gathered are listed in Tables 3, 4 & 5.

When comparing the effects that the crack depth ratio has on the shaft, it's noted that as the crack depth ratio increases then the frequency decreases. Having the same crack depth ratio but in different locations has minimal effect on the frequencies. This can be attributed to the symmetrical spreading of the crack and same crack depth ratio. When there were multiple cracks, then the frequency was decreased more than a single crack or no cracks.

Tables 3, 4 & 5 showed values of frequencies with respect to the modes. The frequency formula ($\omega = 2\pi f = \sqrt{\frac{K}{m}}$) can be used to understand what is happening to the frequency when there is a crack presented.

Table 3. Results of modal comparison of different crack depth ratios ($\mu = 0.5, 1, 1.5$)

	Mode 1	Mode 2	Mode 3	Mode 4	Mode 5
No crack	24.139 Hz	24.181 Hz	49.077 Hz	49.154 Hz	62.278 Hz
Crack at $\mu = 0.5$	24.096 Hz	24.129 Hz	49.079 Hz	49.154 Hz	62.202 Hz
Crack at $\mu = 1$	23.595 Hz	23.903 Hz	48.189 Hz	48.530 Hz	61.939 Hz
Crack at $\mu = 1.5$	23.321 Hz	23.790 Hz	47.727 Hz	48.243 Hz	61.931 Hz

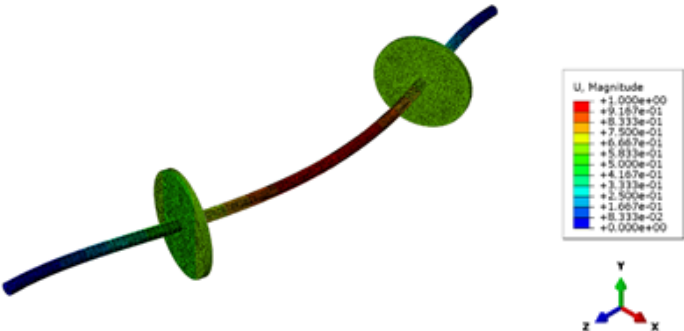
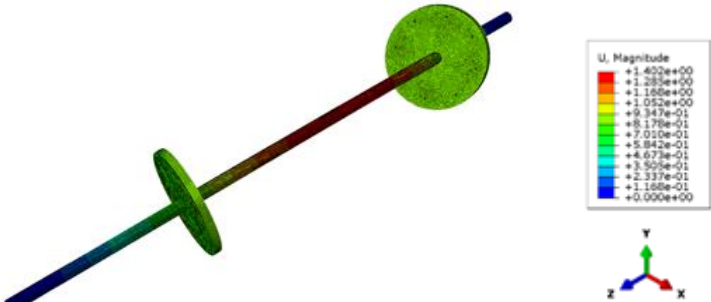
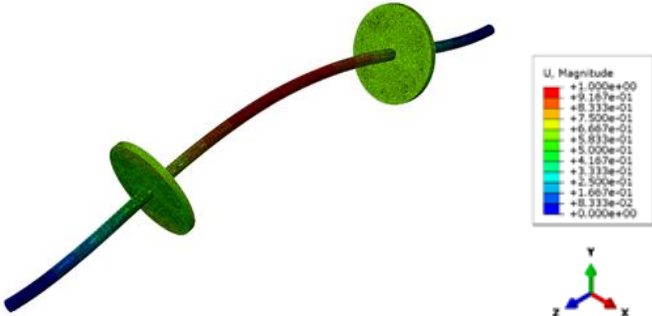
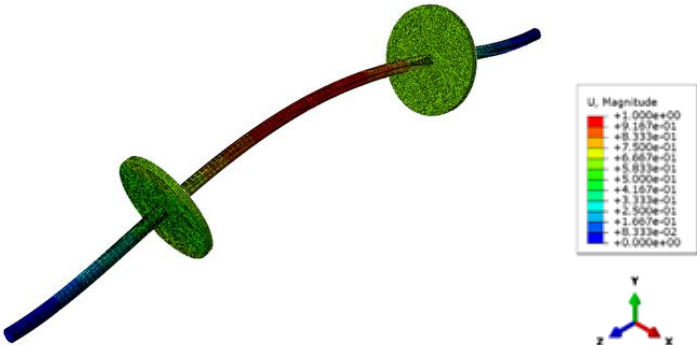
Table 4. Results of Modal comparison of different crack locations

	Mode 1	Mode 2	Mode 3	Mode 4	Mode 5
Crack center of shaft- depth of 362mm on shaft	24.096 Hz	24.129 Hz	49.079 Hz	49.154 Hz	62.202 Hz
Crack right of disc 2- depth of 634 mm on shaft	24.096 Hz	24.129 Hz	49.077 Hz	49.154 Hz	62.277 Hz
Crack left of disc 1 - depth of 90 mm on shaft	24.097 Hz	24.129 Hz	49.077 Hz	49.155 Hz	62.287 Hz

The frequency (f) is related to (K - stiffness factor) and (m - mass of the object). The mass remains constant whether the shaft has cracks or no cracks so the variable which effects the frequency is K . If a crack is present then there is a loss of

stiffness as opposed to a shaft not having a crack. By simply analysing the formula it is possible to postulate that a decrease in K will thus cause a decrease in the frequency. The preliminary results seem to concur with this, a shaft with a bigger crack or multiple cracks, reduces the stiffness to a greater extent, which consequently causes a decrease in the frequency. Conversely, if the shaft has no cracks, the stiffness is higher and the frequency remains higher than shafts with a crack.

Table 2. Mode signatures for shafts

Shaft type	Frequency (Hz)	
Shaft with no crack (Mode 1)	24.139 Hz	
Shaft with crack at $\mu = 0.5$ (Mode 1)	24.096 Hz	
Shaft with crack at $\mu = 1$ (Mode 1)	23.595 Hz	
Shaft with crack at $\mu = 1.5$ (Mode 1)	23.321 Hz	

4. Conclusion

The preliminary findings show that an analytical approach for modal analysis was accomplished by using Abaqus. A cracked shaft was successfully designed followed by the modal analysis conducted by analysing 5 modes and investigating the natural frequencies across the modes with varying crack parameters. Modal analysis was successful in

identifying natural frequencies at different crack depths, locations and by adding multiple cracks. The data obtained identifies the relationship between the shaft's natural frequency to the crack's depth ratio, crack location and number of cracks, and can serve to assist further research in this field to eventually find a method for early crack detection during rotary operation.

Table 5. Results of Modal comparison of the number of cracks

	Mode 1	Mode 2	Mode 3	Mode 4	Mode 5
No crack	24.139 Hz	24.181 Hz	49.077Hz	49.154Hz	62.278 Hz
One Crack with $\mu = 1$	23.595Hz	23.903 Hz	48.189Hz	48.530 Hz	61.939 Hz
Two Cracks with $\mu = 1$. Cracks at 90mm and 362mm	23.323 Hz	23.791 Hz	47.733 Hz	48.245 Hz	61.942

5. Acknowledgements

The authors gratefully acknowledge the financial support from the School of Computing, Engineering, and Mathematics, Western Sydney University, Australia.

6. References

- Jain, J.R., Kundra, T.K. (2003). Model based online diagnosis of unbalance and transverse fatigue crack in rotor systems. *Journal of Mechanics Research communications*, 31(5), 557-578.
- Mobarak, H., Wu, H., Spagnol, J. and Xiao, K. (2017). New crack breathing mechanism under the influence of unbalance force. *Archive of Applied Mechanics*, 88(3), 341-372.
- Sekhar, A. (2004). Crack identification in a rotor system: a model-based approach. *Journal of Sound and Vibration*, 270(4-5), pp.887-902.

The influence of irrigation area and roof size on the economics of rainwater harvesting use in urban agriculture: A case study in Sydney, Australia

Caleb Christian Amos¹ and Fazlul Karim²

¹PhD Candidate, Western Sydney University, NSW, Australia; ¹Postgraduate affiliate, CSIRO, ACT, Australia

²Senior Research Scientist, CSIRO, ACT, Australia

*Corresponding author's email: C.Amos@westernsydney.edu.au

Peer review history

Manuscript submitted: 10 June 2019

Review process completed: 18 July 2019

Manuscript finally accepted: 18 July 2019

Handling Editor: Professor Chin Leo

Abstract: Urban agriculture and Rainwater Harvesting (RWH) have grown in popularity in recent years. The economic viability of RWH systems has been reported with various outcomes. The water demand profile is complex and of all domestic demands, outdoor irrigation use is the most variable and potentially the largest domestic use of potable water. Water for gardening, toilet and laundry does not need the high level of treatment that drinking and cooking water requires. The amount of water a RWH system can supply for these uses is influenced by the rainfall pattern, tank size and roof area. A versatile economic evaluation tool named ERain has been developed to analyse the economics of various RWH system

arrangements. ERain combines performance analysis using daily rainfall data with life cycle cost analysis. Here ERain has been used to assess the effects of varying roof size or irrigation area on the economic viability of RWH systems for tank sizes ranging from 1-7kL. Results show that excluding outdoor use, the benefit cost ratio (BCR) increases with roof size along with reliability, while efficiency decreases. Interestingly, the larger roof area has the most significant effect in terms of reliability on the smaller tanks. Including outdoor use reduced reliability overall but increases both the efficiency and BCR indicating that it is better financially to use the RWH system for outdoor use when reliability is not a concern. The larger NPVs and BCRs occur with the larger irrigation areas as this increases water use and hence monetary water savings. Within the 1-7kL tank range, the 7kL tank is the most favourable when outdoor irrigation use is connected.

Keywords: Rainwater harvesting, Economic analysis, Rainwater tank, Tank size, Roof area.

1. Introduction

Rainwater harvesting (RWH) from roof tops as a result of the millennium drought has become a significant feature in Australia (van Dijk et al., 2013). About 34% of households in Australia have adopted RWH systems which is the highest adoption rate in the world (Beatty and McLindin, 2012). With this has come a significant amount of research and installation guidelines from various sectors including universities, government and other research organisations such as Commonwealth scientific and industrial research organisation (CSIRO). For example, in 2008 the Master Plumbers and Mechanical Services Association of Australia (2008) developed and published a Rainwater Tank Design and Installation Handbook (HB 230-2008) for regulatory authorities, installation professionals and homeowners. In 2010 the Environmental Health Committee produced a timely revision of the 2004 Guidance on use of rainwater tanks (EnHealth, 2010) in response to the ongoing interest in using RWH systems. Various rebate schemes were introduced which have now been reviewed by several authors and government departments (Gato-Trinidad and Gan, 2014; Hall, 2013). RWH reports were prepared for the prime minister and cabinet. In many cases, RWH systems have been mandated for new constructions. In NSW, for example, they were included in Building Sustainability Index (BASIX) requirements. Now we are starting to see reviews of RWH system used globally (Amos et al., 2016; Campisano et al., 2017; Sharma et al., 2016). Since the drought has eased in Australia, and in Sydney particularly, there appears to be a reduced interest in RWH systems, and the desalination plant has also lost its spotlight. BASIX compliance records from 2005 to 2015 (BASIX, 2016) reveal this current trend. However, internationally there is heightened interest in RWH systems and Australia has been criticized for its weak water security (Beatty et al., 2009; Burton et al., 2015), so it is likely that RWH systems will continue to grow across Australia.

Urban agriculture is also on the increase in Australia due to the increasing cost of food and other social trends (Russ Grayson, 2017). Local councils are encouraging the practice and providing guidelines on how to do practice forms urban agriculture in various ways (Sydney, 2017) and gardens along roadsides are becoming popular in the inner city (Marshall, 2017). Urban agriculture may be defined as “agriculture within an urban or peri-urban setting” (Hamilton et al., 2014). As well as vegetables and fruit trees, it can also encompass bees and animal production, such as chickens, and fish in Aquaponics (Orsini et al., 2013). Various countries have already been quite successful in urban agriculture. Cuba has become a world leader in urban agriculture and has developed a system called “organoponics” (Eigenbrod and Gruda, 2015; Orsini et al., 2013), Mexico City produces 20% of its own food (Dieleman, 2016). In many developing countries, home gardens supply family their food, and important nutrition (Gallaher et al., 2013), and to some extent - income (Jayasuriya et al., 2014). There are growing demands to increase urban agriculture (Corbould, 2013; Eigenbrod and Gruda, 2015; Orsini et al., 2013; Suparwoko and Taufani, 2017) to avoid the “food deserts” present in some American cities (Beaulac et al., 2009; Horst et al., 2017; Walker et al., 2010) where fresh vegetables simply aren’t available locally (Eigenbrod and Gruda, 2015; Smith et al., 2013). Measuring up against Goal 11 of the United Nations’ sustainable development goals (SDGs), cleaner and sustainable cities, most - if not all countries - will come short. Australia, although a developed country, does not meet Goal 3 (health and well-being) due particularly to increased diabetes. Urban agriculture as a healthy pursuit can help alleviate this by increased activity, healthier foods and building awareness. Concurrently, in recognition of water shortages, there is a trend in Australia towards using native plants that naturally have a lower water use than many imported ornamentals (Josh Byrne & Associates, 2013). Urbanisation, population increase and changing climates are increasing competition over water resources and arable land worldwide (Corbould, 2013). Urban Agriculture can alleviate the food demand to some degree, but as with the concept of greening cities, this will also increase the water demand. Roof RWH in urban areas may then be able to meet some of this increased water demand. An important question is to what extent roof RWH can provide this water and what are the economic implications of using it to do so.

The economic viability of RWH systems has been reported with various different outcomes, predominantly at a cost, however some report a positive financial evaluation. Assessing the viability of RWH systems faces a number of challenges. Firstly, proper evaluation of the lifecycle costs particularly of the maintenance and replacements costs which are often neglected. Secondly modelling the systems performance is difficult and often based on various assumptions about water consumption, and a standardised site (roof area and tank size particularly). Irrigation and outdoor use is potentially the most variable household water use, with some owners using virtually no water outdoors, to others using large amounts, especially when there are no restrictions in place. The quantity of water available for harvest is influenced especially by roof area supplying the RWH system (its catchment). Roof area can vary considerably with the size of the house, or because parts of the roof are unsuitable for harvesting (e.g. due to overhanging trees or the practicality and/or cost of the guttering arrangement). The rainfall pattern, tank size and water demand profile will also affect how much water can be harvested. Irrigation use particularly will be influenced by the rainfall and the season.

Most studies use a standard roof size and quantity of water used for irrigation. The Australian Bureau of Statistics (2013) reported that in NSW approximately 48% of people use mains water to irrigate. Here we have developed a versatile economic evaluation tool named ERain to investigate the effect of varying roof size and irrigation water use on RWH system performance and the economic viability. ERain combines performance analysis using daily rainfall data and various water demand profile data with a detailed life cycle cost analysis based on AS/NZ Standard AS4536 “Life Cycle Costing – an Application Guide” (Standards Australia, 2014). Model outputs include both performance and economic indicators which can be compared. Economic measures reported include the benefit cost ratio (BCR) and net present value (NPV) and performance indicators include reliability (% of days the demand is met) and efficiency (% of available water used – i.e. not lost to overflow). ERain is designed to be flexible and to be able to account for all the aspects of costs involved, anticipating that innovation will be an ongoing feature of RWH system design and urban agricultural methods for some time to come (Kongo and Jewitt, 2006). System configurations will be greatly affected by Innovation and this will have a direct impact on economics (Gabrielsson et al., 2018; Getnet and MacAlister, 2012; Melville-Shreeve et al., 2014). One of today’s challenges is to make RWH economically viable. It is hoped that developments in Australia can contribute towards meeting SDG goal 2 zero hunger, and goal 6, clean water and sanitation, in developing countries. The technological achievement of putting man on the moon 50 years ago in 1969, should be matched with providing the basic needs of man.

In this study ERain has been used to assess the economic implications of varying the roof size, and the irrigation area of RWH systems with tank sizes ranging from 1-7kL. Parramatta, the geographical centre of Sydney, Australia, has been used as the study site.

2. MATERIALS AND METHOD

2.1. Scenarios

This study considers a single occupancy house in Parramatta with 4 occupants. Site dimensions are similar to those used in previous studies (Hajani et al., 2013; Rahman et al., 2012). In order to reflect the tendency towards smaller lot sizes, the overall site area is reduced from 450 m² to 400 m² and the nominal landscaped area from 150 to 120 m². However, a variety of landscape areas, namely 40, 80, 120, 160 and 200m², are modelled to account for variation in water use. In Sydney currently, while plot sizes are decreasing, house sizes are increasing and so an average roof area of 200 m² was chosen and a variety of roof areas, namely 100, 150, 200, 250 and 300m² were modelled to account for variation in the roof sizes and connection.

The RWH system is commonly used for the toilet and Laundry, with and without irrigation, and outdoor use. Tank sizes ranging from 1-7 kL were considered for toilet and laundry type connections and tanks sizes up to 15kL when irrigation use is included. This size range reflects the tank sizes commonly installed to fulfil or exceed the BASIX legislation requirements. The majority of tanks are in the 0-2kL, and 2-3kL range, with a few being larger than 10kL in the Parramatta area. For cost analysis, “Slimline” tanks have been assumed as these are the most common in urban areas where space is limited. Losses of 1mm per square meter of roof area, a first flush volume equivalent to the first 0.5mm of rain and a mains top up level of 5% of the tanks volume are adopted.

2.2. Rainfall Data

The Rainfall data from 1965 – 2015 for Parramatta (Station No. 066124), was used in this study (Table 1).

Table 1 Summary of daily rainfall data

Country	Location	Type	Rainfall station	Period of rainfall record	Average annual rainfall (mm)	5 th Percentile (mm)
Australia	Parramatta	Urban	066124	1965 - 2015	964	612

2.3. Water Demand Profile

The profile chosen in this research was designed around looking at each specific water use and calculating estimates for each starting with quantities obtained from the Reece Sustainable Bathroom Guide and the distribution of water use between uses reported by Kuczera et al. (2003). The overall usages that these specific values yielded were then compared with the averages given by Sydney water, 297 L/p/d (litres per person per day). This resulted in an average consumption of 172 L/p/d excluding outdoor use (which varies and is ultimately shared between the occupants) and a maximum outdoor use of 1233 L/household. Toilet use is based on two full flushes and one half flush of a 3 star toilet per person/day, resulting in 23.5L/p/d. Laundry use is based on 3 loads for every 2 people each week in a 3 star washing machine, resulting in 150 L/p/week or approximately 10.7L/p/d. Outdoor uses include washing one car per household every 2 weeks, at 180L/wash, and a low estimate for washing hard surfaces of 8min per week (at 18L/min), resulting in 20L/day, assuming that some people may also water the garden or wash the car at the same time. Irrigation use is calculated at 10mm depth of irrigation per household per day multiplied by the irrigation area assumed for the property (generally 120m²) giving 120m²*10mm = 1200L/household/day, which is comparable with assumptions used in other studies (Hajani et al., 2013; Rahman et al., 2012). A sprinkler may use 1000L/hr so it is not unreasonable to think that a property may have 2 sprinklers running for 30-40 min per day which would result in approximately the 1200L of water as assumed in this study. Irrigation is assumed to stop when there are consecutive days of rain. Variation in irrigation use between users is modelled by changing the area of irrigation considering 40, 80, 120, 160 and 200m².

2.4. Economic Inputs

Interest and inflation (other than water) were considered as 4.6% and 2.5% respectively from the WACC biannual update report for the water industry produced by Independent Pricing and Regulatory Tribunal (IPART). The primary benefit of the RWH system is the monetary value of the water saved. This is calculated using the annual average amount of water saved, found by the daily analysis and summary modules, multiplied by the current water price of \$2.28/kL (including a service charge of \$114.04). Prices were obtained from Sydney water's prices for customers 2015 and compared with a recent water bill. The water inflation rate was taken from prices for customers between 2016-2020. Costs have been categorised according to AS/NZ 4536:1999 Life cycle costing - An application guide (Australian Standard, 2014). Predominantly the Acquisition and Use and Maintenance Support categories were considered while renewal and adaption and disposal were not.

Table 1 Acquisition costs

Cost Code	Details	units	per unit	Total
	<u>Catchment and Drainage System</u>			
1104	Roof Treatment to adequate standard		-	
1104	Downpipes to tank	1	\$43	\$43
1104	Guttering		-	
	<u>Tank</u>			
	Tank volume (kl)=(m³)	3		
	Tank slab area	2.2		
3101	Cost of land /m ²	2.2		
3102	Levelling ground (m ²)	2.2	\$13.87	\$32.89
3103	Concrete base for tank (exc.labour) (m ²)	2.2	\$104.22	\$247.16
3104	Tank Cost	1	\$910	\$0.00
	<u>Water Treatment</u>			
1104	Gutter and downpipe screening	1	\$15.00	\$15.00
1104	Tank and inlet screening, passive treatment, outlet height			
1104	First Flush device	1	\$17.00	\$17.00

2.4.1. Life Cycle Phase A – Acquisition

The variety in types of RWH installation leads to a number of complex issues when it comes to costing. For example, the level of advice that may be used to design the system is a costing issue that is often neglected. In this analysis the focus has been the effect of tank size on the economic viability of the system. For this reason, an average price was adopted for most aspects of the system while special attention was given to costs that vary with different size tanks. Prices were obtained from various suppliers and compared with Cordell and Rawlinsons (Rawlinsons, 2015; Solutions, 2015) where they had comparative pricing. The hourly rates for the various trades were taken as the average values given in "Payscale" - an online guide for trade rates. An example of some of the capital costs are shown in Table 1, labour costs are included elsewhere. The red highlighted section shows the values that vary with tank size.

2.4.2. Life Cycle Phase B – Use and Maintenance Support

Dividing the RWH system into separate sections helps identify the various maintenance issues. These costs occur on a scheduled basis rather than at acquisition. Repair and replacements are considered to carry more cost to the owner than general maintenance which the owner is assumed to do himself. The pump is assumed to run for 2 hrs/day using 0.9KW/h at \$0.2122 per kWh.

2.5 Method: “ERain” Analysis Tool

ERain combines performance analysis with economic analysis using daily rainfall data, economic data and scenario inputs. It was originally developed as a spread sheet model and has been upgraded using FORTRAN and RScript programming in conjunction, with information from extensive literature reviews on both RWH (Amos et al., 2016) and Urban Agriculture (Amos et al., 2018). The basic model parameters are shown in Figure 1. ERain uses the yield after spillage model (YAS) which Fewkes et al. (2000) deem to be more conservative than a yield before spillage model.

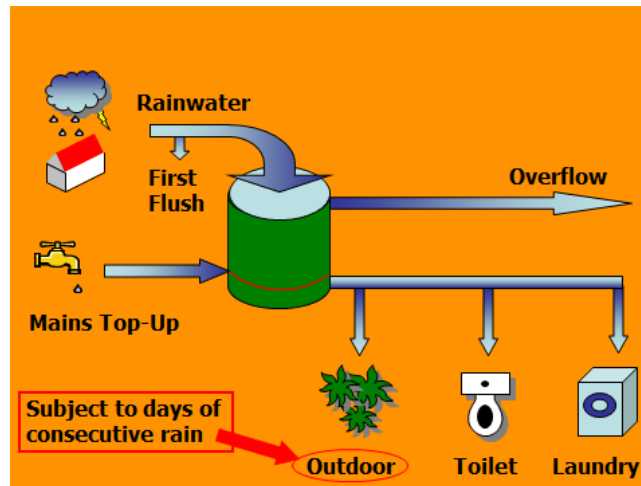


Figure 1. ERain basic parameters model

Following the guidelines in AS/NZ 4536:1999 Life cycle costing - An application guide (Australian Standard, 2014) ERain includes all aspects of a product’s life cycle and presents the benefit cost ratio (BCR), and net present value (NPV) standardised to Australian Dollars (AU\$), using the concept of Present Value (PV). The PV is calculated as shown in equation 1:

$$\text{Discount rate} = \frac{1}{(1+i)^t} \quad \text{PV} = \frac{\text{CF}}{(1+i)^t} \quad (1)$$

Where, CF is the cash flow, i the interest rate, and t the year in which it occurred. The NPV is defined as the sum of PVs over the project and is calculated as shown in equation 2:

$$\text{NPV}(i, N) = \sum_{t=0}^N \frac{\text{CF}_t}{(1+i)^t} \quad (2)$$

Here CF is the difference between cash inflow and outflow reduced by the discount rate appropriate to the time (t) of transaction. N is life cycle length (years). Equation 3 shows how the benefit-cost ratio (BCR) is the sum of discounted costs (C) divided by the sum of discounted benefits (B) as they occur at time (t) over the project lifecycle length N :

$$\text{BCR} = \frac{\sum_{t=0}^N \frac{C_t}{(1+i)^t}}{\sum_{t=0}^N \frac{B_t}{(1+i)^t}} \quad (3)$$

In summary the NPV is the sum of benefits minus the sum of costs over the project’s lifecycle. BCR is a ratio of the benefits and costs. The BCR being a ratio is sometimes considered by analysts to be inaccurate (Cbabuilder, 2016). A basic understanding of basic economics is required to understand the implications of BCR and NPV.

The two main measures of system performance reported by ERain are reliability and efficiency. Reliability is defined as the percentage of days that the demand was met. Efficiency is defined as the percentage of available water used. Among other things, the Efficiency indicates if a greater tank size could help yield more water from the given roof area.

3. RESULTS AND DISCUSSION

3.1. BCR of roof size for a toilet and laundry only installation

Results from varying roof areas for the various tank sizes are shown in Figure 2. For the 3kL tank, the reliability and BCR increase with roof size while the efficiency decreases. Even with a small roof area, only 30% of the available water is

being used with this type of installation. With larger roof areas the efficiency decreases to only 10%, however the system is quite reliable at over 70%. The increase in roof area has the largest effect on efficiency when the tank is small. For example a 1.1kL tank's reliability increases by 10.6% from a minimum of 61.4% to max of 72%, while for a 7kL tank the equivalent increase is only 4.5% from 95.1% to 99.6%. This influences the NPV and BCR results. For example, the NPV of a smaller tank (1.1kL) with a large roof (300m²) has a less negative NPV than a larger tank (3kL) with a smaller roof (100 m²).

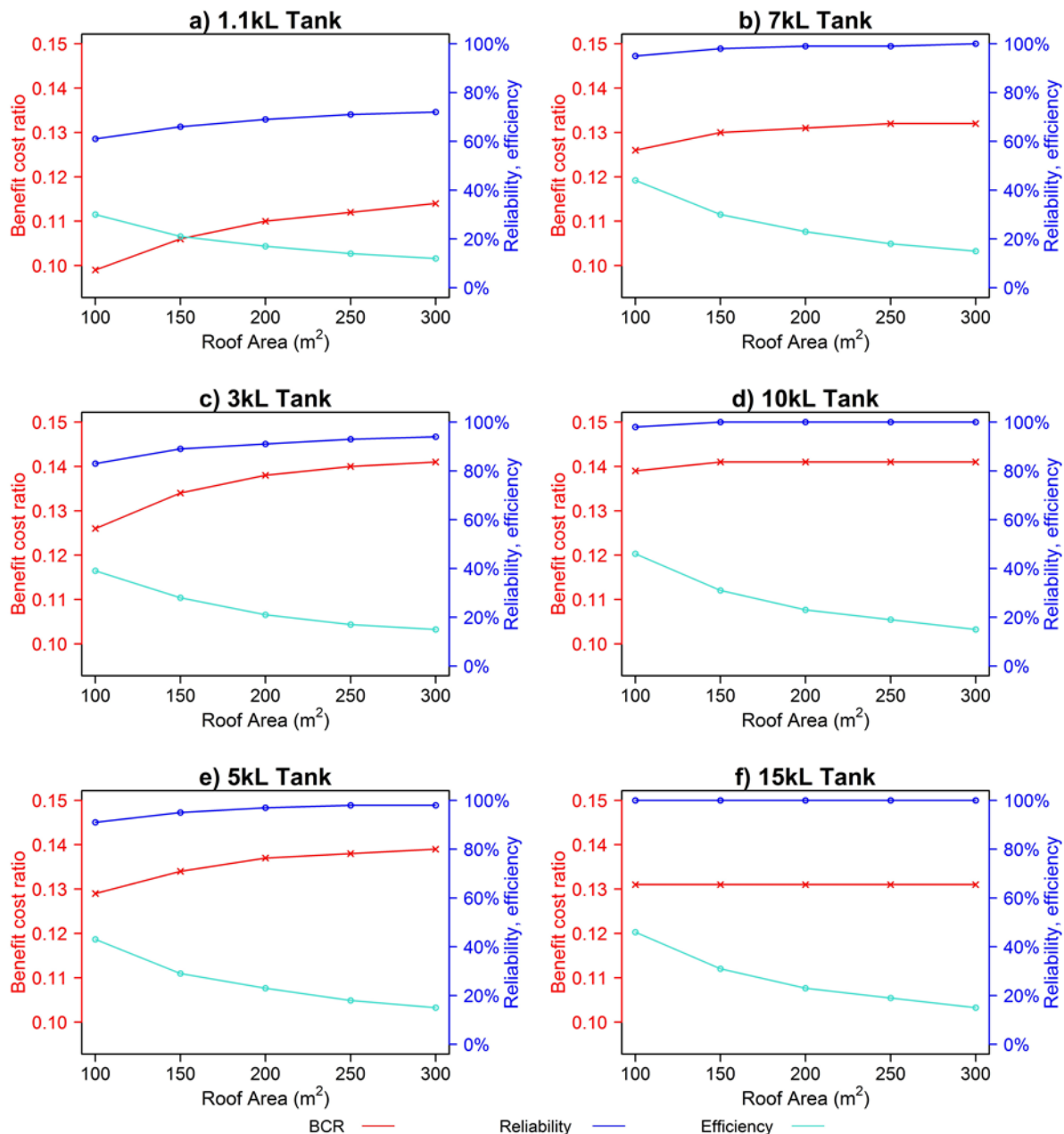


Figure 2 Roof area vs. BCR, reliability and efficiency for toilet and laundry use

3.2. BCR of roof size for a toilet, laundry and outdoor installation

As expected, system reliability is reduced by connecting irrigation while the efficiency increases and so does the BCR, as seen in Figure 3. Therefore, financially, it is an advantage to use the harvested rainwater for irrigation, particularly when mains water is connected as a backup, as it usually is in the urban environment, and where reliability is not an issue. The larger roof catchment means that the smaller rainfall events harvest a more substantial quantity of water and help refill the tank, increasing reliability. The efficiency decreases mainly due to increased overflows, and particularly with the larger

rainfall events. If we again compare the results for the 1.1kL tank and 300m² roof with a 3kL tank and 100m² installation, we find that NPV is now more negative where for the toilet and laundry only installation above the opposite was true. For a toilet and laundry only installation, reliability is quite high even with a smaller tank, and so a larger tank does not increase reliability much. Once outdoor use is connected however, reliability reduces, leaving room for greater increases in reliability with a larger tank size. The highest NPV is still negative (\$16657) and the BCR less than 1. Interestingly the highest (least negative) NPV occurs with a 10kL tank, while the highest BCR is 0.355 with a 15kL tank. It appears that compared to the NPV, the BCR will generally imply that a larger tank size is more economically viable.

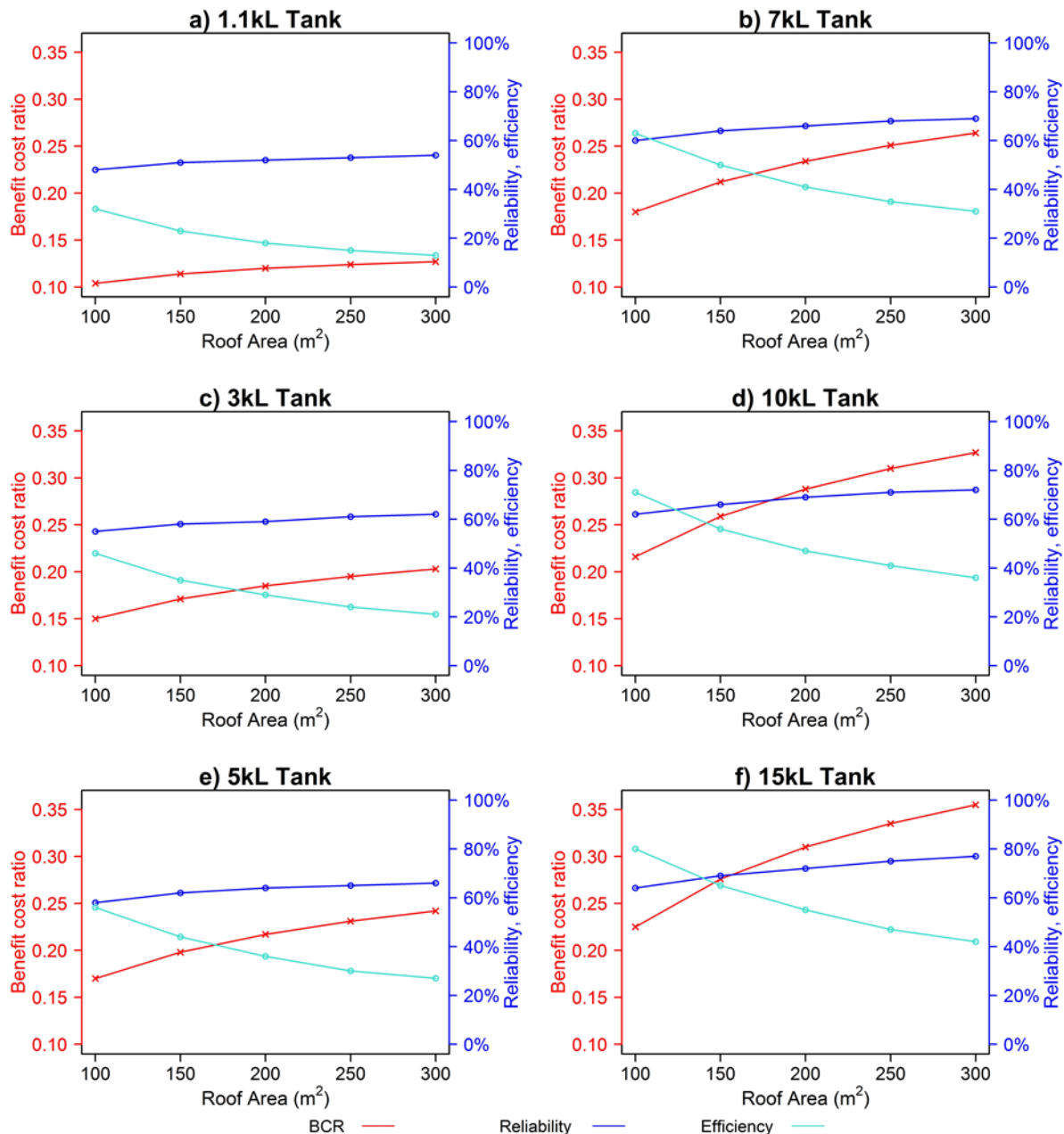


Figure 3 Roof area vs. BCR, reliability and efficiency for toilet, laundry and outdoor use

3.3. Various irrigation areas for a toilet and laundry and outdoor installation

Results for varying irrigation area with a set a roof area of 200m² are shown in Figure 4. For the smallest tank, there is a slight increase in the BCR when increasing the irrigation area from 40 to 80 m², but for larger irrigation areas there is no significant increase. The efficiency and reliability are virtually unchanged implying that the RWH system has already reached its capacity to supply water with a small area being irrigated. The larger 3kL tank has a higher BCR for any irrigation area, and also shows a greater increase in BCR with irrigation area. Efficiency increases only slightly to a maximum of 30%, again implying that the system is already at its capacity to supply water at the lower irrigation areas,

while reliability declines to 60% with the larger irrigation areas. The low efficiency means that lots of water is being lost to overflow. The 5kL tank has

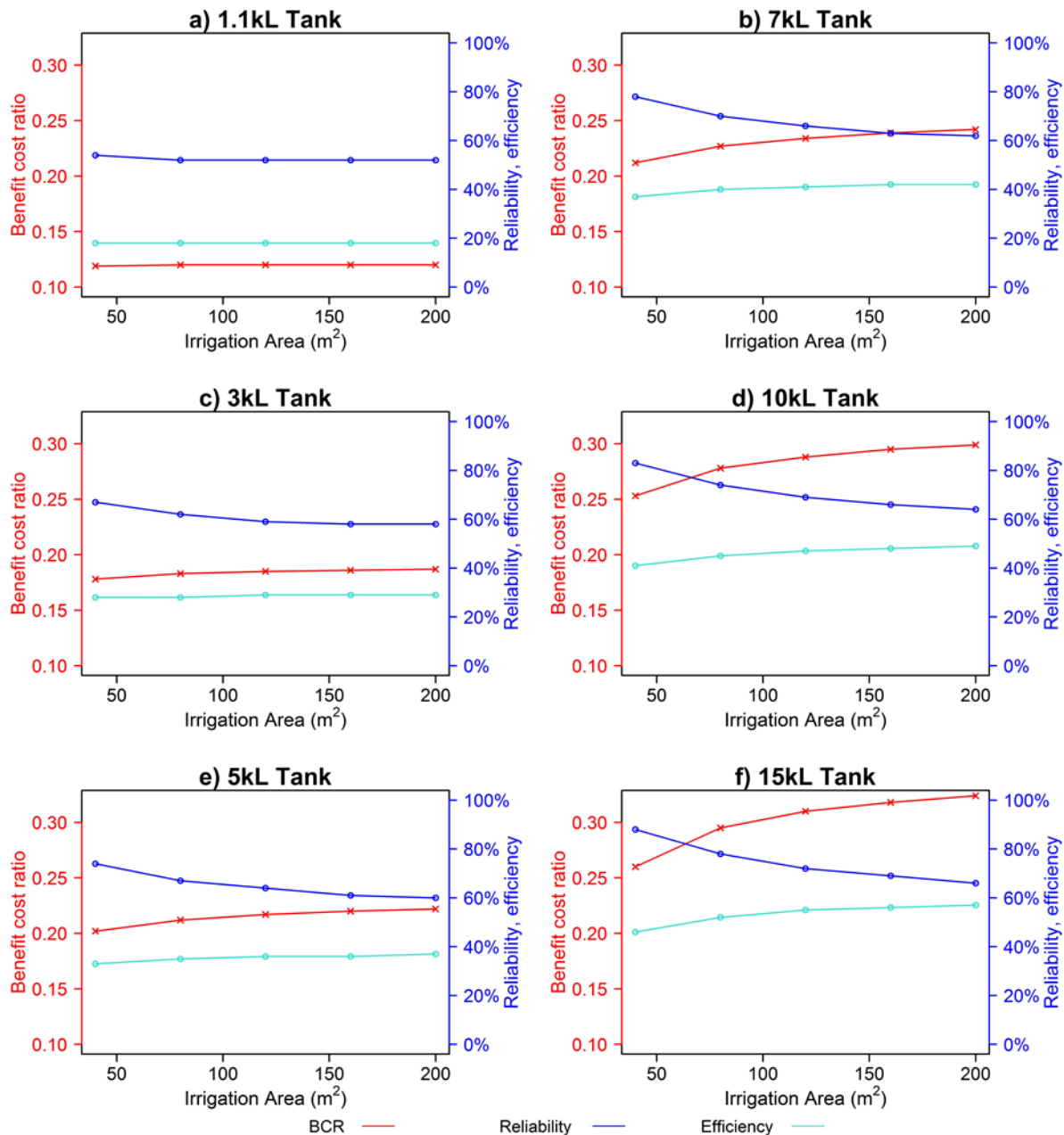


Figure 4 Irrigation area vs. BCR, reliability and efficiency for toilet, laundry and outdoor use

higher BCR than both the 1.1 and 3kL tanks for all areas of irrigation and corresponding higher efficiencies and reliabilities. The relatively small increase in efficiency, and low reliability, implies that the 5kL tank system is again close to capacity to supply water. Exploring larger tank sizes' results showed that larger NPVs and BCRs occur with the larger irrigation areas as this increases water use and hence monetary water savings. The highest BCR was found with a 15kL tank; while the highest (least negative) NPV occurs with a 10kL tank. These results could be affected if future rainfall patterns do not reflect the historical data that is available for, only, the last 100 years or less (Haque et al., 2016).

4. CONCLUSION

Increase in roof area for a toilet and laundry only installation increases both the reliability and BCR while efficiency decreases. For a 3kL tank only 30% of the available water is used with the smallest roof area (100 m²). This decreases to

10% with the largest roof area (300 m²) while reliability increases to over 70%. Interestingly it is with smaller tanks that the increased roof area has the biggest effect in increasing the reliability. This implies that if there is a larger catchment available the tank size can be reduced.

Increase in roof area has a greater effect for an installation that includes outdoor usage. The decreased reliability means that there is greater potential for increasing reliability with a larger tank or roof area. This changes the pattern of BCR and NPV. Without outdoor use, attached reliability is already high with a small tank and so a larger tank offers little increases in reliability. The lower efficiency at larger roof areas compounds the increase in reliability with increasing tank sizes. Without outdoor uses attached, the NPV of a 1.1kL tank with a roof area of 300m² is more favourable than the 3kL tank with a roof area of only 100m². When outdoor uses are attached, this is no longer the case and the 3kL becomes more favourable than the 1.1 kL tank.

Including outdoor use considerably reduces the reliability overall while the efficiency and BCR increase. This indicates that it is financially advantageous to use the RWH system for outdoor use where reliability is not a concern. Increasing the irrigation use increases the NPVs and BCRs as this increases water use and hence monetary water savings. The highest BCR occurs with a 15kL tank; while the highest (least negative) NPV occurs with a 10kL tank. The BCR of smaller tanks do not increase much with larger irrigation areas because the RWH system has already reached its capacity to supply water even with a small area of irrigation. Crop failure due to decreased reliability however may still be an issue if the water supply is not supplemented with mains water.

This study highlighted a number of areas for further research. This study only presented a simplistic method of modelling irrigation use and a more in-depth study focusing on irrigation use would be useful. Some say that, with respect for gardening, a rainwater tank is empty when it is needed most. To address this, the reliability and efficiency of RWH systems in relation to irrigation use could be explored in more depth. Particular attention should be paid to evapotranspiration, water requirements, and yield. Relationships between monthly and seasonal variation in rainfall, rainfall categories, total water available in the various regions of Australia and their influence on reliability and efficiency of RWH systems should also be explored to deepen the understanding of roof RWH's potential use in urban agriculture and the contribution it can make to greener cities and the SDGs.

Acknowledgements

We acknowledge the Australian Bureau of Meteorology for providing rainfall data, Sydney Water, and other organisations for sharing their water use and price data.

REFERENCES

- Amos, C.C., Rahman, A., Gathenya, J.M., 2016. Economic Analysis and Feasibility of Rainwater Harvesting Systems in Urban and Peri-Urban Environments: A Review of the Global Situation with a Special Focus on Australia and Kenya. *Water* 8(4), 149.
- Amos, C.C., Rahman, A., Karim, F., Gathenya, J.M., 2018. A scoping review of roof harvested rainwater usage in urban agriculture: Australia and Kenya in focus. *Journal of Cleaner Production*(202 (2018)), 174-190.
- Australian Bureau of Statistics, 2013. Environmental Issues: Water use and Conservation.
- Australian Standard, 2014. AS/NZS 4536:1999 Life cycle costing — An application guide. Australian/New Zealand Standard, Australia.
- BASIX, 2016. BASIX_Singles_Sydney_Parramatta_AllPostcodes_Water_RainwaterTanks_20160331. <http://datareporting.planning.nsw.gov.au/reporting/basix/pdf.action>. (Accessed 31/3/16).
- Beatty, R., McLindin, M., 2012. Rainwater Harvesting and Urban Design in Australia. *Proceedings of the Water Environment Federation* 2012(9), 6435-6447.

- Beatty, R.J., Coombes, P.J., Kozorovski, P., 2009. Integrated Water Resources Planning Efforts in Australia Need to Grow Up.
- Beaulac, J., Kristjansson, E., Cummins, S., 2009. A systematic review of food deserts, 1966-2007. *Preventing Chronic Disease* 6(3).
- Burton, A., Bambrick, H., Friel, S., 2015. Urban Climate.
- Campisano, A., Butler, D., Ward, S., Burns, M.J., Friedler, E., DeBusk, K., Fisher-Jeffes, L.N., Ghisi, E., Rahman, A., Furumai, H., Han, M., 2017. Urban rainwater harvesting systems: Research, implementation and future perspectives. *Water Research* 115, 195-209.
- Cbabuilder, 2016. Comparing NPV and BCR. <http://www.cbabuilder.co.uk/Results3.html>. (Accessed 1/5/16.
- Corbould, C., 2013. Feeding the Cities: Is Urban Agriculture the Future of Food Security? Future Directions International Pty Ltd.
- Dieleman, H., 2016. Urban agriculture in Mexico City; balancing between ecological, economic, social and symbolic value. *Journal of Cleaner Production*.
- Eigenbrod, C., Gruda, N., 2015. Urban vegetable for food security in cities. A review. *Agron. Sustainable Dev.* 35(2), 483-498.
- EnHealth, 2010. Guidance on use of rainwater tanks. Department of Health and Ageing, Australia.
- Gabrielsson, J., Politis, D., Persson, K.M., Kronholm, J., 2018. Promoting water-related innovation through networked acceleration: Insights from the Water Innovation Accelerator. *Journal of Cleaner Production*.
- Gallaher, C.M., Kerr, J.M., Njenga, M., Karanja, N.K., WinklerPrins, A.M.G.A., 2013. Urban agriculture, social capital, and food security in the Kibera slums of Nairobi, Kenya. *Agriculture and Human Values* 30(3), 389-404.
- Gato-Trinidad, S., Gan, K., 2014. Rainwater tank rebate scheme in Greater Melbourne, Australia. *Journal of Water Supply: Research and Technology—AQUA* 63(8), 601-610.
- Getnet, K., MacAlister, C., 2012. Integrated innovations and recommendation domains: Paradigm for developing, scaling-out, and targeting rainwater management innovations. *Ecological Economics* 76, 34-41.
- Hajani, E., Rahman, A., Al-Amin, M., Rahman, A., 2013. Reliability Analysis for Rainwater Harvesting System in Peri-Urban Regions of Greater Sydney, Australia, MODSIM2013, 20th International Congress on Modelling and Simulation. Modelling and Simulation Society of Australia and New Zealand Adelaide.
- Hall, M.R., 2013. Review of rainwater tank cost-effectiveness in South East Queensland. Urban water security research alliance technical report(105).
- Hamilton, A.J., Burry, K., Mok, H.-F., Barker, S.F., Grove, J.R., Williamson, V.G., 2014. Give peas a chance? Urban agriculture in developing countries. A review. *Agron. Sustainable Dev.* 34(1), 45-73.
- Haque, M.M., Rahman, A., Samali, B., 2016. Evaluation of climate change impacts on rainwater harvesting. *Journal of Cleaner Production* 137, 60-69.
- Horst, M., McClintock, N., Hoey, L., 2017. The Intersection of Planning, Urban Agriculture, and Food Justice: A Review of the Literature. *J. Am. Plann. Assoc.* 83(3), 277-295.
- Jayasuriya, N., Navaratne, C.M., Nandasiri Weerasignhe, K.D., Nawarathna, B., Adams, R., 2014. Roof runoff capture for home garden crop cultivation in Sri Lanka. *Journal of Irrigation and Drainage Engineering* 140(7).
- Josh Byrne & Associates, 2013. A Guide to Water Efficient Landscape & Irrigation, in: Corporation, W. (Ed.). Water Corporation, WA, Australia.
- Kongo, V.M., Jewitt, G.P.W., 2006. Preliminary investigation of catchment hydrology in response to agricultural water use innovations: A case study of the Potshini catchment - South Africa. *Physics and Chemistry of the Earth* 31(15-16), 976-987.

- Kuczera, G., Coombes, P.J., Dunstan, H., Spinks, Holz, L., Kalma, J.D., 2003. Integrated management of the urban water cycle from the allotment to the regional scale: opportunities and benefits. University of Newcastle, Callaghan, NSW, 2308, Australia, Newcastle.
- Marshall, T., 2017. On the Verge, Organic Gardener. ABC Books, Australia.
- Master Plumbers and Mechanical Services Association of Australia, 2008. Rainwater Tank Design and Installation Handbook
- Melville-Shreeve, P., Ward, S., Butler, D., 2014. A preliminary sustainability assessment of innovative rainwater harvesting for residential properties in the UK.
- Orsini, F., Kahane, R., Nono-Womdim, R., Gianquinto, G., 2013. Urban agriculture in the developing world: a review. *Agron. Sustainable Dev.* 33(4), 695-720.
- Rahman, A., Keane, J., Imteaz, M.A., 2012. Rainwater harvesting in Greater Sydney: Water savings, reliability and economic benefits. *Resources, Conservation and Recycling* 61, 16-21.
- Rawlinsons, 2015. Construction Cost Guide for housing, small commercial and industrial buildings, 23 ed.
- Russ Grayson, A.R.-R., Kirsten Bradley, 2017. Urban Farming, Organic Gardener. ABC Books, Australia.
- Sharma, A.K., Cook, S., Gardner, T., Tjandraatmadja, G., 2016. Rainwater tanks in modern cities: A review of current practices and research. *Journal of Water and Climate Change* 7(3), 445-466.
- Smith, D., Miles-Richardson, S., Dill, L.C., Archie-Booker, E., 2013. Interventions to improve access to fresh food in vulnerable communities: A review of the literature. *Int. J. Disabil. Hum. Dev.* 12(4), 409-417.
- Solutions, C.C., 2015. Cordell Housing Building Cost Guide.
- Standards Australia, 2014. AS 4536 - 1999 R2014 Life Cycle Costing - An Application Guide.
- Suparwoko, Taufani, B., 2017. Urban Farming Construction Model on the Vertical Building Envelope to Support the Green Buildings Development in Sleman, Indonesia, in: Tim, T.C., Muller, H.S., Ueda, T. (Eds.), 3rd International Conference on Sustainable Civil Engineering Structures and Construction Materials, SCESCM 2016. Elsevier Ltd, pp. 258-264.
- Sydney, C.o., 2017. Footpath Gardening Policy. cityofsydney.nsw.gov. 2017).
- van Dijk, A.I., Beck, H.E., Crosbie, R.S., de Jeu, R.A., Liu, Y.Y., Podger, G.M., Timbal, B., Viney, N.R., 2013. The Millennium Drought in southeast Australia (2001–2009): Natural and human causes and implications for water resources, ecosystems, economy, and society. *Water Resources Research* 49(2), 1040-1057.
- Walker, R.E., Keane, C.R., Burke, J.G., 2010. Disparities and access to healthy food in the United States: A review of food deserts literature. *Health Place* 16(5), 876-884.

Energy and exergy analyses of a flat plate solar collector using different nanofluids

Mohammad A. Alim ^{a,*}, M.A. Khairul ^b, M. Fazale ^c, R. Saidur ^d, Md Jaynul Abden ^e

^aSchool of Computing, Engineering & Mathematics, University of Western Sydney, Penrith, NSW 2751, Australia

^bDiscipline of Chemical Engineering, The University of Newcastle, Callaghan, NSW 2308, Australia

^cResearch Centre for Nano-Materials and Energy Technology (RCNMET), School of Science and Technology, Sunway University, No. 5, Jalan Universiti, Bandar Sunway, Petaling Jaya, 47500 Selangor Darul Ehsan, Malaysia

^dDepartment of Engineering, Lancaster University, LA1 4YW, UK

^eADP, Taylor's University Lakeside Campus, 47500 Selangor Malaysia

*Corresponding author's email: M.alim@westernsydney.edu.au

Peer review history

Manuscript submitted: 7 June 2019

Review process completed: 25 August 2019

Manuscript finally accepted: 26 August 2019

Handling Editor: Professor Chin Leo

Abstract: This work theoretically investigates the effect of nanofluids on the energy and exergy efficiencies of a flat plate solar collector. Four different types of nanofluids, Al₂O₃/water, SiO₂/water, TiO₂/water and CuO/water, have been taken into consideration to examine the

performance of the solar collector. The efficiencies are determined for a range of volume fractions of each nanoparticle and subsequently compared to each other. It is shown that the application of CuO/water nanofluid as a fluidic medium in a conventional solar collector can enhance its energy and exergy efficiencies by 38.46 and 15.52% respectively, when compared to water. The ultimate objective of the present study is to understand the feasibility of each kind of nanofluid prior to the application in solar to thermal energy conversion.

Keywords: Energy; Exergy; Nanofluid; Solar collector; Dead state; Building.

Nomenclature

A_p	= absorption area, m ²	P	= mechanical power, W	η_{Ex}	= exergy efficiency
C_p	= specific heat, J/kg.K	\dot{Q}	= thermal energy rate, W	η_o	= optical efficiency
e	= exergy loss	\dot{Q}_u	= energy gain rate, W	τ	= transmittance
				α	= absorptance
\dot{E}_g	= exergy gain rate per unit area, W/m ²	s	= entropy per unit mass, J/kg.K	ϕ	= nanoparticles volume fraction, %
\dot{E}_{sun}	= exergy flow from sun, W/m ²	S	= absorbed irradiation, W/m ²	ρ	= density, kg/m ³
F_R	= heat removal factor	T	= temperature, K	σ	= overall entropy production, J/kg.K
F'	= collector efficiency factor	T_c	= absorber plate temperature, K	Subscripts	
g	= gravitational acceleration, m/sec ²	U_l	= overall heat loss, W/m ² .K		
I_T	= incident solar energy per unit area, W/m ²	V	= volume flow rate, L/min	a	= ambient
k	= heat conductivity, W/m.K	z	= height from reference level, m	bf	= base fluid
\dot{m}	= mass flow rate, kg/s	η_{En}	= energy efficiency	$dest$	= destruction
				f, in	= inlet fluid
				f, out	= outlet fluid
				np	= nanoparticles
				nf	= nanofluid

1. Introduction

Implications of renewable energy sources such as sun, wind, water and geothermal, is one of the most common interests among the scientists and engineers across the world these days. The main advantage of these energy sources is the minimal impact on the environment. However, the challenge is still huge in identifying the means of collecting and

converting this energy in forms that are useful. In case of solar energy, the primary devices are solar thermal collectors and photovoltaics (Dziadik, 2012). A typical solar collector is made of a black surface, known as an absorber, and an array of tubes embedded or fused on the surface. The basic principle is that the black surface absorbs thermal energy in the form of heat from the sun and transfers the energy to the fluid flowing inside the attached tubes.

Flat plate solar collectors are considered to be one of the most cost effective devices amongst the existing solar energy conversion appliances (Kostić and Pavlović, 2012; Mahian et al., 2013). It has been documented that the efficiency of this kind of thermal collector is mainly affected by the transfer of heat from the absorber to the working fluid (Otanicar, 2009). Maximizing the heat transfer between these two mediums and minimizing the heat loss to the surrounding environment could result in building a highly efficient solar thermal collector (Otanicar, 2009). However, this study looks at an alternative approach to produce an efficient thermal collector through the replacement of the working fluid, by a highly conductive heat transfer medium such as nanofluid. It has been shown that adding a small amount of nanoparticles in water results in a substantial increase in its thermal conductivity (Yousefi et al., 2012a). A range of studies have reported the properties of particle mixed fluids considering their size in μm or even mm range (Wang and Mujumdar, 2007; Xuan and Li, 2000). The results are promising in some cases, but their disadvantages such as, instability of suspensions, flow resistance, clogging and abrasion, limit their practical applications (Wang and Mujumdar, 2007; Xuan and Li, 2000). However, the recent development in science and technology pave the way for manufacturing solid particles in nanoscale. Nanofluids are a new class of advanced heat-transfer fluids engineered by dispersing nanoparticles smaller than 100 nm (nanometre) in diameter in conventional heat transfer fluids (Choi and Eastman, 1995; Fotukian and Esfahany, 2010).

Conventional solar thermal collectors exhibit poor performance considering the amount of thermal energy received from the sun. It has been documented that the low performance might be attributed to the higher specific heat and low thermal conductivity of the absorbing fluid, higher entropy generation, and low absorber temperatures (Natarajan and Sathish, 2009; Tyagi et al., 2009). Recently, some studies have shown that the performance of a solar collector might be improved by changing the heat transfer medium to nanofluids. Natarajan and Sathish (2009) reported the effect of carbon nanotubes (CNT) on the properties of the base fluid (water). The study observed improved thermal properties and ultimately was able to enhance the efficiency of a solar water heater using CNT nanofluid as the working medium. Tyagi et al. (2009) examined the application of aluminium nanofluids in a direct absorption solar collector (DAC) and reported 10 % enhancement in efficiency compared to the conventional DAC (Yousefi et al., 2012b). A number of studies have reported the improved performance of solar thermal collectors using nanofluids as the working medium (Otanicar and Golden, 2009; Otanicar et al., 2010). However, the exergy analysis along with energy needs to be calculated for a better understanding of the application of nanofluids in solar to thermal energy conversions.

The aim of the present work is to determine the effect of nanofluids on the energy and exergy efficiencies of a flat plate solar collector. Several parameters such as, volume flow rate, nanoparticles volume concentration, density, specific heat and output temperatures are taken into consideration in explaining the performance of the solar thermal collector. An attempt is made to compare the results of the present study to the literature reports.

2. Analytical Approach

2.1 The first law of thermodynamics (analysis of energy efficiency)

The first law of thermodynamics is also known as the law of conservation of energy. It states that the total internal energy for a given system is a function of work and heat that are being done on the system. The amount of heat needs to be added or subtracted to the work in determining the internal energy of the system depending on its flow direction (plus and minus for heat flows in and out of the system, respectively). According to the 1st law, the energy balance Equation for a stationary process observed through a control volume can be written as (Cabrera et al., 2013):

$$\dot{Q} - P = \sum_{outlet} \dot{m}_k \left(h + gz + \frac{w^2}{2} \right)_k - \sum_{inlet} \dot{m}_k \left(h + gz + \frac{w^2}{2} \right)_k \quad (1)$$

where w and h represent mass flow velocity ($\dot{m}/\rho A$) and specific enthalpy (J/kg) assumed at the system inlet and outlet respectively.

The present study considers the flat plate solar thermal collector as the selected system for thermodynamic analysis and nanofluid as its fluidic medium. Therefore, possible heat gain (\dot{Q}_u) by the absorbing medium (nanofluid) can be written as,

$$\dot{Q}_u = \dot{m}C_p(T_{f,out} - T_{f,in}) \quad (2)$$

The heat capacity and density of the nanofluids are calculated using Equations (2) & (3) (Xuan and Roetzel, 2000; Zhou and Ni, 2008)

$$C_{p,nf} = \phi C_{p,np} + C_{p,bf}(1 - \phi) \quad (3)$$

$$\rho_{nf} = (1 - \phi)\rho_{bf} + \phi\rho_{np} \quad (4)$$

Equation (2) does not consider the parameters related to the heat loss from the solar thermal collector to the surrounding. Hottel–Whillier (Struckmann, 2008) proposed a more convenient solution for the calculation of heat gain involving the missing parameters in Equation (2).

$$\dot{Q}_u = A_p F_R [S - U_1(T_{f,in} - T_a)] \quad (5)$$

Absorbed irradiation per unit area of solar collector absorber plate (S) is determined by,

$$S = I_T(\tau\alpha) \quad (6)$$

where $(\tau\alpha)$ is known as optical efficiency (η_o) or product of transmittance – absorptance of the solar collector (Sukhatme and Nayak, 2017).

F_R may be determined from Equation (7)

$$F_R = \frac{\dot{m}C_p}{U_1 A_p} \left[1 - \exp\left\{-\frac{F'U_1 A_p}{\dot{m}C_p}\right\} \right] \quad (7)$$

The energy balance equation, represented by Equation (1), may be written in a simplified form for the absorber plate of a solar thermal collector as (Sukhatme and Nayak, 2017):

$$\dot{Q}_u = A_p S - U_1 A_p (T_c - T_a) \quad (8)$$

The absorber plate temperature (average), plate area, absorbed irradiation flux by the unit area of the absorber plate and overall heat loss are assumed as constant factors or variables with little effect. The efficiency of the flat plate solar collector for a given amount of solar irradiation, absorbed by the collector surface, can be written as follows:

$$\eta_{En} = \frac{\dot{Q}_u}{A_p I_T} = \frac{\dot{m}C_p(T_{f,out} - T_{f,in})}{I_T} \text{ [without considering heat loss]} \quad (9)$$

$$\eta_{En} = F_R(\tau\alpha) - F_R U_1 \frac{T_{f,in} - T_a}{I_T} \text{ [including heat loss]} \quad (10)$$

The present study determines the collector performance for normal incidence conditions, therefore, $F_R(\tau\alpha)$, F_R , and U_1 are assumed to be constant within the range of the tested temperatures (Yousefi et al., 2012a). Considering the above assumptions, one can note that the efficiency definition is only a comparison between quantities, which were metrically homogeneous, but not conceptually equivalent.

2.2 The second law of thermodynamics (analysis for exergy efficiency)

Energy efficiency is not enough to describe a thermodynamic process because the energy equation does not account for the internal losses. The second law of thermodynamics provides more information about the optimal operating stage, inefficiencies, corresponding magnitudes and traces (Farahat et al., 2009; Luminosu and Fara, 2005). It starts with considering that the real processes are not reversible and gains entropy through the processes. Some of the common

irreversible processes are molecular diffusion, friction, hysteresis etc. According to Clausius's statement, the second law can be written as,

$$\sum_{outlet} (\dot{m}.s)_k - \sum_{inlet} (\dot{m}.s)_k = \sum_j \left(\frac{\dot{Q}}{T} \right)_j + \sigma \quad (11)$$

During the first law analysis, there is a term for work, but no consideration for irreversibility. Besides, the second law discusses irreversibility, but avoids the term work. To gather more information, the first and second laws are combined together. By combining Eqs. (1) and (11), one can obtain the Gouy-Stodola equation (Sarhaddi et al., 2010):

$$P = \sum_n \dot{Q}_n \left(1 - \frac{T_a}{T_n} \right) + \sum_{Inlet} \dot{m}_k \left(h - T_a s + \frac{w^2}{2} + gz \right)_k - \sum_{Outlet} \dot{m}_k \left(h - T_a s + \frac{w^2}{2} + gz \right)_k - T_a \sigma \quad (12)$$

Exergy can be expressed as the obstruction of any work proportion to its dead state. There is no further work, when the environment comes to an equilibrium with the system. At this state, the system is defined as dead state. So, for a control volume, Eq. (12) may be rewritten in terms of exergy, as follows:

$$\begin{aligned} (\dot{E}_P)_{out} - (\dot{E}_P)_{in} &= (\dot{E}_Q)_{in} - (\dot{E}_Q)_{out} + (\dot{E}_m)_{in} - (\dot{E}_m)_{out} - \sigma T_a \\ (\dot{E}_P + \dot{E}_Q + \dot{E}_m)_{in} &= (\dot{E}_P + \dot{E}_Q + \dot{E}_m)_{out} + \sigma T_a \end{aligned}$$

Therefore,

$$\sigma T_a = \sum_{in} \dot{E}_j - \sum_{out} \dot{E}_k \quad (13)$$

where exergy of work, \dot{E}_P , exergy of heat \dot{Q} available at temperature T , \dot{E}_Q and exergy of a mass flow, \dot{E}_m are defined as follows:

$$\begin{aligned} \dot{E}_P &= P \\ \dot{E}_Q &= \dot{Q} \left(1 - \frac{T_a}{T} \right) \quad \text{and} \\ \dot{E}_m &= \dot{m} \left[(h - h_o) - T_a (s - s_o) + \frac{w^2 - w_o^2}{2} + g(z - z_o) \right] \end{aligned}$$

The irreversibility can then be quantified as the difference in exergy measured at the inlet and outlet sections of the control volume. The simplest exergy balance equation per unit interception area of a solar collector can be expressed in steady state as shown below (Suzuki, 1988):

$$\dot{E}_g = \eta_o \dot{E}_{sun} - \dot{E}_{loss} \quad (14)$$

The exergy loss due to the fluid pressure drop is assumed to be negligibly small. Eq. (14) can also be written as (Jafarkazemi and Ahmadifard, 2013),

$$\sum \dot{E}_{in} - \sum \dot{E}_{out} = \sum \dot{E}_{dest} \quad (14^*)$$

The exergy collection rate in steady state is exergy gained by the heat transfer fluid while the fluid temperature increases from $T_{f, in}$ at the inlet to $T_{f, out}$ at the outlet. The expression of the exergy collection rate, assuming that the fluid is incompressible, can be obtained by use of the following equation without considering mechanical exergy,

$$\dot{E}_g = \dot{m} C_p \left(T_{f, out} - T_{f, in} - T_a \ln \frac{T_{f, out}}{T_{f, in}} \right) \quad (15)$$

There are two important points that should be noted in considering the exergy available ratio for solar radiation. One is that the solar flux radiating on earth can be assumed as always being in a steady state but never in equilibrium state. The other is that the radiation of the sun is a type of open system which means losses of photons cannot be recovered unlike an equilibrium closed system. From these facts the Carnot's expression of $(1 - T_a/T_s)$ is thought to be appropriate for the solar radiation exergy which has the same form as Jeter's result (Jeter and Stephens, 2012). From the above mentioned, the exergy flux from the sun is defined here as:

$$\dot{E}_{sun} = I_T \left(1 - \frac{T_a}{T_s} \right) \quad (16)$$

The heat transfer process from the sun to the collector's working fluid consists of two main parts, absorbing the solar radiation by the absorber plate and heat transfer from the absorber plate to the working fluid. The exergy destructions occur during these two processes including flowing parts (Suzuki, 1988), as can be seen in **Figure 1**.

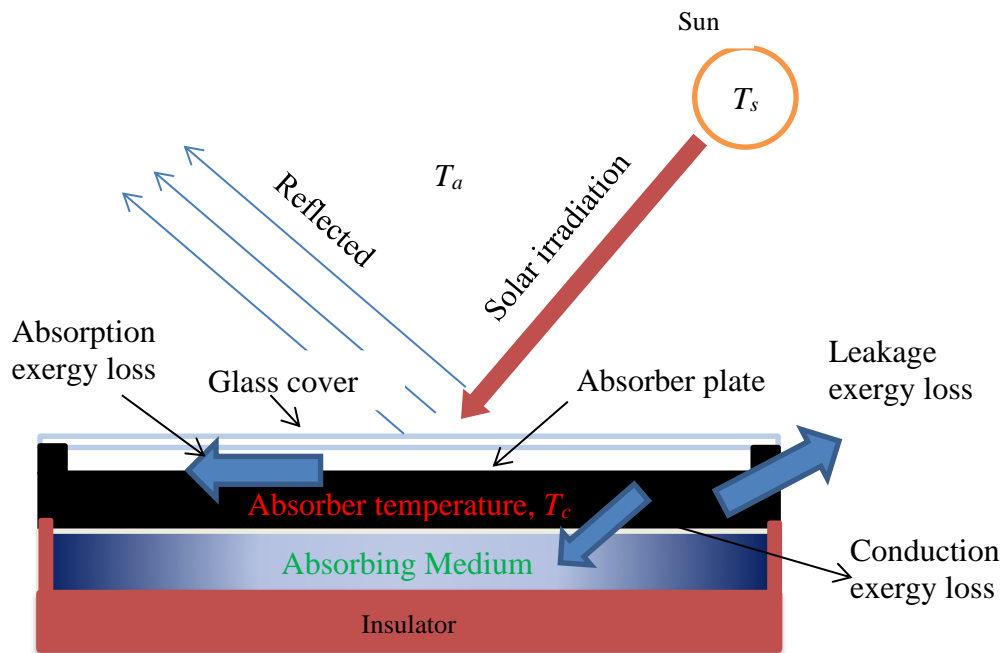


Figure 1. Schematic diagram for different exergy losses

- *Absorption exergy loss (radiation \rightarrow plate):* an exergy annihilation process when the solar radiation at T_s , is absorbed by the absorber at T_c .
- *Leakage exergy loss (plate \rightarrow ambient):* an exergy loss process accompanied with heat leakage from the absorber out into its surroundings.
- *Conduction exergy loss (plate \rightarrow fluid):* an exergy annihilation process caused by heat conduction between the absorber and the heat transfer fluid.

The above three kinds of exergy loss processes are closely related with the corresponding entropy generation rates through Gouy-Stodola's theorem (Bejan, 1982). These three entropy generation rates can be stated from the thermodynamic considerations as follows:

$$\Delta \dot{s}_{rp} = \int_0^1 k I_T \left(\frac{1}{T_1} - \frac{1}{T_s} \right) d\sigma \quad (17)$$

$$\Delta \dot{s}_{pa} = \int_0^1 U_1 (T_1 - T_a) \left(\frac{1}{T_a} - \frac{1}{T_1} \right) d\sigma, \text{ and} \quad (18)$$

$$\Delta \dot{s}_{pf} = \int_0^1 k(T_1 - T_f) \left(\frac{1}{T_f} - \frac{1}{T_1} \right) d\sigma \quad (19)$$

Although Eqs. (17) - (19) cannot be integrated unless a distribution of the local absorber temperature (T_1) and the heat transfer coefficient are known, these equations still can be approximated using the mean absorber temperature as follows:

$$\Delta \dot{s}_{rp} = k I_T \left(\frac{1}{T_c} - \frac{1}{T_s} \right) \quad (17')$$

$$\Delta \dot{s}_{pa} = U_1 (T_c - T_a) \left(\frac{1}{T_a} - \frac{1}{T_c} \right), \text{ and} \quad (18')$$

$$\Delta \dot{s}_{pf} = \int_{T_{f,in}}^{T_{f,out}} \frac{\dot{m} C_p dT}{T} - \frac{\dot{m} C_p (T_{f,out} - T_{f,in})}{T_{f,out}} \quad (19')$$

In Eq. (19'), the first term on the right-hand side is an entropy flow received by the fluid from the absorber and the second term represents entropy of the collected energy as it has been in the absorber. The difference of both terms becomes the entropy generation rate while heat transfers from the absorber to the fluid. The exergy loss term in Eq. (14) can be seen from Eqs. (17') - (19') using Gouy-Stodola's theorem as,

$$\dot{E}_{loss} = T_a (\Delta \dot{s}_{rp} + \Delta \dot{s}_{pa} + \Delta \dot{s}_{pf}) \quad (20)$$

Hence, the exergy-balance-equation of a solar collector in steady state can be derived by substituting Eqs. (15), (16), and (20) into Eq. (14). After a few arrangements, it becomes:

$$\begin{aligned} \dot{m} C_p \left(T_{f,out} - T_{f,in} - T_a \ln \frac{T_{f,out}}{T_{f,in}} \right) &= I_T \left(1 - \frac{T_a}{T_s} \right) \\ &- \left[(1 - \eta_o) I_T \left(1 - \frac{T_a}{T_c} \right) + I_T T_a \left(\frac{1}{T_c} - \frac{1}{T_s} \right) + U_1 (T_c - T_a) \left(1 - \frac{T_a}{T_c} \right) + \dot{m} C_p T_a \left(\ln \frac{T_{f,out}}{T_{f,in}} - \frac{T_{f,out} - T_{f,in}}{T_c} \right) \right] \end{aligned} \quad (21)$$

By rearranging this equation, the following energy balance equation of a solar collector can be easily obtained:

$$\dot{m} C_p (T_{f,out} - T_{f,in}) = \eta_o I_T - U_1 (T_c - T_a) \quad (22)$$

The exergetic efficiency is defined here and is expressed using Eq. (21) as follows:

$$\eta_{Ex} = \frac{\dot{E}_g}{\dot{E}_{sun}} = 1 - \left[(1 - \eta_o) \frac{1 - T_a/T_c}{1 - T_a/T_s} + \frac{1/T_c - 1/T_s}{1/T_a - 1/T_s} + \frac{U_1 (T_c - T_a) (1 - T_a/T_c)}{I_T (1 - T_a/T_s)} + \frac{\dot{m} C_p T_a}{I_T (1 - T_a/T_s)} \left(\ln \frac{T_{f,out}}{T_{f,in}} - \frac{T_{f,out} - T_{f,in}}{T_c} \right) \right] \quad (23)$$

$$= 1 - [e_{opt} + e_{rp} + e_{pa} + e_{pf}] \quad (24)$$

All terms in brackets in Eqs. (23) and (24) represent exergy losses and their physical meanings are given as follows:

- ✓ e_{opt} : optical loss fraction of the absorbed solar radiation due to transmissivity of glazing and absorptance of the absorber.
- ✓ e_{rp} : a loss fraction when the solar radiation at T_s is absorbed by the absorber at T_c . (The high quality energy is degraded by absorption at low temperature.)
- ✓ e_{pa} : a fraction of the exergy leakage from the absorber to the surroundings.
- ✓ e_{pf} : Heat-conduction loss fraction accompanied with the heat transfer from the absorber to the fluid.

Two of the above loss fractions, e_{opt} and e_{pas} , correspond to the terms $(1 - \eta_o)$ and $U_l(T_c - T_a)/I_T$ in a well-known expression of energetic efficiency; the other two fractions have no corresponding term in the energetic analysis because they are not supposed as loss processes. It should be noted here that the term given for heat-conduction loss e_{pf} is closely related with the collector efficiency factor. Considering the correlations of temperature distribution in the collector, the following correlation will be obtained:

$$\frac{T_{f,out} - T_a - S/U_1}{T_{f,in} - T_a - S/U_1} = \exp\left(-\frac{U_1 A_p F'}{\dot{m} C_p}\right) \quad (25)$$

Here also, using the above equation, the component of outlet fluid temperature is omitted from Eq. (23) and the correlation of collector exergy efficiency is rephrased into the following form (Jafarkazemi and Ahmadifard, 2013):

$$\eta_{Ex} = \frac{\dot{m} C_p \left[\left(T_{f,in} - T_a - \frac{S}{U_1} \right) \left(\exp\left(-\frac{U_1 A_p F'}{\dot{m} C_p}\right) - 1 \right) \right] - \dot{m} C_p \left[T_a \frac{\exp\left(-\frac{U_1 A_p F'}{\dot{m} C_p}\right) - 1}{T_{f,in} - T_a - \frac{S}{U_1}} \left(T_{f,in} - T_a - \frac{S}{U_1} \right) + 1 \right]}{A_p I_T \left[1 - \left(\frac{T_a}{T_s} \right) \right]} \quad (26)$$

2.3 Input Data

The present study has some considerations to simplify the analysis. These are constants such as, absorbing fluid properties, exergy flow rate to be equal to the solar flux, area of the absorber plate, overall heat loss and other heat transfer coefficients. Furthermore, the fluid inlet temperature and the ambient temperature are also assumed to be constant and equal. Tables 1-3 (input data tables) list the properties of nanoparticles, the characteristic parameter of the solar collector and the analysis condition, respectively.

Table 1 Properties of different nanomaterial and base fluid (Moghaddami et al., 2011; Pandey and Nema, 2012).

Material	Specific heat, C_p (J/kg.K)	Thermal conductivity, k (W/m.K)	Density, ρ (kg/m ³)
Alumina (Al ₂ O ₃)	773	40	3960
Copper oxide (CuO)	551	33	6000
Titanium oxide (TiO ₂)	692	8.4	4230
Silicon di oxide (SiO ₂)	765	36	3970
Water (H ₂ O), base fluid	4182	0.60	1000

Table 2 Characteristic parameters for two kinds of solar collectors (Suzuki, 1988).

Solar collector type	Optical efficiency, η_o	Overall heat loss, U_1 (W/m ² .K)	Collector efficiency factor, F'
Evacuated tube	0.47	1.1	0.99
Flat plate	0.82	5.0	0.97

3. Results and discussion

Table 3 includes selected environmental and analyses conditions for solar collector. Collector efficiency was determined using Eqs. (9), (10) and (26) and data from Tables 1-3. The results are shown in Table 4.

Obtained results were compared with the data reported by Luminosu et al. (2005) which were reported for the open circuit mode of the solar collector and Farahat et al. (2009) which were reported for computer simulation of the solar collector. The comparison is represented in Table 5.

Table 3 Environmental and analysis conditions for the flat plate solar collector (Alim et al., 2013).

Parameters of collector	Value
Type	Black paint flat plate
Glazing	Single glass
Agent fluids	Water, Al ₂ O ₃ , SiO ₂ , TiO ₂ and CuO nanofluids
Absorption area, A _p	1.51 m ²
Wind speed	20 m/s
Collector tilt, β _o	20°
Fluid inlet and ambient temperature, T _{f,in} ≈ T _a	300 K
Apparent sun temperature, T _s	4350 K
Optical efficiency, η _o	0.84
Emissivity of the absorber plate, ε _p	0.95
Emissivity of the covers, ε _c	0.90
Glass thickness, t	4 mm
Insulation thermal conductivity, k _i	0.06 W/m·K
Incident solar energy per unit area of the absorber plate, I _T	500 W/m ²
Inner diameter of pipes, D _i	0.04 m

Table 4 Energy and exergy efficiency enhancement compared to the base fluid.

Absorbing medium	Maximum η _{En} enhancement, (%)		Maximum η _{Ex} enhancement, (%)	
	φ = 2% and diff. volume flow rate	φ = 3.20% and V = 1 L/s	φ = 2% and V = 2.40 L/s	φ = 3.20% and V = 1 L/s
CuO nanofluid	38.46	13.25	15.52	13.18
TiO ₂ nanofluid	28.84	8.40	5.63	8.10
SiO ₂ nanofluid	28.84	6.40	5.63	6.41
Al ₂ O ₃ nanofluid	28.84	6.40	5.63	6.41

Table 5 Comparison among the present analysis, experimental results and computer simulation.

	T _{f,in} or T _a , (K)	I _T , (W/m ²)	S, (W/m ²)	ΔT, (K)	η _{Ex} , (%)
Present analysis (CuO)	300.00	500	420	62.00	3.35
Luminosu and Fara, (2005)	305.15	788	580	46.00	2.90
Farahat et al. (2009)	300.00	500	420	58.82	2.95

As can be seen, obtained results are in good agreement with the literature reports. **Table 5** allows the following points to be made:

- While the introduction of nanofluids increases viscosity, density and thermal conductivity, specific heat decreases substantially (Pandey and Nema, 2012)
- It is obvious that the lesser entropy generation number leads to higher exergy efficiency of the system. Theoretically one may expect that the entropy generation can be reduced with the application of nanoparticle water (Moghaddami et al., 2011).
- The heat transfer increases with the increase in concentration of nanoparticles (Lelea, 2011).

Figure 2 illustrates the changes in energy efficiency for the volume flow rate of 1 to 3.8 L/min. As can be seen, the energy efficiency increases steadily with the volume flow rate. Energy efficiency was determined using Eq. (9), input data tables, constant output temperature differences and 2% nanoparticles volume fraction. As shown in Figure 2, the energy efficiency of the solar collector increased substantially by 38.46% and 28.84% for CuO and Al₂O₃, respectively. Yousefi et al. (2012b) and Tyagi et al. (2009) reported similar results.

Figure 3 demonstrates the effect of output temperature on energy efficiency. Energy efficiency was calculated from Eq. (9). As can be seen, output temperature of a solar collector has substantial impact on energy efficiency. The reason for higher output temperature is the absorption of heat by the nanoparticles. As we know, specific heat is defined as the heat

required raising the temperature of a unit mass of a substance by one unit of temperature. It is clear from the definition that any substance, which has a lower specific heat, should result in increased temperature for equal heat flow. The effect of nanoparticle volume fraction on the specific heat has been calculated in the study. This property tends to decrease when the volume fraction of nanoparticles is high. Therefore, the output temperature rises and the efficiency also increases. The specific heat of the nanofluid was determined using Eq. (3). The observed specific heats for the nanofluids are in the following order, $\text{CuO} > \text{TiO}_2 > \text{Al}_2\text{O}_3 > \text{SiO}_2$. However, despite their differences in specific heats, all these values are higher than water. Kamyar et al. (2012) and Soheli et al. (2013)'s observation suggested similar results.

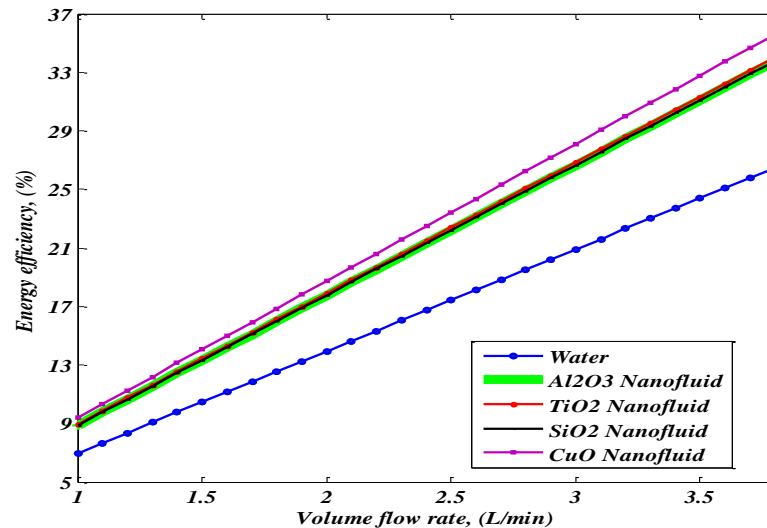


Figure 2. Effect of volume flow rate on energy efficiency

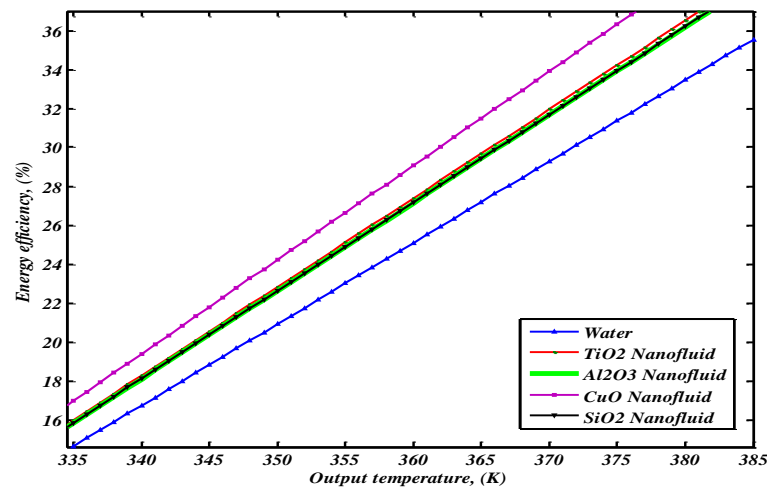


Figure 3. Effect of output temperature on collector exergy efficiency

Figure 4 represents the energy efficiency of solar collectors as a function of nanoparticles volume fraction. Eqs. (3), (4) and (9) were used in determining energy efficiency. As can be seen, efficiency of solar collectors goes up with the increment of nanoparticle percentage in the base fluid. For instance, 3.2% nanoparticles volume fraction increased the efficiency by 13.25 % for CuO nanofluid, 8.4% for TiO_2 nanofluid and 6.40% for Al_2O_3 and SiO_2 .

The exergy analysis of a flat plat solar collector using different nanofluids was also carried out in the present study to evaluate the enhancement of exergic efficiency when compared to a conventional collector. Figure 5 shows the behaviour of the exergy efficiency as a function of the volume flow rate of fluid. Exergy efficiency was calculated from Eq. (26). The analysis represents that the lowest efficiencies belonged with the collector operated by water. Therefore, a large amount of irreversibility belongs to the traditional solar collector. By using nanofluid in solar collectors as an

absorbing medium, exergy efficiency can be increased. CuO nanofluid may be a good choice as an absorbing medium because of their higher exergy efficiency. Hamilton and Crosser model (1962), reported that the thermal conductivity of nanofluids is directly related to the volume fraction and the shape of the nanoparticle. It is expected that addition of nanoparticles leads to increased effective surface area for heat transfer. Additionally, the inherently higher thermal conductivity of nanoparticles will improve the thermal conductivity of the nanofluid. This could be the reason for improved exergy efficiency.

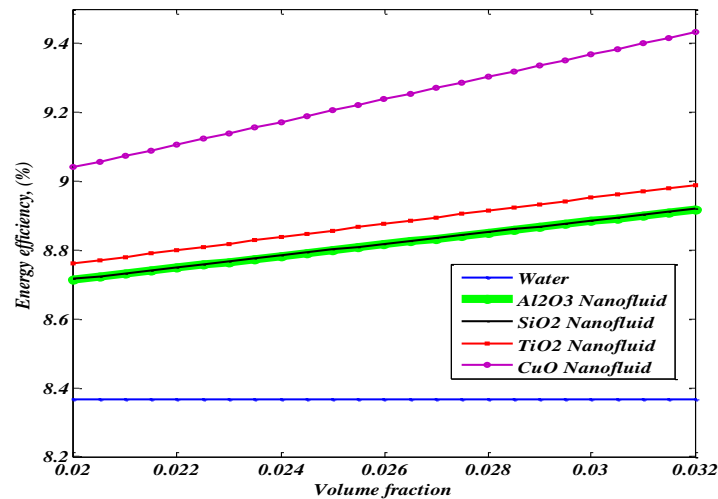


Figure 4. Effect of volume fraction on energy efficiency

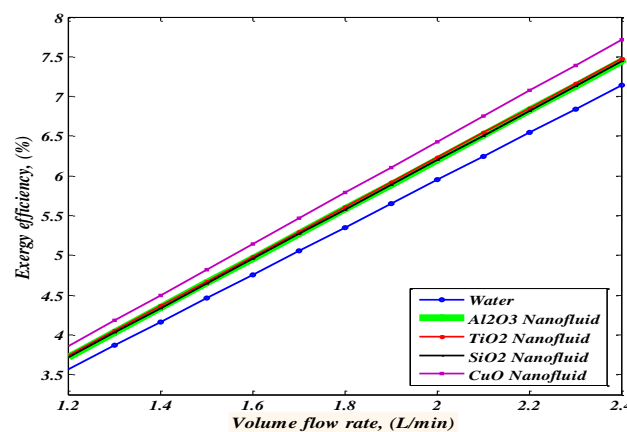


Figure 5. Effect of volume flow rate on exergy efficiency

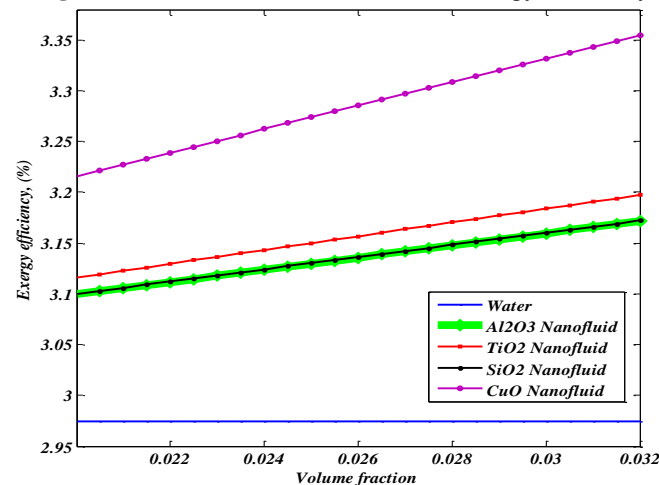


Figure 6. Effect of particle volume fraction on exergy efficiency.

Figure 6 shows the effect of nanoparticle volume fraction on exergy efficiency. For a fixed volume flow rate, the solar collector with CuO nanofluid exhibits highest exergy efficiency. For example, at 2.4 L/s volume flow rate, the exergy

efficiency is higher than the conventional solar collector by 15.52%. Al_2O_3 and SiO_2 showed approximately equal exergy but higher than water. On the other hand, TiO_2 shows better performance compared to the base fluid, Al_2O_3 and SiO_2 nanofluids. The possible reason for this enhancement can be attributed to the following reasons: (I) the nanofluid with suspended nanoparticles increases the thermal conductivity of the mixture and (II) the convective heat transfer coefficient of the nanofluid is higher than that of the base fluid (water) at a given Reynolds number. The results are in good agreement with those obtained from Duangthongsuk and Wongwises (2009), Xuan and Li (2003) and He et al. (2007). According to the exergy efficiency equation, mass flow rate and specific heat have substantial impact on exergy efficiency when the collector absorber area is fixed.

Though output temperature has a greater effect on energy efficiency, it also enhances absorber plate temperature which may cause exergy loss. As mentioned in many articles, the main reason of exergy loss is the difference between the absorber plate temperature and the sun temperature (T_s). The increase in the absorber plate temperature leads to an increase in this difference and consequently a decrease in the collector exergy efficiency. Jafarkazemi et al. (2013) reported that increasing the flow rate to approximately 0.01 kg/s leads to a considerable decrease in the absorber plate's temperature. The decrease in temperature gradient between the absorber plate and the environment results in a decrease in the overall heat loss coefficient and subsequently, an increase in the thermal efficiency of the collector. Figure 7 directly supports that statement. Table 6 lists the parameters, or in other words, a bird's eye view of the present study. According to the results shown in Table 6, it is expected that an efficient solar collector can be produced where nanofluids would be the absorbing medium.

It is very clear from Table 6 that the CuO nanofluid provides maximum efficiency for both energy and exergy. On the other hand, it also requires the highest surface area. This may cause higher costs. But in the case of other nanofluids, it required less area than the traditional solar collector which may reduce the cost.

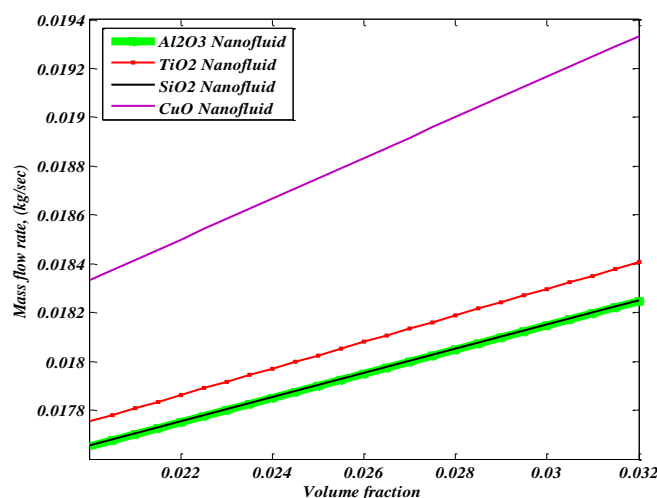


Figure 7. Effect of particle volume fraction on mass flow rate

Table 6 Analytical findings of a flat plate solar collector for different nanofluids and base fluid (equal nanoparticles volume fraction and volume flow rate).

Base fluid/ Nanofluid	C_p , (J/kg.K)	A_p , (m^2)	Mass flow rate, enhancement, (%)	Energy efficiency enhancement, (%)	Exergy efficiency enhancement, (%)
Water	4182.00	1.61	-	-	-
Al_2O_3	4113.82	1.51	9.47	28.84	4.25
TiO_2	4112.20	1.52	10.38	28.84	4.25
CuO	4109.38	2.24	15.95	38.46	15.52
SiO_2	4113.66	1.50	9.47	28.84	4.25

4. Conclusion

In the present study, we have focused on the benefits of using different nanofluids in a flat plate solar collector. We have studied the effects of volume flow rate, nanoparticles volume fraction, mass flow rate, density and specific heat on energy and exergy efficiency of the solar collector.

The following conclusions can be made based on the results:

- a) Analytical outcomes revealed that CuO nanofluid could increase the energy and exergy efficiency of a flat plate solar collector in analogy with water as absorbing fluid, by 38.46% and 15.52%, respectively.
- b) The study also remarked that the increment of volume fraction, mass flow rate and density could enhance both energy and exergy efficiency. For equal volume flow rate, mass flow rate could be increased by injecting nanoparticles in the base fluid. Specific heat is one of the most important parameters for efficiency improvement. By reducing specific heat, the efficiency of a flat plate solar collector can be enhanced, and it is very simple to reduce specific heat of a fluid by dispersing a small amount of nanoparticles.
- c) From this study, we may conclude that the performance of a solar collector can be enhanced by converting the absorbing medium to nanofluid. On the basis of this study, CuO nanofluid may be a good option.

A number of assumptions have been made in this study to reduce the complexity of the analyses, such as the values of the overall heat loss coefficient, nanoparticle properties, inlet temperature, pressure drop, area of the absorber plate and heat removal factor are constant. Future study is required to address those issues.

References

- Alim MA, Abdin Z, Saidur R, Hepbasli A, Khairul MA, Rahim NA. Analyses of entropy generation and pressure drop for a conventional flat plate solar collector using different types of metal oxide nanofluids. *Energy and Buildings* 2013 66, 289-296
- Bejan A. *Entropy generation through heat and fluid flow*: Wiley, 1982.
- Cabrera F, Fernández-García A, Silva R, Pérez-García M. Use of parabolic trough solar collectors for solar refrigeration and air-conditioning applications. *Renewable and Sustainable Energy Reviews* 2013; 20: 103-118.
- Choi SU, Eastman JA. *Enhancing thermal conductivity of fluids with nanoparticles*. Argonne National Lab., IL (United States), 1995.
- Duangthongsuk W, Wongwises S. Heat transfer enhancement and pressure drop characteristics of TiO₂-water nanofluid in a double-tube counter flow heat exchanger. *International Journal of Heat and Mass Transfer* 2009; 52: 2059-2067.
- Dziadik PC. *Solar energy collection system and components*. Google Patents, 2012.
- Farahat S, Sarhaddi F, Ajam H. Exergetic optimization of flat plate solar collectors. *Renewable energy* 2009; 34: 1169-1174.
- Fotukian S, Esfahany MN. Experimental investigation of turbulent convective heat transfer of dilute γ -Al₂O₃/water nanofluid inside a circular tube. *International Journal of Heat and Fluid Flow* 2010; 31: 606-612.
- Hamilton RL, Crosser O. Thermal conductivity of heterogeneous two-component systems. *Industrial & Engineering chemistry fundamentals* 1962; 1: 187-191.
- He Y, Jin Y, Chen H, Ding Y, Cang D, Lu H. Heat transfer and flow behaviour of aqueous suspensions of TiO₂ nanoparticles (nanofluids) flowing upward through a vertical pipe. *International journal of heat and mass transfer* 2007; 50: 2272-2281.
- Jafarkazemi F, Ahmadifard E. Energetic and exergetic evaluation of flat plate solar collectors. *Renewable Energy* 2013; 56: 55-63.
- Jeter SM, Stephens JH. *Systems and methods of thermal energy storage and release*. Google Patents, 2012.
- Kamrath A, Saidur R, Hasanuzzaman M. Application of computational fluid dynamics (CFD) for nanofluids. *International Journal of Heat and Mass Transfer* 2012; 55: 4104-4115.
- Kostić LT, Pavlović ZT. Optimal position of flat plate reflectors of solar thermal collector. *Energy and Buildings* 2012; 45: 161-168.
- Lelea D. The performance evaluation of Al₂O₃/water nanofluid flow and heat transfer in microchannel heat sink. *International Journal of Heat and Mass Transfer* 2011; 54: 3891-3899.

- Luminosu I, Fara L. Determination of the optimal operation mode of a flat solar collector by exergetic analysis and numerical simulation. *Energy* 2005; 30: 731-747.
- Mahian O, Kianifar A, Kalogirou SA, Pop I, Wongwises S. A review of the applications of nanofluids in solar energy. *International Journal of Heat and Mass Transfer* 2013; 57: 582-594.
- Moghaddami M, Mohammadzade A, Esfehiani SAV. Second law analysis of nanofluid flow. *Energy Conversion and Management* 2011; 52: 1397-1405.
- Natarajan E, Sathish R. Role of nanofluids in solar water heater. *The International Journal of Advanced Manufacturing Technology* 2009; 1-5.
- Otanicar TP. Direct absorption solar thermal collectors utilizing liquid-nanoparticle suspensions: Arizona State University, 2009.
- Otanicar TP, Golden JS. Comparative environmental and economic analysis of conventional and nanofluid solar hot water technologies. *Environmental science & technology* 2009; 43: 6082-6087.
- Otanicar TP, Phelan PE, Prasher RS, Rosengarten G, Taylor RA. Nanofluid-based direct absorption solar collector. *Journal of renewable and sustainable energy* 2010; 2: 033102.
- Pandey SD, Nema V. Experimental analysis of heat transfer and friction factor of nanofluid as a coolant in a corrugated plate heat exchanger. *Experimental Thermal and Fluid Science* 2012; 38: 248-256.
- Sarhaddi F, Farahat S, Ajam H, Behzadmehr A. Exergetic performance assessment of a solar photovoltaic thermal (PV/T) air collector. *Energy and Buildings* 2010; 42: 2184-2199.
- Sohel M, Saidur R, Sabri MFM, Kamalisarvestani M, Elias M, Ijam A. Investigating the heat transfer performance and thermophysical properties of nanofluids in a circular micro-channel. *International Communications in Heat and Mass Transfer* 2013; 42: 75-81.
- Struckmann F. Analysis of a flat-plate solar collector. *Heat and Mass Transport, Project Report, 2008MVK160* 2008.
- Sukhatme SP, Nayak J. *Solar energy*: McGraw-Hill Education, 2017.
- Suzuki A. A fundamental equation for exergy balance on solar collectors. *ASME J. Sol. Energy Eng* 1988; 110: 102-106.
- Tyagi H, Phelan P, Prasher R. Predicted efficiency of a low-temperature nanofluid-based direct absorption solar collector. *Journal of solar energy engineering* 2009; 131: 041004.
- Wang X-Q, Mujumdar AS. Heat transfer characteristics of nanofluids: a review. *International journal of thermal sciences* 2007; 46: 1-19.
- Xuan Y, Li Q. Heat transfer enhancement of nanofluids. *International Journal of heat and fluid flow* 2000; 21: 58-64.
- Xuan Y, Li Q. Investigation on convective heat transfer and flow features of nanofluids. *Journal of Heat transfer* 2003; 125: 151-155.
- Xuan Y, Roetzel W. Conceptions for heat transfer correlation of nanofluids. *International Journal of heat and Mass transfer* 2000; 43: 3701-3707.
- Yousefi T, Shojaeizadeh E, Veysi F, Zinadini S. An experimental investigation on the effect of pH variation of MWCNT–H₂O nanofluid on the efficiency of a flat-plate solar collector. *Solar Energy* 2012a; 86: 771-779.
- Yousefi T, Veysi F, Shojaeizadeh E, Zinadini S. An experimental investigation on the effect of Al₂O₃–H₂O nanofluid on the efficiency of flat-plate solar collectors. *Renewable Energy* 2012b; 39: 293-298.
- Zhou S-Q, Ni R. Measurement of the specific heat capacity of water-based Al₂O₃ nanofluid. *Applied Physics Letters* 2008; 92: 093123.

Morphological assessment of a selected reach of the Jamuna River using the Delft3D Model

Orpita Urmi Laz^{1,*}, Umme Kulsum Navera²

¹School of Computing, Engineering and Mathematics, Western Sydney University, Australia

²Department of Water Resources Engineering, Bangladesh University of Engineering and Technology, Bangladesh

*Corresponding author's email: 18317116@student.westernsydney.edu.au

Peer review history

Manuscript submitted: 30 April 2019

Review process completed: 28 August 2019

Manuscript finally accepted: 28 August 2019

Handling Editor: Professor Ataur Rahman

Abstract: The River Jamuna, in Bangladesh, is one of the greatest alluvial rivers in the world. Almost every year severe erosion takes place, which renders tens of thousands of people homeless. In order to improve the livelihoods of floodplain dwellers, understanding the morpho-dynamics of the river is essential. The reach boundaries considered in this study are 30 km upstream and 20 km downstream of Bangabandhu Bridge. The main objective of this paper was to look over the sediment dynamics and the possible changes on riverbed morphology by using the open-source, Delft3D modelling software. Water level and discharge were two important hydrological

parameters that were used as the boundary conditions to investigate the erosion and deposition process. Variation of velocity, erosion and deposition, sediment transport and bed level changes of the Jamuna River were studied using this modeling suite. The frequency of erosion/deposition and shifting of the riverbank were predicted for two consecutive years (2011-2012). Comparisons were made between the simulated results of Delft3D with the results obtained from the Mike 21. Shifting of channels were observed, as erosion and deposition took place simultaneously along the channel bed and bank line. The knowledge regarding the shifting direction and magnitude of shifting generated from the analysis developed herein could be useful in the future projection of planform changes of braided rivers around the world that are similar to the Jamuna river.

Keywords: Morphology; Bangladesh; Jamuna River; Delft 3D; Channel shifting.

1. Introduction

Quantification and prediction of the sediment dynamics and the possible changes on riverbed morphology is one of the most challenging tasks in river management. In alluvial channels or streams, bed aggradation evolves primarily from the passage of flood events. It creates a variety of problems such as the rising of riverbeds and increasing flood heights, meandering and overflows along the banks, choking chocking up of navigation and irrigation canals and depletion of the capacity of storage reservoir (Hossain, 1997). A stream channel at grade provides the impulsion to carry the supplied sediment load to maintain a stable bed elevation (Mackin, 1948). Aggradation occurs in a river if the amount of sediment coming into a given reach of a stream is greater than the amount of sediment going out of the reach. Part of the sediment load must be deposited and hence, the bed level must rise (Ranga Raju, 1980). Alves and Cardoso (1999) investigated the effect of overloading on bed forms, resistance to flow, sediment transport rate and average bed profile of aggrading by overload. Aggradation and degradation phenomenon of alluvial channels beds are also reported by several researchers. (Jain, 1981; Jaramillo, 1983).

Bangladesh is a riverine country with hundreds of rivers overlaying its landscape. Major portion of Bangladesh is formed with heavily charged sediment from the river Ganges, the Jamuna and the Meghna and their distributaries and tributaries. These rivers experience complicated variations of erosion and deposition over time and space due to instantaneous changes of flow and sedimentation. The Jamuna river originates from Himalayas as the Brahmaputra, consisting a network of interlacing channels, with numerous sandbars or chars. Some of these chars are often deposited and destroyed continually, depending upon the sediment-carrying capacity of the flow (Baki et al., 2012). Many poor people reside in char areas where agriculture is the mainstay of their livelihood. Bank erosion of the river strongly depends on monsoonal peak discharge, leads bank retreat to hundreds of meters annually causing destruction of the river

and to public infrastructure (Mosselman, 2006; Mount et al., 2013). Therefore, it is crucial to understand the river's dynamic behaviour to mitigate such sufferings.

The Bangabandhu Bridge is a very important hydraulic structure to connect the east and west parts of Bangladesh over the Jamuna River. Apart from movement of cargo and passenger streams, it promotes conveyance of electricity and natural gas, and telecommunication links (Jenkins & Shukla, 1997). However, due to construction of the bridge, the hydraulic environment of the nearby area of the bridge has undergone a severe change (Mohammad et al., 2010). Hence, the existing hydraulic conditions in the vicinity of the bridge, as well as hydro-morphological forecasts of the river at the critical locations within the bridge surrounding area are essential.

Several modelling studies have been conducted to understand the different behaviours of the various types of rivers in Bangladesh, as well as over the world (Jagers, 2003; Kuehl et al., 1989; Goodbred and Kuehl, 2000b). In Bangladesh, Institute of Water Modelling (IWM) created a mathematical model using Mike 21C to evaluate the hydrodynamics and sediment transport to 20 km upstream and 10 km downstream from Bangabandhu Bridge (IWM, 2011). Most of these models, including Mike 21C, are very expensive and some are very time consuming. On the other hand, Delft3D flow (FLOW), morphology (MOR) and wave (WAVE) modules are available as an open source and has proven its capabilities on many places around the world (Wang et al., 2014). It is a powerful tool for understanding and forecasting river morpho-dynamic behaviour as it takes into account the most relevant factors involved in this process and gives a broad range of results, presented in an accessible manner. Though many studies have been conducted on sediment dynamics and morphology, very little studies have been carried out to investigate the planform change of the rivers of Bangladesh by using the Delft3D model. Delft 3D has been widely applied in coastal, river and estuarine areas for simulation (Van der Wegen, & Roelvink, 2008; Crosato et al., 2011; Crosato et al., 2012). Jagers (2003) carried out two-dimensional depth-averaged morphological simulation of sharp bends to improve the understanding of the physical process of a river. In order to understand the trends and migration patterns, a 3D model Delft3D was used for simulating the hydrodynamic and morphological processes in this study.

2. Methodology

2.1 Water level and bed level calculation

The water level data were recorded at 3 hour intervals using the water level gauges by Institute of Water Modeling (IWM), in 2010 and 2011. These gauges have been fixed to the PWD datum from the benchmark (BM) by direct fly levelling. A Digital echo sounder, fitted with a DGPS, Laptop computer and HydroPro survey software was used to survey the water part of the river.

2.1 Numerical Model Description

Hydrodynamic and Morpho-dynamics modules are considered to be coupled in Delft3D model, in which the flow field adjusts in real time as the bed topography changes (Edmonds & Slingerland, 2007). Conservations of momentum is followed in Delft3D model by applying equations 1 and 2 in the x and y directions, respectively.

$$\frac{\partial U}{\partial t} + U \frac{\partial U}{\partial x} + V \frac{\partial U}{\partial y} + \frac{\omega}{H} \frac{\partial U}{\partial \sigma} - fV = -\frac{1}{\rho_0} P_x + F_x + M_x + \frac{1}{H^2} \frac{\partial}{\partial \sigma} (v_v \frac{\partial u}{\partial \sigma}) \quad (1)$$

$$\frac{\partial V}{\partial t} + U \frac{\partial V}{\partial x} + V \frac{\partial V}{\partial y} + \frac{\omega}{H} \frac{\partial V}{\partial \sigma} - fU = -\frac{1}{\rho_0} P_y + F_y + M_y + \frac{1}{H^2} \frac{\partial}{\partial \sigma} (v_v \frac{\partial v}{\partial \sigma}) \quad (2)$$

Here, U and V defines the velocity components in the x and y directions, respectively, v_v is the vertical velocity, ω is the settling velocity, f is the Coriolis force, P is the barotropic pressure gradients for water of specific density, ρ_0 is the atmospheric pressure, F denotes the horizontal friction (Reynold's stress). Lastly, M represents the discharge or withdrawal of momentum due to the external sources like discharge of water and wave stresses.

The depth-average continuity equation is maintained in the model by Equation 3 (Lesser et al., 2004). The model in this study is calibrated for a single layer.

$$\frac{\partial \zeta}{\partial t} + \frac{\partial [HU]}{\partial x} + \frac{\partial [HV]}{\partial y} = S \quad (3)$$

where, contribution of the discharge of water, evaporation and precipitation per unit area is expressed by S and ζ and H represent water level and depth, respectively.

2.2 Suspended Transport

Advection-diffusion equation (Equation 4) calculates the transport of suspended particles (Deltare, 2011).

$$\frac{\partial c}{\partial t} + \frac{\partial U_c}{\partial x} + \frac{\partial V_c}{\partial y} + \frac{\partial (w - w_s)c}{\partial \sigma} - \frac{\partial}{\partial x} \left(\varepsilon_{s,x} \frac{\partial c}{\partial x} \right) - \frac{\partial}{\partial y} \left(\varepsilon_{s,y} \frac{\partial c}{\partial y} \right) - \frac{\partial}{\partial \sigma} \left(\varepsilon_{s,z} \frac{\partial c}{\partial \sigma} \right) = 0 \quad (4)$$

Where, c is indicating depth averaged mass concentration, w_s is the hindered sediment settling velocity, $\varepsilon_{s,x}$, $\varepsilon_{s,y}$, and $\varepsilon_{s,z}$ are the sediment eddy diffusivities.

2.3 Bed load Transport

In this model, the Van Rijn (1984) equation was used to compute the bed load as stated in equation 5. The wave effects were not considered in the model used in this study.

$$S_b = \begin{cases} 0.053 \sqrt{(s-1)} \cdot g \cdot D_{50}^3 D_*^{-0.3} T^{2.1}; & \text{for } T < 3.0 \\ 0.1 \sqrt{(s-1)} \cdot g \cdot D_{50}^3 D_*^{-0.3} T^{1.5}; & \text{for } T \geq 3.0 \end{cases} \quad (5)$$

where, S_b is bedload transport rate ($\text{kg m}^{-1} \text{s}^{-1}$), S is specific density (ρ_s/ρ), D_{50} is the median particle diameter (m), D_* is dimensionless particle parameter and T is dimensionless transport parameter.

2.4 Profile of the study area

The study reach was selected within two districts of Bangladesh, namely Sirajganj and Tangail, from E463400 m to E486500 m and N680000 m to N730000 m (BTM coordinate) which approximately covers a 50 km reach of the Jamuna River, as shown in Figure 1. The reach considered in this study consisted of an upstream boundary at 30 km upstream of Bangabandhu Bridge and downstream boundary at 20 km downstream of the bridge.

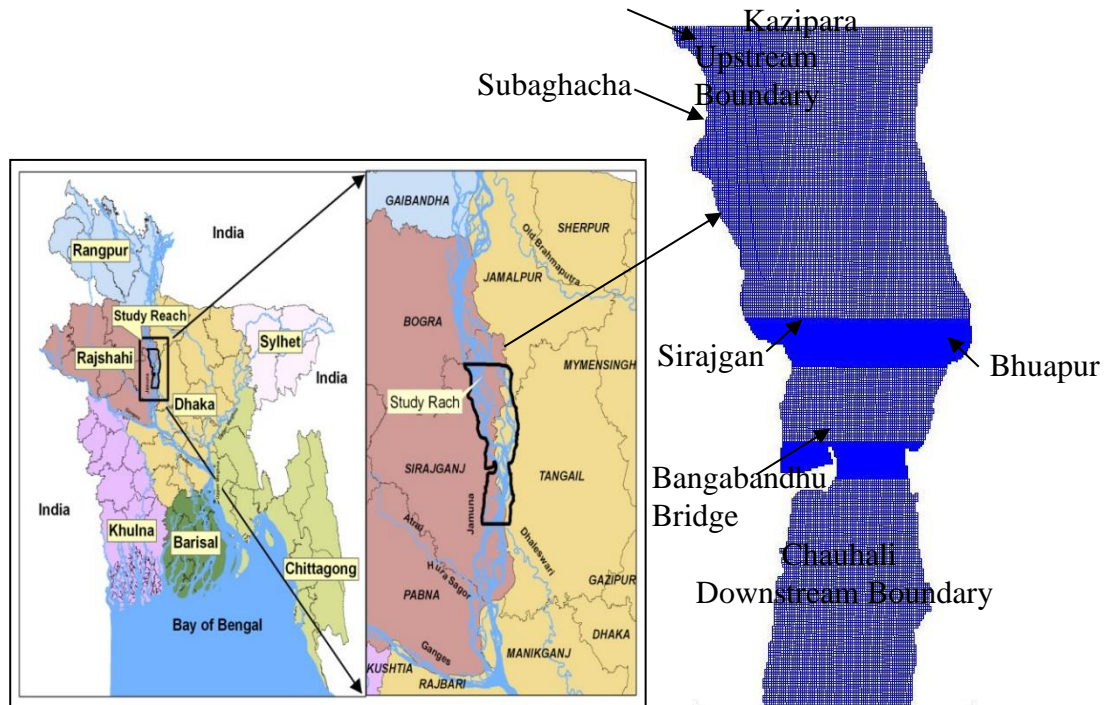


Figure 1. Study Area on the Jamuna River

The number of locations were considered to be crucial in terms of their positions and was specially monitored during the model simulation within the study reach. Sirajganj and Kazipara are located on the right side and Bhuapur is located on the left side of the river at the upstream end and Chauhali is situated at the downstream end of the study reach (Figure 1).

2.3 Model set up

Delft3D numerical model was set up utilizing reliable and sufficient data obtained from IWM to acquire accurate results. Three different basic set-ups for the Delft3D model were prepared in this study. Hydrological data of Jamuna River at April 2010, December 2010 and September 2011 were used for an initial set up to run the model, hydrodynamic calibration and validation, respectively.

2.4 Grid generation

A curvilinear grid was generated, covering the whole selected reach, extending from the upstream border near Kazipara to the downstream border close to Chauhali by Delft3D - RGFRID module to carry out continuous simulation for this study. The total number of grid cells in x and y directions were 299 and 146, respectively, with dimensions of 124 m × 171 m. Before proceeding to further development, orthogonality, aspect ratio, courant number, and grid smoothness were checked to obtain accurate solution. The grid was locally refined to develop high grid resolution in the areas of interest (i.e., near Sirajgonj Hardpoint, Bangabandhu Bridge) in order to attain results faster with accuracy. Surveyed bathymetric data was collected from the Institute of Water Modeling (IWM) and interpolated for all mesh nodes to develop bathymetry by using Delft3D – QUICKIN.

2.5 Boundary setup and Time frame

The flow grid constructed in the model area consists of two open boundaries (upstream & downstream boundaries) and two closed boundaries (east and west bank lines). Time series discharge data created from rating curve at Bahadurabad, located close to Kazipara, were used at the upstream inflow, while boundary and water level data from Sirajganj were applied as downstream boundary near Chauhali. Several simulations were performed by varying time steps and courant number spatially to check the accuracy and stability of the model. In this study, considering one-minute time step, courant numbers were found below 20, which indicates that the model was quite stable for simulation (Deltares, 2011).

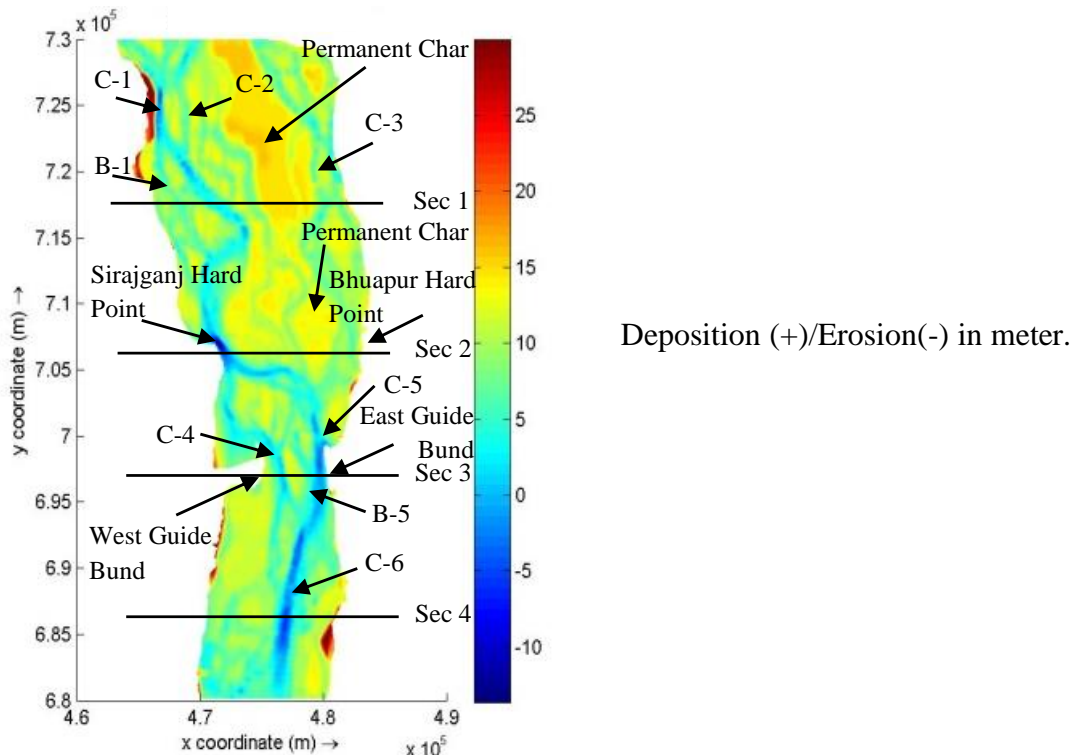


Figure 2. Selected cross section on the study area of the Jamuna River.

3. Results and Discussion

3.1 Simulation of the model

Initially, a bathymetry of April 2010 was taken as the base for simulation as shown in Figure 2. Simulated bathymetries at selected cross-sections 1, 2, 3 and 4 in December 2010 have been compared to that of observed bathymetries. The model

was then simulated for predicting the hydraulic and morphologic responses of the river in the years 2011 and 2012. In the case of morphological simulation, bed levels were computed by upgrading the height of the bed at each time step. Additional features like morphological switch, morphological delay, and morphological time scale factor was included to increase the flexibility.

3.2 Model Calibration and Validation

Roughness and eddy viscosity were the parameters used as a trial to achieve a suitable match with the observed field condition. Manning's roughness coefficient was adjusted with the varying water depth, $n = 0.014$, when water depth was lower than 6 m and $n = 0.025$, when water depth was higher than 6 m. The value of eddy viscosity was considered 1.

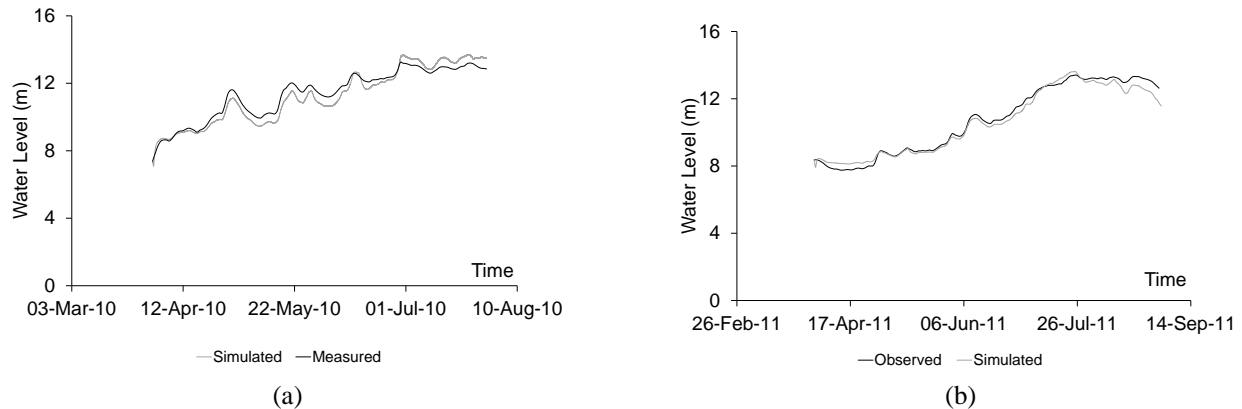


Figure 3. Simulated and measured water levels of Jamuna River for (a) calibration and (b) validation at Sirajganj.

For hydrodynamic calibration, simulated water level elevation was compared with the observed water level elevation at Shirajgonj station for the period of April to July 2010 (Figure 3a). Calibration results showed that the simulated values were within ± 0.6 m of the observed value. The model was also validated at Shirajgonj station after the calibration for the duration of April to August 2011 (Figure 3b) and showed strong agreement conforming the applicability of the model.

3.3 Sensitivity Analysis

A sensitivity analysis was performed to determine the model's performance and how the model responded to several parameter settings. Different parameters, mainly the eddy viscosity and Manning's roughness coefficient, were tested for inspecting the sensitivity of the model, which is shown in Figure 4. Different values considered for the Manning's 'n' regarding char and channel were (0.1 and 0.014), (0.1 and 0.01), (0.025 and 0.014). The value of eddy viscosity taken was 1, 3 and 10 for testing the best match.

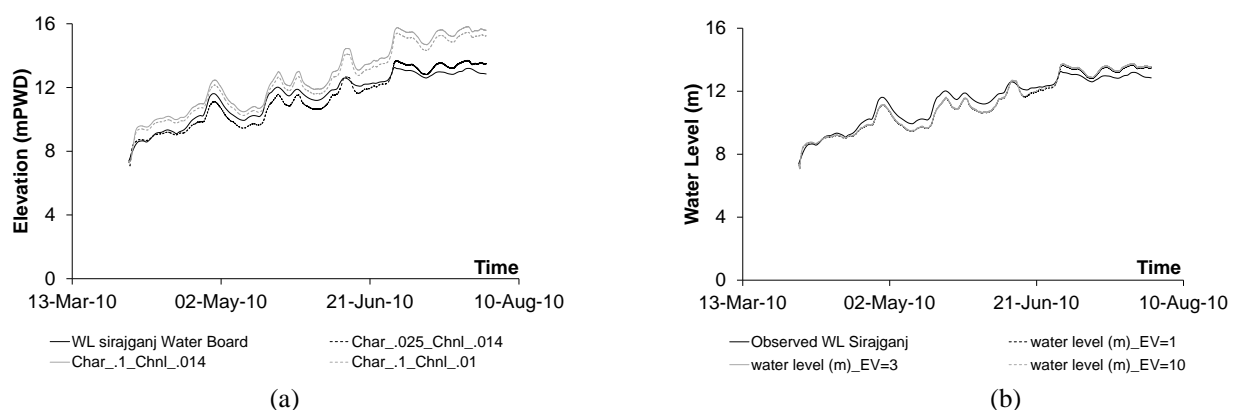
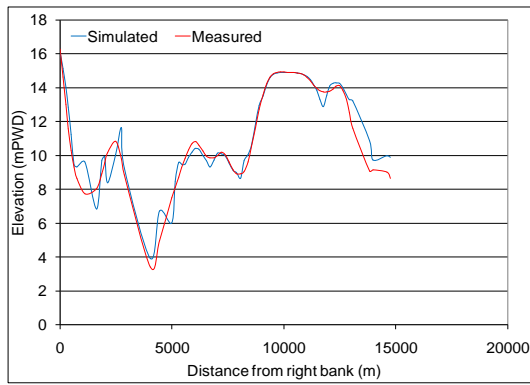


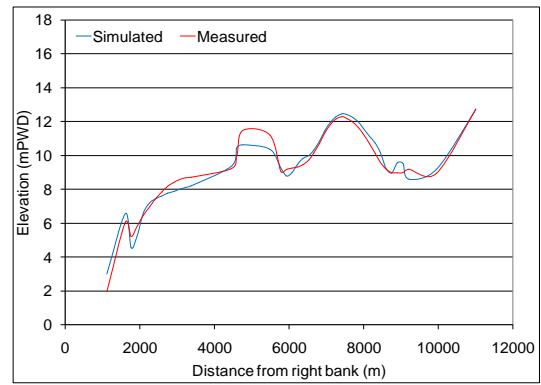
Figure 4. Influence of (a) Manning parameter and (b) Eddy viscosity on amplitudes of water level

3.4 Observed and Simulated Bed Elevations

For sediment model, a comparison was made between the simulated bathymetry of December 2010 with the observed bathymetry in December 2010. The median size of bed material was considered 0.20 mm for morphological computation. Comparison of various sections are shown in Figure 5. Simulated bed elevations adequately matched with the measured bed elevations.

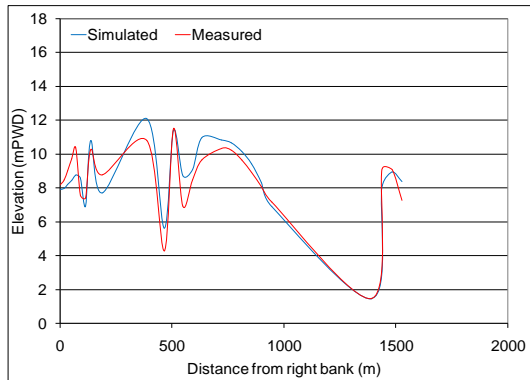


(a) Section 1

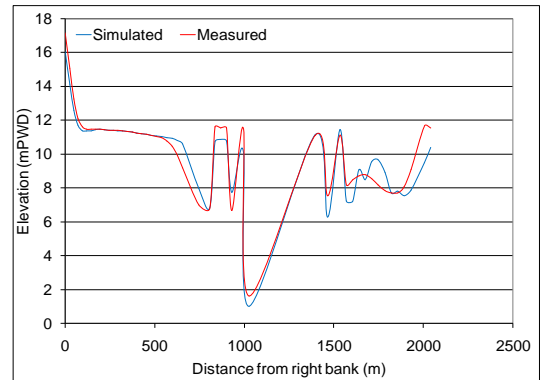


(b) Section 2

Figure 5: Comparison of simulated and observed cross-Sections (contd.)



(c) Sec 3



(d) Sec 4

Figure 5. Comparison of simulated and observed cross-Sections

3.5 Variation in Velocity and Sediment Transport

Sediment transport of the river varies spatially, influenced by the local bathymetry and associated with discharge and velocity. From Figure 6 and 7, it can be visualized that sediment transport rates for the two consecutive years (2011 and 2012) were greater during monsoon compared to the dry season, as discharge increased in wet season along with flow velocity. Velocity seemed to be high near Shuvagacha, Sirajganj hardpoint, Bhuapur hardpoint, Bangabandhu bridge area (closer to east & west guide bands) and downstream of the selected reach in both wet and dry season. These zones appeared to be eroded and carried more sediment. The flow velocity along with sediment transport increased in the successive years; except in Bhuapur hardpoint. In 2012, deposition took place in this location due to the reduction of velocity, as well as the sediment transport rate compared to 2011. Several distributary channels appeared in July 2012 due to significant erosion. The channels bifurcated from Sirajganj station, showed lower flow velocity compared to other locations and consequently possessed lower sediment transport capacity.

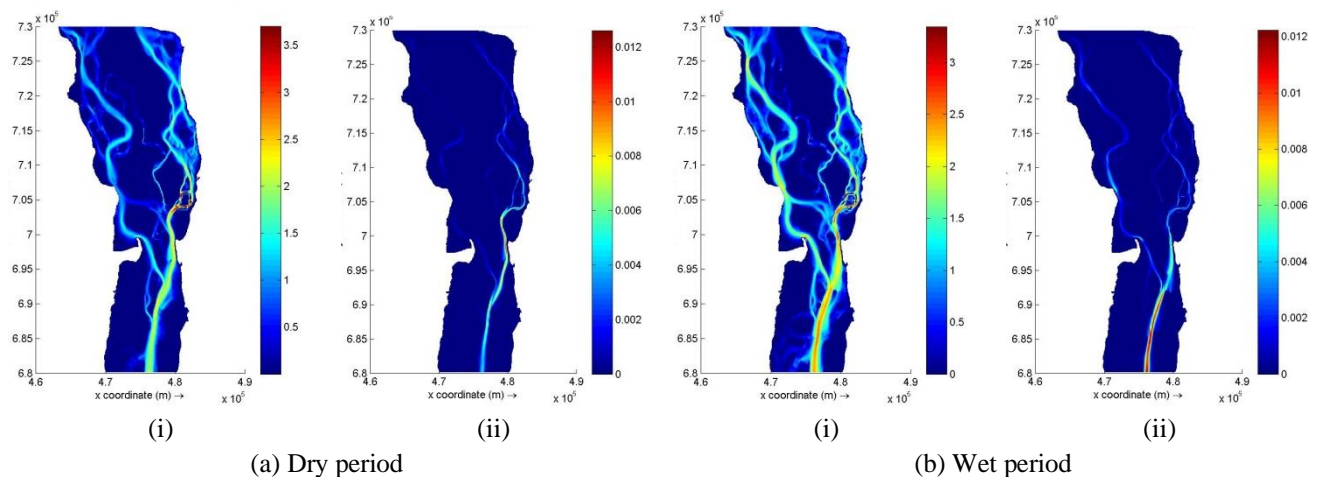


Figure 6. Plan view of Jamuna river for (i) depth averaged velocity and (ii) sediment transport in 2011

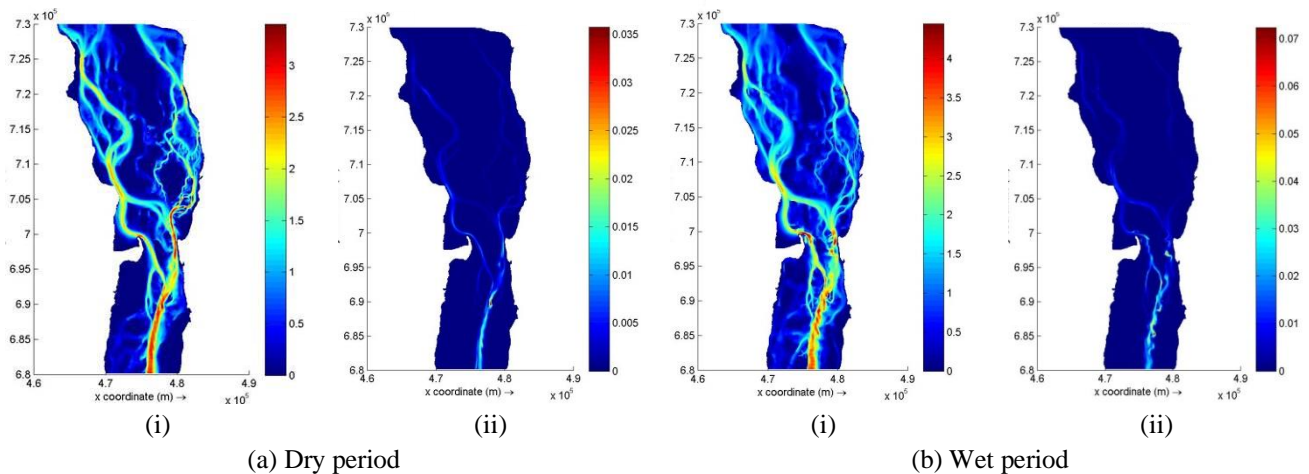


Figure 7. Plan view of Jamuna river for (i) depth averaged velocity and (ii) sediment transport in 2012

3.6 Estimation of Erosion and Deposition

Cumulative erosion or deposition all over the river reach was estimated by using the Delft3D model, for two consecutive years, i.e. 2011 and 2012. Figure 8 reveals that the three morphological years had similar types of erosion and deposition patterns. Deposition near the char areas and development of deep channels were some of the significant morphological features.

In section 1 (Figure 2), a char existed between channel C-1 and a branch channel, appeared from C-1 which is channel B-1. Maximum flow and velocity passes through C-1 due to its bending nature relative to B-1. Severe erosion took place on both of the channels. Superimposed cross-sections indicate both channels shifted westward from their bank lines and resulted in a deeper and narrower channel, due to velocity increment in C-1 & B-1, from 2.24 m/s to 2.98 m/s and 1.2 m/s to 2.3 m/s respectively, in September 2011 and 2012. The channels became narrower as some amount of deposition took place in their respective bank lines (Figure 9(i)).

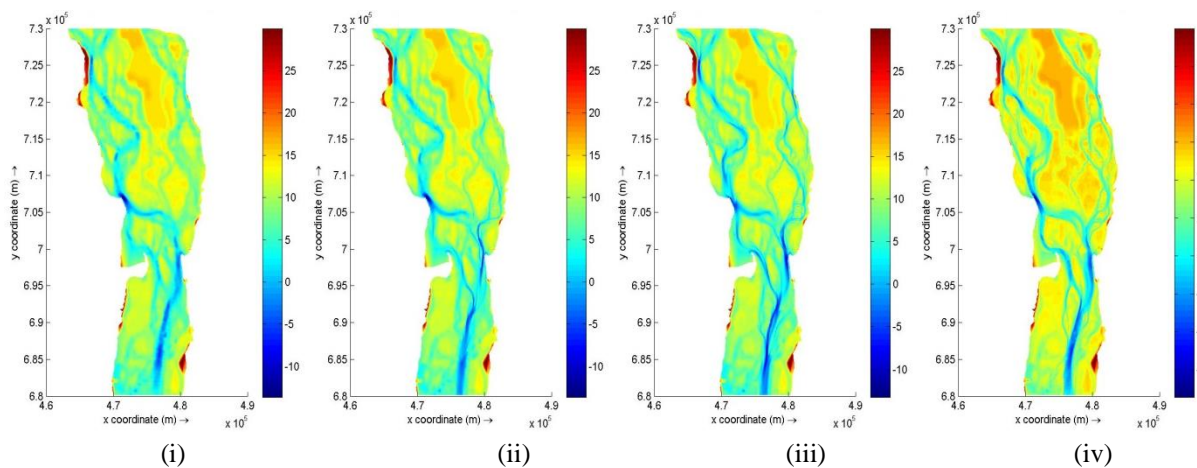


Figure 8. Plan view of Jamuna river for (i) Initial bed level in April 2010 and Simulated bed level in September (ii) 2010 (iii) 2011 (iv) 2012

Section 2 was selected near Sirajganj district, where the channel was wide and shallow in April 2010. In the subsequent years, the channel experienced severe erosions of about 5 m due to the increase of velocity from 2.38 m/s to 3.77 m/s and a shifting of erosion westwards. Also, in September 2012, erosion and deposition took place on both sides of the permanent char due to the fluctuation of velocity (Figure 9(ii)). Overall the width of the char decreased and some shallow and narrow tributary channels appeared on the erosion areas.

Section 3 lies in the portion of the Bangabandhu Bridge and the channels are indicated as C-4 and C-5. Widths of both channels reduced during the monsoon period in the year 2010 and 2011 as deposition took place on their banks due to the

reduction of water velocity. However, from the superimposed cross-sections, it is evident that both channels had undergone severe erosion in the year 2012 due to velocity increment from 2.34 m/s to 3.37 m/s and from 2.36 m/s to 3.69 m/s, respectively (Figure 9 (iii)). Hence, both of the channels changed their direction in the east and west, respectively. A small branch channel B-5 appeared which was also eroded. Besides the erosion process, deposition also took place, about 4 m on both sides of the char that existed between C-4 and C-5 (Figure 9(iii)).

Section 4 passes through the channel located in the downstream portion of the river reach, near to Chauhali. This channel C-6 underwent severe erosion in September 2012 due to increased velocity and the channel was shifted westwards, resulting in a deeper and narrower channel. A huge amount of deposition of around 7.5 m and 3 m took place on both sides of the channel in September 2010 due to the reduction of velocity (Figure 9(iv)). In September 2011, the velocity reduced to 2.05 m/s and again increased abruptly to 3.22 m/s in September 2012. Average erosion and deposition of observed and simulated bathymetries at all selected cross-sections for the year 2010 and 2011 are summarized in Table 1.

Figure 10 (middle portion of the selected reach) shows the simulated images of the bed level in September 2011 using both Delft3D and Mike 21 (IWM, 2011). It can be seen that Delft3D model predicted river bed degradation patterns near Shirajganj Hard Point and east guide bund, which are very similar with the predicted river bed degradation by Mike 21. Aggregation can be observed near the bank lines. It also can be observed that in both the pictures, the significant erosion affected zones are at the same locations of Shirajganj and near the east guide bund of the main channel. The elevations of these zones are below 0 mPWD, whereas, in case of the tributaries, the ranges are from 0 mPWD to 5 mPWD. Also, elevations at the big char areas are above 14 mPWD.

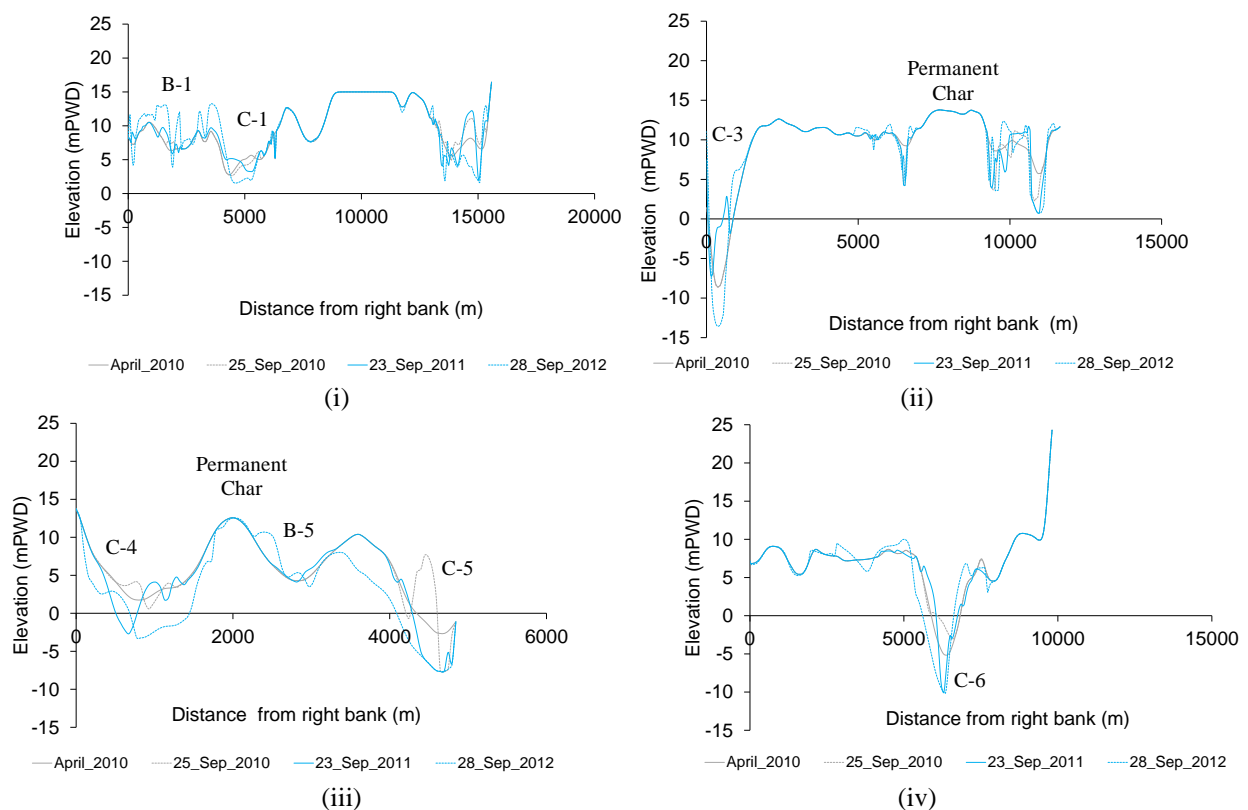


Figure 9. Elevations at cross-section (i) 1, (ii) 2, (iii) 3 and (iv) 4

Table 1 Average Erosion and Deposition of Observed and Simulated Bathymetry

Cross-section	December 10		September 11	
	Observed (m)	Simulated (m)	Observed (m)	Simulated (m)
Section 1	0.205	0.167	0.263	0.173
Section 2	0.002	0.003	-0.024	-0.039
Section 3	0.074	0.051	-0.882	-0.688
Section 4	-0.021	-0.052	-0.280	-0.354

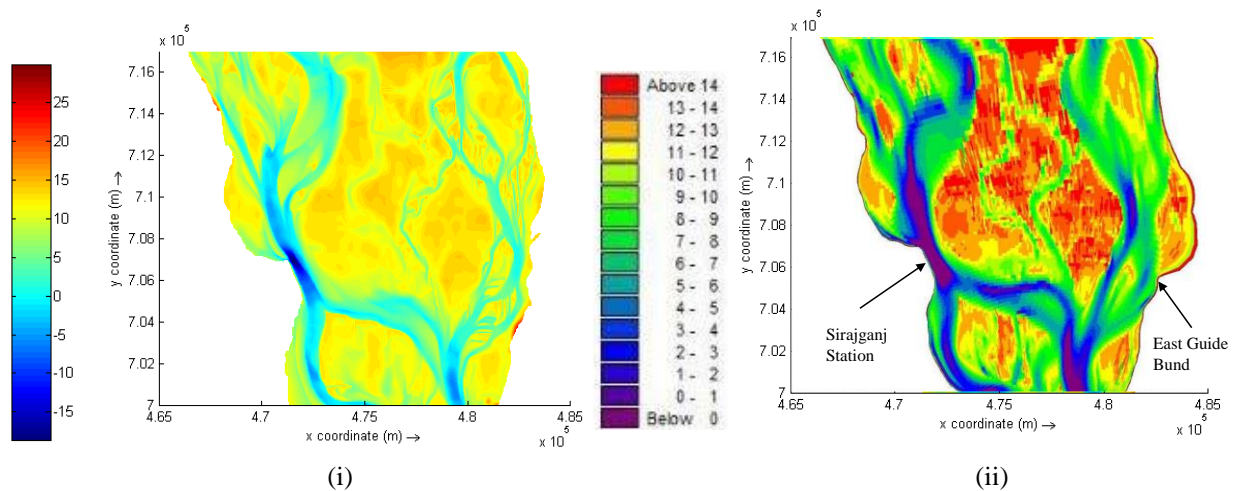


Figure 10. Comparison of the simulated bathymetry in September 2011 by (i) Delft 3D and (ii) Mike21

4. Conclusion

The aim of this research was to determine the morphological changes of the Jamuna river using a Delft3D model. Calibration and validation were carried out effectively against water surface elevations at Sirajganj. An attempt was made to calibrate only the high flow data as most of the morphological activities occur during this period, and the result obtained from the processes adequately matched with the observed values. This analysis was essential to understand the trends of river shift, as well as to identify the zone of high risks. More materials were deposited adjacent to the char areas which were surrounded by the channel branches. Considering the changes during the last two years, appreciable deposition was absent, but a large amount of erosion was observed in the west channel compared to east side of the river. Relation between the sediment transport and depth average velocity was established. A higher velocity increased the rate of sediment transport, forms erosion and the shifting of channels. Plan form analysis revealed that the river appreciably shifted towards the east and west directions in the consecutive years. The shifting activity of the river course, and its successive erosion, as well as accretion processes, caused the destruction and formation of new land continuously. Also, the simulated results by Delft3D model was compared with the results obtained from the Mike 21 model, which is a widely used commercial coastal modelling software. The results obtained from both models showed strong agreement, which demonstrated the strong acceptability of using Delft3D.

5. Acknowledgements

Authors are grateful to all the officials of the River Engineering Division, IWM, Bangladesh for their help and cooperation in collecting the required data and information and also to Deltares for making Delft3D an open source program.

6. References

- Baki, A. B. M., & Gan, T. Y. (2012). Riverbank migration and island dynamics of the braided Jamuna River of the Ganges–Brahmaputra basin using multi-temporal Landsat images. *Quaternary International*, 263, 148-161.
- Bhuiyan, M. A., Rakib, M. A., Takashi, K., Rahman, M. J. J., & Suzuki, S. (2010). Regulation of brahmaputra-jamuna river around jamuna bridge site, Bangladesh: geoenvironmental impacts. *Journal of Water Resource and Protection*, 2(02), 123.
- Crosato, A., Desta, F. B., Cornelisse, J., Schuurman, F., & Uijttewaai, W. S. (2012). Experimental and numerical findings on the long-term evolution of migrating alternate bars in alluvial channels. *Water Resources Research*, 48(6).
- Crosato, A., Mosselman, E., Beidmariam Desta, F., & Uijttewaai, W. S. (2011). Experimental and numerical evidence for intrinsic nonmigrating bars in alluvial channels. *Water Resources Research*, 47(3).
- Deltares (2011), Delft3D-FLOW User Manual: Simulation of multi-dimensional hydrodynamic flows and transport phenomena, including sediments. Version 3.15, revision 14499. pp: 373,356.

- Edmonds, D. A., & Slingerland, R. L. (2007). Mechanics of river mouth bar formation: Implications for the morphodynamics of delta distributary networks. *Journal of Geophysical Research: Earth Surface*, 112(F2).
- Goodbred Jr, S. L., & Kuehl, S. A. (2000). Enormous Ganges-Brahmaputra sediment discharge during strengthened early Holocene monsoon. *Geology*, 28(12), 1083-1086.
- Hossain, T. B. (1997). Study of aggradation and degradation of the Khowai River.
- Hoover Mackin, J. (1948). Concept of the graded river. *Geological Society of America Bulletin*, 59(5), 463-512.
- IWM (2011). Monitoring of Hydraulic and Morphological conditions of Jamuna River for the safety of Bangabandhu Bridge during the year, IWM, Dhaka.
- Jagers, B. (2003). Modelling planform changes of braided rivers, PhD Thesis, Universiteit Twente.
- Jenkins, G. P., & Shukla, G. P. (1997). Linking east and west Bangladesh: the Jamuna Bridge project. *The Canadian Journal of Program Evaluation*, 12, 121.
- Jain, S. C., & Park, I. (1989). Guide for estimating riverbed degradation. *Journal of Hydraulic Engineering*, 115(3), 356-366.
- Jaramillo, W. F., & Jain, S. C. (1984). Aggradation and degradation of alluvial-channel beds. *Journal of hydraulic engineering*, 110(8), 1072-1085.
- Kuehl, S. A., Hariu, T. M., & Moore, W. S. (1989). Shelf sedimentation off the Ganges-Brahmaputra river system: Evidence for sediment bypassing to the Bengal fan. *Geology*, 17(12), 1132-1135.
- Lesser, G. R., Roelvink, J. V., Van Kester, J. A. T. M., & Stelling, G. S. (2004). Development and validation of a three-dimensional morphological model. *Coastal engineering*, 51(8-9), 883-915.
- Mount, N. J., Tate, N. J., Sarker, M. H., & Thorne, C. R. (2013). Evolutionary, multi-scale analysis of river bank line retreat using continuous wavelet transforms: Jamuna River, Bangladesh. *Geomorphology*, 183, 82-95.
- Mosselman, E. (2006). Bank protection and river training along the braided Brahmaputra-Jamuna River, Bangladesh. *Braided rivers: Process, deposits, ecology and management*, 36, 279-287.
- Rijn, L. C. V. (1984). Sediment transport, part II: suspended load transport. *Journal of hydraulic engineering*, 110(11), 1613-1641.
- Raju, K. G. R., (1980). "Aggradation and Degradation", Proceedings of the International Workshop on Alluvial River Problems held at Roorkee, India, pp. 18-20.
- Thorne, C. R., Russell, A. P., & Alam, M. K. (1993). Planform pattern and channel evolution of the Brahmaputra River, Bangladesh. *Geological Society, London, Special Publications*, 75(1), 257-276.
- Van der Wegen, M., & Roelvink, J. A. (2008). Long-term morphodynamic evolution of a tidal embayment using a two-dimensional, process-based model. *Journal of Geophysical Research: Oceans*, 113(C3).
- Wang, L., Zimmermann, N., Trouw, K., De Maerschalck, B., & Vanlede, J. (2014). Numerical modelling of long-term morphology in the surf zone of the Belgian coast. *Coastal Engineering Proceedings*, 1(34), 42.

Impact of urbanization on CO₂ and TVOC in an oasis city in Saudi Arabia

Muhammad Muhitir Rahman^{1,*}, Ziad Shatnawi¹, Md Kamrul Islam¹, Ammar Al-Shayeb¹

¹Department of Civil and Environmental Engineering, College of Engineering, King Faisal University, Al-Hofuf, Al-Ahsa, Saudi Arabia

*Corresponding author's email: 18317116@student.westernsydney.edu.au

Peer review history

Manuscript submitted: 4 July 2019

Review process completed: 15 October 2019

Manuscript finally accepted: 20 October 2019

Handling Editor: Professor Ataur Rahman

Abstract: In the last decade, urbanization in the oasis city of Al-Hofuf, Saudi Arabia has considerably increased in terms of urban population, urban housing and the number of personal automobiles. Al-Hofuf is located in an arid region where different sources of atmospheric pollution occur including heavy oil combustion, suspended soil, industrial emissions, and traffic emissions. Air pollution in terms of carbon dioxide (CO₂) and total volatile organic carbon (TVOC) was investigated to examine the impact of

urbanization. Four key urban locations were selected for CO₂ and TVOC measurement and results were compared with a rural site. Variation of population, housing units and number of cars were reviewed using available data and the trend of air pollution was observed. Results show that CO₂ and TVOC are within the allowable limit in Al-Hofuf in spite of rapid urbanization in the last decade. The measured CO₂ at all the sites varied in the range of 330-430 ppm and TVOC varied between 153 and 341 ppb. CO₂ and TVOC showed an increasing pattern between 2014 and 2018, which is 1.1 times and 3.9 times higher respectively, in the four-year period. Based on the monitored data in five locations, spatial distribution of pollutants is proposed, which can be used to identify pollution hotspots in Al-Hofuf city.

Keywords: Al-Hofuf; Oasis city; Urbanization; Air pollution; Greenhouse Gas (GHG).

1. Introduction

Air pollution is one of the major issues in rapidly growing regions due to its impact on atmosphere and human health. Air pollution may be sourced because of natural, anthropogenic or secondary reasons. Natural sources are not associated with any human activities, i.e. dust, volcanic eruptions, wildfire. Anthropogenic sources are associated with human activities, i.e. urbanization, industrialization, deforestation, construction of roads and houses, burning of fossil fuels etc., whereas secondary sources are formed by both natural and anthropogenic activities (Hickey et al., 2014).

In arid regions, urbanization contributes to the increase of carbon dioxide in natural ecosystems, resulting in less precipitation and increased temperature due to a 'heat island' effect (Koerner and Klopatek 2002). The heat island effect refers to the phenomenon of a warmer area being created compared to its surrounding because of human activities. Higher levels of CO₂, as much as 50%, can occur in urban areas compared to surrounding non-urban areas (Koerner and Klopatek 2002). CO₂ is regarded as a greenhouse gas (GHG), resulting from the combustion of fossil fuels. In urban areas, the combustion of fossil fuels mainly occurs from the transport sector. Automobile emissions released are highly dependent on the type of fuel and the process itself, however, CO₂ and volatile organic carbon (VOC) are among some important pollutants (EEA, 2011). The product of the combustion of hydrocarbons yields CO₂ and H₂O. Carbon monoxide is generated in all hydrocarbon reactions with oxygen as an intermediate, which then further reacts with oxygen to form CO₂. The reaction requires appropriate temperature and availability of oxygen for complete oxidation. If complete oxidation is not met either due to lack of reaction activation energy, low temperature or poor oxygen presence, substantial emissions of carbon monoxide (CO) may occur (EEA, 2011). In Saudi Arabia, in the year 2000, the total emissions of CO₂ were estimated as 2.6 x 10⁵ Gg, of which 92.1% were attributed to the energy sector, and the contribution made by transport sector was 21% (Rahman et al., 2017). The impact of urbanization on air quality is also reported by several other researchers (e.g. Zhang et al., 2017; Gately et al., 2015; Al-Mulali et al., 2013; Bereitschaft and Debbage, 2013; Gratani and Varone, 2005; Cole and Neumayer, 2004).

Total volatile organic compound (TVOC) on the other hand is a group of organic chemical compounds and may be found in ambient air or in the emission of some substances such as natural gas or man-made materials. It can be either gas or

vapour and can enter a human body by breathing. VOC concentration exceeding the recommended limit may hamper eyes and the respiratory tract of humans, induce distortions, and can even cause cancer (USEPA, 1998). Also, it may have an effect on animals and plants. TVOCs are considered as one of the causes of smog and it may have impacts on water and soil (Deng et al., 2018). TVOCs have effects on the environment depending on the VOCs composition and its concentration (Kettrup and Risse, 1997).

Typically, TVOCs may consist of VOCs of different chemical classes including aliphatic hydrocarbon, halogenated hydrocarbon, carbonyl compounds, alcohols, aromatic hydrocarbons and chlorinated hydrocarbons, terpenes, glycol, ketones and esters (Al Khulaifi et al., 2014; Tanaka-Kagawa et al., 2005). In many oil rich middle east countries, VOCs may result from flaring activities and crude oil facilities, refineries, petrochemical plants, power and desalination plants and from the traffic and transport sector (Al Khulaifi et al., 2014). Also, outdoor VOCs may be sourced from waste disposal areas and wastewater treatment plants. Outdoor VOC levels can be affected by seasonal meteorological conditions (i.e. temperature, humidity and wind speed), and types and nature of surrounding emission sources (Tong et al., 2013; Jia et al., 2008).

In Saudi Arabia, during the last five decades, a considerable shift towards urbanization was observed. According to Abdelatti et al. (2017), the urban population in Saudi cities has increased from 49% in 1974 to 74% in 1992 and to 80% in 2004, of the total population; the urban population in Saudi Arabia reached 25,612,976 in 2014, with annual growth rate of 2.5 %, and the proportion of the people living in the largest city reached to 24.2%. According to the World Bank (2016), the rural population in Saudi Arabia decreased from 23.4% in 1990 to 17.1% in 2014. Reasons for this urbanization may be that urban residents get better education, healthcare facilities, easy access to social services, as well as social and cultural participation (Abou-Korin and Al-Shihri 2015), which are not easily accessible by rural residents. With the increase of the urban population, the number of passengers, as well as commercial vehicle sales have increased. According to Statista (2019), the number of vehicle sales in Saudi Arabia increased more than 45% in a decade from 563,000 in 2005 to 830,000 in 2015. Shift of population and thus urbanization caused the increased number of automobiles and industries in the cities, which may have impact on urban air pollution.

Air quality in big cities of Saudi Arabia was monitored by different researchers and organizations, i.e. Al Harbi et al. (2014) monitored O₃, CO, NO₂, SO₂ and H₂S at five air quality monitoring network stations of King Abdulaziz City for Science and Technology (KACST), in Riyadh city. The authors concluded that Riyadh city air was in good condition for 71% of the time during the study period. Al-Jeelani (2009) investigated air quality for similar parameters in Makkah city and found that concentrations of nitrogen oxides and carbon monoxide increased at the starting hours of the day. Salama et al. (2017) investigated air quality in the Eastern Province for CO₂ and VOC in addition to the other stated parameters and concluded that the pollutants exceeded the recommended exposure limit during morning and noon time. Radaideh and Shatnawi (2015) investigated the air quality in Al-Hofuf city in the Eastern Province and reported a strong correlation between indoor and outdoor air quality. Most of the mentioned research reported overall ambient air quality, however more research is needed to examine the relationship between urbanization and air quality in the Al-Ahsa region. Therefore, specific aims of this research were to (a) monitor ambient air quality in terms of CO₂ and TVOC using ground-based air quality monitoring device at five locations of Al-Hofuf city and (b) evaluate the impact of urbanization on air quality.

2. Methodology

2.1 Study Area

The study was conducted in five different places in Al-Hofuf city (Figure 1). Two site-types, urban and rural were selected for this study to carry out air quality measurements and to assess varying air quality. Four of the places were selected from urban areas and one from a rural area. All selected sites are residential areas except the rural area. The selected urban sites were Village Market, Riyadh road (near Al-Rumansiah), Riyadh Road (near Al-Mujjammah), Qaisariyah Market and the rural site was in Al-Jaffer. The rural site was selected far away from the urban areas.

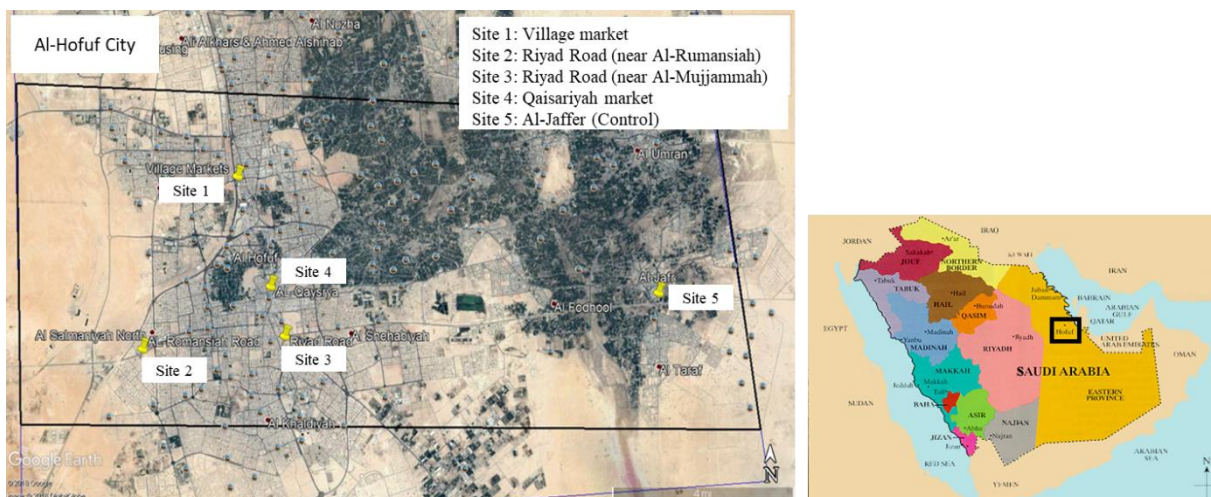


Figure 1. Monitoring sites in Al-Hofuf city

2.2 At site monitoring and spatial distribution

The measurement at the sites were conducted beside the road during the peak hour. Peak hour was assumed to be after 4 pm in week days. Peak hour was selected to measure the maximum pollution due to increased number of cars compared to off-peak times. In this study, no off-peak hour reading was taken. The monitoring was conducted two times in each location (except Al-Jaffer) during November and December 2018 (Table 1). GrayWolf® analyzer was used to monitor CO₂, TVOC, temperature, and relative humidity. GrayWolf® is a mobile analyzer which provides fully integrated systems for measuring air quality using probes (Wolf sense, 2012). The analyzer was set in a place from where it was easy to monitor the number of cars; most of the time near the traffic signal. The analyzer was powered by a portable DC converter. The height of the analyzer was maintained as close as possible to the average height of human noses. This was done to simulate the pollution exposure to human. A wooden table was used to raise the height of the analyzer. The number of cars were counted manually. Traffic was counted in one way, which was closer to the monitoring location. In this study, geographic information system (GIS) was used to present spatial distribution of the collected data and to pinpoint the air pollution hot spot. Contour lines gave better understanding of the pollution exposure covering the Al-Hofuf city from on-site measurement data of five sites.

2.3 Statistical analysis

The results obtained were statistically analysed using the SPSS Statistics 19.0 package. One-way ANOVA and the t-test was carried out to explain the result. Pearson's correlation coefficient was determined to evaluate correlation between pollutant and meteorological parameters, which is widely considered as the degree of intensity and the direction of correlation by many researchers. The probability value (*p*-value) less than 0.05 are considered significant results (Kim et al., 2007; Han et al., 2006).

The measured CO₂ at all the sites varied between 330-430 ppm, which is within usual limit of ambient air. Generally, 0.03% CO₂ in the ambient air is considered safe for human health (Cetin and Sevik 2016). In all the sites, the level of CO₂ was about 50% less than a frequently polluted place, i.e. bus terminal (Salama et al., 2017, shown in Table 1). A similar pattern was observed for TVOC. It should be noted that TVOC in all urban sites was almost double than the control site (Al-Jaffer), except Qaisariyah Market site. This may be because of the very minimal or non-existent traffic near the control site compared to urban sites. However, no correlation was observed with the number of automobiles passing the monitoring stations and the level of TVOC. On an average, number of automobiles passing the monitoring point of Sites 1, 2, 3, and 4 were 48, 42, 41 and 36 vehicles/min, respectively. Therefore, it could not be confirmed that automobiles were solely responsible for the measured level of CO₂ and TVOC in the urban sites. Another source of the ambient air pollutants may be the smoke dispersed from date palm farms in Al-Hofuf. Al Ahsa oasis caters an estimated 25,000 to 27,000 acres of date palm gardens (Vidal, 1954). It is a common practice in Al-Hofuf to burn dry date tree branches, which was observed during the monitoring events.

Table 1. At-site monitoring results of pollutants and meteorological parameters

Site description	Month of sampling	CO ₂ (ppm)	TVOC (ppb)	RH(%)	Temp (°C)
Village Market (25°23'25.7"N 49°32'45.5"E)	November 2018	*415.84±8.22	336.69±50.93	32.33±0.09	29.48±0.1
Riyad road (Rumansiah) (25°21'29.6"N 49°32'50.0"E)	November 2018	434.1±11.34	304.04±43.63	31.62±0.09	26.27±0.27
Riyad road (Mujjammah) (25°21'53.2"N 49°35'06.1"E)	November 2018	331.68±11.72	341.4±41.49	62.89±0.51	25.76±0.08
Qaisariyah Market (25°22'39.4"N 49°35'20.3"E)	November 2018	396.24±8.18	177.43±25.73	43.32±0.58	26.86±0.48
Jaffer (Control site) (25°22'43.7"N 49°44'33.8"E)	December 2018	328.26±3.95	152.96±30.52	49.18±1.49	25.05±0.31
Salama et al. (2017)	Feb 2014- Jun 2014	664-791	170-450	49-51	20-25

*Mean ± SD

Table 2. Testing the statistical significance of the observations by t-test

Parameters	Compared site	p-value	Differences between measurements
CO ₂ (ppm)	Site1-Site5	< 0.001	Extremely significant
	Site2-Site5	< 0.001	Extremely significant
	Site3-Site5	0.003	Significant
	Site4-Site5	< 0.001	Extremely significant
TVOC (ppb)	Site1-Site5	< 0.001	Extremely significant
	Site2-Site5	< 0.001	Extremely significant
	Site3-Site5	< 0.001	Extremely significant
	Site4-Site5	< 0.001	Extremely significant
Temperature (°C)	Site1-Site5	< 0.001	Extremely significant
	Site2-Site5	< 0.001	Extremely significant
	Site3-Site5	< 0.001	Extremely significant
	Site4-Site5	< 0.001	Extremely significant
RH (%)	Site1-Site5	< 0.001	Extremely significant
	Site2-Site5	< 0.001	Extremely significant
	Site3-Site5	< 0.001	Extremely significant
	Site4-Site5	< 0.001	Extremely significant

Note: Site 1: Riyad Road (near Al-Mujjammah); Site 2: Riyad Road (near Al-Rumansiah);
Site 3: Village market; Site 4: Qaisariyah market; Site 5: Al-Jaffer (Control)

The at-site monitoring results confirmed higher pollutant levels in urban sites than the control, however, since the monitoring was not conducted continuously, statistical analyses could be an appropriate way to provide statistical significance of the observations made in this study between the urban and control sites. For this purpose, a t-test was carried out between pairs of urban as well as control sites, for all the parameters (Table 2). Table 2 statistically compares the differences between the selected two sites and identifies whether it is extremely significant ($p < 0.001$), significant ($p < 0.05$) or insignificant ($p > 0.05$). Results show that all the observed parameters in urban sites were significantly different than that of the control site, which confirms the acceptability of monitoring results. In addition, Pearson's correlation coefficient was evaluated between measured pollutants and meteorological parameters. It was found that CO₂ is highly correlated to RH ($p < 0.001$) and temperature ($p < 0.001$) and TVOC is highly correlated to temperature ($p < 0.001$). Poor correlation was found between TVOC and RH (p -value = 0.062). Similar observation was made by Tong et al. (2013) and Jia et al. (2008).

At-site pollutant measurement of five sites were used to generate spatial distribution of CO₂ and TVOC over the whole study area. This was done using contour lines by GIS software. The distribution is shown in Figure 2. The spatial distribution of pollutants will help to identify the overall extent and direction of pollution hot spots in the study area. In the case of CO₂ (Figure 2a), more pollution was observed on north of Riyadh Road towards Village Market and less pollution towards the control site at Al-Jaffer. The present data sets provide an idea of the average status of the measured pollutants, however, more data points are needed for an accurate representation of the CO₂ distribution in this area. Similar observation was made for TVOC (Figure 2b).

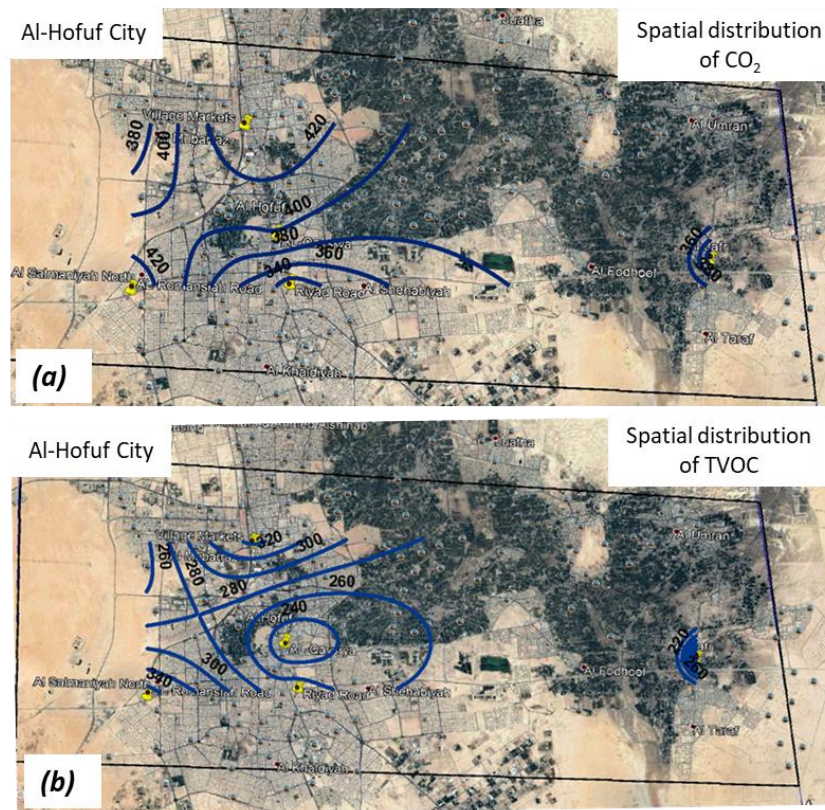


Figure 2. Spatial distribution of (a) CO₂ and (b) TVOC in the study area along with the control site

3.2 Urbanization and air quality

Impact of urbanization in Al-Hofuf on air quality was assessed based on population, number of vehicles and number of houses. The data was collected from the General Authority for Statistics (GAS). According to GAS (2019), the population of Al-Ahsa in 2004 was about 907,734 people, including Saudis and non-Saudis. In addition, the population of Al-Ahsa in 2010 was about 1,067,691 people, including Saudis and non-Saudis. This was an annual increase of 2.94%. Based on this, the growth rate projected population in Al-Ahsa in 2014 and 2018 was 1,174,329 and 1,280,967, respectively. In the Al-Ahsa province, a major portion (62-63%) of the population live in Al-Hofuf and Al-Mubarraz city (Abdelatti et al., 2017). According to Abdelatti et al. (2017), in Saudi Arabia, the number of people living near urban centers increased from 49% in 1974 to 80% in 2004. As a result, the number of traditional houses in this area reduced and to cope with the demand, the number of urbanized accommodation (i.e. two and three floors apartments) increased. From 1994 to 2011, the proportion of the apartments increased from 66.2% to 85.8% (Al-Ahsa Municipality, 1998) of the total houses. According to GAS (2019), the number of apartments in 2004 and 2010 was 28,043 and 58,395, respectively. The projected number of apartments in 2014 and 2018 are shown in Figure 3. An important aspect of urban housing related CO₂ can be attributed to the use of grid-electricity for electric stoves and heaters, lighting, air conditioning and other electric appliances. The remainder of household emissions are due to the on-site burning of fuels. With the increase of urban population and housing, the number of cars have also increased from 99,479 in 2004 to 2,388,49 in 2018 (Figure 3). In reality, automobiles are the most important urbanization factor causing more air pollution due to its direct production of GHG. According to Rahman et al. (2017), a strong correlation ($r^2 > 0.995$) was observed between the number of registered cars and energy consumption, thus production of GHG. The authors also found a considerable correlation among GHG

production, urban population and Gross National Income. Overall, the registered car ownership in Saudi Arabia is 209 vehicles per 1000 people. In Al-Ahsa, car ownership increased from 110 vehicles in 2004 to 149 per 1000 people in 2010 (GAS, 2019). This increase of car ownership represents the broad scenario in Saudi Arabia, where only 2% of the total population uses public transport, while 85% relies on personal vehicles for commuting purposes (Al-Fouzan, 2012).

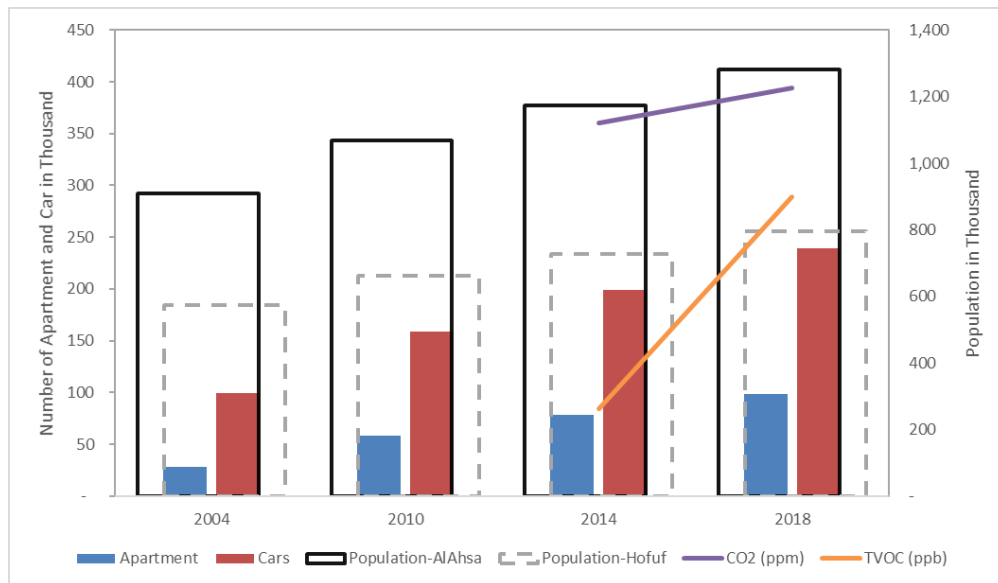


Figure 3. Trend of urbanization and air quality in Al-Hofuf, Al-Ahsa

No doubt, urbanization in Al-Hofuf in terms of population, urban housing and cars has an impact on air quality, but it was not possible to get a clear correlation between factors of urbanization and the air quality due to lack of multi-year data. However, available literature data reported by Radaideh and Shatnawi (2015) was plotted along with this study to get an impression of the trend of CO₂ and TVOC in the study area. It is worth mentioning that Radaideh and Shatnawi (2015) conducted the monitoring in a similar location as the current study. The trend line of CO₂ shows an increase of 1.1 times higher value in four years, which is 3.9 times that of TVOC. Further monitoring at the same location can support such trends of air pollution.

3. Conclusion

Ensuring a clean and sustainable environment is one the goals of Saudi Vision 2030. Urbanization is a positive indicator for a nation's economic and social development; however, this should be commensurate to the national policy for a sustainable environment. Unplanned urbanization in terms of population, housing and transportation may hamper such an environment. It can be concluded from the study that:

- CO₂ and TVOC are within the allowable limit in Al-Hofuf in spite of rapid urbanization in the last decade; the measured CO₂ at all the sites varied in the range of 330-430 ppm and TVOC varied between 153 and 341 ppb;
- CO₂ and TVOC showed an increasing pattern, which is 1.1 times and 3.9 times higher respectively, in a four-year period; and
- Based on the monitored data in five locations, spatial distribution of pollutants is proposed, which can be used to identify pollution hotspots in Al-Hofuf city.

It should be mentioned that air pollution is a process, which is impacted by many other factors in addition to urbanization. In this study only two parameters of air quality are discussed, which can be improved by the monitoring of CO, SO_x, NO_x and Particulate matter (PM₁₀ and PM_{2.5}). Classification of TVOC is also important to pin point the mitigation measures. Lastly, long-term monitoring is crucial for a comprehensive mitigation plan, which can be ensured by establishing permanent monitoring stations at key points of the city.

4. Acknowledgements

The lead author acknowledges the Department of Civil and Environmental Engineering, College of Engineering, King Faisal University for providing support in conducting this research.

5. References

- Abdelatti, H., Elhadary, Y. & Babiker, A.A. (2017). Nature and Trend of Urban Growth in Saudi Arabia: The Case of Al-Ahsa Province–Eastern Region. *Resources and Environment*, 7(3), 69-80.
- Al-Ahsa Municipality. (1998). Al-Ahsa Structural Plan (Hofuf & Mubarraz): A Study of Current Situation. Al-Ahsa, Saudi Arabia.
- Al-Fouzan, S.A. (2012). Using car parking requirements to promote sustainable transport development in the Kingdom of Saudi Arabia. *Cities*, 29(3), 201–11.
- Al-harbi, B.H., Pasha, M.J. & Tapper, N. (2014). Assessment of ambient air quality in Riyadh City, Saudi Arabia. *Current World Environment*, 9(2), 227.
- Al-Jeelani, H.A. (2009). Air quality assessment at Al-Taneem area in the Holy Makkah City, Saudi Arabia. *Environmental monitoring and assessment*, 156(1-4), 211.
- Al-Khulaifi, N.M., Al-Mudhaf, H.F., Alenezi, R., Abu-Shady, A.-S.I. & Selim, M.I. (2014) Seasonal and Temporal Variations in Volatile Organic Compounds in Indoor and Outdoor Air in Al-Jahra City, Kuwait. *Journal of Environmental Protection*, 5, 310-326. <http://dx.doi.org/10.4236/jep.2014.54034>
- Al-mulali, U., Fereidouni, H.G., Lee, J.Y. & Sab, C.N.B.C. (2013). Exploring the relationship between urbanization, energy consumption, and CO2 emission in MENA countries. *Renewable and Sustainable Energy Reviews*, 23, 107-112.
- Bereitschaft, B. & Debbage, K. (2013). Urban form, air pollution, and CO2 emissions in large US metropolitan areas. *The Professional Geographer*, 65(4), 612-635.
- Cetin, M. & Sevik, H. (2016). Change of air quality in Kastamonu city in terms of particulate matter and CO2 amount. *Oxidation Communications*, 39(4), 3394-3401.
- Cole, M.A. & Neumayer, E. (2004). Examining the impact of demographic factors on air pollution. *Population and Environment*, 26(1), 5-21.
- Deng, C., Jin, Y., Zhang, M., Liu, X. & Yu, Z. (2018). Emission Characteristics of VOCs from On-Road Vehicles in an Urban Tunnel in Eastern China and Predictions for 2017–2026. *Aerosol and Air Quality Research*, 18, 3025-3034.
- European Environment Agency (2011). Annual European Community LRTAP Convention Emission Inventory 1990-2004: Submission to EMEP Through the Executive Secretary of the UNECE. Publications Office of the European Communities.
- Gately, C.K., Hutyra, L.R. & Wing, I.S. (2015). Cities, traffic, and CO2: A multidecadal assessment of trends, drivers, and scaling relationships. *Proceedings of the National Academy of Sciences*, 112(16), 4999-5004.
- General Authority for Statistics (GAS) (2019). Population and housing atlas for 2004 and 2010. <https://www.stats.gov.sa/en/391>
- Gratani, L. & Varone, L. (2005). Daily and seasonal variation of CO2 in the city of Rome in relationship with the traffic volume. *Atmospheric Environment*, 39(14), 2619-2624.
- Han, Y., Lau, S.L., Kayhanian, M. & Stenstrom, M.K. (2006). Characteristics of highway stormwater runoff. *Water Environment Research*, 78(12), 2377-2388. <http://data.worldbank.org/indicator/SP.RUR.TOTL?end=2015&locations=SA&start=1960&view=chart>.
- Jia, C., Batterman, S. & Godwin, C. (2008) VOCs in Industrial, Urban and Suburban Neighborhoods, Part 2: Factors Affecting Indoor and Outdoor Concentrations. *Atmospheric Environment*, 42, 2101-2116. <http://dx.doi.org/10.1016/j.atmosenv.2007.11.047>
- Kettrup, A. & Risse, O. (1997). Total Volatile Organic Compounds (WOC) in Indoor Air Quality Investigations. https://www.buildingecology.com/wp-content/uploads/2018/12/ECA_Report19.pdf
- Kim, G., Yur, J. & Kim, J. (2007) Diffuse pollution loading from urban stormwater runoff in Daejeon city, Korea. *Journal of Environmental Management*, 85, 9–16. Doi:10.1016/j.jenvman.2006.07.009
- Koerner, B. & Klopatek, J. (2002). Anthropogenic and natural CO2 emission sources in an arid urban environment. *Environmental Pollution*, 116, S45-S51.

- Rahman, S.M., Khondaker, A.N., Hasan, M.A. & Reza, I. (2017). Greenhouse gas emissions from road transportation in Saudi Arabia-a challenging frontier. *Renewable and Sustainable Energy Reviews*, 69, 812-821.
- Salama, K.F., Alhajri, R.F. & Al-Anazi, A.A. (2017). Assessment of air quality in bus terminal stations in Eastern Province, Kingdom of Saudi Arabia. *International Journal of Community Medicine and Public Health*, 4(5), 1413-1418
- Statista (2019). Estimated sales volume of new motor vehicles in Saudi Arabia. <https://www.statista.com/statistics/375695/motor-vehicle-sales-in-saudi-arabia/>
- Tanaka-Kagawa, T., Uchiyama, S., Matsushima, E., Sasaki, A., Kobayashi, H., Kobayashi, H., Yagi, M., Tsuno, M., Arao, M., Ikemoto, K. & Yamasaki, M. (2005). Survey of volatile organic compounds found in indoor and outdoor air samples from Japan. *Bull. Natl. Inst. Health Sci.*, 123, 27-31.
- Tong, L., Liao, X., Chen, J., Xiao, H., Xu, L., Zhang, F., Niu, Z. & Yu, J. (2013) Pollution Characteristics of Ambient Volatile Organic Compounds (VOCs) in the Southeast Coastal Cities of China. *Environmental Science and Pollution Research*, 20, 2603-2615. <http://dx.doi.org/10.1007/s11356-012-1187-3>
- USEPA (1998). Carcinogenic effects of benzene: An update (Draft Report). U.S. Environmental Protection Agency, Office of Research and Development, National Center for Environmental Assessment, Washington Office, Washington, DC, EPA/600/P-97/001F.
- Vidal, F.S. (1954). Date Culture in the Oasis of al-Hasa. *Middle East Journal*, 8, 417.
- Wolf Sense (2018). Application Software manual 2012, Introduction to GrayWolf Sensing Solutions, page 3, Viewed in 17 March 2018.
- World Bank. (2016). Saudi Arabia: Rural population 1960-2015. Retrieved from: <http://data.worldbank.org/indicator/EN.URB.LCTY?end=2015&locations=SA&start=1960&view=chart>
- Zhang, N., Yu, K. & Chen, Z. (2017). How does urbanization affect carbon dioxide emissions? A cross-country panel data analysis. *Energy Policy*, 107, 678-687.

Selection of the best-fit probability distribution for Brisbane River Catchment

S M Anwar Hossain

Master of Philosophy Scholar, School of Computing, Engineering and Mathematics, Western Sydney University, Australia.

*Corresponding author's email: Ahossain1995@gmail.com

Peer review history

Manuscript submitted: 10 June 2019

Review process completed: 19 August 2019

Manuscript finally accepted: 20 August 2019

Handling Editor: Professor Ataur Rahman

Abstract: Flood is one of the worst natural hazards worldwide. Brisbane, Queensland, has experienced many severe flood events causing damages worth billions of dollar and human deaths. Accurate estimation of design floods with less uncertainty helps to minimise flood risk, damage and loss of human life. Among many design flood estimation methods, flood frequency analysis (FFA) is a widely used method. The primary step in FFA is the selection of a suitable probability distribution that fits the observed flood data adequately. As it is still not possible to select the best fit distribution from a large number of candidate distributions and associated parameter estimation procedures for a particular catchment with certainty, selection of probability distribution

is still remain a difficult task. This study examines the selection of the best fit probability distribution for FFA. Brisbane River catchment of Queensland is selected as the study area. The annual maximum (AM) flood data from 26 stream gauging stations are selected with AM flood record lengths ranging from 20 to 91 years with a mean value of 47 years. Five different probability distributions and three goodness-of-fit tests are adopted. Based on a relative scoring method, Log Pearson Type III is found to be the most suitable probability distribution, followed by Generalised Pareto for the study area. To investigate the impact of high floods on the selection of the best fit probability distribution and flood quantile estimation, FFA are carried out twice; with the high flood values being included in the data and excluded from the data. It is found that the best fit probability distribution changes and magnitude of flood quantiles reduces notably if high floods are excluded from the data series.

Keywords: Flood; Goodness-of-fit tests; Flood frequency analysis; Probability distribution.

1. Introduction

Floods impact on both individuals and communities, and have notable social, economic, and environmental consequences (OQCS, 2016). Brisbane, the state capital of Queensland, Australia, experienced many dangerous floods including 2011 flood. Flood risk can be minimised through more accurate estimation of flood magnitude and frequency of occurrence of the flood. There are various methods available for flood estimation. Most of these methods of flood estimation use some types of probability concept including fitting some well established probability distribution with sample data. Flood frequency analysis is a statistical technique which fits a probability distribution to recorded streamflow data observed at a given location within a catchment (Haddad and Rahman, 2008). The fitted probability distribution is used for predictions of events beyond the range of the observed data period. If adequate and quality data is available, Australian Rainfall and Runoff (ARR) (Ball et al., 2016) recommend using at-site flood frequency analysis (FFA) for estimation of design peak floods.

Many different probability distributions and parameter estimation methods have been tested and recommended around the globe (Cunnane, 1989). Many probability distributions are available for modeling annual maximum (AM) flood series. Some of the commonly used distributions are Log Pearson Type 3 (LP3), General Extreme Value (GEV), Generalised Pareto (GP) Normal, Log Normal (LN), Pearson Type 3 (P3), Gamma, Extreme Value Type 1 (EV1), Extreme Value Type 2 (EV2), Two component Extreme Value, Exponential, Weibull and Wakeby (Cunnane 1989; Bobee et al. 1993). Many studies have been carried out by different researchers to find the appropriate probability distribution model for design flood estimation using FFA method (e.g., Alam et al., 2014; Rahman A S. et al. 2013; Haddad and Rahman., 2008; Laio et al., 2009; Stedinger et al. 1992; Vogel RM 1993; Markiewicz et al. 2006; Mitosek et al. 2006; Cunnane., 1989; Ishak et al., 2010; Haddad et al., 2011; Haddad et al., 2012; Haddad and Rahman, 2012; Zaman et al., 2012; Haddad et al., 2013). However, due to the limited length of observed flood data as compared to the return period of interest, this

becomes a challenging task and often FFA is associated with controversies (Bobee et al. 1993).

Selection of a probability distribution is of fundamental importance in FFA, as the wrong choice could lead to significant error and bias in design flood estimates (as high as 100% different to the optimum estimation), particularly at higher return periods, leading to either under- or over-estimation, which may have serious implications in practice (Rahman et al., 2013).

Several probability models are available to explain the distribution of AM flood data at a single site. However, the choice of a suitable probability model is still a major problem since there is no general agreement as to which distribution, or distributions is the best fit probability distribution for design flood estimation through FFA. Therefore, it is ideally necessary to evaluate many available distributions in order to find a suitable probability distribution that could provide more accurate design flood estimates (Tao et al., 2002). In ARR 1987, LP3 distribution coupled with method of product moments (MPM) was recommended for general use, similar to the USA (I. E. Aust., 1987; USWRC, 1967). However, the most recent version of ARR did not recommend any specific probability distribution for flood frequency analysis (Ball et al., 2016). Rahman et al. (2013) investigated the feasibility of 15 different probability distributions for Australia and found that a single distribution could not be specified as the best-fit distribution for all Australian states. They identified LP3, generalized extreme value (GEV), and generalized Pareto (GP) distributions as the top three best-fit distributions. Haddad and Rahman (2010) in their study found the two parameter Log Normal (LN) to be the best-fit distribution for Tasmania. Zhang et al. (2017) recommended GEV as the best statistical distribution for 34 stations in the Pearl River Delta during a period of about 60 years.

Various methods are used for estimating the parameters of a probability distribution. Methods of moments (MOM), maximum likelihood (MLE), L moments, LH moments and Bayesian methods are commonly used parameter estimation procedures. The MOM equates sample moments to parameter estimates. The product moments of a data series in MOM are equally influenced by low values in data series same as by the higher observations. Also in MOM, the coefficient of variation and skewness are much affected by extremes in the data series. On the other hand L moments are less affected by extremes in the data series (Hosking 1990). The LH moments provide more weighting to the larger values in the flood series and hence are expected to provide better fits to the upper tail of the distribution (Wang 1997). MLE is an alternative to MOM and often statisticians give it preference over MOM (Bickel and Doksum 1977; Martins and Stedinger 2000). Bayesian inference is an alternative to MOM and MLE. In Bayesian inference both the likelihood function and the parameters to be estimated are described by probability distributions. Bayes produces a complete characterization of the parameter from the single dataset. The use of Bayes' theorem for combining prior and sample flood information was introduced by Bernier (1967). Many researchers have adopted bayesian approach in FFA (e.g., Halbert et al., 2016; Parkes et al., 2016; Griffiths et al., 2017; Kuczera 1982, 1983a, b, 1999, Smith et al., 2015; Viglione et al., 2013; Liang et al., 2012).

In Australia, there has been a lack of studies comparing different probability distributions, in particular for the Brisbane River catchment, which has a known history of severe flooding. Hence, this study research is devoted to finding the best fit probability distribution for flood estimation at the Brisbane River catchment under stationary assumption.

2. Methodology

2.1 Study area and data

The Brisbane River basin, Australia has been selected as the study area. It is located in the south-east corner of Queensland. The catchment of the Brisbane River system has an area of 13,570 km². The Brisbane River catchment includes the sub-catchments of the Upper Brisbane, Stanley, Lockyer and Bremer Rivers. The Brisbane River is the largest river in the catchment. The Brisbane River is a large and complex river system. It has a long history of flooding with significant flood events in 1974 and 2011 that caused widespread damage. The Cooyar Creek, Emu Creek and Cressbrook Creek are the main tributaries of the upper Brisbane River. The Brisbane River catchment drains to Moreton Bay, a shallow bay sheltered from the Pacific Ocean by the islands of Moreton and North Stradbroke to the east. Figure 1 illustrates the Study area with seven main Brisbane River sub-catchments.

The Brisbane river system has many stream gauges. In this study, up-to-date continuous stream gauge recordings from the Department of Natural Resources and Mines (DNRM) is collected via the DNRM website. Data includes daily maximum

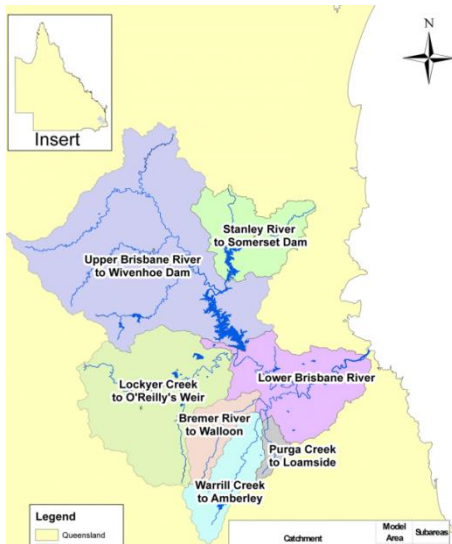


Figure 2. Location of the selected stream gauges in the Brisbane River Catchment

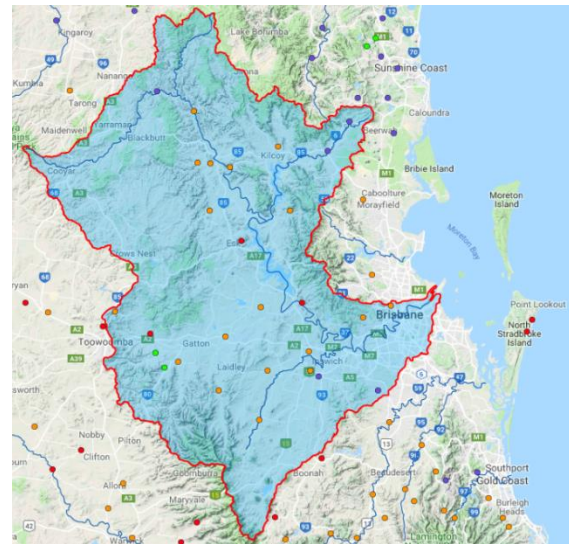


Figure 1. Location of the selected stream gauges in the Brisbane River Catchment

Table 1: Selected catchments with annual maximum flood record length

Station ID	Description	Period of Record	Record Length (Year)
143001C	Brisbane River at Savages Crossing	1958-2017	60
143007A	Brisbane River at Linville	1964-2017	54
143009A	Brisbane River at Gregors Creek	1962-2017	56
143010B	Emu Creek at Boat Mountain	1967-2017	51
143015B	Cooyar Creek at Taromeo Creek	1969-2017	49
143028A	Ithaca Creek at Jason Street	1972-2017	46
143032A	Moggill Creek at Upper Brookfield	1976-2017	42
143033A	Oxley Creek at New Beith	1976-2017	42
143107A	Bremer River at Walloon	1961-2017	57
143108A	Warrill Creek at Amberley	1961-2017	57
143110A	Bremer River at Adams Bridge	1962-2015	54
143113A	Purga Creek at Loamside	1973-2017	45
143203C	Lockyer Creek at Helidon Number 3	1927-2017	91
143207A	Lockyer Creek at O'Reillys Weir	1948-2014	67
143209B	Laidley Creek at Mulgowie	1967-2016	50
143210B	Lockyer Creek at Rifle Range Road	1988-2017	30
143212A	Tenthill Creek at Tenthill	1968-2017	50
143213C	Ma Ma Creek at Harms	1995-2017	23
143219A	Murphys Creek at Spring Bluff	1979-2017	39
143229A	Laidley Creek at Warrego Highway	1990-2017	28
143232A	Sandy Creek at Forest Hill	1995-2014	20
143233A	Flagstone Creek at Brown-Zirbels Road	1995-2017	23
143303A	Stanley R at Peachester	1927-2017	91
143306A	Reedy Creek at Upstream Byron Creek Junction	1975-2011	37
143921A	Cressbrook Creek at Rosentretters Crossing	1986-2015	30
143307A	Byron Creek at Causeway	1975-2010	36

flow and AM flow time series. After preliminary investigation of the data series, particularly record length and the data quality, 26 stream gauging stations are selected for this study. Stations graded as ‘poor quality’ or with specific comments by the gauging authority regarding the quality of the data are assessed in greater detail; if they are deemed ‘low quality’ they are excluded. The network of these 26 gauging stations across the Brisbane River catchment are shown in Figure 1.

The average catchment area of the selected 26 stations is 1075 km². The majority of the gauge records are from the post-1960 period. All gauging records have flow records from the 2011 flood, one of the most recent severe flood events after 1974. The AM flood series record lengths of the selected 26 stations are in the range of 20 to 91 years, with a mean value of 47 years. Most of the stations show that the the highest peak flow event occurred in 2011 during the recorded data period. Details of 26 selected stream gauging stations is shown in Table 1.

2.2 Method

Abstraction of raw data from the DNRM website and review of the available flow data is the first step of the methodology. The characteristics of the available flood data at the particular site is vital in the selection of the best probability distribution. To find a more appropriate probability distribution that is closer to the parent distribution, longer periods of observed flood data is recommended. However, at most of the stream gauging sites, measured data lengths are commonly shorter compared to return periods of interest. The minimum record length used in this study is 20 years. In this study three-step methodology is adopted, i.e. (i) selection of candidate probability distributions; (ii) selection of appropriate parameter estimation methods; (iii) carrying out hypothesis testing to evaluate goodness-of-fit of the hypothesised probability distributions to the observed annual maximum flood (AMF) data, and applying selection criteria for choice of statistical distribution.

2.2.1 Selection of candidate probability distributions

A list of probability distributions applied in practice is summarised by Cunnane, 1989. AM flood data are often found to be skewed, which has led to the development and use of many skewed distributions in flood frequency analysis (Rahman et al., 2013). Based on the recommendations in relevant literature, five commonly used parametric distributions, i.e., LN, LP3, Gumbel, GP and GEV are selected for this study. The LP3 distribution as recommended in the Australian Rainfall and Runoff (I. E. Aust., 2001; Pilgrim, 2001) is included in this study. The GEV distribution which had been favoured by many recent studies is also included. The mathematical formulation of these probability distributions are available in many literatures (i.e. FLIKE, 2017). Two statistical software, EasyFit (Mathwave, 2017; Drokin, 2018) and FLIKE (Kuczera and Franks, 2016; Kuczera, 1999), are used in this study.

2.2.2 Selection of candidate parameter estimation methods

Estimation the parameters of the selected probability distributions using the selected flood data is the next step in selecting best-fit probability distribution. This study uses number of parameters estimation procedures. EasyFit software used in this study uses the method of moments (MOM) for Gumbel and for LP3 distributions, maximum likelihood method (MLM) for LN and method of L-moments for GEV and for GP distributions. The FLIKE software includes Bayesian and L-moment fitting for all distributions including GEV, and for GEV, FLIKE includes additional LH-moment fitting. Both EasyFit and FLIKE softwares provide graphical fitting of the selected probability distributions, which provides a clear visual assessment of the fitted distributions to the given AM flood data.

2.2.3 Selection of candidate goodness-of-fit tests

To test whether a particular probability distribution provides an adequate fit to the observed flood data series, three different widely used goodness-of-fit tests are considered. The Chi-squared (C-S) test, Kolmogorov–Smirnov (K-S) test, and Anderson–Darling (A-D) test, are adopted in this study. These tests calculate test-statistics are used to ascertain the suitability of a given distribution to fit the flood data. The goodness of fit tests are carried out using EasyFit, software (Mathwave, 2017; Drokin, 2018). EasyFit supports all popular goodness-of-fit tests, including the K-S, A-D, and C-S tests. Once the distributions are fitted, EasyFit displays the goodness-of-fit reports which included the test statistics and critical values calculated for various significance levels. These tests are briefly described below. Visual observation of the fitted distributions is done using FLIKE-produced plots and comparing with Easyfit results.

2.2.3.1 Kolmogorov-Smirnov test

Kolmogorov-Smirnov test is used to determine whether a sample has come from an assumed continuous probability

distribution. For a detailed description of the test see Chakravarti et al. (1967). This test is based on the empirical cumulative distribution function (ECDF), which is given by:

$$F_n(x) = \frac{1}{n} \cdot [\text{Number of observations} \leq x] \quad (1)$$

The Kolmogorov-Smirnov test statistic (D) is given by the largest vertical difference between the theoretical and empirical cumulative distribution functions:

$$D = \max_{1 \leq i \leq n} \left(F(x_i) - \frac{i-1}{n}, \frac{i}{n} - F(x_i) \right) \quad (2)$$

$$D = \max |(X_m) - F(X_m)| \quad (3)$$

$$\text{Where } P(X_m) = \left(F(x_i) - \frac{i-1}{n}, \frac{i}{n} \right)$$

$P(X_m)$ is the cumulative probability distribution for each of the ordered observations X_m using Weibull's formula, and $F(X_m)$ is the theoretical cumulative probability for each of the ordered observations X_m using the assumed distribution (Sharma et al., 2016). The large values of D indicate the presence of non-normality in the time series (Machiwal and Jha, 2012).

2.2.3.2 Anderson-Darling test

Anderson-Darling test compares the fit of an observed cumulative distribution function to an expected cumulative distribution function. This test gives more weight to the tails of the distribution than the Kolmogorov-Smirnov test. The A-D test has been used as an alternative to the K-S and Chi-Squared goodness-of-fit tests. The Anderson-Darling test statistic (A^2) is given by:

$$A^2 = -n - \frac{1}{n} \sum_{i=1}^n (2i-1) \cdot [\ln F(X_i) + \ln(1 - F(X_{n-i+1}))] \quad (4)$$

Where, X_i, X_{i+1}, \dots, X_n are data series, F = cumulative distribution function (CDF), and n = size of the sample
The hypothesis that the distribution is normal is rejected if the value of A is greater than the critical value

2.2.3.3 Chi-squared test

Chi-squared test is used to find if a sample has come from a population with a given distribution. This is applied to the binned data, and hence the value of the test statistic depends on how the available data is binned. The Chi-squared test statistic is given by:

$$\chi^2 = \sum_{i=1}^k \frac{(O_i - E_i)^2}{E_i} \quad (5)$$

where O_i is the observed frequency, i is the number of observations (1, 2, ..., k) and E_i is the expected frequency for bin i obtained by:

$$E_i = F(x_2) - F(x_1) \quad (6)$$

Where, F is the cumulative distribution function of the probability distribution being tested, and x_1, x_2 are the limits for bin i . Although there is no optimal choice for the number of bins (k), there are several formulas which can be used to calculate this number based on the sample size (N). The observed number of observations/bins (k) in interval ' i ' for sample size of N is computed by:

$$k = 1 + \log_2 N \quad (7)$$

The hypothesis that the data are from a population with the specified distribution is rejected,

if $\chi^2 > \chi^2_{(\alpha, \kappa \square \chi)}$

Where, $\chi^2_{(\alpha, k-c)}$ is the critical test-statistic value with $k-c$ degrees of freedom and a significance level (α).

2.2. Selection of the best fit probability distribution

The three goodness-of-fit tests (as mentioned in Section 2.2.3) were applied to the AM flood data series at each of the selected 26 stations. The test statistics corresponding to each of these tests were computed and hypothesis testing was carried out at the 0.05 level of significance. The selected 5 probability distributions are ranked on a scale of 1 to 3 for all the three tests independently, with rank 1 indicating the best fit distribution, and rank 2 the second best one, and so on. The final selection was made based on total test scores derived by combining all the three goodness-of-fit tests. A maximum score of 3 was awarded to rank 1 probability distribution, and score 2 for rank 2 distributions, and score 1 for rank 3.

2.3. Graphical observation test

A visual inspection method or graphical test of the distribution can be used for assessing the goodness of fit tests. A graphical test is one of the most simple and powerful techniques for selecting the best-fit model. The frequency distribution (histogram), stem-and-leaf plot, boxplot, P-P plot (probability-probability plot), and Q-Q plot (quantile-quantile plot) are used for visual checking. The frequency distribution plots the observed values against their frequency and provides both a visual judgment about whether the distribution is bell shaped, and insights about gaps in the data and outlying values (Ghasemi and Zahediasl, 2012). In this study, graphical testing is applied to compare the observed and estimated flood values. EasyFit software provides graphical (Q-Q plot) fitting of the selected probability distributions, which is used for visual comparison of the fitted distributions to the given data. FLIKE software is used for visual comparison of graphical quantile plot between plot of expected probability quantile and observed flow with annual exceedance probability (AEP) for each probability distribution which is used for visual comparison of the fitted distributions to the given data. The plots for different distributions were generated for visual assessment of the quality of fit. FLIKE plots of the observed AMF data and the fitted distributions were examined to make a visual assessment of the goodness-of-fit test results.

2.4. Flood quantile estimation

Probability distribution is used to estimate the quantile i.e. exceedance probability of a given value of X or alternatively to estimate the p -quantile of X (where p denotes the non-exceedance probability). FLIKE software is used in this study for flood quantile estimation. Flood quantiles for 2, 5, 10, 20, 50 and 100-year ARIs were estimated along with 90% confidence limits.

2.5. Sensitivity analysis

This study has carried out a sensitivity analysis of the flood quantile estimation and selection of the best-fit probability distribution by (i) removing the highest recorded flow of a station's AMF data series, (ii) removing both the first and second highest from the AMF data series and (iii) removing the first, second and third highest recorded flow from AMF data series. Parameter estimations, goodness of fit tests and selection of best-fit probability distribution, and quantile estimation are carried out for these three scenarios.

3. Results and discussion

3.1 Goodness of fit tests

Each of the 5 selected distributions is fitted to the AM flood data set at each of the 26 stations. The results of the A-D, K-S and C-S Goodness of fit (GoF) tests for Stations 143009A is summarised in Tables 2. To select the best-fit distribution, a comparative assessment of all five distributions at each site is carried out. Figure 3 shows a summary of GoF test results with rank 1 for selected stations. To identify the best fit probability distribution overall i.e. the distribution that fits the highest numbers of the selected stations, a relative scoring method based on the results given by the three goodness-of-fit tests is adopted. The scoring results of the distribution selection are summarised in Table 3.

The best fit probability distribution is identified based on the highest score that was determined based on the three goodness-of-fit tests. The combine score of the GoF test results in Table 3 shows that LP3 distribution is the most preferred probability distribution with score 179; followed by GP with score 114. It is also seen that Gumbel distribution

is the least preferred probability distribution with score 16, as only the K-S GoF test selects this for only one station as rank 1.

Table 2. Summary of GoF test results for candidate probability distributions for Station 143009A

Distribution	Kolmogorov Smirnov (K-S)	Kolmogorov Smirnov (K-S)	Anderson Darling (A-D)	Anderson Darling (A-D)	Chi-Squared (C-S)	Chi-Squared (C-S)	Avg. Rank
	Statistic	Rank	Statistic	Rank	Statistic	Rank	
Log Pearson type III	0.07086	1	0.40106	1	0.86208	1	1.0
Lognormal	0.07529	2	0.42323	2	1.1246	2	2.0
Generalised. Pareto	0.15407	4	1.5218	3	3.5449	3	3.3
Gen. Extreme Value	0.14498	3	1.72	4	3.6029	4	3.7
Gumbel	0.30794	5	7.1698	5	14.587	5	5.0

Bold value indicates the best-fit probability distribution as per GoF tests

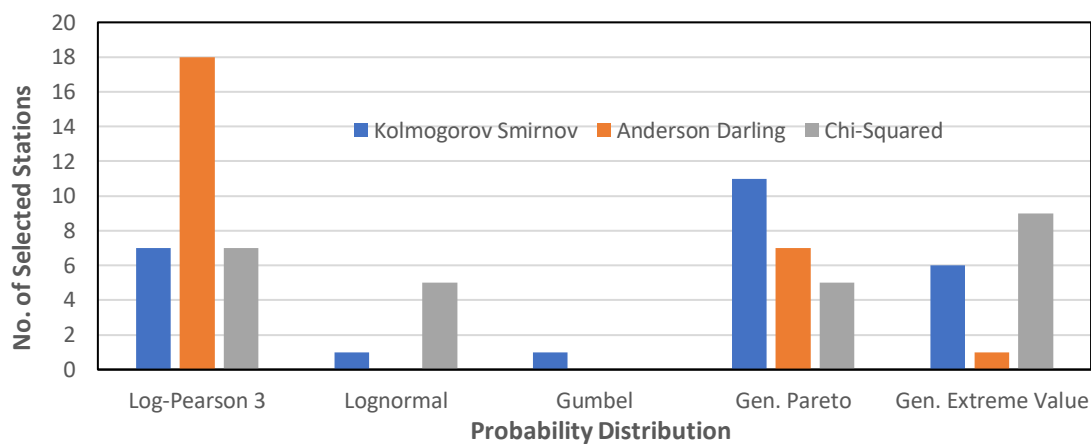


Figure 3. Summary of GoF tests for the 26 stations

Table 3. GoF results Combined Score (ranks 1, 2, and 3 for all stations with weights for rank 1, 2 and 3)

Probability Distribution	K-S test	A-D test	C-S test	K-S test	A-D test	C-S test	K-S test	A-D test	C-S test	All Stations
Method	Number of stations with GoF test Rank 1			Number of stations with GoF test Rank 2			Number of stations with GoF test Rank 3			Combine Scores
	Weight = 3			Weight = 2			Weight = 1			
Log Pearson type III	21	54 (69%)	21	28	12	16	4	2	10	179
Lognormal	3	0	15	14	22	6	5	8	6	81
Gumbel	3	0	0	2	0	6	1	2	2	16
Generalised. Pareto	33	21 (27%)	15	4	2	10	6	10	5	114
Gen. Extreme Value	18	3	27	4	16	14	10	4	3	104

The probability density functions (PDF) for the five probability distributions as shown in Figure 4 for stations 143028A show that LP3, GEV and LN distributions are most likely to fit best the observed AMF data. The histogram of AMF data reveals a positive skewed distribution and shows a unimodal distribution which is skewed to the right. The PDFs of the distributions are plotted to fit the empirical histograms of available records. The PDF shows that the Lognormal and LP3 distributions exhibit similar probability densities which are different from that of the GP and Gumbel distributions. The cumulative distribution function (CDF) (Figure 4b) shows the non-exceedance probability for a given magnitude. The probability-probability(P-P) plot (Figure 4c), which is a graph of the empirical CDF values plotted against the theoretical

(fitted) CDF values, is used to determine how well a specific distribution fits the observed AMF data. It is recommended that if the maximum absolute difference is less than 0.05 (or 5%), the fit can be considered 'good'.

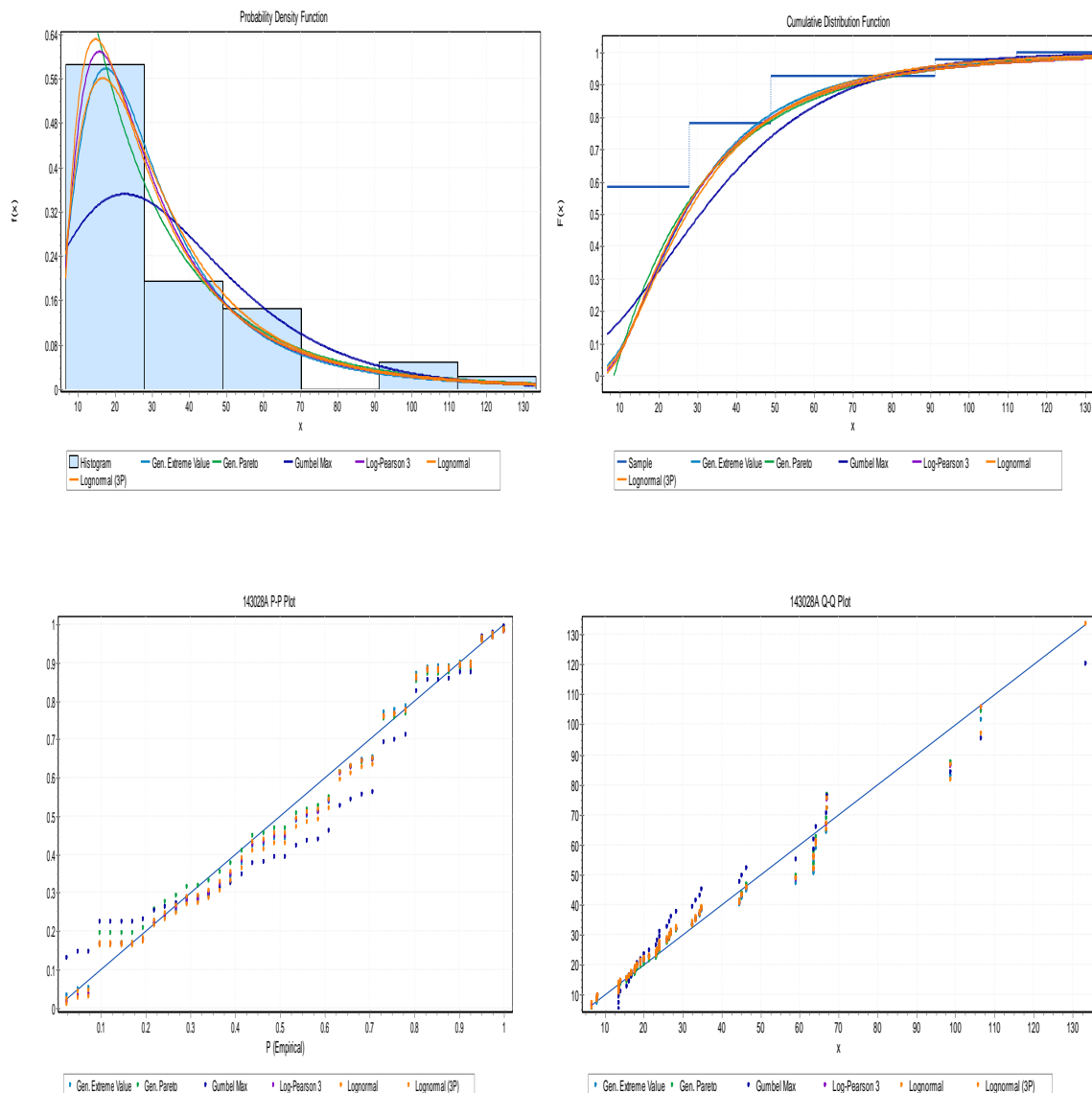


Figure 4. (a) Probability density functions (b) cumulative distribution functions, (c) probability-probability plots and (d) Q-Q plot for the five probability distributions for Station 143028A

3.2 Visual inspection and comparison with Goodness-of-fit test results

The best-fit probability distribution from the goodness of fit test is compared with graphical presentation from FLIKE which exhibits the AMF data and the fitted distributions. It is seen that the most appropriate probability distribution based on graphical observation does not fully agree with the goodness of fit test result for many stations. LP3 distribution is found to be the most preferred one according to the goodness of fit test results, followed by GP distribution as discussed in the earlier part of this chapter. However, according to graphical assessment, LP3 is the best-fit distribution for 9 stations only. The visual assessment of the AMF data and the fitted probability distributions for Station 143001C is shown in Figure 5. It can be seen from Figure 5 that for Station 143001C, LP3 is the best-fit probability distribution for quantile estimation. However, according to the goodness of fit test, GP is the best-fit distribution. Figure 6 show the plot AMF data estimated flood quantile for Station 143032A. It is seen in Figure 6 that for station 143010B, LP3 is the best-fit probability distribution as per A-D test and with visual inspection it is also LP3. These results highlight the importance of visual inspecting the data when selecting the best fit distribution for application.

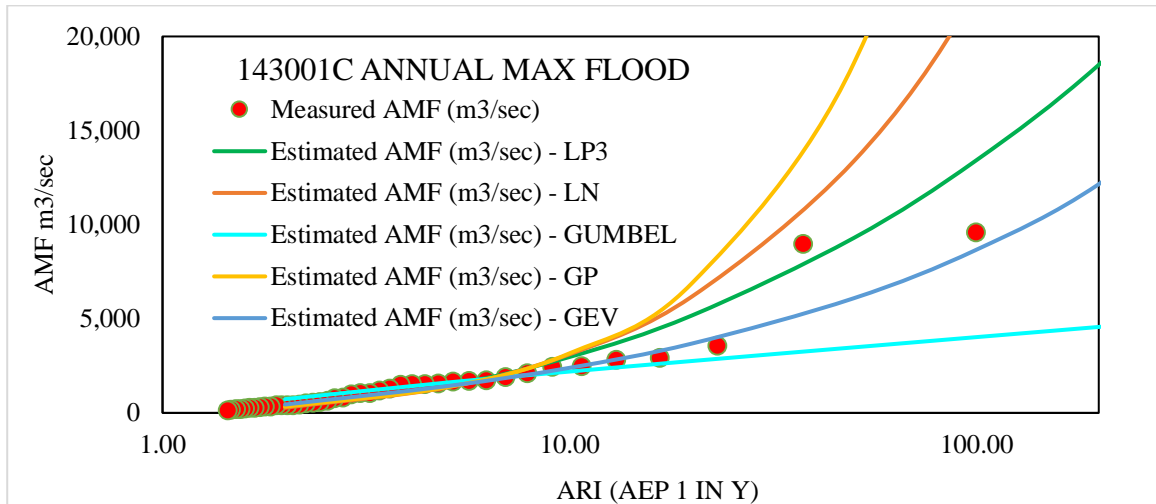


Figure 5. Comparison of flood quantile and AM flood data for five probability distributions for Station 143001C

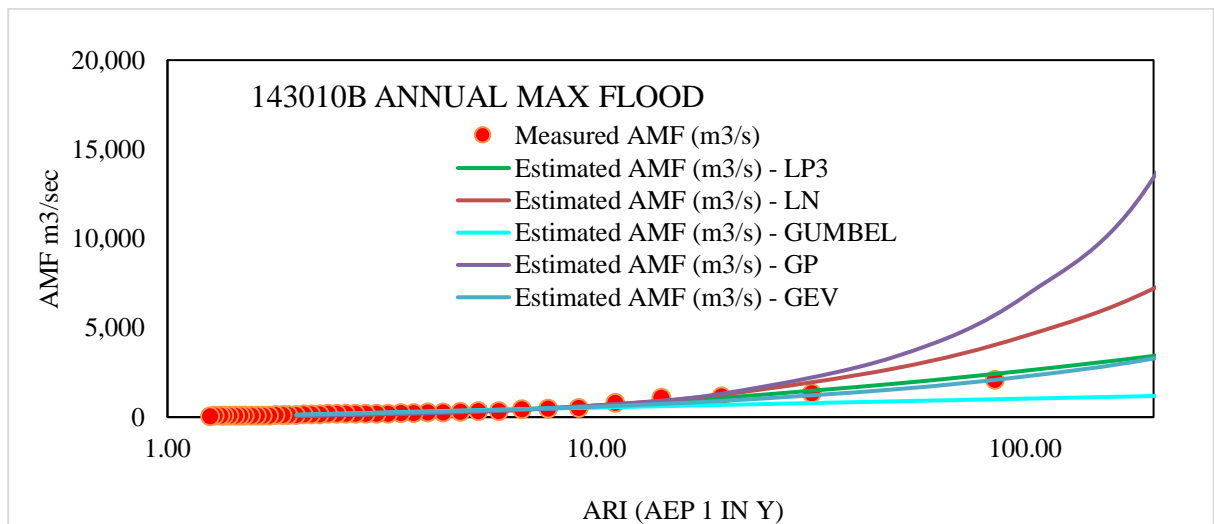


Figure 6. Comparison of flood quantile and AM flood data for five probability distributions for Station 143010B

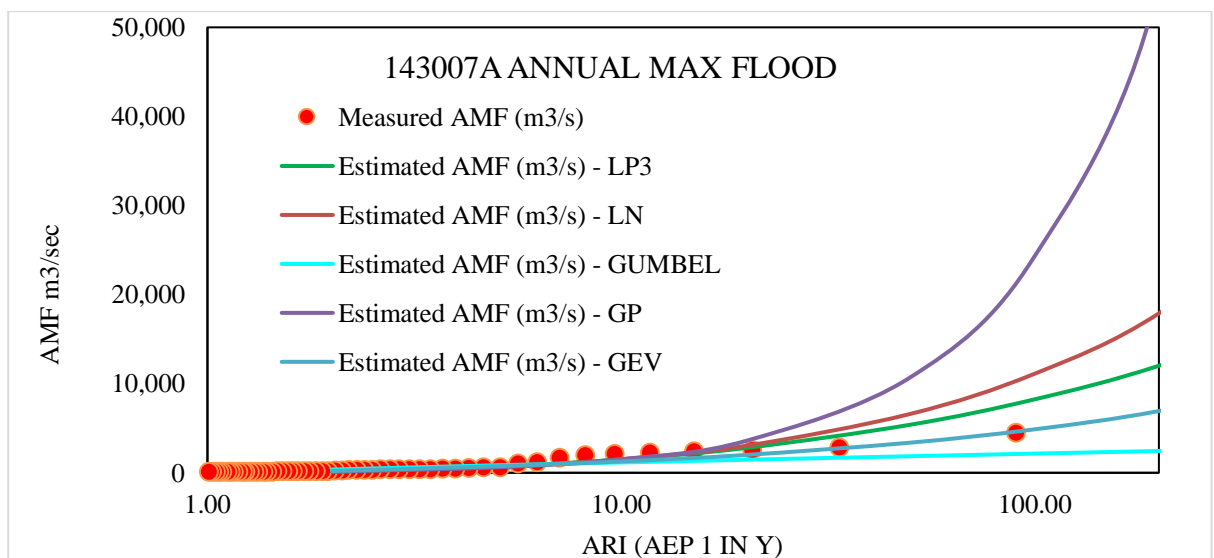


Figure 7. Comparison of flood quantiles using five different probability distributions for Station 143007A (period of record = 1964-2017)

3.3 Flood quantile estimation

Quantile estimation is done using FLIKE software corresponding to different return periods (for ARIs of 2, 5, 10, 20, 50 and 100 years). Figures 7 and 8 show quantile for all 5 distributions for stations 143007A and 143028A, respectively. Quantile plots (Figure 7 and 8) show that at low return periods, a good match is observed among observed AMF and quantile values. However, for higher return periods, especially 100 ARI or more, it becomes more difficult to choose the most preferred distribution. Table 4 shows the flood quantiles for 143010B with 5 different distributions. It is seen from the table that flood quantiles for 100-year ARI is quite different among the distributions and this is valid for all 26 stations. It is found that for almost all the stations, flood quantile estimates with Gumbel and Lognormal are notably different than that of LP3, GP and GEV distributions.

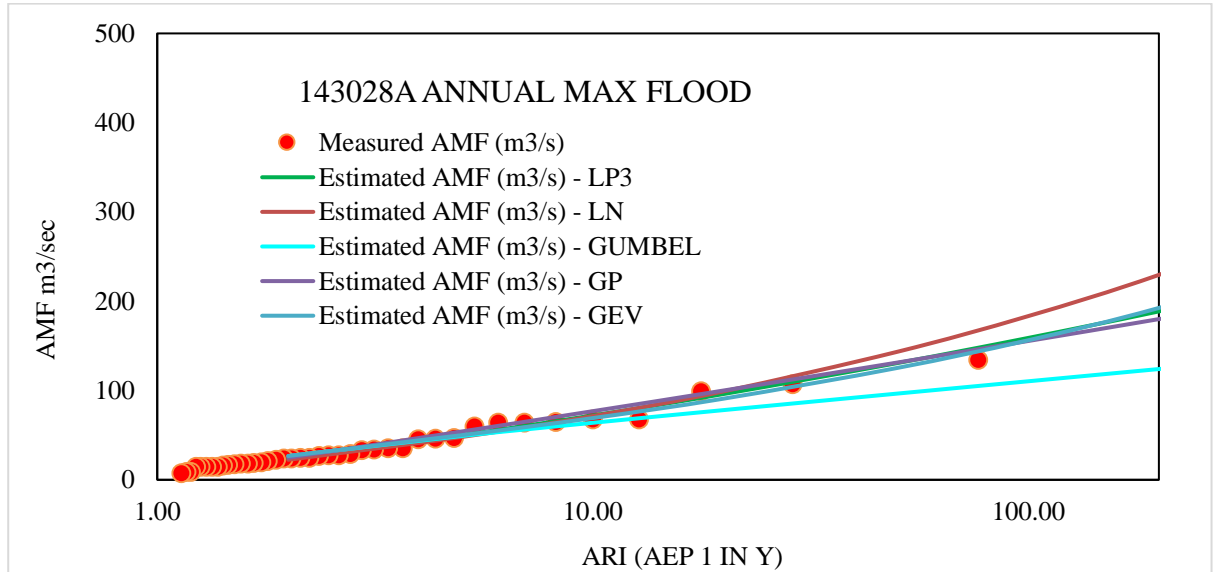


Figure 8. Comparison of flood quantiles using five different probability distributions for Station 143028A (period of record = 1972-2017)

Table 4. Flood Quantile estimation using 5 different probability distributions for station 143010B

ARI (years)	Quantile (m ³ /s) - LP3	Quantile (m ³ /s) - LN	Quantile (m ³ /s) - Gumbel	Quantile (m ³ /s) - GP	Quantile (m ³ /s) - GEV
2	67	61 (91%)	133 (197%)	74 (111%)	124 (185%)
5	321	290 (90%)	374 (117%)	290 (90%)	352 (110%)
10	649	655 (101%)	534 (82%)	643 (99%)	590 (91%)
20	1099	1283 (117%)	687 (63%)	1341 (122%)	918 (84%)
50	1878	2738 (146%)	886 (47%)	3397 (181%)	1560 (83%)
100	2600	4537 (175%)	1035 (40%)	6771 (260%)	2277 (88%)
200	3427	7204 (210%)	1183 (35%)	13425 (392%)	3286 (96%)

Note: The % value is the difference of Quantile using 4 probability distributions and using LP3

Table 5 shows that the observed AMF values in 2011 (Q_{2011}) (a devastating flood occurred in 2011) were larger than estimated 100-year flood quantiles for 2 stations and 3 stations were similar to Q_{2011} , however, in 21 cases, the Q_{2011} values were smaller than 100-year flood quantiles.

Table 5: Goodness of Fit test result summary of 26 stations excluding outliers in data

Station	Observed Q_{\max} / Q_{2011} (m^3/s)	Estimated Quantile with $T=100$; Q_{100} (m^3/s)	% Difference (Quantile/Observed)
143203C	3643	1989	55
143219A	362	348	96
143108A	2108	2117	100
143303A	710	721	102
143107A	2057	2107	102
143113A	411	434	106
143001C	9533	10784	113
143028A	133	159	119
143209B	349	416	119
143207A	2977	3582	120
143033A	385	469	122
143010B	2036	2600	128
143015B	2335	3080	132
143306A	175	231	132
143307A	462	624	135
143210B	1401	1958	140
143110A	370	520	141
143232A	45	63	141
143212A	1359	2213	163
143032A	297	533	179
143921A	590	1058	179

3.4 Sensitivity analysis

Selection of best fit distribution may be changed if the highest flood record from the AMF data series is ignored. To investigate the sensitivity of the selection of the best-fit distribution and quantile estimation, FFA is carried out by removing the first highest flood record from the AMF data series, FFA is carried out by removing two highest flood records and FFA is carried out by removing three highest flood records. Figure 9 shows best-fit distribution with 3 different goodness-of-fit tests by removing the highest flood event from each of the 26 station's AMF data.

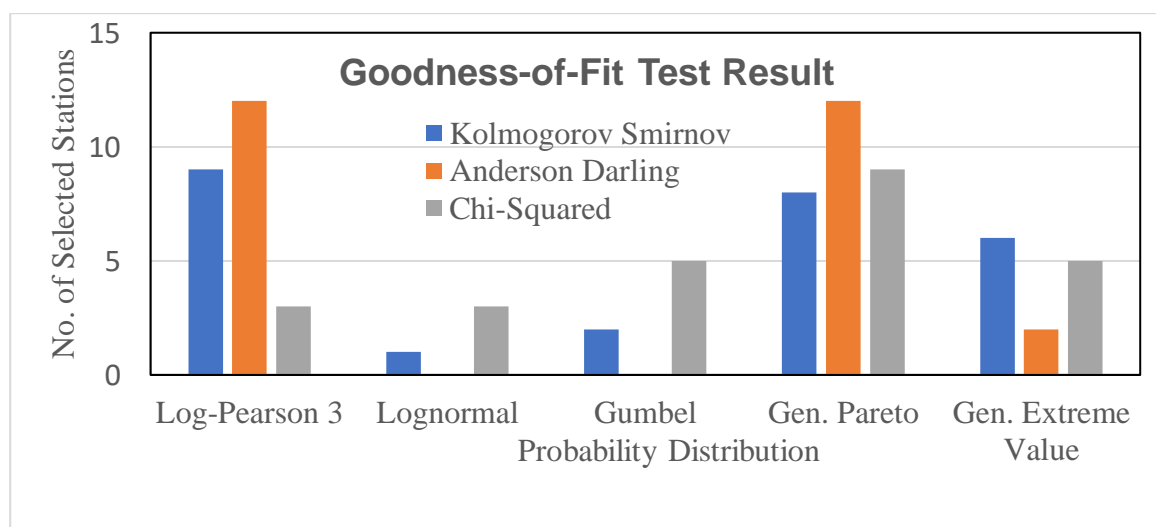


Figure 9. Summary of GoF tests for the 26 stations by removing the first highest, second highest and third highest AM flood data points

It is seen combined score that GP is the best fit distribution followed by LP3. As shown earlier that without removing highest records LP3 becomes the best fit distribution. Therefore presence of extreme records in the AMF time-series has influenced selection of distribution.

4. Conclusion

This paper examines the selection of the best fit probability distribution for annual maximum (AM) flood data in Brisbane River catchment. A total of 26 stations are used in this study. Missing data are very few in numbers (smaller than 2% cases) and are infilled through regression analysis. Presence of outliers in AM flood time series data have been tested using FLIKE software and all outliers in data are censored in flood frequency analysis. Five different probability distributions and three goodness-of-fit tests, Kolmogorov-Smirnov, Anderson-Darling and Chi-squared tests are adopted. It has been found that there is no single distribution that fits the AM data for all the 26 stations. Based on relative scoring method (Table 3), the LP3 distribution is found to be fitting the maximum number of stations with 69% (based on Anderson-Darling test) of the selected stations followed by GP distribution with 27% stations. Sensitivity analysis shows that the best fit probability distribution is sensitive to highest recorded AM flood data. Since the quantile estimates of higher ARIs are greatly influenced by skewness, a longer record length is desirable in order to reduce the uncertainty in higher quantile estimates. The AM flood data series for majority of the study stations show a positive skewness. In Australia, some previous studies (e.g. Srikanthan and McMahon, 1981; Rahman et al., 2013) find LP3 as the most favourable distribution for FFA since the skewness of logged AM flood data in Australia generally do not exceed the desirable limit of ± 1.4 (Rahman et al., 2016; Griffis and Stedinger, 2005, 2009).

Flood quantile is estimated for every station using all the five probability distributions. It appears (Table 5) 100- year quantile estimation with LP3 distribution for majority of the stations are within 95%-140% of the maximum flood value in the respective AMF data series. It has been found that the best-fit probability distribution can change if FFA is made by removing maximum recorded flow from the AMF data series.

References

- Al Mamoon, A., & Rahman, A. (2017). Selection of the best fit probability distribution in rainfall frequency analysis for Qatar. *Natural hazards*, 86(1), 281-296.
- Alam, S., Sabbir, M., & Khan, M. (2014). Statistical Characterization of Extreme Hydrologic Parameters for the Peripheral River System of Dhaka City. *J. Water Resour. Ocean Sci*, 3, 30-37.
- Ball, J. E., Babister, M. K., Nathan, R., Weinmann, P. E., Weeks, W., Retallick, M., & Testoni, I. (2016). Australian Rainfall and Runoff-A guide to flood estimation.
- Bernier, J. (1967). Sur la théorie du renouvellement et son application en hydrologie. *Electricité de France, (HYD67)*, 10.
- Bickel, P. J., & Doksum, K. A. (1976). *Mathematical statistics: basic ideas and selected topics*. 1977.
- Chakravarti, I. M., Laha, R. G., & Roy, J. (1967). *Handbook of methods of applied statistics*. Wiley Series in Probability and Mathematical Statistics (USA) eng.
- Cunnane, C. (1989). Statistical distributions for flood frequency analysis. Operational hydrology report (WMO).
- Drokin Antony (2018), Director, MathWave Technologies; developer of EasyFit software via web <http://www.mathwave.com>
- FLIKE Manual, (2017). Flike Statistical Software developed by Professor George Kuczera from the School of Civil Engineering at the University of Newcastle Australia
- FLIKE, (2017). FLIKE software (<https://flike.tuflow.com/>) flikehelp.htm Theory Flood probability models, access on July 2017
- Griffis, V. W., & Stedinger, J. R. (2005). The LP3 distribution and its use for flood frequency analysis. In *Impacts of Global Climate Change* (pp. 1-12)
- Griffis, V. W., & Stedinger, J. R. (2009). Log-Pearson Type 3 distribution and its application in flood frequency analysis. III: Sample skew and weighted skew estimators. *Journal of Hydrologic Engineering*, 14(2), 121-130.
- Griffiths, G. A., McKerchar, A. I., & Renard, B. (2017). Flood frequency analysis: combining a systematic record with historical, regional, model and analogue information. *Journal of Hydrology (New Zealand)*, 56(1), 1.
- Haddad, K., & Rahman, A. (2008). Investigation on at-site flood frequency analysis in south-east Australia. *IEM Journal, The Journal of The Institution of Engineers, Malaysia*, 69(3), 59-64.

- Haddad, K., & Rahman, A. (2012). Regional flood frequency analysis in eastern Australia: Bayesian GLS regression-based methods within fixed region and ROI framework-Quantile Regression vs. Parameter Regression Technique. *Journal of Hydrology*, 430, 142-161.
- Haddad, K., Rahman, A., & Kuczera, G. (2011). Comparison of ordinary and generalised least squares regression models in regional flood frequency analysis: a case study for New South Wales. *Australasian Journal of Water Resources*, 15(1), 59-70.
- Haddad, K., Rahman, A., & Stedinger, J. R. (2012). Regional flood frequency analysis using Bayesian generalized least squares: a comparison between quantile and parameter regression techniques. *Hydrological Processes*, 26(7), 1008-1021.
- Haddad, K., Rahman, A., Zaman, M., & Shrestha, S. (2013). Applicability of Monte Carlo cross validation technique for model development and validation in hydrologic regression analysis using ordinary and generalised least squares regression. *Journal of Hydrology*, 482, 119-128.
- Halbert, K., Nguyen, C. C., Payraastre, O., & Gaume, E. (2016). Reducing uncertainty in flood frequency analyses: A comparison of local and regional approaches involving information on extreme historical floods. *Journal of Hydrology*, 541, 90-98.
- Hosking, J. R. (1990). L-moments: Analysis and estimation of distributions using linear combinations of order statistics. *Journal of the Royal Statistical Society: Series B (Methodological)*, 52(1), 105-124.
- Institution of Engineers Australia (I. E. Aust.) (1987). *Australian Rainfall and Runoff A Guide to Flood Estimation*, Vol. 1, I. E. Aust., Canberra, 1987.
- Institution of Engineers Australia (IE Aust) (1987, 2001) In: Pilgrim DH (ed) *Australian Rainfall and Runoff: a guide to flood estimation*, vol. 1. I. E. Aust. Canberra
- Ishak, E. H., Rahman, A., Westra, S., Sharma, A., & Kuczera, G. (2010). Preliminary analysis of trends in Australian flood data. In *World Environmental and Water Resources Congress 2010: Challenges of Change* (pp. 115-124).
- Kuczera, G. (1982). Combining site-specific and regional information: An empirical Bayes approach. *Water Resources Research*, 18(2), 306-314.
- Kuczera, G. (1983a). A Bayesian surrogate for regional skew in flood frequency analysis. *Water Resources Research*, 19(3), 821-832.
- Kuczera, G. (1983b). Effect of sampling uncertainty and spatial correlation on an empirical Bayes procedure for combining site and regional information. *Journal of Hydrology*, 65(4), 373-398.
- Kuczera, G. (1999). Comprehensive at-site flood frequency analysis using Monte Carlo Bayesian inference. *Water resources research*, 35(5), 1551-1557.
- Kuczera, G., & Franks, S. (2016). At-site flood frequency analysis. *Australian Rainfall and Runoff: A Guide to Flood Estimation*; Ball, JE, Babister, M., Nathan, R., Weeks, W., Weinmann, E., Retallick, M., Testoni, I., Eds.; Engineers Australia. <http://book.arr.org.au/>
- Laio F, Di Baldassarre G, Montanari A (2009) Model selection techniques for the frequency analysis of hydrological extremes. *Water Resour Res* 45:W07416. doi:10.1029/2007/WR006666
- Liang, Z., Chang, W., & Li, B. (2012). Bayesian flood frequency analysis in the light of model and parameter uncertainties. *Stochastic environmental research and risk assessment*, 26(5), 721-730.
- Machiwal, D., & Jha, M. K. (2009). Time series analysis of hydrologic data for water resources planning and management: a review. *Journal of Hydrology and Hydromechanics*, 54(3), 237-257.
- Markiewicz, I., Strupczewski, W. G., Kochanek, K., & Singh, V. P. (2006). Discussion on "Non-stationary pooled flood frequency analysis" by JM Cunderlik and DH Burn [J. Hydrol. 276 (2003) 210-223]. *Journal of Hydrology*, 330(1-2), 382-385.
- Martins, E. S., & Stedinger, J. R. (2000). Generalized maximum-likelihood generalized extreme-value quantile estimators for hydrologic data. *Water Resources Research*, 36(3), 737-744.
- Mathwave, (2017). MathWave Technologies, EastFit version 6.5, <http://www.mathwave.com>
- Mitosek, H. T., Strupczewski, W. G., & Singh, V. P. (2006). Three procedures for selection of annual flood peak distribution. *Journal of Hydrology*, 323(1-4), 57-73.
- OQCS (2016). *Understanding Flood*, Office of the Queensland Chief Scientist, Australia 2016. Accessed via www.chiefscientist.qld.gov.au/publications/understanding-floods/flood-consequences on 27 June 2018
- Parkes, B., & Demeritt, D. (2016). Defining the hundred year flood: A Bayesian approach for using historic data to reduce uncertainty in flood frequency estimates. *Journal of Hydrology*, 540, 1189-1208.
- Pilgrim, D. H. (Ed.). (2001). *Australian rainfall and runoff: a guide to flood estimation*. Vol. 1. Institution of Engineers, Australia.

- Rahman A., Haddad K., Kuczera G., Weinmann P.E. (2016). Regional flood methods. In Australian Rainfall & Runoff, Chapter 3, Book 3, edited by Ball et al., Commonwealth of Australia.
- Rahman, A. S., Rahman, A., Zaman, M. A., Haddad, K., Ahsan, A., & Imteaz, M. (2013). A study on selection of probability distributions for at-site flood frequency analysis in Australia. *Natural hazards*, 69(3), 1803-1813.
- Sharma, P.J., Patel, P.L. and Jothiprakash, V. (2016). At-site flood frequency analysis for upper Tapi Basin, India, *ISH - HYDRO 2016 INTERNATIONAL*.
- Smith, T., Marshall, L., & Sharma, A. (2015). Modeling residual hydrologic errors with Bayesian inference. *Journal of Hydrology*, 528, 29-37.
- Srikanthan, R., & McMahon, T. A. (1981). Log Pearson III distribution-An empirically-derived plotting position. *Journal of Hydrology*, 52(1-2), 161-163.
- Stedinger J. R., Vogel R.M. and Foufula-Georgiou E. (1992). Frequency analysis of extreme events, in *Handbook of Hydrology*, edited by R. Maidment, chap. 18, pp. 18.1-18.66, McGraw-Hill, New York.
- Tao, D. Q., Nguyen, V. T., & Bourque, A. (2002, June). On selection of probability distributions for representing extreme precipitations in Southern Quebec. In *Annual conference of the Canadian society for civil engineering* (Vol. 5, pp. 1-8).
- United States Water Resources Council (USWRC) (1967). "A Uniform Technique for Determining Flood Flow Frequencies", Bulletin 15, USWRC, Washington DC, 1967
- Viglione, A., Merz, R., Salinas, J. L., & Blöschl, G. (2013). Flood frequency hydrology: 3. A Bayesian analysis. *Water Resources Research*, 49(2), 675-692.
- Vogel, R. M., McMahon, T. A., & Chiew, F. H. (1993). Floodflow frequency model selection in Australia. *Journal of Hydrology*, 146, 421-449.
- Wang, Q. J. (1997). LH moments for statistical analysis of extreme events. *Water Resources Research*, 33(12), 2841-2848.
- Zaman, M. A., Rahman, A., Haddad, K., & Hagare, D. (2012). Identification of the best-fit probability distributions in at-site flood frequency analysis: A case study for Australia using 127 stations. In *Hydrology and Water Resources Symposium 2012* (p. 939). Engineers Australia.
- Zhang, W., Cao, Y., Zhu, Y., Wu, Y., Ji, X., He, Y., ...& Wang, W. (2017). Flood frequency analysis for alterations of extreme maximum water levels in the Pearl River Delta. *Ocean Engineering*, 129, 117-132.

Water Education: A Case Study in New South Wales Australia

Jenis F Islam^{1,*}, Sumya Rahman², Imran Rahman³

¹School of Computing, Engineering and Mathematics, Western Sydney University, Australia

²EnviroWater Sydney, Sydney, Australia

³University of Technology Sydney, Australia

*Corresponding author's email: jenisislam04@gmail.com

Peer review history

Manuscript submitted: 16 July 2019

Review process completed: 19 August 2019

Manuscript finally accepted: 20 August 2019

Handling Editor: Professor Aatur Rahman

Abstract: Water is vital source of life. In developed countries, we are extremely fortunate to be able to access water at our fingertips, with little cost. Consequently, our water use is so much that per capita, per day water demand in Sydney is about 303 litres. In contrast, about 1 billion of the world's population does not have access to as little as 5 litres of safe drinking water per day. Access to safe drinking water is regarded as a basic human right, but to our surprise, approximately one-fifth of the

world's population does not have access to safe drinking water. Water is also an integral part of the eco-system. Educating our school students about water is important so that this precious resource is preserved and enhanced for all the human beings. This paper presents an overview of water education in New South Wales. It has been found that New South Wales' school children receive basic education on water such as learning about the hydrologic cycle and water recycling but limited mathematical aspects of water management are taught. Due to climate change, increasing water demand and increasing pollution will make water accessibility a challenging issue in the near future. Water education will assist to achieve sustainable water development practices in Australia.

Keywords: Water, School education, Water education, Teaching and learning.

1. Introduction

Water is one of the most important resources for our survival on this planet. Water is directly consumed by human beings and is the cornerstone of sustainable development. Water is further used in recreational activities and most of our food production directly depends on water. To manage water resources, we need to educate the society at different levels. We need water experts who can treat, transport and reserve water for us. At the same time, an ordinary person needs to know how to save the water. In many locations, a person has to travel long distance to fetch drinking water. Many people in the world do not have access to clean drinking water, which hinders their growth and undermines their quality of life.

Water is linked with many different disciplines of knowledge (Rahman et al., 2018). Water education starts from early childhood at the household level, e.g. distinguishing clean water from contaminated water, washing hands with clean water before taking food and turning off the tap when it is not needed. School children learn water science in many different subjects. In the universities, there are subjects that teach water science or engineering at a greater depth in order to produce water experts. These water experts manage water resources in a country and their typical jobs include provision of clean drinking water, flood management, irrigation project management, wastewater treatment, clean-up of rivers and bays and water recycling and conservation. A water expert needs diverse knowledge often encompassing multiple disciplines such as mathematics, physics, chemistry, biology, economics and sociology. They often study specialist subjects such as fluid mechanics, hydraulics, hydrology, water treatment, fluid dynamics and water resources management. Due to the intrinsic relationship of water with the environment, water has been made as a subject of study in many disciplines of knowledge (Grimmond, 2010).

This paper presents an overview of water education in Australia. At the beginning, it presents general aspects of water. This is followed by an overview of grand water challenges. The importance of water education is then highlighted, which is followed by an overview of water education in NSW schools.

2. Water: Origin, Composition Myths and Importance

Water has been an integral part of every facet of society. It has presented itself from religious texts to agriculture and urban planning. The various stories of water indicate the long-standing curiosity and affinity humans have had with water.

As noted by Biswas (1970), the history of mankind can be written in terms of human interactions and interrelations with water.

Throughout the ages water has permeated into the stories, legends and myths of cultures around the world; Scottish mythology describes a translucent water creature that is mistaken for ghosts. Scandinavian folklore claims the existence of a horse that would lurk near rivers during foggy weather. If anyone tried to ride the horse, the horse would jump into a river and drown their rider who would be trapped and unable to separate itself from the horse. Aboriginal stories talk about an evil spirit, the Bunyip who lived in water areas, eating humans and spreading disease through water. Dragon Kings from Chinese mythology ruled over the four seas of China. From the Kraken, Jengy, Grindylows and Leviathan - creatures of the water are myriad. Just as many stories exist about creatures of water, there are legends where water plays a significant part in the story, such as the River Styx which granted invincibility to Achilles' entire body, excluding his heels. This became his eventual downfall when an arrow was shot into his heels, or the story of Manu from Hindu mythology, who survives a flood when he finds a fish in the form of a God in the river.

Stories of the past show the fascination humans have always had with water. As science progressed, the knowledge and importance of water progressed also. It is almost common knowledge now, that water is essential for human survival whereby humans would be unable to survive 3-5 days without water. Water makes up about 60% of the human body. It is required in the transport of nutrients to cells and maintaining the blood volume for healthy functioning of the heart. It is also common knowledge that water is composed of hydrogen and oxygen molecules in the ratio of 2:1, respectively. Humans have discovered what exactly water is with regards to its chemical composition, however fascinating questions still remain - water is recycled on Earth, but where exactly does water come from, how did it first come to Earth? Why has water only been found on Earth, not in our neighbouring planets?

3. Grand Issues in Water Management

The biggest issue in water management is drinking water supply to the millions of people living in developing countries. More than 1.2 billion people lack access to clean drinking water out of 7.2 billion people (i.e. about 17% of people living in the world). This is equivalent to 40 times of the current Australian population. It is surprising that even in this age of superior technology, we cannot serve 1.2 billion of our fellow human beings with as little as 5 litres of clean drinking water. Our scientific community and world leaders should take this as one of their gross failures.

The second biggest challenge is death and damage due to flooding. For example, in 2017 alone, flood damage in USA cost the economy about US\$ 60.7 billion. Due to climate change, flood severity and damage will increase in the near future. In Australia, between 1852 and 2011, at least 951 people were killed by floods and another 1326 were injured. The third biggest water related challenge is the lack of water for agricultural use i.e. drought. These costs billions of dollars of damage worldwide every year. Most of the droughts are followed by famine, deaths and displacement.

Another challenge is how to provide clean water to war displaced people who live in camps where there is little infrastructure for the provision of drinking water.

As noted by Rahman (2017), we have done very well in many areas of water resource management, but our failures in certain areas have caused misery to millions of people such as increased salinity due to over irrigation, failure of dam causing deaths and destruction, and water contamination by micro-plastics.

4. Water and Sustainability Education: Example in Literature

Middlestadt et al. (2001) presented a case study on water conservation education in Jordanian schools. This study measured the effectiveness of advising water conservation within homes and the impact of educating students and families to promote water conservation behaviours. The participants were selected at random, where comparisons were made among 671 students in high school in central Jordan, where 424 of the students were 'experimental' and 247 students were the 'control'. The investigated groups consisted of students whom existed in classes where the teachers implemented an interactive curriculum and promoted water conservation practice. The control group, however, did not participate in classes with curriculum implementation but were exposed to lectures about biodiversity issues. The results show that the students involved in the interactive curriculum activities had a higher level of knowledge and understanding about water conservation and demonstrated better water conservation behaviour, more frequently than students within the controlled group.

Blanton et al (2007) presented a case study on the role of school children in the promotion of point-of-use water treatment and hand washing in schools and households in Western Kenya. This study examined the effect of training teachers to promote water treatment and in addition they installed drinking water and hand washing stations in 17 rural schools. They also aided in treating the water by giving schools flocculent-disinfectant powder and hypochlorite solution. They conducted a baseline water handling survey of students' parents from 17 schools and tested stored water for chlorine. They then conducted follow-up surveys and chlorine testing at 3 and 13 months. It was found that parental awareness of the flocculent-disinfectant increased, awareness of hypochlorite remained high, and also household use of flocculent-disinfectant and hypochlorite increased and were maintained after 13 months. Furthermore, the absentee rates of students decreased by 26% after implementation and also a significant increase in household water treatment procedures were also observed.

Laurence et al (2007) presented a case study on the effect of health after promoting schools' approaches to increasing consumption of fruit and water in Australia. The 'Fresh Kids' program formulated an agenda where they concentrated on promoting behaviours related to healthy eating and reducing the risk factors associated with childhood obesity. The objective of the program was to increase fruit and water consumption among school children over a period of 2 years. The study involved four primary schools in the inner west of Melbourne, Australia. Baseline data were collected to assess the frequency of children with fresh fruit, water and sweet drinks, which were either brought from home or bought from the canteen. The lunchbox inspection was repeated continuously for up to 2 years following the program implementation to assess the sustainability of dietary changes. Within all participating schools, increases between 25% and 50% were observed of children bringing fresh fruits. Furthermore, all schools recorded increases between 15% and 60% of children bringing filled water bottles to school and a reduction between 8% and 38% of children bringing sweet drinks were observed. These important changes were present and sustained for up to 2 years following the program implementation.

Higgs and McMillan (2006) presented a case study on teaching through modelling and the experiences in sustainability education. The authors examined how four innovative secondary schools' model sustainable practices to their students. The authors frequently visited the four schools to conduct interviews. Furthermore, they observed daily interactions and reviewed school documents. They found that modelling is an effective approach to sustainability education. The four primary methods in which the schools model sustainability is individual role modelling, school facilities and operations, school governance, and school culture. Other schools interested in promoting sustainability education will likely find these approaches to modelling effective.

Zheng et al. (2018) conducted a study to compare textbooks between China and USA in relation to water education. They noted that when introducing 'water' knowledge, the American edition uses 271 declarative sentences with lots of information covering use, distribution and protection of water resources; however, the Chinese books contains 16 declarative sentences and mainly introduces the nature, distribution and protection of water without much interpretation. Zhan et al. (2018) presented a case study on developing elementary school children's water conversation action competence in China. In a Shanghai primary school, 69 children (aged 6-8) participated in the water education program for 7 consecutive weeks. The results obtained, based on the 'drawing and telling' approach and pre-survey demonstrated that the participants only have a superficial understanding of water, low awareness of saving water, and limited knowledge of water conservation methods before they joined the programme. After completing the programme, the results show that the children's water conservation knowledge (willingness, self-efficacy, and behaviour) enhanced notably.

The above studies show that water education can be enhanced in schools by adopting specially designed projects. Water Education and Research Committee in Australian Water Association has a number of programs to promote water education in schools and universities in Australia. Water education depends on the status of science education as explained in Rahman et al. (2018).

5. Water Education in Australian Schools

5.1 Curriculum Overview

Australian high school education is based on the Australian Curriculum, Assessment and Reporting Authority. This report will focus on the NSW Education Standards' (NESA) syllabus, providing an overview of water content delivered in NSW

Table 1. Syllabus explaining students' learning requirements regarding water (NSW)

Stage (years)	Syllabus Points
Stage 1 (K-2)	<p>Describe what plants and animals, including humans, need to stay alive and healthy, e.g. food, water and air (page 37)</p> <ul style="list-style-type: none"> Identify that some common resources are obtained from the Earth, including soil, minerals and water (page 44) Share their observations and ideas about the ways that water is used by people in their daily lives (page 44) Identify some actions which could be taken to care for and use water sustainably, e.g. turning off dripping taps and/or taking shorter showers (page 44)
Stage 2 (3-4)	<ul style="list-style-type: none"> Describe some changes in the landscape that have occurred over time as a result of natural processes, e.g. erosion by wind and water (page 55)
Stage 3 (5-6)	<ul style="list-style-type: none"> Identify some physical conditions of a local environment, e.g. temperature, slope, wind speed, amount of light and water (page 69)
Stage 4 (7-8)	<ul style="list-style-type: none"> (a) Identify that water is an important resource that cycles through the environment (b) Explain the water cycle in terms of the physical processes involved (c) Demonstrate how scientific knowledge of the water cycle has influenced the development of household, industrial and agricultural water management practices (page 109) Explain that the systems in multicellular organisms work together to provide cell requirements, including ...water...and to remove cell wastes (page 112) Describe the importance of water as a solvent in daily life, industries and the environment (page 115)
Stage 5 (9-10)	None
Stage 6 (11-12)	<p>Biology:</p> <ul style="list-style-type: none"> Trace the digestion of foods in a mammalian digestive system, including...water (page 39) <p>Chemistry:</p> <ul style="list-style-type: none"> Demonstrate, explain and predict the relationships in the observable trends in the physical and chemical properties of elements in periods and groups in the periodic table, including but not limited to...reactivity with water (page 37) Describe and analyse the processes involved in the dissolution of ionic compounds in water (page 51) What is the role of water in solutions of acids and bases? (page 53)

schools across the major Key Learning Areas including Geography, History, Science and Personal Development, Health and Physical Education' (PDHPE).

Geography has the largest focus on water education whereby an entire Stage 4 (years 7-8) module is dedicated to water. The module is called "Water in the World" and the content is divided into the topics of water resources, water cycle, Australia's water resources, water scarcity and water management and the value of water. A few examples of specific syllabus points surrounding the topic of water from the Geography syllabus are outlined below:

- **"Space:** the significance of location and spatial distribution, and ways people organise and manage spaces that we live in e.g., water resources.
- **Interconnection:** no object of geographical study can be viewed in isolation, e.g. how people are affected by the environment with regard to use of water on its quality and availability as a resource.

- **Sustainability:** the capacity of the environment to continue to support our lives and the lives of other living creatures into the future, e.g. pressures on the Earth's water resources, the need to manage environments for a long-term future; and sustainable management approaches.
- Students examine water as a resource and the factors influencing water flows and availability of water resources in different places.
- They investigate the nature of water scarcity and assess ways of overcoming it.
- Students discuss variations in people's perceptions about the value of water and the need for sustainable water management.
- Students also investigate processes that continue to shape the environment including an atmospheric or hydrologic hazard such as flood.

Science teaches aspects surrounding water beginning from Stage 1 (K-2) until Stage 6 (years 11-12). Table 1 describes syllabus points students are required to learn regarding water. In addition to direct content related to water, Science in NSW also explores the chemical composition of water, beginning from Stage 4. As of 2019, Stage 6 (year 11-12) Biology is no longer required to teach specific diseases, however teachers often include diseases spread through water.

History has elective topics in Stage 3 (5-6) and 4 (7-8) which explore the social aspects of water. Topics from the syllabus include:

- Stage 3: The diversity and longevity of Australia's first peoples and the ways Aboriginal and/or Torres Strait Islander peoples are connected to Country and Place (land, sea, waterways and skies) and the implications for their daily lives.
- Stage 4: The cultural achievements of the Khmer civilisation, including its system of water management and the building of the temples of Angkor.
- Stage 4: Theories of the decline of Angkor, such as the overuse of water resources.

PDHPE focuses on physical water safety with students in the form of swimming beginning from Stage 1 to 5. Various topics of water safety are also expanded on such as:

- Stage 3: Describe the place of water-based recreational activities in Australian society and how communities come together to enjoy water-based activities.
- Stage 5: Plan and practise responses to emergencies by explaining priority actions and where they may be required to administer first aid, e.g. in and around water.

5.2. Case Study

An informal study was conducted where randomly selected school students were asked few basic questions to test their knowledge on water. Ten questions were asked to three age groups, where different groups were asked different sets of questions. The questions can be seen within Tables 2, 3 and 4. The three age groups were 'KG-6', 'grade 7-10' and 'grade 11-12'. The answers provided by the students were marked out of 10 for each question depending on how correct their answers were. This was assessed by the last author, who is a water expert.

Table 2. Questions for KG-6 students

Serial	Questions
1	Where can you find water?
2	Can you drink any water?
3	How do you know when water is not drinkable?
4	What is the main source of water?
5	Can you swim in all types of water?
6	How much time do you spend having a shower?
7	Is water free?
8	Can you drink water in poor countries?
9	What diseases can be caused by dirty water?
10	Why do you need to wash your hand before eating?

Table 3. Questions for 7-10 students

Serial	Questions
1	What molecules are water composed of?
2	Have you heard about the water cycle?
3	Which activity consumes the highest amount of water?
4	What are the dangers of flooding?
5	Where does water from our taps come from?
6	How can we minimise wasting water?
7	How many people in the world have access to less than 5L of water a day?
8	Name 3 diseases caused/transmitted by water?
9	If there were no water taps, where could you get water from?
10	What is the price of tap water in Sydney?

Table 4. Questions for 11-12 students

Serial	Questions
1	What components can water be broken into and how?
2	Do any planets other than Earth have water?
3	How would you access water in the Australian desert?
4	What components can water be broken into and how?
5	How much does the tap water in Sydney cost?
6	Where does toilet water go?
7	How can you save water?
8	What is a flood? How many people die during floods each year?
9	How much damage was caused by the Queensland flood in 2010?
10	What is meant by "drought?" How do droughts affect the Australian community?

Table 5. Results of responses from KG-6 students

Question	P1	P2	P3	P4	P5	P6	P7	AVERAGE
Q1	10	10	10	0	5	10	10	7.86
Q2	10	10	10	10	10	10	10	10.00
Q3	0	5	5	5	0	5	0	2.86
Q4	0	10	10	5	5	10	0	5.71
Q5	10	5	0	10	0	10	10	6.43
Q6	10	10	10	10	10	10	10	10.00
Q7	0	0	10	10	5	10	10	6.43
Q8	10	0	0	10	0	5	0	3.57
Q9	5	5	5	0	5	5	5	4.29
Q10	10	5	10	10	10	10	5	8.57
TOTAL	65	60	70	70	50	85	60	65.71

From our gathered results, we can see that average marks for 'KG-6', 'grade 7-10' and 'grade 11-12' were 65.71%, 43.33% and 47.5%, respectively (seen in Table 5, Table 6 and Table 7). The slight increase of 'KG-6' results compared to the other age groups may indicate that the relative knowledge based on their age group are generally satisfactory. Furthermore, if we analyse the results from Table 5 (KG-6) we can observe low scores for question 3, question 8 and question 9. These questions address the issue "which water is safe to drink". The low average score of these questions indicate that individuals within that age group are unaware of the danger of contaminated water.

Moving on in Table 6 (grade 7-10), it can be observed that the average score is 0 for question 3. This exemplifies that individuals within the age group of 'grade 7-10' do not know which of their home appliances uses the most water. This inadequacy of knowledge can also be seen in the age group 'grade 11-12' where the average of question 9 is '2.5' (seen from Table 7). From this it can be argued that individuals within this age group have little knowledge about the Queensland flood, which was one of the worst floods in our living memory, causing over a \$30 billion loss to the

Australian economy. These results indicate that the overall the knowledge of water is not very high within the investigated school students. However, a formal survey is needed involving more schools and a greater number of students to confirm this initial finding.

6. Conclusion

This paper presents an overview of water education in Australia. It has been found that the NSW school curriculum contains water conservation topics quite well; however, mathematical aspects of water science are not covered well. It is important that water is taught at schools at a higher level to make water-educated citizens who value this important resource and so a further group of students take up water education at the university level to become water expert. This will help us to tackle water challenges in a warmer climate more effectively, where water demand will be higher, but water availability will reduce and water disasters will increase in frequency and intensity. Water education will assist to achieve sustainable development of water in Australia.

Table 6. Results of responses from 7-10 students

Question	P1	P2	P3	AVERAGE
Q1	5	5	10	6.67
Q2	10	10	10	10
Q3	0	0	0	0
Q4	5	5	5	5
Q5	0	5	5	3.33
Q6	5	5	5	5
Q7	5	10	0	5
Q8	5	0	5	3.33
Q9	10	0	5	5.00
Q10	0	0	0	0
TOTAL	45	40	45	43.33

Table 7. Results of responses from 11-112 students

Question	P1	P2	P3	P4	AVERAGE
Q1	10	10	5	10	8.75
Q2	10	0	0	10	5
Q3	0	5	5	5	3.75
Q4	0	0	0	0	0
Q5	0	0	0	0	0
Q6	10	10	10	0	7.5
Q7	5	0	5	5	3.75
Q8	5	0	10	10	6.25
Q9	0	0	5	5	2.5
Q10	10	10	10	10	10
TOTAL	50	35	50	55	47.5

7. Acknowledgements

We acknowledge the school students who voluntarily took part in this study.

8. References

- Blanton, E., Ombeki, S., Oluoch, G. O., Mwaki, A., Wannemuehler, K., & Quick, R. (2010). Evaluation of the role of school children in the promotion of point-of-use water treatment and handwashing in schools and households—Nyanza Province, Western Kenya, 2007. *The American journal of tropical medicine and hygiene*, 82(4), 664-671.
- Grimmond, J. (2010). Special Report on Water. *The Economist*, 22 May 2010.

- Higgs, A. L., & McMillan, V. M. (2006). Teaching through modeling: Four schools' experiences in sustainability education. *The Journal of Environmental Education*, 38(1), 39-53.
- Laurence, S., Peterken, R., & Burns, C. (2007). Fresh Kids: the efficacy of a Health Promoting Schools approach to increasing consumption of fruit and water in Australia. *Health Promotion International*, 22(3), 218-226.
- Middlestadt, S., Grieser, M., Hernandez, O., Tubaishat, K., Sanchack, J., Southwell, B., & Schwartz, R. (2001). Turning minds on and faucets off: Water conservation education in Jordanian schools. *The Journal of Environmental Education*, 32(2), 37-45.
- Rahman, A. (2017). Social hydrology. Chapter 155, pp. 155-1 to 155-10, In: *Handbook of Applied Hydrology*, edited by Singh V P, McGraw-Hill.
- Rahman, S., Bhathal, R., & Rahman, A. (2018). Teaching science to engineering students: Application of student-centered and blended learning approaches. In *Blended Learning in Engineering Education* (pp. 223-234). CRC Press.
- Rahman, A., Kordrostami, S., & Purdy, D. (2018). Statistical hydrology teaching using a blended learning approach. *Blended Learning in Engineering Education: Recent Developments in Curriculum, Assessment and Practice*, 1.
- Zhan, Y., He, R., & So, W. W. M. (2018). Developing elementary school children's water conversation action competence: a case study in China. *International Journal of Early Years Education*, 1-19.
- Zheng, Z., Zhou, L., & Zhao, M. (2019, January). The Difference between Chinese and American Primary School Science Textbooks in Arrangement of Knowledge. In *2nd International Conference on Social Science, Public Health and Education (SSPHE 2018)*. Atlantis Press.

Application of water quality index to identify deteriorated river sections – A case study for the Hawkesbury Nepean River System in Australia

Upeka Kuruppu^{1,*}, M Azizur Rahman²

¹School of Computing, Engineering and Mathematics, Western Sydney University, Australia

²Federation University, Victoria, Australia

*Corresponding author's email: u.kuruppu@westernsydney.edu.au

Peer review history

Manuscript submitted: 16 June 2019

Review process completed: 26 August 2019

Manuscript finally accepted: 27 August 2019

Handling Editor: Professor Ataur Rahman

Abstract: The world's water resources are increasingly being threatened with rapid urbanisation. A comprehensive water quality management program is necessary to protect the valuable freshwater resources and to safeguard public health. River water quality assessment mainly involves two components: measurement of water quality variables and comparison of measurements to benchmark with guidelines and water quality objectives to assess the degree of change and its impacts on aquatic environment and human health. Traditionally, water quality data is summarised in technical reports that are valuable to individuals who understand the technical content; however, this information is not always useful to non-technical individuals and community

members. A Water Quality Index (WQI) provides a convenient means of summarising complex water quality data and facilitates its communication to a general audience. This paper presents the use of WQI to identify changes in river water quality over time, identify and assess deteriorated river sections and the water quality parameters which contributed to the deterioration and their relative contributions. The Hawkesbury Nepean River System (HNRS), which is the main source of drinking water supply to more than 4.8 million people living in and around Sydney, Australia, was assessed using a Canadian WQI. Water quality data obtained from 9 sampling stations along the HNRS during the last 21 years (1993 to 2013) were used to identify changes in water quality at different sampling stations over time, and to compare water quality parameters among the stations. The results provide an estimate of the overall water quality against the Australian and New Zealand Water Quality guidelines. It has been found that the overall water quality at the HNRS is at marginal to poor state.

Keywords: Water quality index; Hawkesbury Nepean River System; River water quality.

1. Introduction

Many rivers in world have been highly degraded over the past few decades due to rapid urbanisation (Pinto and Maheshwari, 2011; Edet et al., 201; Zhang et al., 2015). The main reasons for such water quality degradation are discharge of treated sewage into the river system and increased stormwater runoff from urban areas. Rivers that are badly impacted due to anthropogenic activities are said to have suffered from 'Urban stream syndrome' (Walsh et al., 2005). Once a river is deteriorated, it is difficult and costly to purify it to an acceptable level. Algal blooms in Australian rivers cost the country between AUD180 and AUD240 million annually (Atech, 2000). Thus, prediction of water quality is important to prevent possible effects and also it is required by a wide range of river users such as urban water supply authorities, farmers and environmentalists (Pinto et al., 2012; Memarzadeh et al., 2013).

The concept of Water Quality Index (WQI) is based on the comparison of water quality parameters with respective regulatory standards and gives a single value, which can be used to describe the overall quality of a water body (Boyacioglu, 2010). The number of variables with exceedances, frequency of exceedances, and magnitude of exceedances of regulatory standards for specific parameters are reflected in the WQI.

The first studies on WQI were done in 1848 in Germany that developed WQI based on 8 water quality parameters (Sarkar and Abbasi, 2006). Dede et al. (2013) used 5 WQI methods (Oregon WQI, aquatic toxicity index, overall index of pollution, universal WQI, and the Canadian Council of Ministers of the Environment (CCME) WQI) to evaluate surface water quality, and concluded that CCME WQI is the only method that allows utilization of all the available parameters in the calculation of an overall index value. However, it is important to note that the CCME WQI is not a substitute for

detailed analysis of water quality data and should not be used as a sole tool for management of water bodies (Al-Janabi et al., 2012). It was simply developed to provide a broad overview of environmental performance (Khan et al., 2004). The objective of this study was to apply WQI for assessing river water quality.

The Hawkesbury Nepean River System (HNRS) provides 97% of the fresh drinking water for more than 4.8 million people living in Greater Sydney and nearby towns; and hence, the water quality of this river is of great importance (Kuruppu and Rahman, 2013). Although there are a number of dams and in-stream structures in the HNRS, it is considered to be an unregulated river (Kuruppu et al., 2012). This river system is characterized by complex land use ranging from agriculture, commerce, industry, urban and forest. The outcomes of this study would provide an insight into the overall water quality of the HNRS that can be used in developing management strategies to improve the water quality of the HNRS.

2. Methodology

This study uses the CCME WQI, which is based on a formula developed by the British Columbia Ministry of Environment, Lands and Parks and modified by Alberta Environment. This WQI incorporates three elements: (a) Scope (F_1) – the number of variables not meeting water quality objectives; (b) Frequency (F_2) – the number of times these objectives are not met; and (c) Amplitude (F_3) – the amount by which the objectives are not met.

Scope (F_1) assesses the extent of water quality guideline non-compliance over the time period of interest, which means the numbers of parameters whose objective limits are not met. F_1 is defined by:

$$F_1 = \frac{\text{Total number of failed variables}}{\text{Total number of variables}} \times 100 \quad (1)$$

Where the variables indicate those water quality parameters whose objective values (threshold limits) are specified and observed values at the sampling sites are available for the index calculation.

Frequency (F_2) – the frequency (i.e. how many occasions the tested or observed value are off the acceptable limits) with which the objectives are not met, which represents the percentage of individual tests that does not meet the objectives (failed tests):

$$F_2 = \frac{\text{Number of failed tests}}{\text{Total number of variables}} \times 100 \quad (2)$$

Amplitude (F_3) is the amount by which the objectives are not met (amplitude) that represents the amount by which the failed test values do not meet their objectives, and is calculated in three steps. The number of times by which an individual concentration is greater than (or less than, when the objective is a minimum) the objective is termed an “excursion” and is expressed as follows. When the test value must not exceed the objective:

$$\text{excursion}_i = \left(\frac{\text{Failed test value}_i}{\text{Objective}_j} \right) - 1 \quad (3)$$

For the cases in which the test value must not fall below the objective:

$$\text{excursion}_i = \left(\frac{\text{Objective}_j}{\text{Failed test value}_i} \right) - 1 \quad (4)$$

The collective amount, by which the individual tests are out of compliance, is calculated summing the excursions of individual tests from their objectives and then dividing the sum by the total number of tests. This variable, referred to as the normalized sum of excursions (nse) is calculated as:

$$\text{nse} = \frac{\sum_{i=1}^n \text{excursion}_i}{\text{Number of tests}} \quad (5)$$

F_3 is then calculated by an asymptotic function that scales the normalized sum of the excursions from objectives (nse) to yield a value between 0 and 100:

$$F_3 = \left(\frac{\text{nse}}{0.01\text{nse}+0.01} \right) \quad (6)$$

The CCME WQI is finally calculated as:

$$\text{CCME WQI} = 100 - \left(\frac{\sqrt{F_1^2 + F_2^2 + F_3^2}}{1.732} \right) \quad (7)$$

The factor of 1.732 has been introduced to scale the index from 0 to 100. Since the individual index factors can range as high as 100, it means that the vector length can reach a maximum of 173.2 as shown below:

$$\sqrt{100^2 + 100^2 + 100^2} = \sqrt{30000} = 173.2 \quad (8)$$

The index produces a number between 0 (worst water quality) and 100 (best water quality). These numbers are divided into 5 descriptive categories to simplify presentation, as listed below.

- Excellent: (CCME WQI Value 95-100) – water quality is protected with a virtual absence of threat or impairment; conditions very close to natural or pristine levels.
- Good: (CCME WQI Value 80-94) – water quality is protected with only a minor degree of threat or impairment; conditions rarely depart from natural or desirable levels.
- Fair: (CCME WQI Value 65-79) – water quality is usually protected, but occasionally threatened or impaired; conditions sometimes depart from natural or desirable levels.
- Marginal: (CCME WQI Value 45-64) – water quality is frequently threatened or impaired; conditions often depart from natural or desirable levels.
- Poor: (CCME WQI Value 0-44) – water quality is almost always threatened or impaired; conditions usually depart from natural or desirable levels.

3. Study area and data description

This study uses data from the HNRS in the Australian State, New South Wales (NSW). The Hawkesbury-Nepean catchment is one of the largest coastal basins in NSW. With an area of 21,400 square kilometres, over 70 per cent of the catchment consists of mountainous terrain, with about 10 per cent of flat terrain. The south terrain, around 10 per cent of the total catchment, comprises undulating plateau type country. The maximum elevation is about 1,290 metres. The HNRS supports a \$259 million agriculture industry. Major water users in this catchment include Sydney Water



Figure 1. Water quality monitoring stations along the HNRS

Corporation, local councils, the irrigated agriculture, tourism, fishing and oyster industries, and various recreational users. Sydney Water supplies water to most homes and businesses within the Greater Sydney Metropolitan area. Thus, monitoring and assessing the water quality of this river system is of immense importance. Many government organizations, researchers and environmental agencies monitor and collect water quality data along the HNRS; however, the full capacity of the water quality data set has not been well used to draw meaningful conclusions describing the state of the river due to the complexity of analysing the data and summarizing the results in ways that can be easily understood by the general people, water distributors, planners, managers and policy makers. In this study, water quality data obtained from 9 sampling stations along the HNRS during the last 21 years (1993 to 2013) are evaluated for track changes at different stations over time, and for comparisons among the stations. Figure 1 showed the water quality monitoring stations along the HNRS. A schematic diagram of the monitoring stations along the HNRS with the land use details and all the inflows are presented in Figure 2.

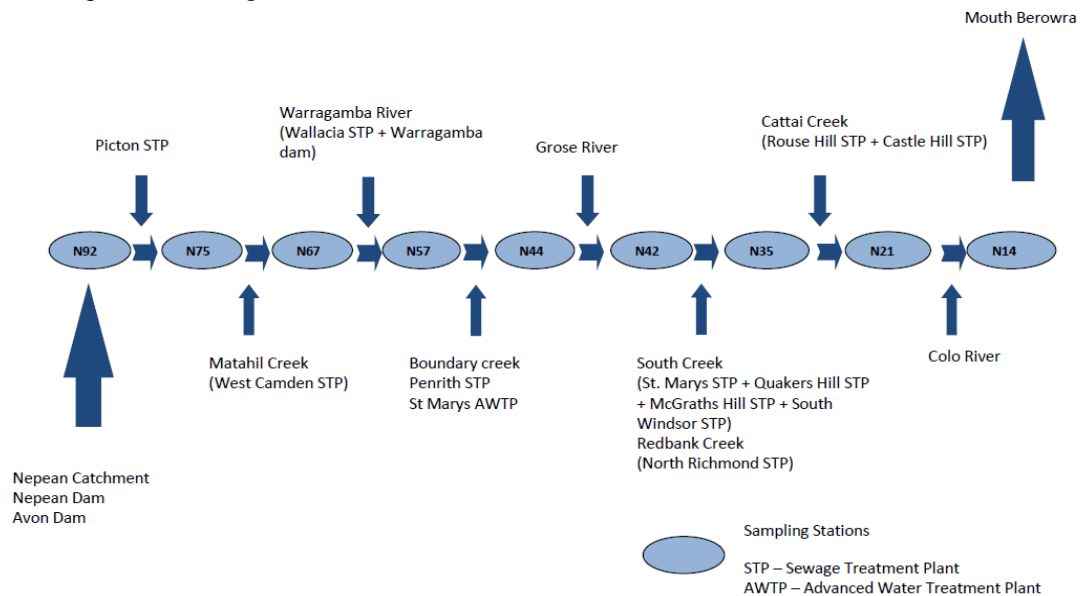


Figure 2. Schematic diagram of the monitoring stations along HNRS with the land use details

Table 1. ANZECC Guidelines for Fresh and Marine Water Quality

Water quality parameter	ANZECC trigger value		Unit
	Maximum	Minimum	
pH	8	6	
Nitrogen Total	0.35		mg/L
Phosphorous Total	0.05		mg/L
Chlorophyll	5		µg/L
Dissolved Oxygen		5	mg/L
Turbidity	20		NTU
Iron Total	0.3		mg/L
Aluminium Total	0.2		mg/L
True Colour	15		
Alkalinity	20		
Suspended Solids	20		
Conductivity	0.35		mS/cm

For the calculation of CCME WQI, 12 water quality parameters were selected based on the importance and the availability of data (Kuruppu and Rahman, 2015). The water quality data was obtained from Water New South Wales who adopted a standard laboratory procedure to test/monitor water quality from the HNRS. These selected water quality parameters and Australian and New Zealand Guidelines for Fresh and Marine Water Quality (ANZECC, 2000) are presented in Table 1.

4. Results and Discussion

WQIs were primarily developed for each year between 1993 and 2013 at 9 sampling locations to investigate the water quality changes along the HNRS over time. An improvement of water quality over time was observed at most of the stations (Figure.3). Also, the results shows a marginal water quality with WQI of 45 – 64 at all the stations except N14 and N35, which have WQIs less than 40 over the years.

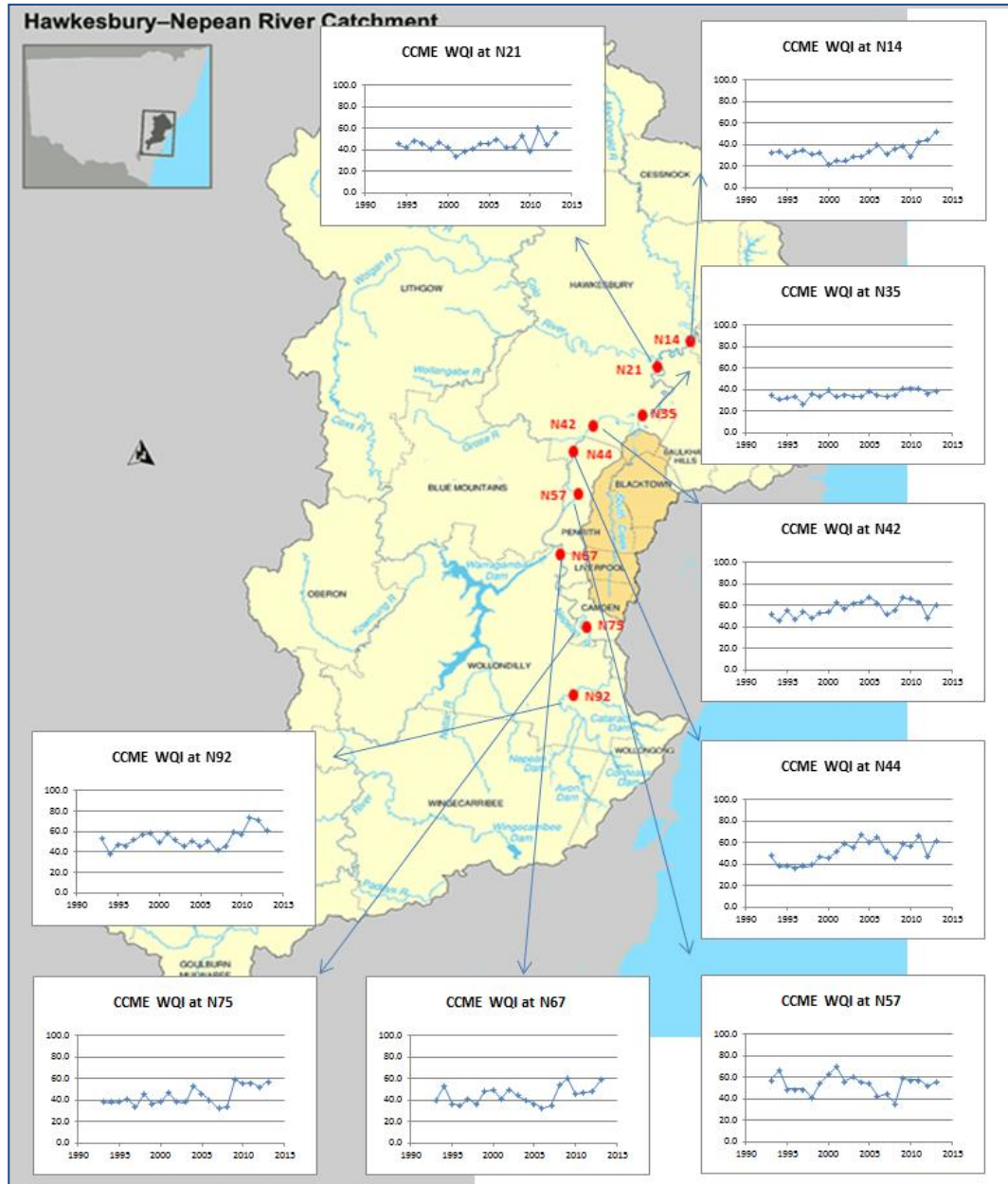


Figure 3. Change in WQI over time for 9 monitoring stations in HNRS

Medians of CCME WQI values over the 21 years range from 33 to 57. All the monitoring stations indicate marginal or poor water quality. Water quality at N21, N42, N44, N57 and N92 is frequently threatened or impaired. WQIs at N14, N35, N67 and N75 are below 40 indicating that water quality at these stations is almost always threatened or impaired (Figure 4).

Scope, frequency, and amplitude values at 9 monitoring stations are presented in Figure 5. At station N35, nearly 90% of water quality values are beyond the ANZECC guideline values. Station N35 shows the highest frequency and highest amplitude (46.3) among 9 monitoring stations. The upstream of N35 is affected by quality and magnitude of flows

coming from the South Creek that carries discharges from St. Marys Sewage Treatment Plant (STP), Riverstone STP, Quakers Hill STP, McGraths Hill STP and South Windsor STP and North Richmond STP. The dominant land use in this part of the catchment includes rural use, grazing, commercial gardening, intensive agriculture, and urban and industrial activities. These land uses can be attributed to the low WQI at station N35.

At station N14, 81% of the water quality data is outside the ANZECC guidelines. This station also has an amplitude of 70%. Between 1993 and 2008, amplitudes were greater than 60%. Table 2 presents the amplitudes at 9 stations during 1993 - 2013. The years with higher amplitude (greater than 60%) are indicated in red.

Further data exploration was done at station N14 as it shows the worst WQI among the 9 stations. Table 3 presents details of percentage failed tests for different water quality parameters (the total number of tests, number of failed tests, and percentage failed for each parameter for different years). Total nitrogen, chlorophyll-a (Chl-*a*), total iron, total aluminium, alkalinity, and conductivity exceeded the ANZECC guidelines in many occasions. The water quality at Stations N14 (and N21 and N35) are highly affected by discharges from South Creek and Cattai Creek which receive effluents from 6 STPs as shown in Figure 2.

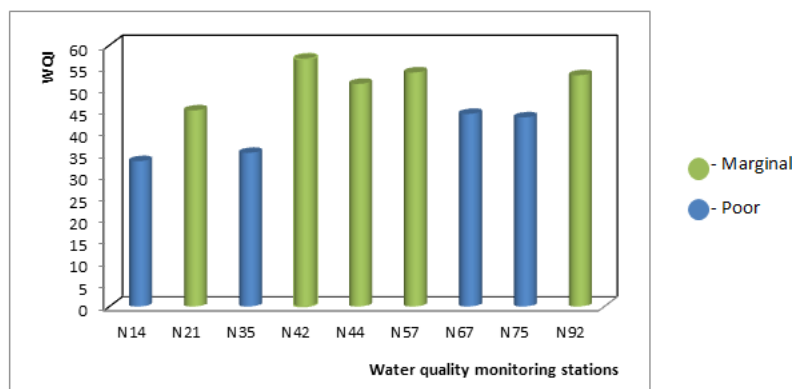


Figure 4. Average WQI along the HNRS

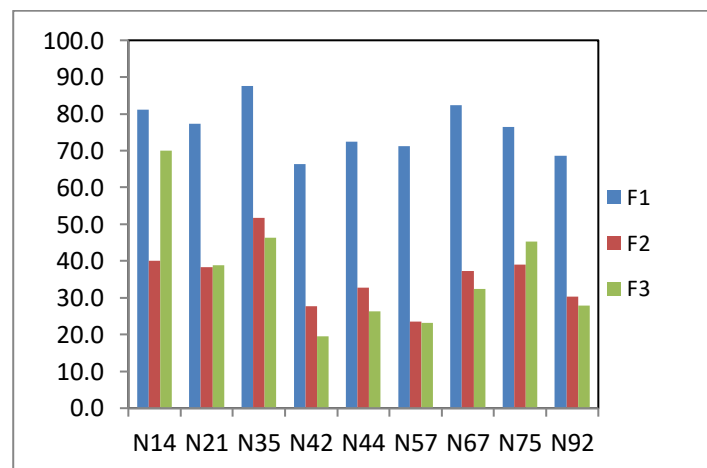


Figure 5. Scope, frequency, and amplitude values at 9 monitoring stations in HNRS

Table 3 indicates that water quality at station N14 is poor with respect to nitrogen, Chl-*a*, iron, aluminium and conductivity. Nitrogen is a nutrient used by plants within natural ecosystems, with minimal leakage into surface or groundwater (Vitousek et al., 2002). Nitrogen concentrations in streams generally increase due to discharge of sewage water, pollutant wash off from urban and agricultural land, and atmospheric deposition. Increased nitrogen may result in an overgrowth of algae, resulting in an increase in eutrophication of the aquatic system and decrease in dissolved oxygen content of the water, thereby harming or killing fish and other aquatic species (USEPA, 2005). Control of nitrogen load in urban river systems is viewed as a priority by many river management authorities as this affects the growth of algae (algal bloom) and other aquatic plants. Harmful algal bloom is considered to be a serious event in regard to water quality as some species of these aquatic organisms can excrete toxic chemicals (e.g. microcystis produced by a blue-green algae

Microcystis aeruginosa). A number of episodes of harmful algal bloom and rapid growth of aquatic weeds were observed in the HNRS in the past causing public concern. For example, the shallow mid Nepean River section was affected heavily by aquatic weed *Egeria densa* (Roberts et al., 1999) and the Berowra Creek estuarine section of the river was infested by toxic dinoflagellate algal blooms (SMEC, 1997).

The long-term persistence of elevated levels of Chl-*a* is a significant concern to water authorities. An excessive growth often leads to poor water quality, noxious odours, oxygen depletion, and human health problems and fish death. It may also be linked to harmful (toxic) algal blooms. Poor water quality associated with high Chl-*a* concentration needs to be distinguished from the natural variation observed with the seasons and those associated with hydrodynamic features (e.g. upwelling). However, there is very little information to make this distinction (Ward et al., 1998). Observed increases in the concentrations of Chl-*a* may be related to increased nutrient concentrations (nitrogen in particular), decreased flow/changed hydrodynamics (increased residence times) and/or decreased turbidity (increased light penetration) (i.e. the increasing eutrophication).

If the alkalinity level is too high, the water can be cloudy, which inhibits the growth of aquatic plants and algae. This may be considered to be a controlling measure of harmful algal bloom; however, a higher alkalinity may raise the pH level, which in turn can harm or kill fish and other aquatic organisms which are very sensitive to higher pH levels. High alkalinity may result from the presence of the bicarbonate ion, which is derived from the dissolution of carbonates by carbonic acids due to factors such as weathering of limestone and dolomite rocks mainly composed of calcite.

Table 2. Amplitudes at 9 stations in different years

Index Period	Stations								
	N14	N21	N35	N42	N44	N57	N67	N75	N92
2013	39.0	31.2	39.9	29.5	34.8	30.1	35.5	24.7	20.2
2012	44.4	32.1	43.4	31.4	35.4	23.0	26.4	20.6	16.8
2011	49.9	24.8	34.7	7.2	14.8	18.8	21.9	15.5	7.5
2010	50.8	40.4	35.7	17.1	18.7	22.9	25.1	24.4	22.3
2009	52.3	33.1	37.4	10.8	22.3	35.4	31.1	36.8	31.3
2008	65.9	32.0	42.6	24.9	30.6	49.7	41.0	53.4	43.5
2007	71.0	38.5	43.6	22.3	33.4	50.5	46.4	57.2	55.8
2006	81.6	43.2	45.3	15.9	22.2	41.5	47.0	60.9	50.7
2005	76.3	43.4	44.7	13.9	23.8	32.3	41.1	53.9	39.3
2004	82.9	45.2	46.6	15.2	26.7	35.3	37.0	55.4	38.9
2003	80.2	39.3	43.7	17	26.7	41.3	37.7	54.8	43.3
2002	78.7	37.7	41.4	19.2	26.3	29.7	30.6	52.8	40.1
2001	78.2	35.3	38.9	16.7	23.4	3.6	29.4	40.0	26.0
2000	87.1	35.2	41.0	16.3	22.0	6.9	25.8	49.3	30.2
1999	65.1	42.7	50.4	22.5	38.2	18.8	35.5	55.6	19.9
1998	75.0	39.9	50.7	19.5	22.8	10.6	30.6	49.2	20.7
1997	81.2	46.4	58.3	21.5	27.0	7.4	34.5	59.1	19.7
1996	69.2	39.0	54.7	20.6	30.4	9.4	33.3	60.1	13.5
1995	80.4	37.7	58.0	18.2	24.3	12.2	27.8	50.3	7.9
1994	85.3	60.1	60.9	20.1	20.7	2.0	18.0	51.4	17.8
1993	74.8		61.5	31.4	29.2	4.1	23.4	24.5	18.9

Table 3. Water quality results at N14 (yellow colour indicates 25% to 49% failure and red colour indicates $\geq 50\%$ failure)

Index Period	pH			Nitrogen Total			Phosphorous Total			Chlorophyll			Dissolved Oxygen			Turbidity		
	Number of Tests	Number of Failed Tests	Percent Failed (%)	Number of Tests	Number of Failed Tests	Percent Failed (%)	Number of Tests	Number of Failed Tests	Percent Failed (%)	Number of Tests	Number of Failed Tests	Percent Failed (%)	Number of Tests	Number of Failed Tests	Percent Failed (%)	Number of Tests	Number of Failed Tests	Percent Failed (%)
2013	4	0		4	3	75.0	4	0		4	4	100.0	4	0		4	0	
2012	13	0		14	11	78.6	14	0		15	12	80.0	13	0		13	2	15.4
2011	13	0		13	7	53.8	13	0		13	13	100.0	13	0		13	3	23.1
2010	12	1	8.3	12	10	83.3	12	1	8.3	12	11	91.7	12	1	8.3	10	4	40.0
2009	13	1	7.7	13	8	61.5	13	0		13	12	92.3	13	0		13	1	7.7
2008	12	0		12	8	66.7	12	0		12	11	91.7	12	0		12	2	16.7
2007	13	0		12	11	91.7	12	1	8.3	13	8	61.5	13	0		13	4	30.8
2006	13	0		13	8	61.5	13	0		13	7	53.8	13	0		13	0	
2005	12	0		12	8	66.7	12	0		12	11	91.7	12	0		12	1	8.3
2004	13	0		13	7	53.8	13	1	7.7	13	7	53.8	13	0		13	2	15.4
2003	13	1	7.7	13	11	84.6	13	1	7.7	13	10	76.9	13	0		12	1	8.3
2002	14	0		14	10	71.4	14	3	21.4	14	9	64.3	14	1	7.1	14	5	35.7
2001	17	0		11	8	72.7	11	1	9.1	17	11	64.7	17	2	11.8	17	5	29.4
2000	21	2	9.5	16	12	75.0	16	1	6.3	27	12	44.4	21	1	4.8	21	2	9.5
1999	12	1	8.3	26	25	96.2	26	7	26.9	26	22	84.6	12	0		0	0	
1998	24	2	8.3	24	20	83.3	24	7	29.2	24	13	54.2	24	0		0	0	
1997	23	0		23	9	39.1	23	3	13.0	23	18	78.3	23	0		0	0	
1996	19	1	5.3	26	16	61.5	26	2	7.7	26	18	69.2	26	0		0	0	
1995	26	1	3.8	26	18	69.2	26	3	11.5	25	11	44.0	25	0		0	0	
1994	25	2	8.0	26	13	50.0	24	0		26	5	19.2	25	0		0	0	
1993	7	1	14.3	8	8	100.0	25	1	4.0	25	9	36.0	24	0		0	0	

Index Period	Iron Total			Aluminium Total			True Colour			Alkalinity			Suspended Solids			Conductivity		
	Number of Tests	Number of Failed Tests	Percent Failed (%)	Number of Tests	Number of Failed Tests	Percent Failed (%)	Number of Tests	Number of Failed Tests	Percent Failed (%)	Number of Tests	Number of Failed Tests	Percent Failed (%)	Number of Tests	Number of Failed Tests	Percent Failed (%)	Number of Tests	Number of Failed Tests	Percent Failed (%)
2013	4	3	75.0	4	2	50.0	4	3	75.0	4	4	100.0	4	0		4	3	75.0
2012	14	10	71.4	14	8	57.1	14	5	35.7	14	11	78.6	14	2	14.3	13	10	76.9
2011	13	9	69.2	13	7	53.8	13	5	38.5	13	9	69.2	13	2	15.4	12	8	66.7
2010	12	9	75.0	12	7	58.3	12	5	41.7	12	11	91.7	12	1	8.3	9	7	77.8
2009	13	8	61.5	13	6	46.2	13	3	23.1	13	13	100.0	13	1	7.7	11	8	72.7
2008	12	9	75.0	12	9	75.0	12	5	41.7	12	12	100.0	12	1	8.3	11	10	90.9
2007	12	9	75.0	12	8	66.7	12	3	25.0	12	11	91.7	12	4	33.3	13	12	92.3
2006	13	5	38.5	13	6	46.2	13	0		13	13	100.0	13	2	15.4	12	11	91.7
2005	12	7	58.3	12	6	50.0	12	2	16.7	12	12	100.0	12	4	33.3	12	12	100.0
2004	13	6	46.2	13	5	38.5	13	2	15.4	13	13	100.0	13	1	7.7	13	13	100.0
2003	13	6	46.2	13	6	46.2	13	0		13	13	100.0	13	4	30.8	12	12	100.0
2002	14	10	71.4	14	11	78.6	14	4	28.6	14	12	85.7	14	8	57.1	14	13	92.9
2001	6	5	83.3	6	5	83.3	6	1	16.7	6	6	100.0	17	8	47.1	17	17	100.0
2000	0	0		0	0		0	0		0	0		27	1	3.7	21	18	85.7
1999	0	0		0	0		0	0		0	0		26	1	3.8	12	11	91.7
1998	0	0		0	0		0	0		0	0		24	7	29.2	24	20	83.3
1997	0	0		0	0		0	0		0	0		23	3	13.0	23	23	100.0
1996	0	0		0	0		0	0		0	0		26	6	23.1	19	19	100.0
1995	0	0		0	0		0	0		0	0		26	4	15.4	26	25	96.2
1994	0	0		0	0		0	0		0	0		23	8	34.8	24	24	100.0
1993	0	0		0	0		0	0		0	0		16	1	6.3	8	8	100.0

There are number of factors that can lead to high conductivity levels in river water. For examples, streams that run through clay catchments may have a higher conductivity level as the presence of clay particles ionize when they enter into the river system (DSEWPC, 2013). Groundwater inflows can have the same effects if it contains clay particles (Tutmez et al., 2006). An underperforming STP could raise the conductivity level because of the presence of chloride, phosphate and nitrate (Morrison et al., 2001).

5. Conclusion

This study applies WQI method to effectively derive information from complex water quality data sets to assess the water quality of the HNRS in NSW, Australia. Water quality data obtained from 9 sampling stations along the HNRS during the last 21 years were evaluated for track changes at different water quality monitoring stations over time, and for comparisons among stations. The CCME WQI method with Australian and New Zealand Guidelines for Fresh and Marine Water Quality (ANZECC) have been applied to identify the deteriorated zones of the HNR and identify the water quality parameters which contribute to poor WQI. Among the 9 sampling stations in the HNRS examined here, 5 demonstrate a marginal water quality and 4 demonstrate poor water quality. Stations N14 and N35 are the most polluted stations. These stations are mainly affected by the effluents of six sewage treatment plants. At N14, it has been found that total nitrogen, chlorophyll-a (Chl-a), total iron, total aluminium, alkalinity, and conductivity have exceeded the ANZECC guidelines in many occasions. Overall, the water quality in the HNRS is at a marginal to poor state. The findings of this study can be used to devise an intervention program to improve the overall water quality of the HNRS.

References

- Al-Janabi, Z. Z., Al-Kubaisi, A. R., & Al-Obaidy, A. H. M. J. (2012). Assessment of Water Quality of Tigris River by using Water Quality Index (CCME WQI). *Al-Nahrain Journal of Science*, 15(1), 119-126
- ANZECC (2000). Australian and New Zealand Guidelines for Fresh and Marine Water Quality, Accessed at <https://www.environment.gov.au/water/quality/publications/australian-and-new-zealand-guidelines-fresh-marine-water-quality-volume-1> dated 25/01/2015.
- Atech, (2000). Cost of algal blooms. LWRDC Occasional paper 26/99. Land and Water Resources Research and Development Corporation, Canberra, ACT, Australia, 42 pp.

- Boyacioglu, H. (2010). Utilization of the water quality index method as a classification tool, *Environmental Monitoring and Assessment*, 167(1-4), 115-124.
- Dede, O. T., Telci, I. T., & Aral, M. M. (2013). The use of water quality index models for the evaluation of surface water quality: a case study for Kirmir Basin, Ankara, Turkey, *Water Quality, Exposure and Health*, 5(1), 41-56.
- DSEWPC. 2013. Characterising the relationship between water quality and water quantity. Final Report, August 2013. Department of Sustainability, Environment, Water Population and Communities, Australian Government.
- Edet, A., Ukpong, A., & Nganje, T. (2013). Hydrochemical studies of Cross River Basin (southeastern Nigeria) river systems using cross plots, statistics and water quality index. *Environmental earth sciences*, 70(7), 3043-3056.
- Khan, A. A., Paterson, R., & Khan, H. (2004). Modification and Application of the Canadian Council of Ministers of the Environment Water Quality Index (CCME WQI) for the Communication of Drinking Water Quality Data in Newfoundland and Labrador, *Water Quality Research Journal of Canada*, 39(3), 285-293.
- Kuruppu, U., & Rahman, A. (2015). Trends in water quality data in the Hawkesbury-Nepean River System, Australia, *Journal of Water and Climate Change*, 6, 4, 816-830.
- Kuruppu, U. & Rahman, A. (2013). An Exploratory Analysis of Water Quality in the Nepean River, Australia, 35th IAHR World Congress. September 8 to 13, 2013 Chengdu, China, 1-6.
- Kuruppu, U., Al-Mamoon, A., Rahman, S. & Rahman, A. (2012). Environmental monitoring and impact assessment: a case study for the Hawkesbury-Nepean River system in Australia, *International Journal of Environmental Science and Engineering Research*, 3(3), 25-34.
- Memarzadeh, M., Mahjouri, N., & Kerachian, R. (2013). Evaluating sampling locations in river water quality monitoring networks: application of dynamic factor analysis and discrete entropy theory. *Environmental earth sciences*, 70(6), 2577-2585.
- Morrison, G., Fatoki, O. S., Persson, L., & Ekberg, A. (2001). Assessment of the impact of point source pollution from the Keiskammahoek Sewage Treatment Plant on the Keiskamma River-pH, electrical conductivity, oxygen-demanding substance (COD) and nutrients. *Water SA*, 27(4), 475-480.
- Pinto, U. & Maheshwari, B. L. (2011). River health assessment in peri-urban landscapes: An application of multivariate analysis to identify the key variables. *Water Research*, 45(13), 3915-3924.
- Pinto, U., Maheshwari, B. L., Shrestha S. & Morris C. (2012). Modelling eutrophication and microbial risks in peri-urban river systems using discriminant function analysis. *Water Research*, 46, 6476-6488.
- Roberts D.E., Church A.G. & Cummins S.P. (1999). Invasion of *Egeria* into the Hawkesbury-Nepean River, Australia, *Aquatic Plant Management*, 37, 31-34.
- SMEC (1997). Options for sewage treatment and effluent disposal for west Hornsby and Hornsby Heights Sewage Treatment Plants, Prepared for Sydney Water, SMEC Australia.
- Sarkar C, Abbasi S. A. (2006). Qualindex - a new software for generating water quality indices. *Environmental Monitoring and Assessment*, 119(1-3), 201-231
- Tutmez, B., Hatipoglu, Z. & Kaymak, U. (2006). Modelling electrical conductivity of groundwater using an adaptive neuro-fuzzy inference system. *Computers & geosciences*, 32(4), 421-433.
- Vitousek, P. M., Cassman, K., Cleveland, C., Crews, T., Field, C. B., Grimm, N. B. & Sprent, J. I. (2002). Towards an ecological understanding of biological nitrogen fixation, *Biogeochemistry*, 57(1), 1-45.
- Walsh, C.J., Allison, H.R., Feminella, J.W., Cottingham, P.D., Groffman, P.M. & Li, R.P.M. (2005). The urban stream syndrome: current Knowledge and the Search for a Cure. *Journal of the North American Benthological Society* 24, 706-723.
- Ward, S. N. (1998). On the consistency of earthquake moment release and space geodetic strain rates: Europe, *Geophysical Journal International*, 135(3), 1011-1018.
- Water NSW. Accessed via, <http://www.water.nsw.gov.au/water-management/basins-and-catchments/hawkesbury-catchment>
- Zhang, Y., Sillanpää, M., Li, C., Guo, J., Qu, B., & Kang, S. (2015). River water quality across the Himalayan regions: elemental concentrations in headwaters of Yarlung Tsangpo, Indus and Ganges River. *Environmental Earth Sciences*, 73(8), 4151-4163.

IoT based car accident detection and prevention using Naïve Bayes Classifier

Mohammad Sanaullah Chowdhury^{1,*}, Mubashir Murshed²

Department of Computer Science and Engineering University of Chittagong, Chittagong, Bangladesh h

*Corresponding author's email: ¹s.chowdhury@cu.ac.bd, ²mubashir.ma98@gmail.com

Peer review history

Manuscript submitted: 19 August 2019

Review process completed: 14 October 2019

Manuscript finally accepted: 17 October 2019

Handling Editor: Professor Chin Leo

Abstract: *Internet of Things (IoT) together with Machine Learning has a great impact on the new era of technology. Technological advancement and invention of smarter devices are going neck and neck in today's world. A common incident such as car accidents hampers the advancement of human life. Most common reasons for the accidents are - driver's unawareness and uncontrolled speed of*

vehicle. We have developed an IoT based solution to detect and prevent such incidents. This paper focuses on a smart system that alerts and controls the speed of the vehicle. It measures real-time distance between vehicles and/or obstacles in front of the vehicle using Ultrasonic sensor. It controls speed of the vehicle and alerts respective individuals if an accident occurs. The core processing unit of the proposed system is Raspberry Pi incorporating Naïve Bayes Classifier. The proposed system is implemented and the experimental results show that the system works properly in different road traffic situations.

Keywords: *Internet of Things (IoT), Car Accidents, Ultrasonic Sensor, Raspberry Pi, Naïve Bayes Classifier.*

1. Introduction

Internet of Things (IoT) brings the human civilization one step closer to direct communication between machines. It enables devices to communicate and exchange information between them, which lead them to take decisions and perform actions [1]. IoT allows real world devices a secure connection and exchange of real-time data [2]. By using this technology, billions of smart devices such as sensors or actuators connected to the internet, collect and share real world data and information [3].

Machine Learning is a fascinating term in this modern era of advanced technology that can enrich IoT by enabling devices to take decisions on their own [4]. Emerging IoT devices apply Machine Learning technologies that capture and understand data from the environment and help in more intelligent decision [4] [5]. Sensors, actuators, etc. collect data the from environment which can be used as raw materials for the Machine Learning that help IoT devices perform more intelligently [5] [6].

As technology advances, human civilization is facing problems also. Car accidents is one of them, which is a destructive incident that interferes with civilization advancement by taking valuable lives. According to a statistic of the World Health Organization (WHO), every year about 1.25 million people die in road traffic crashes [7]. In addition to that, approximately 20-50 million become injured or disabled. According to a study, 2.2% of deaths occur due to road traffic crashes, establishing it as the 9th leading cause of death around the globe. This phenomenon cost USD \$518 billion globally, which is 1-2% of annual GDP of an individual country.

The advancement of technology helps us to aid the challenge of reducing the number of road traffic accidents. IoT and Machine Learning application on vehicles can provide us a better solution to preventing road accidents and therefore increase the numbers of lives saved. A proper alert system to the responsible persons like police, ambulance, relatives can save many injured people from losing their lives.

In this paper, a smart system for vehicles is proposed which can reduce the number of accidents by controlling the vehicle speed, together with a proper alert system. One of the main focuses of this system is its speed controlling mechanism. As the vehicle speed can vary from road to road and also time to time, a light Machine Learning strategy named Naive Bayes Classifier, is used in this proposed system to update the speed control mechanism and alert the system behavior of a

vehicle.

The strategy is to have a control over the brake of a vehicle along with the gear system, that is applicable for both auto and manual transmission vehicle. Also, it provides real-time alerts to the driver to control the speed of the car. An email alert is available, to accountable persons if an accident occurs. The proposed method uses Naive Bayes Classifier to learn from the environment and also provides an updated alert and speed control mechanism depending on some parameters. Ultrasonic sensors can provide the real-time distance between two vehicles. This distance data is the raw material used by the Naive Bayes Classifier to update the system mechanism in order to understand road traffic situations. The proposed system is able to control speed, focusing on the busy and regular conditions of road traffic. The gear and braking system of the vehicle is controlled by using Servo Motor. Sound and visual alert equipments such as LED, buzzer, etc. provide an alert to the driver with a graphical user interface and voice feedback.

The rest of this paper is organized as follows: section II compares the proposed system with other related proposals. Section III describes the methodology of our proposed system, while section IV discusses its implementation and results. Section V contains the conclusion.

2. RELATED WORKS

In this section, related works regarding our proposed system is described in detail. Here, we focus on works done in the field of IoT. We proposed a straightforward approach of the alert and speed control mechanism without the application of Machine Learning in [8]. This system is designed to alert the driver. It does so by depending on certain criteria such as measuring a safe distance for suggesting a driver either to slow down or push brakes of the vehicle. When the distance between two vehicles becomes critical, the system will put the brake or change the gear by using Servo Motor to slow down the vehicle. There is also an email alert service for when an accident occurs. Limitation of this system is that it does not work with real time traffic.

In paper [9], the authors developed a system that detects car accidents. In their system, a vibration sensor detects accidents by a micro electro mechanical system and sends it to the microcontroller. GPS location address of the accident spot is provided to a police control room or a rescue team via the GPS modem. But this system carried no accident prevention mechanisms such as speed control or an alert system to control the speed before an accident takes place.

In [10], a system is proposed which is used for monitoring the eye closure ratio of the driver and detects the drowsiness of the driver by using Pi camera. If the eye closure ratio is less than the standard ratio, the driver gets an alert from a buzzer. This paper focuses on building an alert system to mitigate drowsiness of a driver. There is no speed control mechanism of the system. The authors in [11] proposed a system that detects accidents using vibration sensors, accelerometers and the accident location is detected by using a GPS and GSM module that informs nearby persons and hospitals through a text message. It also checks the driver drowsiness or unstable state using eye blink monitoring system, alcohol detection sensor, etc. This system has limitations, one of which is that the driver has to wear glasses at all times to be connected to the system. It can be quite uneasy for a person to wear glasses. Also, there is no speed control mechanism in this system. In [12], the authors proposed a system which has both accident prevention and detection mechanisms. This is done by using IR sensors that can detect accidents. SMS alert is available to the predefined numbers with location address using GSM module. Accident prevention is carried out by IR sensors by warning the driver when the distance between vehicles is close. This system still lacks a speed controlling mechanism and no machine learning approach is applied to make it smarter. The reference [13] proposed an alert system either for an accident or theft by providing the accident location using microcontrollers, embedded sensors and cloud services. It also has no mechanism to prevent accident from happening.

To the best of our knowledge, there exists no system that detects and prevents accidents for the real time traffic scenario as described. Therefore, we propose an IoT based car accident detection and prevention system using machine learning in this paper.

3. METHODOLOGY

This section describes the methodology of our proposed system in detail. In this paper, a smart system is proposed which helps to prevent car accidents, alerts the driver from time to time to control the speed of that car, and controls the speed of

the car by the system when necessary, based on real-time captured data from the environment. It also alerts responsible persons when an accident has occurred for any uncertain situation. This smart system is easily applicable for both existing and new vehicles.

A. Proposed System Overview

Our proposed system is composed of a few components that perform operations individually to run the overall system. An ultrasonic sensor is placed in front of the vehicle which always measures the distance between vehicles or obstacles in front of the vehicle. This measurement data is preserved to update the Naive Bayes Classifier's dataset which is used to predict the behavioral performance of our proposed system. The alert and speed control systems work differently for busy and idle periods of road traffic, which is predicted using criteria such as time, location, etc. Servo Motor is used to control the braking mechanism as well as for controlling the gear system of a vehicle. Sound and visual alert equipment like Buzzer, LED, etc. are used to provide an alert in different situations. A Graphical User Interface (GUI) is placed in front of the driver which provides alerts with real-time distance between vehicles in order to concern the driver. An email alert system is available for any uncertainty. Raspberry Pi is the main processing unit of our proposed system to control and process the whole operation. The block diagram of our proposed system is shown in Figure 1.

B. Processing Unit

The processing unit of our proposed system is Raspberry Pi [14], which is a single-board computer with BCM43438 wireless LAN and Bluetooth Low Energy (BLE), GPIO, USB and HDMI Port. It is a low-cost device with a relatively high processing unit of 1.4GHz and a 64bit quad-core processor. The main features of Raspberry Pi are: it is portable, easily programmable and interfaceable to a large number of hardwares and sensors. Raspberry Pi consumes low power as well, and can perform operations with real-time sensor data. This is suitable for our proposed system to perform the desired operations efficiently.

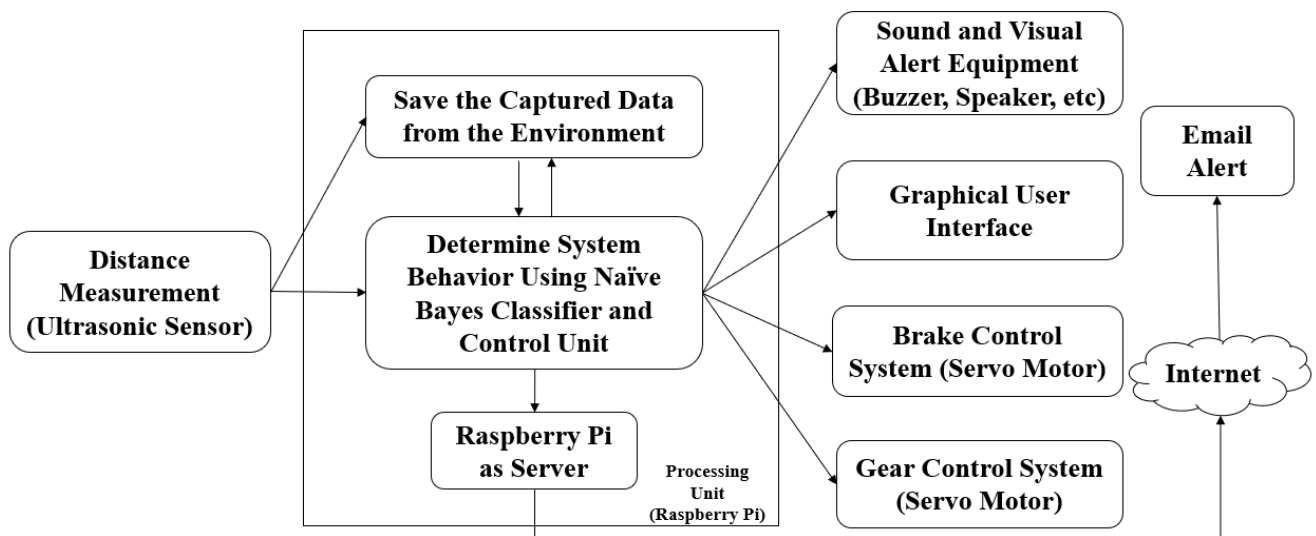


Figure 1. Block diagram of the proposed system

C. Distance Measurement

In our proposed system, in order to measure the distance between two vehicles or to measure the distance between the vehicle and an object in front, an Ultrasonic Sensor is used. This sensor uses sound waves to measure the distance. It does so by calculating the emission and reception time of the sound wave. This sensor can measure a large distance which is enough for road side data and has a desirable accuracy rate which is not affected by the accumulation of dust or dirt. The performance of the Ultrasonic Sensor is adaptable for road side real-time distance data, because its initialization time of measuring distance is a few microseconds.

The HC-SR04 Ultrasonic Sensor was used for building the prototype of our proposed system. It can initialize its measuring operation within 10 micro seconds of time.

D. System Behavior Determination using Naïve Bayes Classifier

The system behavior of our proposed system varies depending on road traffic situations. During a busy traffic period, its alert and speed control mechanism work on a closer distance than regular road traffic conditions. The system behavior can be determined by using some parameters/predictors, such as time, day, location, last 15 minutes of average speed of the vehicle, etc. If we look at the situation of roads, traffic in a commercial area is heavier than a residential area and traffic is also higher during peak hour. Tourist spots are busier in holidays. We have used Naive Bayes Classifier to determine the behavioral approach of this system.

a) Naïve Bayes Classifier

Naive Bayes is a classification technique based on Bayes Theorem, which can assume predictors independently, that is all the predictors have an equal effect on the outcome [15] [16] [17]. The mathematical expression [15] [16] of Bayes theorem is stated in equation no. 1,

$$P(y|X) = \frac{P(X|y)P(y)}{P(X)} \quad (1)$$

The variable y is the class variable (busy, normal, free condition of a road), variable X represent the parameters that helps to predict the class, shown in equation no 2,

$$X = x_1, x_2, x_3, \dots, x_n \quad (2)$$

Here $x_1, x_2, x_3, \dots, x_n$ represent the predictors, i.e. they are mapped to location, day, time and last 15 minutes of average speed of the vehicle. By substituting for X and expanding using the chain rule, we arrive at the result of y, such as busy, normal, free. The equation is shown in equation no. 3,

$$P(y|x_1, \dots, x_n) = \frac{P(x_1|y) P(x_2|y) \dots P(x_n|y) P(y)}{P(x_1) P(x_2) \dots P(x_n)} \quad (3)$$

As we are using Raspberry Pi as the main processor of our proposed system, we need a light Machine Learning technique to cope with the low processing unit. Naive Bayes is faster and easier to implement with less data and it does not require an extra training period to train the dataset, which helps to have a higher performance rate on the Raspberry Pi board.

Additionally, it can also be maintained by addition or removal of parameters, which is useful for predicting in any road around the whole world. Another notable feature of the Naïve Bayes Classifier is that it is not reliant on any fixed dataset, so it is not required to monitor the accuracy of any trained model or dataset. Our proposed system can predict the class (free, normal, busy) in a real-time manner by capturing data from the environment.

b) Dataset

Our proposed system uses a dataset that is captured and learned from the environment. A vehicle runs faster on a highway and sometimes there is a speed limit. During festive season, highways can be busier than on regular days. Also, a commercial area is busier during office hours than others. Our system can understand road traffic conditions by using distance data provided by Ultrasonic Sensor.

As road traffic condition varies, we cannot use a fixed Machine Learning model. Our proposed system learns from the environment and captures location, day, time, last 15 minutes of speed of the vehicle which are used for the dataset. Using these data, system behavior is determined and the dataset is updated for certain conditions/situations.

Some default rules are inbuilt, such as alert for when the distance reaches 30 meters between two vehicle and the speed control mechanism performs within 5m distance etc. The dataset gets updated even if a certain location cannot provide a good prediction using the captured data or due to unavailability of internet to identify any location along with other uncertain situations. An example of a dataset in Chittagong City of Bangladesh is shown in Table 1.

The GPS location is captured by using the GPS module that is interfaced with the Raspberry Pi board. The latitude and longitude, which is acquired by using the GPS module, is converted to a textual form of the location's name to perform operation for predicting a class in discrete manner. Date and time can easily be acquired from the OS using simple Python programming. The speedometer of the vehicle provides the last 15 minutes of speed, which is further processed by Raspberry Pi.

c) System Behavior Determination by using Real-Time Captured Data

Ultrasonic Sensor provides real-time distance data between vehicles. The alert and the speed control mechanism operate

based on the distance data between vehicles or object in front of the vehicle. The parameters/features of the dataset are used to predict a certain class. In our proposed system, three classes have been used for operating on busy (class 3), normal (class 2), free (class 1) road traffic situations (shown in the dataset in Table no 1).

In Chittagong city of Bangladesh, there is a rush hour in the evening on the GEC Road. A car where our system has been installed, has a dataset including GPS location, day, time and last 15 minutes of speed. It also has an Ultrasonic Sensor which provides data of the nearest object distance in front of the car. By using all of these data, Naïve Bayes Classifier predicts class 3, which means the vehicle will alert or control the speed within a short distance as the road seems busy.

E. Speed Control Mechanism

In this paper, our proposed method focuses on prevention of accident. A vehicle should have speed control system of its own when the driver doesn't respond or failed to control the speed at a critical distance from another vehicle or object. Here, we propose a smart system which is workable for both Automatic and Manual Transmission Vehicle/Car.

a) Manual Transmission Car

In a manual transmission car, to control the speed of a vehicle i.e. slowing down a car needs control over the brake and clutch with the shifting of gear [18] [20]. Reduction in gearing is a proper way to slow down a car engine that run at high speeds. The gearbox which provides a selection of gears to control the car speed in different situations. The lower gear turns the car wheels slower, with comparison to the engine speed. The clutch system can stop a car without killing the engine [18]. The clutch can smoothly perform the operation of engaging a spinning engine to a non-spinning engine.

Servo Motor which is a rotary or linear actuator that allows for precise control of angular or linear position, is also suitable to use in a closed-loop control system [19]. As we see the clutch and the gear control mechanism, they can be controlled by using the Servo Motor working principle.

A Servo Motor has to be placed on the gearbox, near the fork of the gear. This motor can change the gear by performing its angular movement. Another is placed beside the clutch and the brake paddle in order to press on them. The Servo Motor is able to return to its previous position by angular movements [19]. This explains how the speed control system is able to be back in the initial position after each operation. Figure 2 shows the block diagram of the gearbox with Servo Motor in the proposed position and Figure 3 shows the block diagram of the clutch system with the Servo Motor.

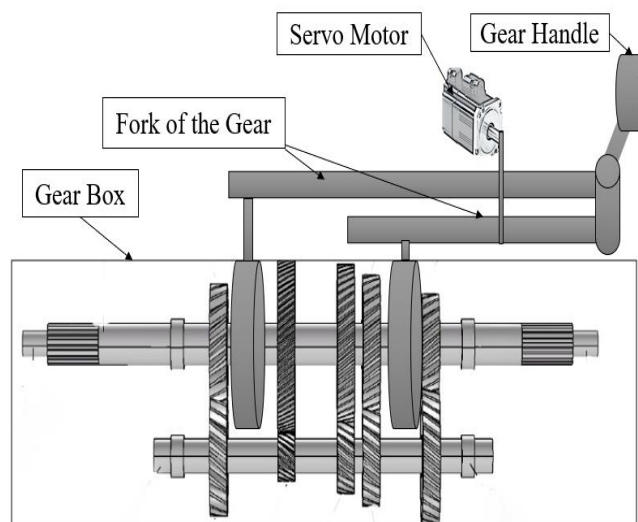


Figure 2. Block diagram of the gear control system with servo motor

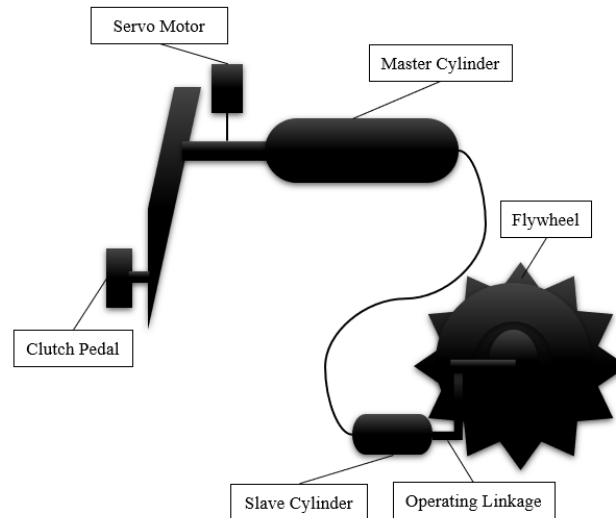


Figure 3. Block diagram of the clutch system of a car with servo motor

b) Auto Transmission Car

In the current age, most modern vehicles are following the auto transmission system. They have brakes on all four wheels of the hydraulic system to control vehicle speed [21] [22]. In a hydraulic brake circuit, the fluid-filled master and slave cylinders are connected by pipes. As soon as the brake pedal is pressed, it depresses a piston in the master cylinder, forcing fluid along the pipe. The fluid travels to the slave cylinders at each wheel and fills them, forcing the pistons out to apply the brakes [20] [21] [22]. This setup allows greater force to be applied by the brakes, in the same way a lever does its work.

According to an auto transmission car braking system, we only need to press the brake pedal to have control over the car speed [21]. A Servo Motor placed beside the brake pedal can perform pressing operations with its working principle. In figure 4, the block diagram of the braking system with is shown with the Servo Motor proposed position indicated in the figure.

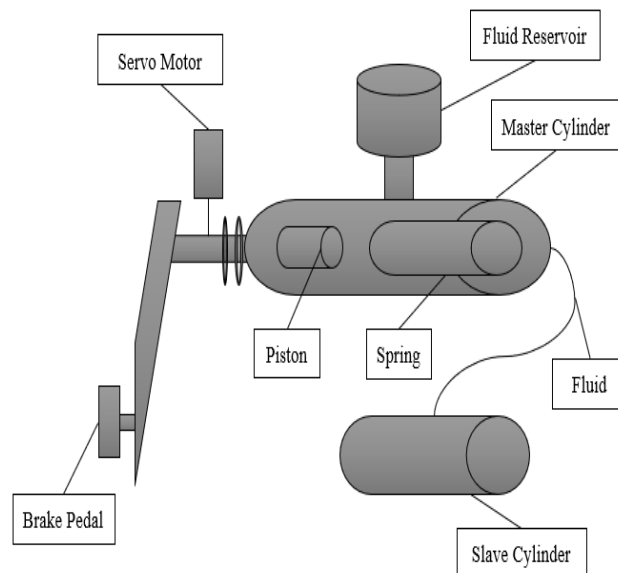


Figure 4. Block diagram of the braking system of auto transmission car with servo motor

F. System's Alert Working Principle

The proposed system provides different types of alerts depending on the road traffic condition. This alert system works for both alerting the driver and the responsible person for any uncertainty. The system sends an alert to the driver depending on the different traffic situations of a road. When two vehicles come close, an alarm in the car is placed as an

initial awareness. The yellow led alert with a Buzzer sound and voice feedback plays as a risk indication. If there comes a critical position between two vehicles, the red LED alert is shown with a Buzzer sound and voice alert. The system constantly keeps showing the distance between two vehicles on a Graphical User Interface. The calculated distance helps driver to determine actual distance between two vehicles. Our system also includes alarm to alert the driver. When the distance between two vehicles becomes critical and the driver doesn't respond, the system performs its operation of slowing down or stopping the vehicle by itself. Hypothetically, if an accident happens, the system will send an email as a rescue alert with car details and a GPS location of the accident spot to the authorities. The flow chart of our proposed system is shown in Figure 5.

4. IMPLEMENTATION AND RESULTS

The method of implementation of our proposed system is discussed in this section with results. For implementing our proposed system, we have used hardware, such as Ultrasonic Sensor, Servo Motor, Buzzer, LED, GPS module and a normal sound system for voice feedback. Raspberry Pi has been used as the main controlling unit. We programmed the system with the Python programming language which is efficient and easy to program with large numbers of library functions that deal with hardware components.

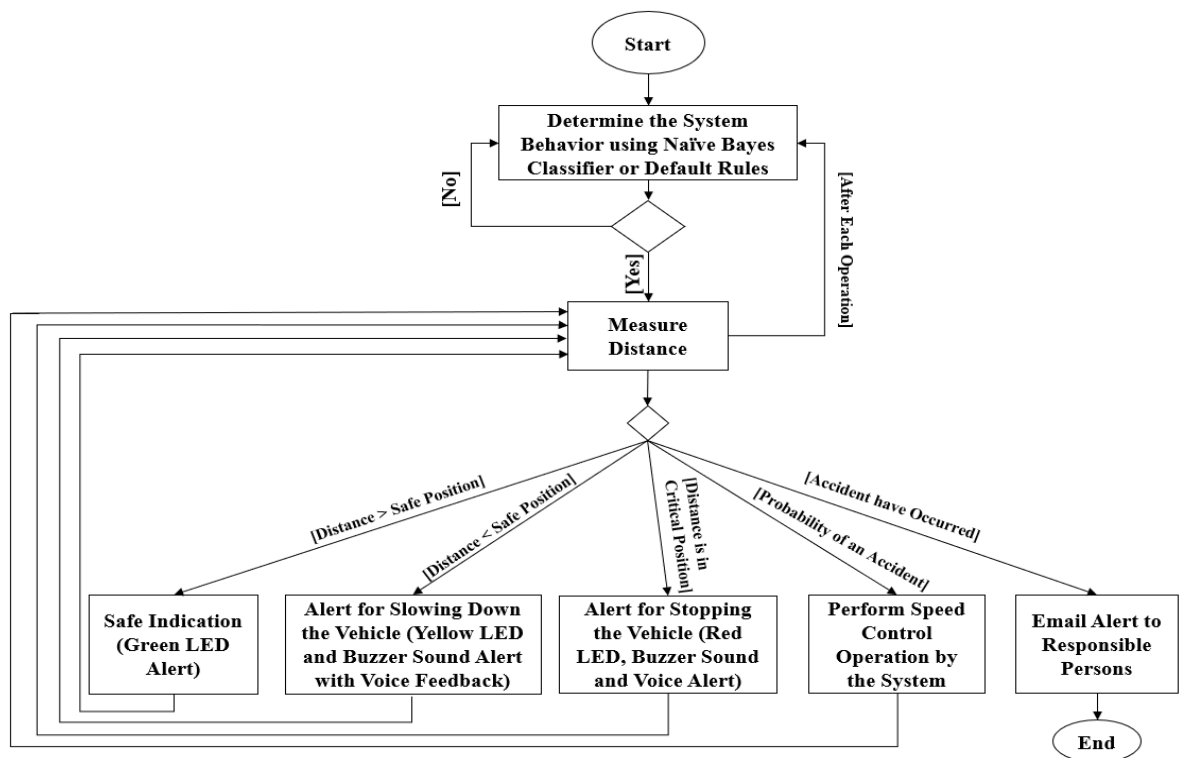


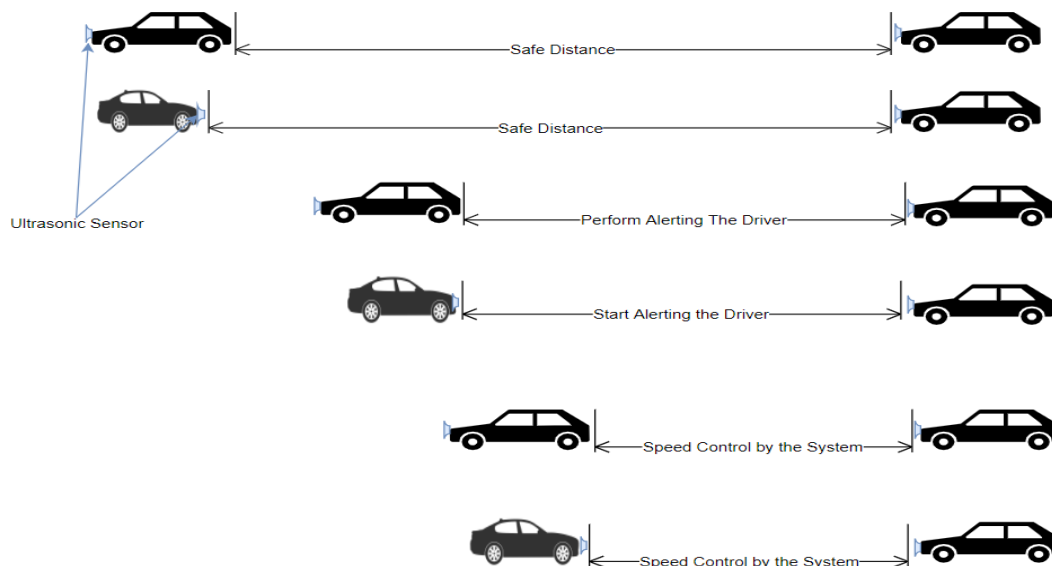
Figure 5. Flow chart of the proposed system

Ultrasonic Sensor captures real-time distance data which is shown in Figure 8 and is also saved in a text/excel file (shown in Table 1) for further processing by using simple Python programming language. This data is necessary for Naïve Bayes Classifier operation handling, which is programmed by a Machine Learning tool named Scikit-Learn. GPS location address which is captured by using the GPS module on a road, will be preserved in a text/excel file that is usable for updating dataset, and for providing location address as Email alert when necessary. The GPS location address (longitude and latitude) is converted to the location name by simple Python programming for discrete class prediction by Naïve Bayes Classifier.

Table 1 shows an example of a captured dataset from an experimental environment. Our proposed system always checks the current location's dataset. When a new GPS location address is retrieved, the dataset of that location is updated for that certain city. If the system has less data or no data to perform the operation of Naïve Bayes Classifier at a certain location,

Table 1. Example of a dataset

Location	Day	Time	Last 15 avg minutes speed	Class
New market road	Sat	Morning	40	1
Agrabad road	Mon	Evening	8	3
GEC road	Tue	Evening	5	3
Oxygen road	Wed	Night	50	1
GEC road	Mon	Evening	9	3
New market road	Sun	Noon	20	2
GEC road	Fri	Morning	40	3
Oxygen road	Wed	Night	45	3
2no gate road	Fri	Morning	40	3
New market road	Sun	Evening	5	1
GEC road	Fri	Evening	20	2
Oxygen road	Sun	Noon	8	1
2no gate road	Mon	Noon	5	1
GEC road	Mon	Night	40	3
New market road	Thurs	Evening	10	1

**Figure 6.** Some experimental scenarios of the proposed system

or it does not have a probability greater than the threshold value for any class, it applies the default rules and updates datasets for later processing. This system gathers knowledge about traffic conditions of a road by analyzing distance data which is captured by Ultrasonic Sensor. It always checks the last 15 minutes of average speed of a vehicle, and then compares it with the distance data in order to analyze the situation of traffic on a road for certain periods of time. We have used location, day, time and the last 15 minutes of speed of the car as the parameters for the Naive Bayes Classifier. There are three classes (busy, normal, free) to determine the road traffic situation. Our prototype used a threshold of 0.4 to select a class. If Naive Bayes Classifier provides a class probability greater than 0.4, that class will be selected for determining system behavior. If a situation arises where no class has a probability greater than the threshold, the proposed system performs its default rules to select the system behavior on that location. It also updates the dataset of that location for future operation. The threshold of our prototype was selected at 0.4 to cope with four parameters efficiently, and to maintain a large range of probability values of a class, in comparison with others, when selected as the system behavior.

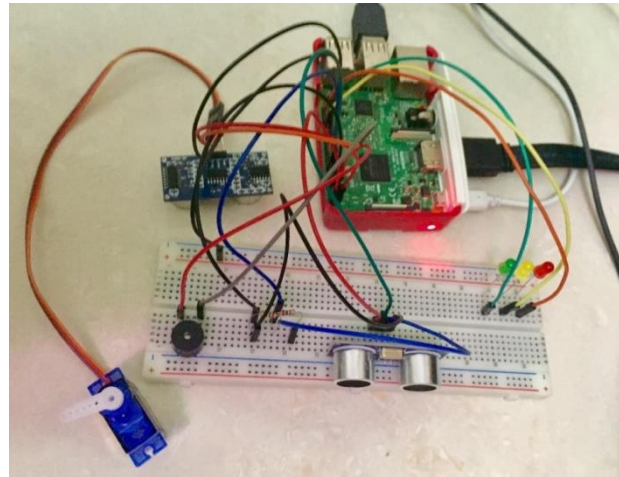


Figure 7. Experimental setup of the proposed system

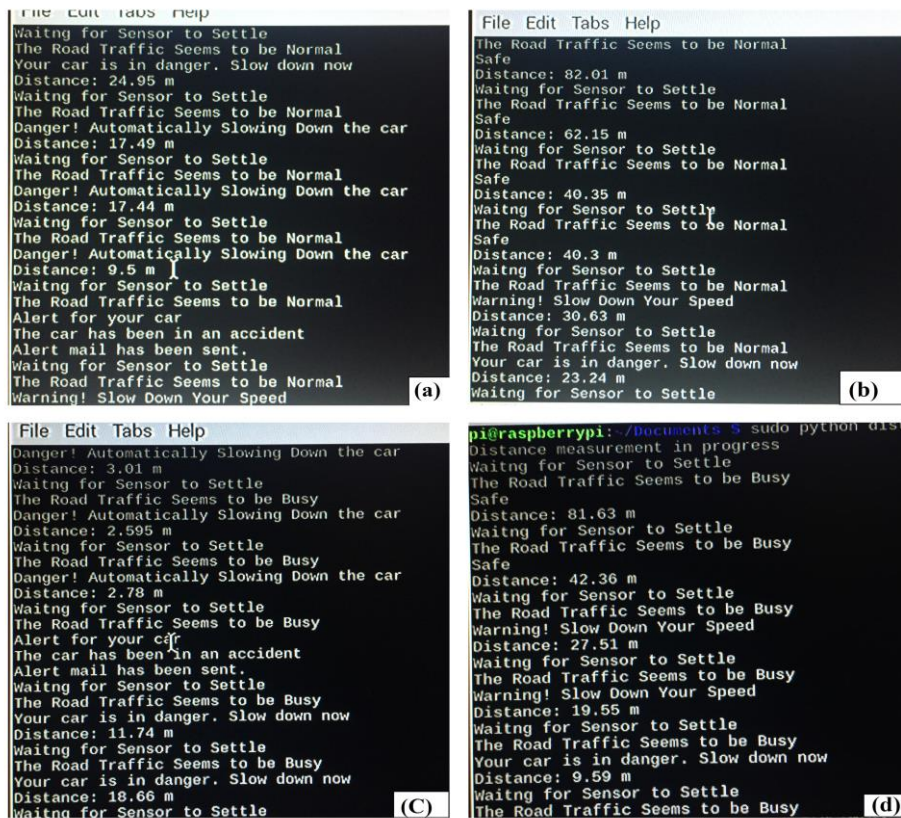


Figure 8: Awareness text produced for the driver

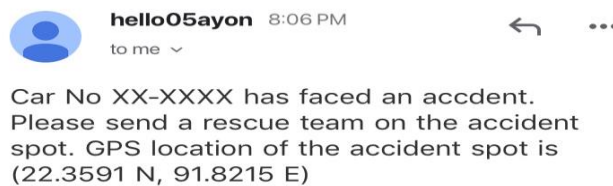


Figure 9: Email alert to the responsible person

The predicted result of Naïve Bayes Classifier is always between the ranges of 0 to1. Hence, we consider a certain value in between this range effective for predicting a class. We focus on a threshold for our proposed system. The dataset

always gets updated according to the different traffic condition depending on time and place. Therefore a fixed dataset or model cannot be applied and we should not deal with a pre-trained model in order to maintain accuracy for determining system behavior in a real time manner.

Some experimental scenarios of our proposed system on the road is shown in Figure 6. Our proposed system is implemented as shown in Figure 7. The results are shown in Figure 8 and Figure 9.

Figure 8 shows the Graphical User Interface that will be placed in front of the driver's seat. It displays the various road traffic situations and how the system acts. Figures 8(a) and 8(b) show the system behavior for regular traffic on a road, and Figures 8(c) and 8(d) show a busy road traffic condition. The proposed system predicts busy traffic conditions on the road, in which case the system performs its operation on a closer distance than regular road traffic situations. In this proposed system, Email Alert service is implemented by using Python library and Gmail Server which is free. Others email servers can also be used. Figure 9 shows the Email Alert system which will be available to responsible persons if an accident occurs.

5. CONCLUSION

We have introduced a low cost, reliable, reusable and easily maintainable system, focusing on the detection and prevention of car accidents. We have implemented a smart IoT based system, which can control the speed of a vehicle automatically whenever there is a risk of an accidental incident. The experimental results show that it works with real-time data from the environment which is processed by Naïve Bayes Classifier efficiently. One of the most useful traits of Naïve Bayes classifier is that it can work with low processing units (in our case, Raspberry Pi). Our proposed system predicts and determines the system behavior by considering the threshold value for the real-time captured dataset. As a result, the system performs well. The results show that the integration of IoT and Naïve Bayes Classifier yields detection and prevention of car accidents in real time traffic.

The proposed system fulfills most of the necessities of a smart system with minimal effort and maximum gain. Our proposed system works in an efficient manner on roads with a 4G/high speed internet connection.

Moreover, the location provided by the GPS module used in this system helps in rescuing victims by providing prompt email alerts.

The motivation behind designing this system is the desire to reduce car accidents and reach increased system performance overall. The future works of this system may include concentrating on integrating new features with technological advancements.

References

- [1] Khan, Rafiullah, et al. "Future internet: the internet of things architecture, possible applications and key challenges." 2012 10th international conference on frontiers of information technology. IEEE, 2012.
- [2] Ammar, Mahmoud, Giovanni Russello, and Bruno Crispo. "Internet of Things: A survey on the security of IoT frameworks" *Journal of Information Security and Applications* 38 (2018): 8-27.
- [3] Ray, P. P. (2018). A survey on Internet of Things architectures. *Journal of King Saud University-Computer and Information Sciences*, 30(3), 291-319.
- [4] Mahdavinjad, Mohammad Saeid, et al. "Machine learning for Internet of Things data analysis: A survey." *Digital Communications and Networks* 4.3 (2018): 161-175..
- [5] Tang, Jie, et al. "Enabling deep learning on IoT devices." *Computer* 50.10 (2017): 92-96.
- [6] Mishra, Nilamadhab, Chung-Chih Lin, and Hsien-Tsung Chang. "A cognitive adopted framework for IoT big-data management and knowledge discovery prospective." *International Journal of Distributed Sensor Networks* 11.10 (2015): 718390.
- [7] Road Traffic Crash Statistic, "World Health Organization (WHO)".
- [8] Mubashir Murshed and Md Sanaullah Chowdhury, "An IoT Based Car Accident Prevention and Detection System with Smart Brake Control" – International Conference on Application and Techniques on Information Science (ICATIS), January 2019. [in press]

- [9] Prabha, R.Sunitha , R.Anitha “Automatic Vehicle Accident Detection and Messaging System Using GSM and GPS Modem” International Journal of Advanced Research in Electrical, Electronics and Instrumentation Engineering, Vol. 3, Issue 7, July 2014.
- [10] M. Y. Hossain and F. P. George, "IOT Based Real-Time Drowsy Driving Detection System for the Prevention of Road Accidents," 2018 International Conference on Intelligent Informatics and Biomedical Sciences (ICIIBMS), Bangkok, 2018, pp. 190-195.
- [11] S. Nanda, H. Joshi and S. Khairnar, "An IOT Based Smart System for Accident Prevention and Detection," 2018 Fourth International Conference on Computing Communication Control and Automation (ICCUBE), Pune, India, 2018, pp. 1-6.
- [12] N. T. S. A. Wadhahi, S. M. Hussain, K. M. Yosof, S. A. Hussain and A. V. Singh, "Accidents Detection and Prevention System to reduce Traffic Hazards using IR Sensors," 2018 7th International Conference on Reliability, Infocom Technologies and Optimization (Trends and Future Directions) (ICRITO), Noida, India, 2018, pp. 737-741.
- [13] Sarasvathi, Nahalingham and Fong, Jason Zu XiN (2018) “Study and Implementation of Internet of Things (IoT) Based Vehicle Safety Alert and Tracking Syste” - INTI Journal, 1 (10). pp. 1-11. ISSN e2600-7920.
- [14] Richardson, Matt, and Shawn Wallace. Getting started with raspberry PI. " O'Reilly Media, Inc.", 2012.
- [15] Tina R. Patil, Mrs. S. S. Sherekar, “Performance Analysis of Naive Bayes and J48 Classification Algorithm for Data Classification” - International Journal of Computer Science and Application, Vol. 6, No.2, Apr 2013 ISSN: 0974-1011.
- [16] Rish, Irina. "An empirical study of the naive Bayes classifier." IJCAI 2001 workshop on empirical methods in artificial intelligence. Vol. 3. No. 22. 2001.
- [17] Dewan Md. Farid, Li Zhang, Chowdhury Mofizur Rahman, M.A. Hossain, Rebecca Strachan, “Hybrid decision tree and naive Bayes classifiers for multi-class classification tasks” Expert Systems with Applications, Volume 41, Issue 4, Part 2, March 2014, Pages 1937-1946.
- [18] Orthwein, William C. Clutches and brakes: design and selection. CRC Press, 2004.
- [19] Andrews, Nicholas W. "Adaptive servomotor control." U.S. Patent No. 4,609,855. 2 Sep. 1986.
- [20] Linde, Arvid. How your car works-Your guide to the components & systems of modern cars, including hybrid & electric vehicles. Veloce Publishing Ltd, 2011.
- [21] Nice, Karim. "How automatic transmissions work." HowStuffWorks. com (2000).
- [22] Milanés, V., González, C., Naranjo, J.E., Onieva, E. and De Pedro, T., 2010. Electro-hydraulic braking system for autonomous vehicles. International Journal of Automotive Technology, 11(1), pp.89-95.

Table of Contents

Stability analysis of continuous welded rails using new non-destructive technology <i>Ralph Zhang, Helen Wu, and Chunhui Yang</i>	1
Experimental and numerical studies on SCFs of empty SHS-SHS T-joints under in-plane bending. <i>Feleb N Matti1 and Fidelis R Mashiri</i>	17
Numerical investigation of modified splice plate beam-to-beam connections for prefabricated composite structure. <i>Md Kamrul Hassan and Susma Tajhya</i>	27
Experimental study of bending stiffness variation during a full rotation of cracked shafts. <i>Erfan Taheri, Helen Wu and Ming Zhao</i>	36
Modal analysis of cracked shafts. <i>Erfan Taheri, Helen Wu and Ming Zhao</i>	42
The influence of irrigation area and roof size on the economics of rainwater harvesting use in urban agriculture: a case study in Sydney, Australia. <i>Caleb Christian Amos and Fazlul Karim</i>	48
Energy and exergy analyses of a flat plate solar collector using different nanofluids. <i>Mohammad A. Alim, M.A. Khairul, M. Fazal, R. Saidur, Md Jaynul Abden</i>	59
Morphological assessment of a selected reach of the Jamuna River using the Delft3D Model. <i>Orpita Urmi Laz and Umme Kulsum Navera</i>	72
Impact of urbanization on CO2 and TVOC in an oasis city in Saudi Arabia <i>Muhammad Muhitir Rahman, Ziad Shatnawi, Md Kamrul Islam and Ammar Al-Shayeb</i>	82
Selection of the Best-fit Probability Distribution for Brisbane River Catchment <i>S M Anwar Hossain</i>	90
Water Education: A Case Study in New South Wales Australia <i>Jenis F Islam, Sumya Rahman and Imran Rahman</i>	104
Application of water quality index to identify deteriorated river sections—A case study for the Hawkesbury Nepean River System in Australia <i>Upeka Kuruppu and M Azizur Rahman</i>	124
IoT Based Car Accident Prevention and Detection Using Machine Learning <i>Mohammad Sanaullah Chowdhury and Mubashir Murshed</i>	132



IJECC
International Journal of Engineering,
Construction and Computing

***International Journal of Engineering, Construction and
Computing***

(IJECC)

ISSN: 2209-332X(Print)

